A major purpose of the Technical Information Center is to provide the broadest dissemination possible of information contained in DOE's Research and Development Reports to business, industry, the academic community, and federal, state and local governments.

Although a small portion of this report is not reproducible, it is being made available to expedite the availability of information on the research discussed herein.

ORNL--5960

DE83 013725

ORNL-5960
Distribution
Category UC-77

GAS-COOLED REACTOR PROGRAMS

# HIGH-TEMPERATURE GAS-COOLED REACTOR TECHNOLOGY DEVELOPMENT PROGRAM

## ANNUAL PROGRESS REPORT FOR PERIOD ENDING DECEMBER 31, 1982

Paul R. Kasten, Program Director

P. L. Rittenhouse, Base Technology Program Manager

D. E. Bartine, Physics and Shielding Program Manager

J. P. Sanders, Component Flow Testing Program Manager

Date Published — June 1983



Prepared by the
OAK RIDGE NATIONAL LABORATORY
Oak Ridge, Tennessee 37830
operated by
UNION CARBIDE CORPORATION
for the
DEPARTMENT OF ENERGY
under Contract No. W-7405-eng-26

CONTENTS

## FOREWORD

During 1982 the High-Temperature Gas-Cooled Reactor (HTGR) Technology Program at Oak Ridge National Laboratory (ORNL) continued to develop experimental data required for the design and licensing of cogeneration HTGRs. Our program involves fuels and materials development (including metals, graphite, ceramic, and concrete materials), HTGR chemistry studies, structural component development and testing, reactor physics and shielding studies, performance testing of the reactor core support structure, and HTGR application and evaluation studies.

Our work in fuels has provided detailed statistical information on the fission product-retention performance of irradiated coated particle fuels, and this work will continue to be an important part of our program. The materials studies provide basic data on the mechanical, physical, and chemical behavior of HTGR materials, including concrete. We also perform experimental studies on the behavior of actinides in graphite. Our work in component development and testing has continued to emphasize construction of the core support performance test, fabrication of an assembly to mock up the lower portions of an HTGR core for use in a shielding experiment, testing the performance of weld cladding as deposited on material to be used in steam generators, and testing of core support ceramics. Our studies and evaluations have concentrated on relatively small modular reactor studies, for which we are serving as peer reviewer of modular HTGR designs being developed by GA Technologies, Inc. (GA), and General Electric Company (GE). Work was also performed on preliminary evaluation of the national need for developing HTGRs, with emphasis on the longer term HTGR applications to fossil conversion processes.

It is anticipated that the near-term national program will continue to emphasize the cogeneration HTGR as a means of decreasing future imports of oil, that there will be greater recognition of the national importance of HTGR commercialization, and that ORNL will continue to have an important participation in HTGR development.

Paul R. Kasten

## SUMMARY

### 1. HTGR CHEMISTRY

The objective of this task is to develop data needed for the prediction of actinide and fission product transport in HTGR systems under both operating and off-normal conditions. Two studies were pursued in 1982. In the first, diffusion coefficients were determined for uranium (as $UO_2$ and $UC_2$) in H451 graphite from 900 to 1400°C. Diffusion coefficients were higher for $UC_2$ but significantly so at only the highest temperature. The second study involved the vapor pressure of plutonium adsorbed on H451 graphite. At 1400°C the vapor pressure was about 0.4 mPa for an adsorbed plutonium concentration of 0.6 $mg/m^2$. The data were collected in a regime of flow rates over which the plutonium vapor density remained constant.

### 2. FUELED GRAPHITE DEVELOPMENT

The Fueled Graphite Development Program at Oak Ridge National Laboratory (ORNL) continues as part of the national High-Temperature Gas-Cooled Reactor (HTGR) fuel development effort being conducted in cooperation with GA Technologies, Inc. (GA). The ORNL portion of the program includes irradiation testing of fuel fabrication by GA in irradiation capsules assembled by ORNL and operated in ORNL reactors. ORNL also conducts postirradiation examinations on the irradiated fuel in special equipment developed for this purpose.

In addition to the cooperation with GA, the ORNL program includes specific cooperative tasks with the German Nuclear Research Center at Jülich [Kernforschungsanlage (KFA) Jülich]. The cooperation with KFA is part of a formal agreement between the U.S. and German governments for gas-cooled reactor development, under which several cooperative projects have been completed during the past several years. Two areas of cooperation were active during this reporting period.

The Fueled Graphite Development Program is organized around four subtasks: (1) Irradiation Testing, (2) Postirradiation Examination (PIE), (3) U.S./Federal Republic of Germany (FRG) Cooperative Work, and (4) PIE Equipment Development and Maintenance. In the irradiation testing area, capsule design was completed for a fuel hydrolysis experiment. This experiment is designated HRB-17 and -18 (two capsules). The experiment will feature injection of controlled quantities of moisture into an operating capsule that contains failed fuel. The major goal of the experiment is to measure the behavior of the failed fuel in the presence of moisture. In addition, postirradiation thermal analysis for capsule HRB-16 was completed. Eighteen fuel rods were irradiated in this capsule, for which the time-averaged irradiation temperatures ranged from 1044°C (for rod 1) to 1212°C (for rod 10 at the center of the capsule).

In the PIE area, evaluation of coated fuel specimens irradiated in capsule HT-35 was partially completed during the reporting period. Transmission electron microscopy (TEM) examinations of SiC coatings irradiated on inert (carbon) kernels revealed that stacking faults appear to be a strong sink for point defects. Void formation was not observed in the coatings examined. Irradiation appears to have caused no significant restructuring of the coating. Irradiated microsphere gamma analyzer (IMGA) examinations showed good retention of fission products. Histograms of several fission product activity ratios were obtained, but no detailed analysis of the data have been completed as yet.

Cesium and fission gas retention data obtained from capsule HRB-15b were summarized. Examination of coated fuel specimens irradiated in capsule HRB-15a was completed. The thermal performance of the four candidate kernel types ($UO_2$, $UC_2$, $UC_xO_y$, and buffered $UO_2$) was generally about as expected. However, the performance of the ZrC-buffered $UO_2$ kernels was surprisingly good. The examination of HRB-15a irradiated specimens confirmed our conclusion that palladium attack of SiC and silver diffusion through SiC were independent of kernel type but were dependent on the quality of SiC coatings.

Under the U.S./FRG cooperative program, final reporting of work under PWS FD-12 (pyrocarbon coating permeability to fission gas) and PWS FD-13 [IMGA/postirradiation annealing and beta autoradiography (PIAA) comparison] was completed. Examination of the first set of German particles under PWS FD-20 [IMGA, postirradiation gas analyzer (PGA), and electron microprobe examination of German irradiated fuels] was completed and reported.

In the area of equipment development and maintenance, several maintenance problems were encountered with the IMGA system. A new system was specified and bids placed; the new system is expected to be purchased and installed during 1983. The PGA system was upgraded by the addition of a quadrupole mass spectrometer for use with the hot-particle breaking station.

## 3. STRUCTURAL COMPONENT DEVELOPMENT AND TESTING

The Structural Component Development and Testing research and development task consists of generic studies designed to provide technical support for ongoing prestressed concrete reactor vessel (PCRV)-related activities, to contribute to the technological data base, and to provide independent review and evaluation of the relevant technology. During this reporting period, work was organized into three subtask areas: (1) analysis methods development, (2) concrete properties for reactor applications, and (3) structural component testing. Highlights of work under each of these subtask areas are

### Analysis Methods Development

- Completed implementation of the set of computer subroutines for finite-element computation of creep effects in concrete structures.

A series of simple test problems and one large reactor problem were considered to illustrate program capabilities. Routines provide for the consideration of concrete aging and temperature effects on creep rate and rate of aging.

- Completed implementation of embedded-rebar modeling concept into ORNL two- and three-dimensional versions of the ADINA finite-element code. Analyses were conducted of end anchor test specimens simulating the anchorage zones of posttensioned tendons in secondary containment vessels of nuclear power plants. The technique that was developed facilitates modeling of complex arrays of rebars in concrete structures.

Concrete Properties for Reactor Applications

- Completed a review of aggregate sources and impact of aggregate availability on production of high-strength concrete. The results indicated that suitable supplies of aggregate materials are available but that in some areas a cost penalty may result from transportation charges to obtain suitable aggregates for high-strength concrete production.

- Completed revision of performance specification for concrete elevated-temperature multiaxial material testing system. The revision was based on the impact from potential vendors. When fabricated, the system will provide data representative of PCRV concrete behavior under normal and postulated accident conditions.

Structural Component Testing

- Completed fabrication of PCRV models and all ancillary equipment required for demonstration of model testing techniques developed. Successful testing of models will show validity of techniques developed to prestress PCRV models circumferentially and will provide model liner systems that do not leak prematurely.

- Completed first phase of structural response testing of thermal barrier hard ceramic materials. Rotations, axial and circumferential strains, and acoustic emission data were obtained from pads subjected to mechanical loading conditions representative of those imposed on the pads by thermal gradients. Results obtained provide an indication of the ability of typical ceramic pads to withstand thermal gradient and mechanical loading conditions.

## 4. HTGR STRUCTURAL MATERIALS

The ORNL work on HTGR structural alloys and ceramics is an integrated part of the U.S. effort to generate the data required for design of major components of the steam cycle-cogeneration HTGR plant. Activities in 1982 are noted by major task areas of the ORNL materials program.

## Mechanical Properties

A number of creep tests of Hastelloy X and 2 1/4 Cr-1 Mo steel are approaching 50,000 h. Other alloys emphasized during the year were Inconel 617 and 618. The former has exhibited very low creep fracture strain at about 650°C, and the latter is a possible substitute in this temperature range. Creep testing of Inconel 718 was initiated late in the year.

Samples of Inconel 617 and Hastelloy X were tested following 20,000-h exposures to inert gas and to HTGR He. Fracture strain at ambient temperature was reduced significantly by these exposures, the reduction being greater in those samples aged in the latter environment. Some samples have now reached 40,000 h of aging.

Low-cycle fatigue, creep-fatigue, and high-cycle fatigue testing was conducted on Hastelloy X at 760°C. The introduction of tension or compression hold periods resulted in lower fatigue lives compared with continuous cycle tests; increasing the hold period from 0.5 to 1.0 h had no apparent effect. High-cycle fatigue tests of up to 60,000,000 cycles were completed.

A system was developed for the stress relaxation testing of ceramics in a controlled atmosphere, and exploratory tests were run. Creep tests were conducted on two grades of alumina and on fused silica.

## Corrosion and Compatibility of Alloys

Relationships were developed between the supply rates of impurity species and the carburization of Hastelloy X and alloy 800H in simulated HTGR-He environments. A parameter describing test gas conditions at the specimen surface was used to estimate the extent of impurity depletion at each specimen position in a test rig.

A study to determine the kinetics of the decarburization of 2 1/4 Cr-1 Mo steel in an environment characteristic of a steam cycle-cogeneration HTGR was initiated, and the first 1000-h run was completed. Experiments to assess the compatibility of boronated graphite with type 316 stainless steel and alloy 800H were also begun.

## Joining Technology

Weld cladding of a large alloy 800H forging with ERNiCr-3 weld metal was accomplished. A total of seven layers was deposited to achieve the desired cladding thickness of 19 mm. On the basis of visual examinations and observations during the weld cladding, no weldability problems were apparent. Side-bend test specimens showed that the clad fusion line had good ductility. Metallographic examination gave no evidence of fusion line defects or hot cracking, even though a wide range of microstructures existed in the forging. However, an area of as-cast structure on the bottom of the forging was later clad, and a few fissures were found at or

near the fusion line in the heat-affected zone. Tensile specimens taken from various areas in the cladding and across the fusion zone showed acceptable properties but tended to fail at or near the fusion line.

### Structural Ceramics

No structural changes were observed in fine-grained fused silica that had been creep tested to 0.6% strain in about 1500 h at 538°C. Two grades of alumina were examined by optical and transmission electron microscopy; existing glassy phases and porosity were characterized. The room-temperature fracture toughness of these aluminas was also determined by a short-rod geometry method.

### Fission Product-Materials Interactions

Samples of Hastelloy X, Inconel 617, and other nickel-base alloys were exposed to tellurium for up to 5000 h at 704°C. Grain boundary embrittlement to a depth of 0.1 mm resulted. An alloy with an addition of 1% Nb was resistant to embrittlement by tellurium.

### Liner and Penetration Studies

Tests to define a reference fracture toughness $K_{IR}$ curve for PCRV penetration steels continued. Compact tension specimens [50 mm thick (2 in.)] of A 508, class 1, steel were tested at −75 and −25°C and at room temperature. Tests valid by ASTM criteria were achieved only at the lowest temperature.

## 5. GRAPHITE DEVELOPMENT

Graphite creep irradiation experiment OC-5 was irradiated in the Oak Ridge Research Reactor for 64.6 full-power days to a peak fast fluence of $1.12 \times 10^{25}$ neutrons/m$^2$ ($E > 29.3$ fJ). The capsule contained graphite specimens previously irradiated in capsules OC-1 and OC-3. All were irradiated at a nominal 900°C specimen temperature, while a compressive stress of 13.8 MPa (20.7 MPa for selected specimens) was applied to two columns. Two similar columns of specimens served as unstressed control specimens. Results indicated that internal portions of the capsule shifted to one side during operation. Postirradiation examination of the specimens is proceeding.

Two High Flux Isotope Reactor target capsules, HTK-5 and -6, were irradiated in experiments conducted in cooperation with the FRG. The HTK-5 capsule contained five FRG experimental graphites, Great Lakes Carbon Corporation H451 graphite, and POCO AXF graphite. Capsule HTK-6 contained grades of H451 and improved H451, Union Carbide Corporation TS-1621 graphite, and selected FRG grades. A parametric study of fracture mechanics behavior was completed on selected specimens of the irradiated graphites. The finely grained highly isotropic materials had the best fracture toughness characteristics, H451 graphite had an intermediate

value, and Stackpole 2020 graphite had the lowest value of the specimens studied. The results demonstrate that irradiation lifetime depends not only on the graphite's ability to withstand the internal shears mechanically but also on the action of internal flaws and porosity to reduce the internal strains.

Virtually all the irradiation data appear to imply that the decrease in reactor life expectancy of graphite with increasing temperature is only mildly related to growth-rate changes. The major cause of the lifetime reduction is the loss of void volume by thermal expansion to accommodate the differential anisotropic irradiation growth.

Graphite corrosion was studied in a number of graphite-steam oxidation runs made in two loops operating under steady-state conditions and at 0.1 MPa (1 atm) pressure. These experiments are directed to obtaining better behavior data on Stackpole 2020 graphite at 900°C, including information on the effects of interrupting the oxidation, and on the sensitivity of the oxidation rate to variability in the graphite billet, as determined by testing specimens obtained from various locations in the billet. Fracture toughness of the graphites decreased with increasing porosity, with porosity increasing as a result of steam oxidation. Fracture toughness of 2020 graphite seemed to decrease somewhat more rapidly with increasing porosity than did that of H451.

A development program to obtain an improved H451 graphite with more desirable mechanical properties has been initiated with GA and Great Lakes Research Corporation. Obtaining improved mechanical properties without a loss in the fracture toughness or irradiation resistance of the base material appears to be realistic. Improving the mean strength is helpful, but the key improvement is to decrease the occurrence of disparate flaws.

## 6. HIGH-TEMPERATURE REACTOR PHYSICS STUDIES

The reactor physics studies performed this past year under the HTGR analysis effort were mainly on the performance of the prismatic HTGR. The thermal-hydraulic effort extended previous work so that the use of one-dimensional fluid flow calculations in a three-dimensional neutronics problem became available for routine use in our analysis. Fuel temperature distributions and averages were included in the outputs to allow meaningful comparisons between cases. Options on coolant flow orificing were studied and made available to the code user.

The depletion-perturbation theory was tested further for use in sensitivity and optimization studies. Results from one-dimensional models of the small-core modular reactor are encouraging. Benchmarking of low-enriched uranium cross sections was initiated under an agreement between ORNL and GA. The thermal-hydraulics modeling of a continuously fueled pebble-bed reactor was upgraded to calculate fuel temperature distributions under various fueling conditions.

## 7. HIGH-TEMPERATURE REACTOR SHIELDING STUDIES

Configurations for the HTGR bottom reflector and support block neutron streaming experiment were designed conceptually, preanalyzed and modified, fabricated, and delivered to the Tower Shielding Facility. The experiment has two major objectives: (1) to determine the shielding effectiveness of the boron pins and (2) to determine the extent of neutron streaming through the large coolant holes in the bottom reflectors and support blocks. To fit the experiment within the project funding, the experiment was divided into two parts along the line of the two objectives. The first part is the boron pin effects experiment (to be performed in fiscal year 1983), and the second is the neutron streaming experiment (to be performed in fiscal year 1984). Portions of the experimental configurations were set by design parameters and are nearly exact replicas of the HTGR lower support structure. Other portions, in particular the spectrum modifier, the side reflecting materials, and the peripheral reflector poisoning at the boron pin sections, were adjusted to obtain neutron spectra and detector response distributions very similar to those obtained for the HTGR design. The indications from the preanalysis are that we were successful in designing the experimental configurations so that the spectra and detector responses will be representative of those for the HTGR design.

## 8. HIGH-TEMPERATURE REACTOR COMPONENT FLOW TEST LOOP STUDIES

The Component Flow Test Loop (CFTL) is a large high-pressure high-temperature test facility capable of circulating helium with controlled levels of impurity through primary-system HTGR components. During 1982 modifications were made in the loop to perform a series of Core Support Performance Tests (CSPTs). These modifications included the fabrication and installation of a test vessel to contain the test structure, the manufacture and the installation of a 500-kW helium heater, and the installation of the necessary instrumentation and controls to measure and control the concentrations of specified impurities in the circulating helium. Modifications were made in the existing control system to permit the circulation of gas at a controlled temperature and pressure past a graphite test structure for an extended period of time.

The CSPT series was proposed to examine the chemical and physical response of an appropriately sized segment of the core support structure at typical operating conditions of temperature, pressure, and flow. This structure in the HTGR is designed to remain in place for the lifetime of the reactor core. This lifetime is assumed to be 40 actual years or an equivalent operating time of 32 full-power years. To accelerate the response of the structure to its environment, the concentration of the impurities will be increased so that both the amount of corrosion and its characteristics of penetration from the surface will be reproduced in a six-month test. This goal requires that the equilibrium constants and the reaction kinetics for the graphite and each of the impurities be known at the operating temperature and pressure. A series of accompanying studies

has been initiated to determine these relationships for a special "nuclear grade" Stackpole 2020 graphite, which has been specified as the material for both the core support post and its mating post seat.

Preliminary small-loop tests indicated the occurrence of a reverse water-gas shift reaction either on the surfaces of the loop or in the gas phase. Thus, a preliminary test, designated as TEST P-1, was included in the CSPT series to measure the effect of this reaction in the absence of the graphite test structure. It was then necessary to conduct a test of limited duration with a referencable graphite to establish the anticipated corrosion rate. This reference test, designated as TEST ZERO, will use a test structure fabricated from off-the-shelf Stackpole 2020 graphite. The test structure for TEST ZERO will be a stack of right circular cylinders with only sufficient structural loading to hold them in place. The first test of the actual structure, designated as TEST ONE, will then be performed with a representation of the actual geometry at the post-seat interface together with an imposed structural load equivalent to that of the core on the post in actual application. The initial parts of TEST P-1 were begun in December 1982.

## 9. APPLICATION AND PROJECT ASSESSMENTS

Work on High-Temperature Gas-Cooled Reactor (HTR)* application assessments continues to show that the most promising application of very high-temperature process heat reactors (VHTRs) is in the steam reforming of methane for chemicals production. A review of the experience in industry with the occurrence of steam-methane-reformer fires and explosions indicates that these occurrences are rather rare and that they would be less likely if an HTR were used as the energy source. An assessment of the national need for HTRs indicates that they provide a unique way to generate nuclear process heat for displacing oil and natural gas in industrial use; this is projected to be very important after the year 2000. Work performed on economic ground rules and cost factors helped to establish sound and consistent economic bases for use in the national HTR program for estimating the economic performance of HTRs.

Our assessment work on modular HTRs provides a peer review of the technical and economic performance of designs specified by GA and General Electric Company (GE). Both prismatic and pebble-bed fuel designs are being considered. With regard to fuel cycle costs, the pebble-bed reactor has a significant advantage, with fuel cycle costs being 25 to 30% less than corresponding costs in prismatic-fueled modular HTRs. We have estimated the maximum fuel temperature at which fuel retains nearly all fission products during extreme accident conditions in modular HTRs; 1600°C was determined as a prudent design value. In our evaluation of pressure vessels, we find that the cost of fabricating and installing a

*The term HTR is used here rather than HTGR to indicate that either prismatic-fueled HTGRs or pebble-bed-fueled Pebble-Bed Reactors (PBRs) are considered.

prestressed concrete reactor vessel is less than that of a steel vessel on the basis of the direct costs of the pressure vessel and comparable associated systems. However, other factors, such as the impact of vessel choice on plant construction schedule, are also important and were not considered here. With regard to the construction schedule of a modular HTR, that developed by Bechtel Group, Inc. (BGI), appears to be optimistic but might be attainable on the basis of currently available information. Overall, the estimated economic performance of a modular HTR plant is sufficiently favorable to warrant continued study of the concept.

# 1. HTGR CHEMISTRY (WBS ORL106)

R. P. Wichner

The purpose of this study is to obtain data to calculate or estimate the rate of transport of important actinides and fission products throughout a High-Temperature Gas-Cooled Reactor (HTGR) under both normal and accident conditions. The diffusion rates of actinides and fission products present as oxides or carbides in H451 graphite and the vapor pressures of the substances when adsorbed on graphite are being investigated.

## 1.1 DIFFUSION OF URANIUM IN GRAPHITE — O. K. Tallent and R. L. Towns

The diffusion of uranium (as a stand-in for plutonium) was investigated under conditions approximating those of the primary coolant loop in the reactor. Profiles were obtained for uranium penetration in H451 graphite from 900 to 1400°C. Diffusion coefficients were calculated from the observed concentration profiles using the expression

$$\left[\mathrm{erf}^{-1}\left(1 - C/C_0\right)\right]^2 = x^2/4Dt \ , \qquad (1)$$

where $C$ is the concentration of uranium at time $t$ for a distance $x$ into the pellet, $C_0$ is a constant representing the uranium concentration at $x = 0$ for all $t$, and $D$ is the diffusion coefficient.

Diffusion coefficients for uranium dicarbide at 1000 and 1400°C were found to be defined by

$$D_{UC_2} = 3.5 \times 10^{-3} \exp(-4.8 \times 10^{-4}/RT)\mathrm{cm}^2/\mathrm{s} \ , \qquad (2)$$

where $R$ is the gas constant and $T$ is the temperature in kelvins. For

uranium dioxide at 900, 1000, and 1400°C, diffusion coefficients are defined by

$$D_{UO_2} = 2.34 \times 10^{-6} \exp(-3.2 \times 10^4/RT)\text{cm}^2/\text{s} \ . \qquad (3)$$

Arrhenius plots of the diffusion coefficients are shown in Fig. 1.1. The diffusion coefficients calculated from Eq. (2) are greater than preliminary values reported previously.[1] The greater values reflect slight changes and improvements made in the experimental method during the year.

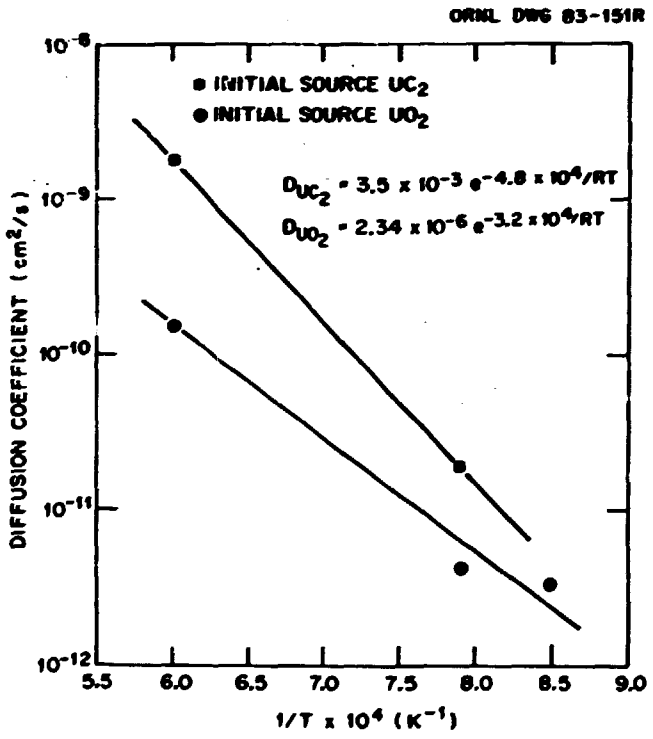


Fig. 1.1. Arrhenius plots of uranium diffusion coefficients in H451 graphite.

## 1.2 VAPOR PRESSURE OF PLUTONIUM ADSORBED ON GRAPHITE — O. K. Tallent and R. L. Towns

The vapor pressure of plutonium adsorbed on H451 graphite at 1400°C was measured as 0.39 ± 0.03 mPa ($3.9 \pm 0.3 \times 10^{-9}$ atm) by a transpiration method with helium carrier gas. Data were collected at gas flow rates ranging from about 40 to about 75 mL/min where the plutonium vapor

density remained approximately constant with flow rate (Fig. 1.2). At lower flow rates the vapor density varied with flow rate as a result of thermal diffusion.[2-4] Variation of the vapor pressure with surface-adsorbed plutonium concentration will be investigated in the future. The graphite specimen for the above measurements contained 0.63 ± 0.08 mg of adsorbed plutonium per square meter of graphite surface area.

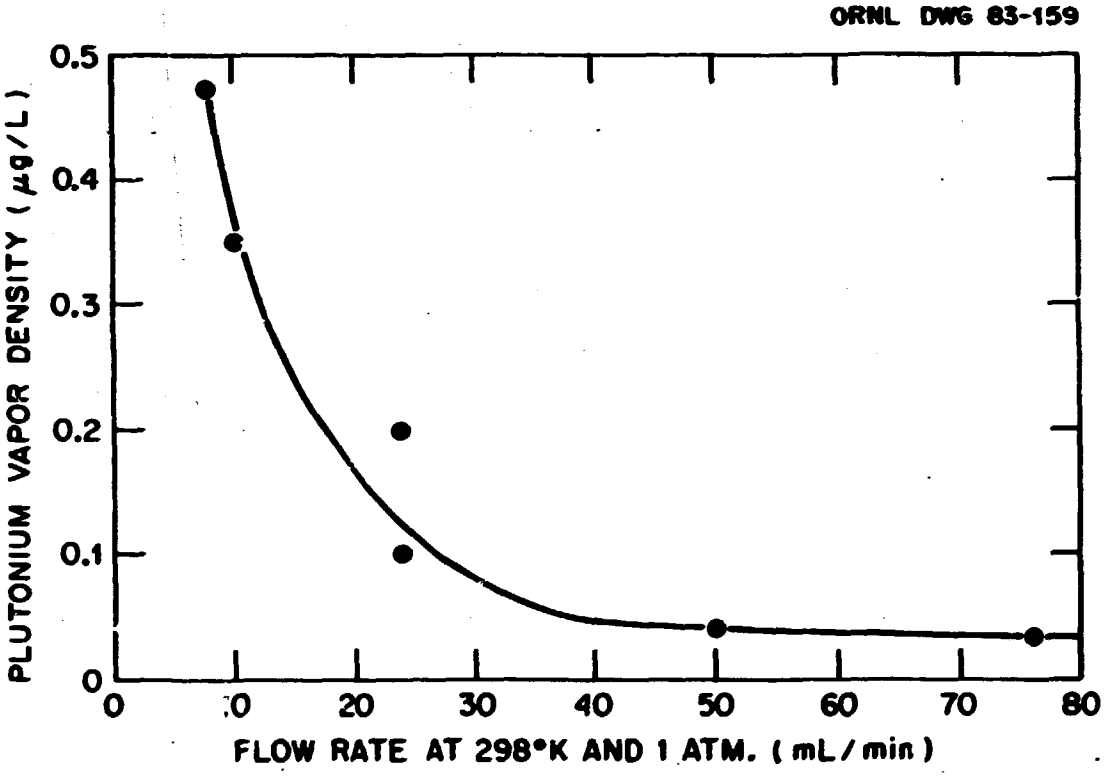


Fig. 1.2. Variation of plutonium vapor density with helium gas flow rate (gas passed over plutonium-bearing graphite pellet at 1400°C).

## 1.3 REFERENCES

1. O. K. Tallent and R. L. Towns, "Uranium and Plutonium Diffusion in Graphite," pp. 1–4 in *High-Temperature Gas-Cooled Reactor Technology Development Program Annual Progress Report for Period Ending December 31, 1981*, ORNL-5871, June 1982.

2. B. A. Phillips and M. H. Rand, *A Transpiration Apparatus for Measuring Vapor Pressures: The Vapor Pressure of Gold*, AERE-R 5352, Atomic Energy Research Establishment, Harwell, England, 1967.

3. P. L. Harris et al., *The Volatility of Plutonium Carbides*. AERE-R 5353, Atomic Energy Research Establishment, Harwell, England, 1967.

4. Halvor Kronde and P. G. Wahlbeck, "Theory of Determination of Vapor Pressures by the Transpiration Method," *Acta Chem. Scand.* A30, 297–302 (1976).

# 2. FUELED GRAPHITE DEVELOPMENT (WBS ORI101, ORI102, and ORI501)

F. J. Homan and M. J. Kania

## 2.1 INTRODUCTION

The Fueled Graphite Development Program at Oak Ridge National Laboratory (ORNL) continues as part of the national High-Temperature Gas-Cooled Reactor (HTGR) fuel development effort being conducted in cooperation with GA Technologies, Inc. (GA). The ORNL portion of the program includes irradiation testing of fuel fabricated by GA in irradiation capsules assembled by ORNL and operated in ORNL reactors. We also conduct postirradiation examinations on the irradiated fuel in special equipment developed for this purpose. The GA responsibilities include interface with core designers and with licensing activities and development of fuel performance models with data developed from the irradiation tests conducted at ORNL. GA Technologies also has responsibility for fuel manufacturing, including design, process development, and quality control.

In addition to the cooperation with GA, the ORNL program includes specific cooperative tasks with the German Nuclear Research Center at Jülich [Kernforschungsanlage (KFA) Jülich]. The cooperation with KFA is part of the formal agreement between the U.S. and German governments for gas-cooled reactor development. Several cooperative projects have been completed during the past several years. The two active areas of cooperation during this reporting period are described in this chapter.

At the end of 1982 the Fueled Graphite Development Program was organized around four subtasks: (1) Irradiation Testing, (2) Postirradiation Examination (PIE), (3) U.S./Federal Republic of Germany (FRG) Cooperative Work, and (4) PIE Equipment Development and Maintenance. Over the years the program has also included a product and process development subtask, but this work was completed during FY 1982, and no further efforts are planned in this area.

### 2.1.1 Irradiation Testing

- A capsule design was completed for a fuel hydrolysis experiment. This experiment is designated HRB-17 and -18 (two capsules). The experiment will feature injection of controlled quantities of moisture into an operating capsule in which failed fuel is operating. The major goal of the experiment is to measure the behavior of the failed fuel in the presence of moisture. We anticipate an increase in the fission gas release to birth rate (R:B) as a result of a density decrease in the carbide-containing fuel kernels. The magnitude of this increase in R:B is an important design parameter for the reactor core.
- The postirradiation thermal analysis for capsule HRB-16 was completed. There were 18 fuel rods irradiated in this capsule, and the time-averaged irradiation temperatures ranged from 1044°C (for rod 1) to 1212°C (for rod 10 at the center of the capsule).

### 2.1.2 Postirradiation Examination

- Capsule HT-35 completed irradiation in November 1980. Postirradiation examination of this capsule was delayed in order to complete the examination of the HRB-15a capsule, which was of higher priority. Examination of specimens irradiated in capsule HT-35 was partially completed during the reporting period.

  1. Transmission electron microscopy (TEM) of silicon carbide (SiC) coatings irradiated on inert (carbon) kernels revealed that stacking faults appear to be a strong sink for point defects. Void formation was not observed in the coatings examined to date, and irradiation appears to have caused no significant restructuring of the coating.
  2. Irradiated microsphere gamma analyzer (IMGA) examinations completed to date show good retention of fission products. Histograms of several fission product activity ratios are presented in Sect. 2.3.1, but no detailed analysis of the data have been completed as yet.

- Capsule HRB-15b examinations were mostly completed before 1982 and were reported in previous annual reports. The final report on this capsule has been delayed for reanalysis of the silver retention data. Cesium and fission gas retention data are summarized in Sect. 2.3.2.
- Examination of specimens irradiated in capsule HRB-15a was completed in 1982. This is a very important capsule because it contained specimens of the four candidate fissile particles for the low-enriched uranium (LEU) fuel cycle. Detailed IMGA, metallographic, and microprobe results are included in Sect. 2.3.3. The thermal performance of the four candidate kernel types ($UO_2$, $UC_2$, $UC_xO_y$, and buffered $UO_2$) was about as expected. The performance of the ZrC-buffered $UO_2$ kernels was surprisingly good. This was an experimental kernel at the time the HRB-15a experiment was planned, and very little was known about its behavior under irradiation. The good performance of this kernel was a pleasant surprise. The examination of HRB-15a-irradiated specimens confirmed our conclusion that the palladium attack of the SiC and the silver diffusion through SiC were not dependent on kernel type but were dependent on SiC coating quality.
- Disassembly of capsule HRB-16 is reported in Sect. 2.3.4. Detailed PIE of fuel specimens irradiated in this capsule will begin after examination of the HT-35 specimens is complete.

### 2.1.3 US-FRG Cooperative Program

- Final reporting of work done under FWS FD-12 (pyrocarbon coating permeability to fission gas) and FWS FD-13 [(IMGA/postirradiation annealing and beta autoradiography (PIAA) comparison] was completed in 1982. Abstracts of the final reports are included in Sect. 2.5.
- Examination of the first set of German particles under FWS FD-20 [IMGA, postirradiation gas analyzer (PGA), electron microprobe examination of German irradiated fuels] was completed and reported in 1982. This work is also reported in Sect. 2.5.

### 2.1.4 Equipment Development and Maintenance

- Several problems were encountered with the IMGA system in 1982. The system was available less than 30% of the time because of both hardware and software problems. Details are given in Sect. 2.6.1. Essentially, the pulse height analyzer (the heart of the spectrum analysis portion of IMGA) is "worn out." The analyzer was purchased in the mid-1970s from a company that is no longer in business; therefore, repair or refurbishing of the system is not possible. A new system was specified and bids placed in 1982, and we expect the new system to be purchased and installed in 1983.
- The PGA system was upgraded by the addition of a quadrupole mass spectrometer for use with the hot-particle-breaking station. The quadrupole spectrometer is located in the PGA glove box. We found that operation of the hot station with the time-of-flight mass spectrometer (located outside the glove box) resulted in contamination of the flight tube with cesium, which would cause unacceptable operator exposure if continued. The portions of the quadrupole spectrometer contaminated by operation with the hot station are disposable and can be discarded when contaminated to undesirable levels.

## 2.2 IRRADIATION CAPSULE ASSEMBLY AND OPERATION — J. A. Conlin

### 2.2.1 Hydrolysis Experiments HRB-17 and HRB-18 -- R. L. Senn

The next irradiation experiment in the series to qualify fuel for the LEU fuel cycle has been designated HRB-17/-18. This will be a hydrolysis experiment to determine the behavior of Triso-coated dense UCO (mixture of $UO_2$ and $UC_2$) fissile particles that fail in a moist environment. Work during 1982 on the design and construction of this experiment has been documented internally;[1] an abstract of this documentation follows:

> Design data are needed on the behavior of failed Triso-coated dense UCO kernels in a moist environment. An irradiation experiment is planned in FY 1984 to provide these data. This experiment, designated HRB-17/-18, will require modifications to the standard HRB (HFIR removable beryllium) capsule and to the

irradiation facility located in the HFIR (High Flux Isotope Reactor). These modifications are needed to permit injection and monitoring of controlled amounts of moisture into the operating capsules. The primary purpose of this report is to document progress on design and implementation of the modifications.

Because of the complexity of this experiment and the need for unambiguous fission gas release to birth (R:B) rate data, it was decided not to include fuel in the upper and lower portions of the capsules, where neutron fluxes swing widely during the 23-d HFIR operating cycle. Stainless steel cylinders will be located in these regions instead of fuel. The GA technical specification for this experiment calls for the fuel centerline temperature to be about 800°C to avoid having the injected moisture react with the graphite sleeve prior to encountering the fuel particles. Details of the fuel specimen configuration, design thermal analysis, and fuel loading evaluation are presented in this report.

2.2.2 HRB-16 Thermal Analysis — I. I. Siman-Tov

The thermal analysis for capsule HRB-16 was completed in this reporting period and documented internally.[2] An abstract of this document follows.

A postirradiation thermal analysis was completed on fuel rods irradiated in capsule HRB-16. This analysis took into account the dimensional change data provided by GA Technologies, Inc. (GA). Detailed temperature calculations for the fuel rod specimens and graphite sleeve are presented in this report along with the postirradiation dimensional data. Fission and gamma heating calculations are also included. The time-averaged fuel rod temperatures calculated in this analysis ranged from a low of 1044°C in rod 1 to a high of 1246°C in rod 16. A maximum fuel rod temperature of about 1300°C was calculated for rod 10 at the beginning of cycle 1 and again at the end of the irradiation.

2.3 POSTIRRADIATION EXAMINATION OF IRRADIATION EXPERIMENTS — M. J. Kania

During this reporting period, irradiation capsule HRB-16, which completed irradiation late in 1981, was disassembled in the High-Radiation-Level Examination Laboratory (HRLEL). This capsule contained only GA fuel, which was stored for future examination. Postirradiation examinations were completed on ORNL fuel from capsule HRB-15b and on GA fuel from

capsule HRB-15a. The PIE of ORNL fuel in capsule HT-35 was delayed until October 1982 to complete the HRB-15a examinations. A final report was written on the performance of ORNL fuel from capsule HRB-15b, but this report is being extended to include updated $^{110m}Ag$ release calculations for the GA fissile fuel in this capsule.

2.3.1 Capsule HT-35 — M. J. Kania and R. J. Lauf

Irradiation capsule HT-35 (ref. 3) was a cooperative experiment between GA and ORNL, with ORNL fuel occupying about 75% of the available test space and GA specimens occupying the remaining test space. Test specimens for ORNL consisted of Biso-coated fertile fuel and Triso-coated low-enriched fissile particles. Specific ORNL objectives[4] were to

1. assess the irradiation performance of low-temperature isotropic (LTI) pyrocarbon coatings derived by use of standard coating gases diluted with $CO_2$ and prepared in a 0.13-m coating furnace;
2. investigate the influence of fabrication process variables, coating properties, and postcoating annealing on overall performance of Biso-coated $ThO_2$ particles;
3. investigate $^{110m}Ag$ retention and metallic fission-product interaction with SiC and correlate results with deposition conditions;
4. perform a detailed study of fast-neutron-induced damage in SiC employing TEM and small-angle x-ray scattering (SAXS) measurements; and
5. assess the irradiation performance of Triso-coated dense $UC_xO_y$ kernels and compare results from Triso-coated weak acid resin (WAR)-derived kernels.

The capsule was irradiated in the High Flux Isotope Reactor (HFIR) target facility for 2140.5 h of full reactor power (100 MW) and was discharged from the reactor on November 19, 1980. A detailed description of the fuel burnup and fluence accumulation of the test specimens was reported.[3] Capsule disassembly began in December 1980, and the results of the metrology performed on the capsule graphite and fuel components were reported.[5]

### 2.3.1.1 Examination of SiC Coatings from Carbon Particles

Silicon carbide coatings from inert (carbon) kernels were examined by TEM before and after irradiation in capsule HT-35. The first SiC batch examined (OR-2882H, SC-531) was deposited at 0.28 μm/min at 1550°C. Samples were irradiated in the bottom-end plug of magazine 1 at 900°C to a total fast neutron fluence of about $6.8 \times 10^{25}$ neutrons/m$^2$ ($E > 29$ fJ). A comparison of the as-fabricated SiC microstructure [Fig. 2.1(*a*)] with the irradiated microstructure [Fig. 2.1(*b*)] shows that stacking faults appear to be a strong sink for point defects. Void formation does not appear to have taken place.

The second SiC batch examined (SC-530) was deposited at 0.55 μm/min at 1550°C. This batch was irradiated in the bottom-end plug of magazine 4 at about 900°C to a fast fluence of $3.95 \times 10^{25}$ neutrons/m$^2$. Batch SC-530 is somewhat less dense in the as-fabricated condition [Fig. 2.2(*a*)] than batch SC-531. This is a result of the higher coating rate in SC-530. Transmission electron microscopy revealed numerous cavities in the as-fabricated coating; the cavities are 500 to 1000 Å in diameter and are arranged circumferentially in the coating layer. These cavities were not repaired or otherwise altered by irradiation [Fig. 2.2(*b*)]. No significant restructuring of the coating (grain size or morphology) or of irradiation-induced void formation is apparent. As observed in SC-531, the stacking faults appear to be efficient sinks for vacancies and interstitials, resulting in the partial elimination of stacking faults and the formation of dislocation loops in their place. The degree to which this process has taken place in SC-530 is less than that in SC-531 because of the lower fluence experienced by SC-530 as well as its initially higher stacking fault density.

Future work will include the TEM examination of irradiated SiC coatings from fuel particles. This will allow us to study fission product behavior and radiation damage together.

### 2.3.1.2 Postirradiation Examination of Irradiated Fuels

The postirradiation examination of capsule HT-35 fuel was delayed until November 1982 because of requirements to complete the examination of

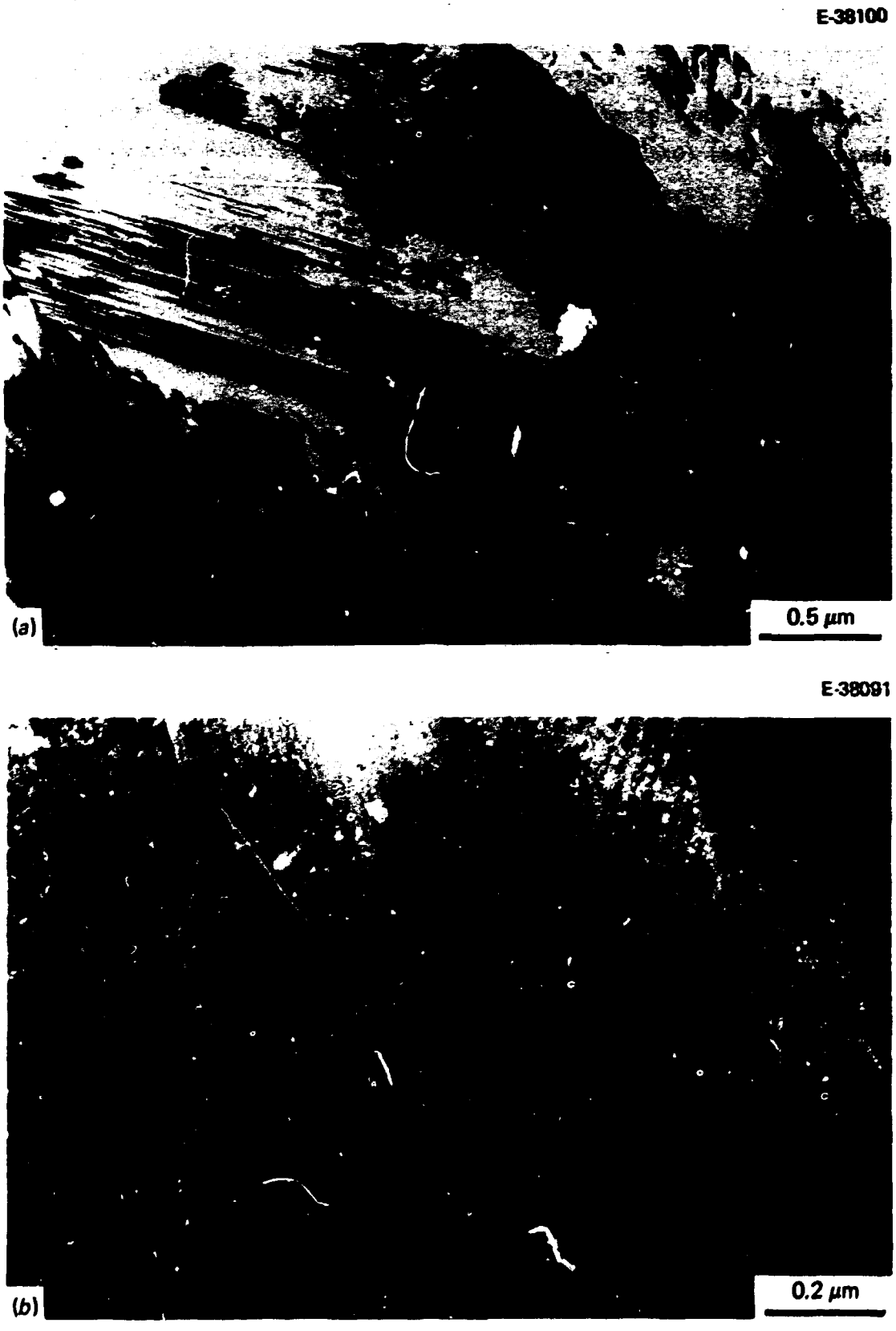


Fig. 2.1. (*a*) Silicon carbide coating SC-531 as fabricated. (*b*) Silicon carbide coating SC-531 irradiated at 900°C to $6.8 \times 10^{25}$ neutrons/m$^2$ ($E > 29$ fJ). Arrow indicates coating direction.

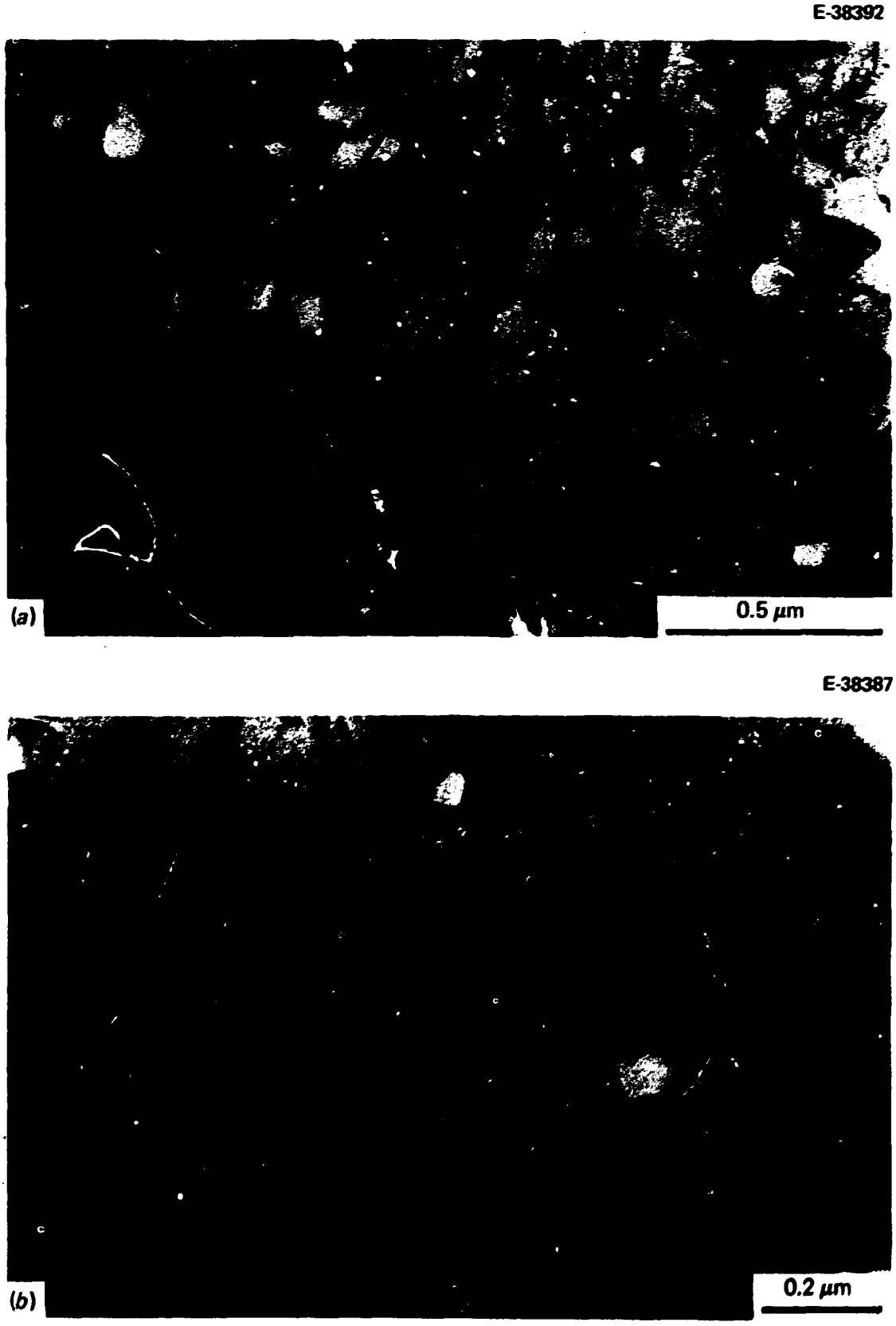


Fig. 2.2. (*a*) Silicon carbide coating SC-530 as fabricated. (*b*) Silicon carbide coating SC-530 irradiated at 900°C to $3.95 \times 10^{25}$ neutrons/$m^2$ ($E > 29$ fJ). Arrow indicates coating direction.

HRB-15a specimens (Sect. 2.3.3) and equipment problems involving the IMGA systems. The first priority is to examine the Triso-coated WAR and UCO particles to complete objectives 3 and 5. The coatings from these fuels will also be used in part to achieve objective 4. The particles of interest were irradiated in driver fuel rods, which were deconsolidated after irradiation to obtain unbonded particles necessary for IMGA and PGA examination. The results of analysis for uranium and thorium in the electrolyte used in the deconsolidation are presented in Table 2.1. None of the analyses indicated excessive amounts of uranium or thorium; however, the results from rods 14 and 39 were somewhat above the detection limit.

The Triso-coated WAR-UCO fuel from rods 1 through 25 are now being analyzed for fission product retention with the IMGA system. Only one rod (No. 3) has been completed because an equipment problem with the IMGA has

Table 2.1. Results of analysis for deconsolidated driver fuel rods from irradiation capsule HT-35

| Fuel rod | Particle batch | | Fissile fuel type | Concentration (mg/cm$^3$) | |
|---|---|---|---|---|---|
| | Fissile | Fertile | | Uranium | Thorium |
| 1 | OR-2884 H | A-700 HT | WAR-UCO[a] | <0.001 | <0.0001 |
| 3 | OR-2888 H | | WAR-UCO | <0.001 | |
| 6 | OR-2885 H | | WAR-UCO | <0.001 | |
| 9 | OR-2887 H | | WAR-UCO | <0.001 | |
| 12 | OR-2886 H | A-898 HT | WAR-UCO | <0.001 | <0.0001 |
| 14 | OR-2884 H | A-901 HT | WAR-UCO | 0.006 | 0.0020 |
| 16 | OR-2888 H | | WAR-UCO | <0.001 | |
| 19 | OR-2885 H | | WAR-UCO | <0.001 | |
| 22 | OR-2887 H | | WAR-UCO | <0.001 | |
| 25 | OR-2886 H | | WAR-UCO | <0.001 | |
| 28 | A-976 | | Dense UCO | <0.001 | |
| 31 | A-976 | | Dense UCO | <0.001 | |
| 34 | A-976 | | Dense UCO | <0.001 | |
| 37 | OR-2887 H | | WAR-UCO | <0.001 | |
| 39 | OR-2886 H | A-[illegible] HT | WAR-UCO | 0.002 | <0.0001 |
| 41 | A-976 | A-914 HT | Dense UCO | <0.001 | <0.0001 |
| 44 | A-976 | | Dense UCO | <0.001 | |
| 47 | A-976 | | Dense UCO | <0.001 | |
| 50 | OR-2887 H | | WAR-UCO | <0.001 | |
| 52 | OR-2886 H | A-735 | WAR-UCO | <0.001 | <0.0001 |

[a]WAR, weak acid resin; UCO, mixture of $UO_2$ and $UC_2$.

limited its operation. The activity ratios, $^{110m}Ag$:$^{106}Ru$, $^{137}Cs$:$^{106}Ru$, and $^{144}Ce$:$^{106}Ru$ are presented in Fig. 2.3 for fuel rod 3. Corresponding fission product inventory calculations have not been made, so only a qualitative interpretation can be made. Comparisons of the $^{137}Cs$:$^{106}Ru$ and $^{144}Ce$:$^{106}Ru$ ratios show very tight distributions and no particles indicative of having low cesium or cerium inventories compared with the ruthenium inventory. The $^{110m}Ag$:$^{106}Ru$ ratio exhibits a broader distribution, but this is a direct result of counting statistics rather than defective particles. This preliminary data indicates that all the particles from batch OR-2888 H irradiated in rod 3 have performed similary, with no obviously defective particles.

### 2.3.2 Capsule HRB-15b — M. J. Kania

The objectives, fabrication, operation, disassembly, and initial PIEs on ORNL fuel have been published.[6-9] Postirradiation examination was completed in this reporting period, and Figs. 2.4 and 2.5 summarize

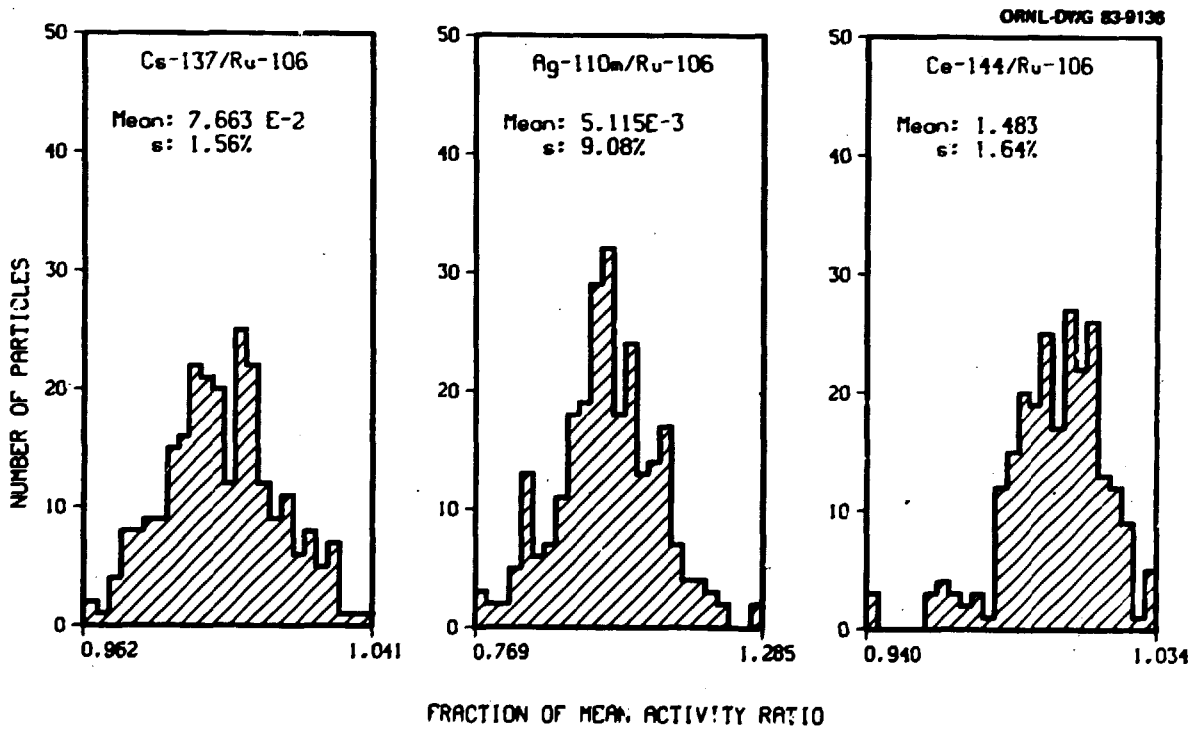


Fig. 2.3. Capsule HT-35, irradiation position 3, fissile particle batch OR-2888 H.

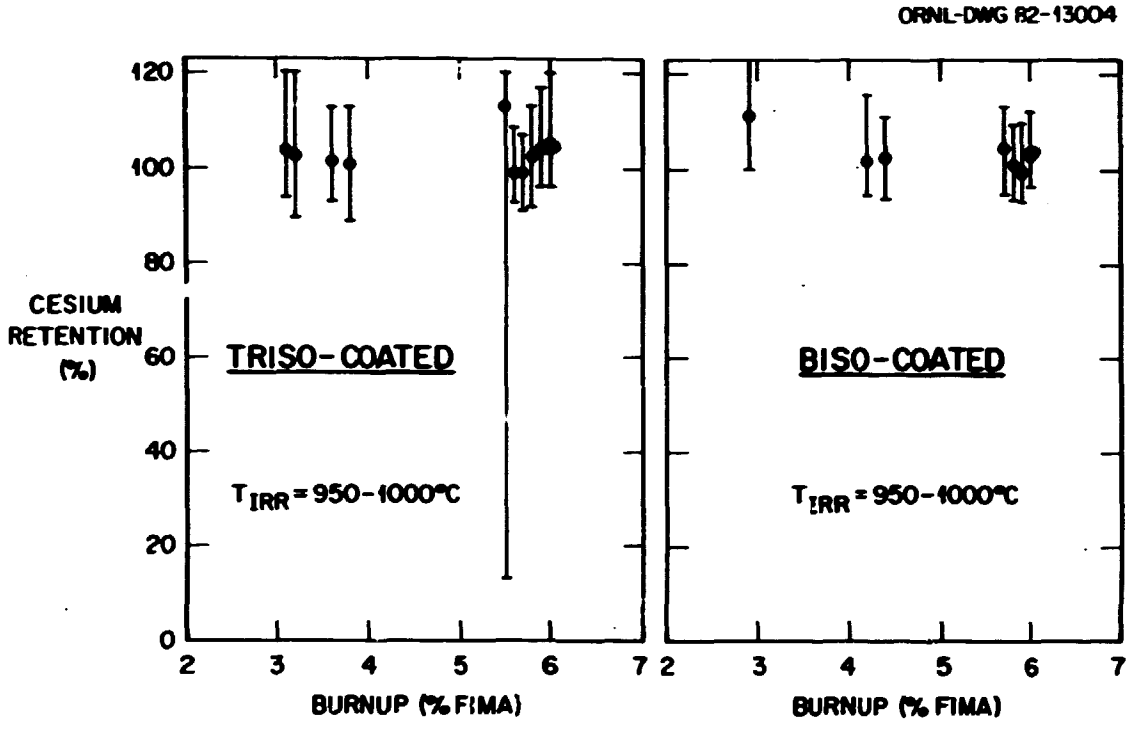


Fig. 2.4. Cesium retention derived from gamma spectrometric measurements revealed good retention for Biso- and Triso-coated $ThO_2$ particles irradiated in capsule HRB-15b.

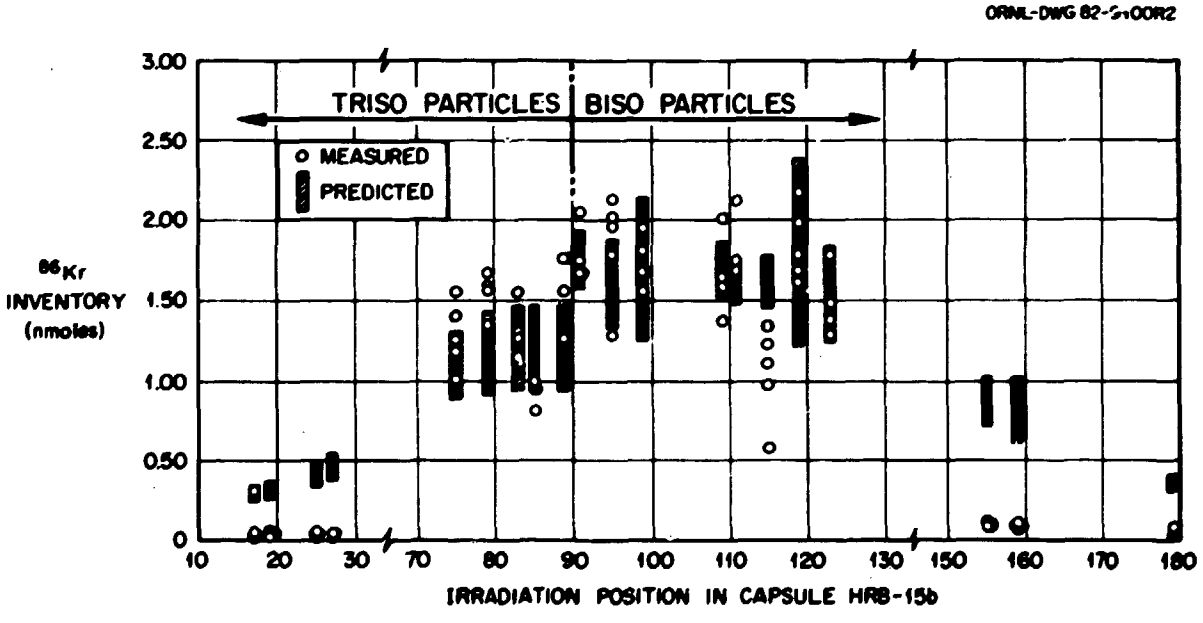


Fig. 2.5. Comparison between measured and predicted fission gas release from Biso- and Triso-coated fertile particles irradiated in capsule HRB-15b.

the IMGA and PGA results. Only one fertile particle batch showed cesium loss, batch A-825. The mean retention for the batch was 106% (over 100% retention because of uncertainties in the calculated cesium inventory). Only one particle in this batch was failed, and it released more than 90% of its cesium. For burnups of more than 5% fissions per initial metal atom (FIMA), the agreement between predicted and measured gas release for both the Triso- and Biso-coated particles was excellent with one exception: batch J-491 (position 115), which was fabricated for the OF-2 irradiation experiment.[10] The agreement at the ends of the capsule was very poor. These positions represent fuel burnups of less than 5% FIMA. We believe that the fuel in these positions did not lose its fission gas during irradiation but, rather, that the gas release model used[11] was inadequate for low-burnup fuel. A final report documenting these results has been written.[11]

We are now holding publication of the HRB-15b final report to include updated information on the release of the activation product $^{110m}Ag$ measured on GA fuels. GA has published the results of examinations on their fuel, including ORNL IMGA measurements.[12] The initial data indicated a range in release of 20 to 30% for the Triso- and Si-Biso-coated $UC_2$, $UO_2$, UO,* and UCO fuel types. These release values were based on calculations by use of the best available neutronics data for $^{110m}Ag$ in the HFIR Removable Beryllium (RB) Facility at that time. A recent examination of the fission product cross section data sets reveals that the removal cross section for $^{110m}Ag$ may be in error because resonance adsorption was not considered. Preliminary calculations show that use of a newly derived removal cross section including resonance parameters results in retention calculations of 100% for this same GA fuel. The new data are being evaluated, and the results of this evaluation for the GA HRB-15b fuel will be included in the ORNL final report.

2.3.3 Capsule HRB-15a — M. J. Kania, F. J. Homan, G. A. Moore, and L. A. Shrader

Postirradiation examination of selected fuel specimens irradiated in capsule HRB-15a was completed in this reporting period. The fuel for

---

*$UO_2$, Buffered $UO_2$ kernel.

this capsule was fabricated by GA. After irradiation in HFIR, the capsule was disassembled in the ORNL hot cells and returned to GA for PIE. After some examinations were performed at GA (dimensional inspection, fission gas R:B in TRIGA), six of the fuel rods and unbonded particles from three of the wafer-tray assemblies were returned to ORNL for additional examinations. This work is documented in an internal report,[13] the abstract of which follows.

> The HRB-15a experiment contained 18 fuel rod specimens and 17 wafer-tray assemblies. All the fuel specimens were fabricated by GA Technologies, Inc. (GA). The capsule was assembled at ORNL and irradiated in the High Flux Isotope Reactor (HFIR). After irradiation the specimens were returned to GA for postirradiation examination. Six of the fuel rods were returned to ORNL after dimensional inspection in the GA hot cells and measurement of the fission gas release to birth (R:B) rates in the GA TRIGA facility. The fertile particles from three of the wafer-tray assemblies were also returned to ORNL for examination.
>
> At ORNL a number of additional examinations were performed to supplement the data collected by GA. Included in the ORNL examinations were electrolytic deconsolidation of the fuel rods, gamma spectroscopic examinations [with the irradiated microsphere gamma analyzer - (IMGA)], metallographic examinations, and microprobe examinations. This report documents the examinations performed at ORNL.
>
> Some problems were encountered with the electrolytic deconsolidation, and significant amounts of debris were left attached to the particles. A second cleaning was required after some repairs were made to the equipment. More than the expected amount of uranium and thorium was found in the electrolyte solution. An IMGA examination showed good retention of cesium but some loss of silver from the fissile particles. Work is still being done to refine the cross section values for silver, and the initial estimates of silver loss are being revised downward. Metallographic and microprobe examinations revealed trends that have been observed in previous irradiation experiments. More mobility was noted for the rare earth fission products from the kernel toward the coatings in carbide fuels than for oxide fuels. The rare earths remain tied up as oxides in $UO_2$ kernels. Palladium attack of the SiC layer was noted frequently and appeared to be most severe in the Triso-coated UCO fissile particles. We concluded that this attack was not associated with the kernel type ($UO_2$, UCO, $UC_2$, or buffered $UO_2$) but, rather, was associated with coating quality. The fissile particles containing UCO kernels were prepared in large-scale

equipment, whereas the other fissile batches were fabricated in laboratory-scale equipment, with better control over coating conditions.

Overall conclusions concerning the performance of fuel in capsule HRB-15a will be documented in a final report prepared by GA (with contributions from ORNL). The ORNL postirradiation examination results will be combined with the GA results. This final report will be issued when the ongoing evaluations of silver cross sections and silver retention are complete.

2.3.4 Capsule HRB-16 — M. J. Kania

Irradiation capsule[14] HRB-16, which contained only GA-fabricated fuel, was discharged from the HFIR on December 23, 1981, after operating for nearly 4082 h of full reactor power (100 MW). The capsule was allowed to cool in the HFIR pool and was then shipped to the HRLEL for disassembly. The capsule was received at the HRLEL in February 1982, and disassembly began on March 1, 1982; a GA representative was present to assist and direct the work.

The dissembly sequence prepared by GA was followed closely, with no problems or unanticipated events. The fueled graphite sleeve was removed from the stainless steel containments, and the thermocouples were pulled from the sleeve without incident. The fueled graphite sleeve was gamma scanned to ensure proper fuel positioning and to indicate any unusual fuel behavior. After scanning, diameter measurements were made on the fueled sleeve at each specified location along the axial length of sleeve at both 0 and 90° orientations. Irradiated bonded rods and loose particle trays were removed by cutting the graphite sleeve. Three axial cuts were made 120° apart along the entire length in a specially designed fixture. The sleeve was then cracked along the length of each slit, and two sections were removed to expose the rods and graphite trays. This method of fuel removal was used to reduce the possibility of fuel rod breakage or debonding encountered in earlier experiments when the rods were pushed out of the sleeve.

The entire length of fuel was visually examined and photographed in place before fuel handling occurred. Each fuel rod and tray was then removed and placed in appropriately identified containers for future

examination. The loose particle trays were not opened at that time. As the fuel was removed from the sleeve, it became evident that several trays had opened and that a portion of their contents had spilled into the graphite sleeve. Later examination of the tray contents revealed those particle types that had been lost. Piggyback samples were recovered from the ends of the graphite sleeve without difficulty. The three pieces of graphite sleeve were scored for gamma spectrometry measurements.

Each fuel rod was visually examined with the stereomicroscope, and photographs were taken of the rod surfaces and of unusual areas. Each graphite tray was opened, and its contents were poured into a glass container and visually examined under the stereomicroscope. Photographs were taken of the contents of each of the 27 graphite trays. Dimensional measurements were made on each fuel rod, with diameter measurements at the top, middle, and bottom of each rod at both 0 and 90° orientations. Length measurements were also made on each rod. The graphite trays were measured diametrally at one axial position and at both 0 and 90° orientations.

Gamma spectrometry of the empty graphite sleeve from capsule HRB-16 was completed; however, we were not able to provide a quantitative radioisotopic analysis as originally requested by GA because of the lack of a detector calibration in the configuration used for gamma scanning. A longitudional gamma scan of the sleeve was obtained, and those areas along the sleeve indicating high activity were noted and investigated further. Compared with background levels near the gamma-scanning facility, only two areas along the sleeve had high levels of activity. A subsequent gamma energy spectrum was acquired at these two areas and analyzed. The results indicated that the high activity was due to activation products in the stainless steel centering pins in the graphite sleeve at these two locations. No $^{110m}Ag$ was detected in the sleeve, and the levels of $^{134}Cs$ and $^{137}Cs$ were only slightly above the background. Compared with other HRB experiments, the graphite sleeve of capsule HRB-15a had orders of magnitude lower activity levels.

Documentation of capsule HRB-16 disassembly, graphite component and fuel rod dimensional measurements, fuel rod and unbonded particle photography, and graphite sleeve gamma spectrometry were provided to GA.

Postirradiation examination of the fuel rods and unbonded particles is scheduled to begin in April 1983. Until then, all HRB-16 fuel not shipped to GA is being stored at the HRLEL.

## 2.4 PRODUCT AND PROCESS DEVELOPMENT

### 2.4.1 Dense UCO Kernel Fabrication — D. P. Stinton

We recently developed a two-step sintering process that produces dense kernels with well-controlled chemistry and requires sintering temperatures no higher than 1550°C (refs. 15 and 16). Since developing this process and using it in producing laboratory-scale quantities of material for irradiation testing, our work has focused on equipment scaleup for production-scale operation. The scaleup work has proceeded in two areas: evaluating and processing material provided by GA and direct development of large-scale equipment for processing kernels.

A statistically designed experiment involving eight batches of material was undertaken as a cooperative effort between ORNL and GA. GA Technologies, Inc., produced the material and sent unsintered kernels to ORNL for evaluation. We performed differential thermal analysis (DTA), thermogravimetric analysis (TGA), mass spectrometry, differential scanning calorimetry (DSC), and sintering studies on these batches. To avoid biasing the results of the experiment, we were not informed of the production parameters until the experiment was completed. The results of this work have been published.[17]

The main emphasis in the equipment development port of the program has been directed at design of a kilogram quantity rotary furnace for sintering dense UCO kernels. The laboratory-scale work was in a 50-g static bed furnace. Numerous runs were made during the reporting period with the rotary furnace, but the work was largely unsuccessful. The system had air leaks that could not be located and repaired, and the presence of oxygen during sintering caused a very poor-quality product. Efforts at GA to scale up the sintering process resulted in a successfully operated furnace. Therefore, the ORNL effort at equipment scaleup for kernel sintering was abandoned. No further effort in this area is anticipated.

## 2.4.2 SiC Coating Characterization

### 2.4.2.1 Fission Product–Silicon Carbide Interaction Studies in Out-of-Reactor Tests – R. J. Lauf

A paper was written for the open literature summarizing all out-of-reactor fission product interaction studies.[18] This paper includes results published in ORNL/TM-8059, ORNL/TM-7209, ORNL/TM-6991, ORNL/TM-6741, and ORNL/TM-7343. An abstract of the paper follows.

> The interactions of SiC with several high-yield fission products were studied out of reactor by doping "cold" $UO_2$ or $UC_2$ fuel kernels with selected fission product elements before Triso-coating. The doped particles were annealed in a thermal gradient, and SiC–fission product interactions were observed and quantified by metallography, radiography, scanning and transmission electron microscopy, and electron microprobe analysis. The results of these studies are discussed in terms of predicting SiC performance and fuel behavior during irradiation.

### 2.4.2.2 Raman Spectroscopy of SiC Coatings – P. Krautwasser, G. M. Begun, and P. Angelini

Raman studies of SiC coatings of nuclear fuel particles started in 1981 were extended into the first part of 1982. Raman spectra characterize the chemical composition and the degree of crystallinity of a material. For the Raman studies of SiC coatings, the 514.4-nm excitation line of an argon ion laser was used. In Raman spectra the initial laser wavelength is shifted to a series of longer wavelengths (Stokes lines) as a result of the interaction of the material studied with the laser beam. These energy losses result from the stimulation of the vibrational energy levels of the molecules under investigation. We measured single fuel particles that were held by suction on the tip of a hypodermic needle. Data were obtained with a Ramanor HG-2S spectrophotometer consisting of a double monochromator with curved holographic gratings, photon counting electronics, and a cooled S-20-type photomultiplier. The spectrometer was controlled and the data stored with a Nicolet 1170 signal averager. To eliminate the plasma lines from the laser, a spike filter was used. Monochromator slit widths were used. The Raman spectra of SiC coatings reveal whether a coating is stoichiometric or contains excess silicon or excess carbon and also provide information about the degree of crystallinity of the coating.

Changes in Raman spectra during heat treatment of irradiated SiC coatings

Neutron-induced structural defects led to a strong decrease in SiC line intensity [Fig. 2.6(*b*)] compared with the initial SiC Raman spectrum [Fig. 2.6(*a*)]. At high irradiation temperatures, fast neutron defect production was partially compensated for by the annealing of structural defects. A similar recovery occurred during the out-of-pile heat treatment of irradiated SiC coatings. Figure 2.6 (*c*) and (*d*) shows an increasing recovery of SiC line intensity after heat treatments of 5 h at 1500°C and 1 h at 2000°C, respectively. The carbon-rich surface layer, developed by thermal decomposition of SiC during heat treatment, was removed by polishing before taking spectra in both cases. However, the SiC line intensity at about 790 $cm^{-1}$ was still lower and the peak broader than in the initial spectrum. This indicates that the long-range order in the irradiated and annealed coating was still disturbed compared with the as-deposited coating. This decrease in long-range order may be related to the increase of grain boundaries in irradiated SiC, which can be seen in scanning electron micrographs.

All coatings with an SiC line at 970 $cm^{-1}$ in the Raman spectrum of the as-produced coatings showed a distinct recovery of this line after postirradation annealing. In contrast, irradiated or unirradiated SiC without the SiC line at 970 $cm^{-1}$ in the spectrum of the as-produced material did not develop this line even after annealing for 15 h at 2000°C.

Comparison of Raman spectra and metallic fission product release of SiC-coated fuel particles

The release of silver or cesium (measured by out-of-pile annealing experiments at KFA Jülich or GA on particles from HOBEG, KFA Jülich, and GA) was neither clearly related to the type of Raman spectrum nor to the intensity ratios of the lines. Coatings with excess silicon tended to have a somewhat better retention capability. In this study, irradiated particles for which diffusion data were available were not investigated by Raman spectroscopy. We are therefore not certain that the lack of correlation between the Raman spectra of as-deposited coatings and the fission

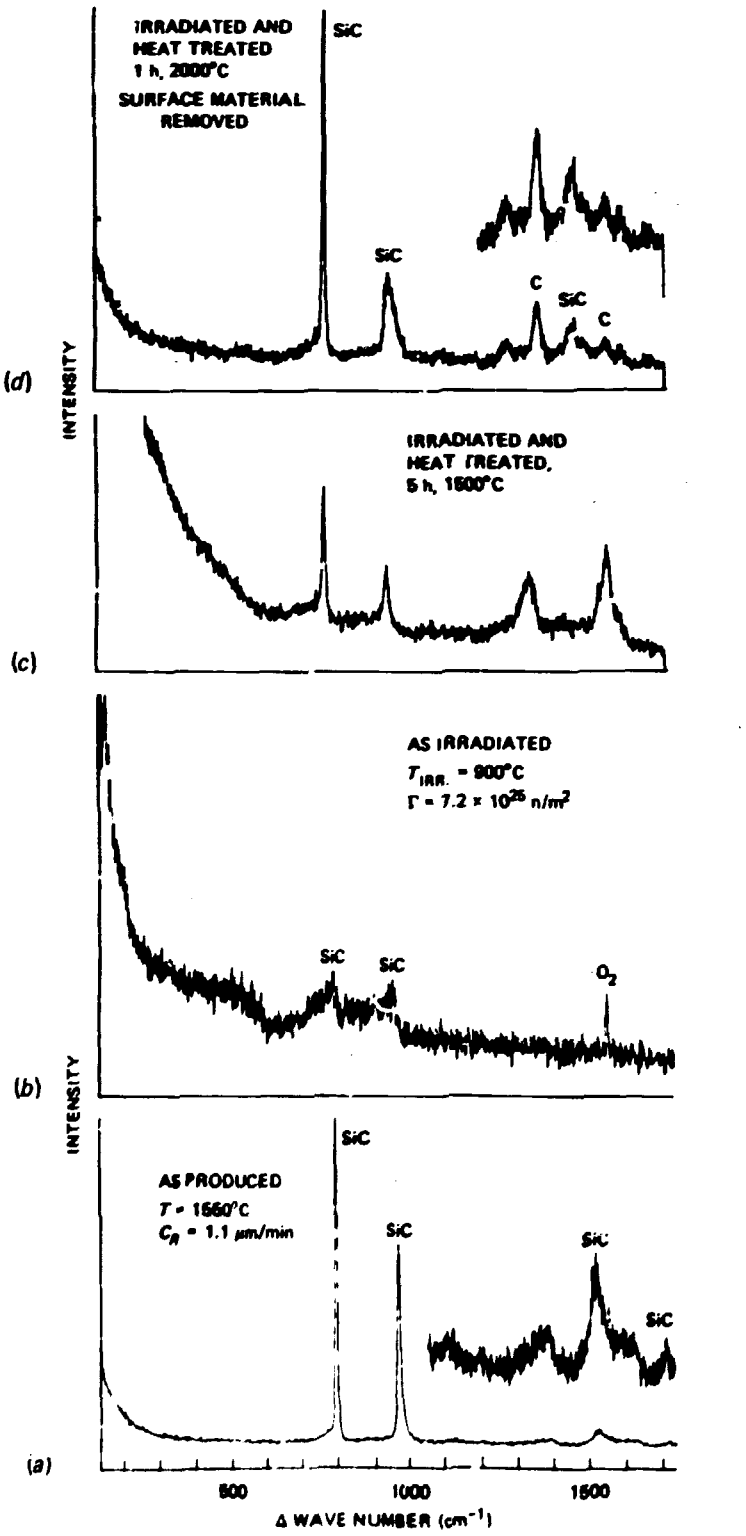


Fig. 2.6. After removal of the graphite surface, the bulk properties of batch ORN-2879 H show a recovery of SiC line intensity with heat treatment.

product release of irradiated and long-term heat-treated particles was due to structural changes during heat treatment (described in the last section). This question may be answered by measurement of fission product inventory with the IMGA system after irradiation and again after a subsequent long-term heat treatment.

## 2.5 US-FRG COOPERATIVE PROGRAM — M. J. Kania

This work is being performed under the Fuel, Graphite, and Fission Product Subprogram, which is one of several programs included under the Umbrella Agreement between the United States and the FRG. The fuel development work covered in this subprogram is being performed by ORNL, GA, and KFA-Jülich. During this reporting period, final reports on the activities of PWS FD-12 and PWS FD-13 have been published.[11,19] Sections 2.5.1 and 2.5.2 contain the abstracts of these publications. Only PWS FD-20 remains open in the fuel development area; the activities during this reporting period were centered around this PWS and are reported in Sect. 2.5.3.

### 2.5.1 PWS FD-12 — M. J. Kania, B. A. Thiele, and F. J. Homan

The purpose of PWS FD-12 was the quantification of irradiation-induced permeability in pyrocarbon coatings. During this reporting period a final report was published, an abstract of which is presented below.[11]

> Two U.S. irradiation experiments were planned to provide information to supplement data from the German program on irradiation-induced permeability in pyrocarbon coatings. Hopefully, the data from both programs could be combined to define the onset of neutron-induced permeability in a variety of Biso coatings produced with different process variables (coating temperature, coating gases, and coating rates). The effort was not successful. None of the preirradiation characterization procedures were able to adequately predict irradiation performance. A large amount of within-batch scatter was observed in the fission gas and cesium release data along with significant within-batch variation in coating properties. Additional preirradiation characterization might result in a procedure that could successfully predict irradiation performance, but little can be done about the within-batch variation in coating properties. This variation is probably the result of random movement of particles within the coating furnace during pyrocarbon deposition.

2.5.2 PWS FD-13 — M. J. Kania, F. J. Homan, and A.-W. Mehner

The objective of PWS FD-13 was to compare U.S. and FRG PIE techniques to measure statistically significant failure fractions of irradiated coated-particle fuels. During this reporting period a final report was published,[19] the abstract of which is presented below.

> Two methods for measuring failure fraction on irradiated coated-particle fuels have been developed, one in the United States (the IMGA system — irradiated microsphere gamma analyzer) and one in the Federal Republic of Germany (FRG) (the PIAA procedure — postirradiation annealing and beta autoradiography). A comparison of the two methods on two standardized sets of irradiated particles was undertaken to evaluate the accuracy, operational procedures, and expense of each method in obtaining statistically significant results.
>
> From the comparison, the postirradiation examination method employing the IMGA system was found to be superior to the PIAA procedure for measuring statistically significant failure fractions. Both methods require that the irradiated fuel be in the form of loose particles, each requires extensive remote hot-cell facilities, and each is capable of physically separating failed particles from unfailed particles. Important differences noted in the comparison were
>
> - failure fraction results with IMGA were more accurate;
> - the IMGA system is fully developed, automated, and in routine use;
> - the IMGA method allows fission product identification and quantification of fission product release;
> - failure fraction determinations are independent of particle coating type and failure mechanism with IMGA; and
> - the high initial cost of an IMGA system is offset by increased through-put.
>
> We recommend that the failure fraction determinations on irradiated coated-particle fuels be made with the IMGA system for the candidate high-temperature reactor fuels from both the U.S. and FRG development programs.

2.5.3 PWS FD-20 — M. J. Kania and H. Nabielek

Through PWS FD-20, irradiated High-Temperature Reactor (HTR) fuel specimens from the FRG development program are shipped to ORNL for detailed postirradiation examinations. Examinations of interest to the German program are IMGA, PGA, x-radiography, and electron microprobe.

Irradiated fuels from three experiments in the FRG program were selected as the first set of fuel to be examined under this PWS. The fuel selected was of one type, a $(Th,U)O_2$ with a high-temperature isotropic (HTI) Biso-coating derived from methane. A final report[20] describing the IMGA examination of these fuels along with an assessment of their performance has been prepared, the abstract of which follows.

> Irradiated fuel from three experiments in the German HTR fuel development program was examined at ORNL with the irradiated microsphere gamma analyzer (IMGA) under PWS FD-20. The fuel consisted of two HTI Biso-coated $(Th,U)O_2$ particle batches: batch E0 1232-1234 irradiated in experiments HFR-K1 and FRJ2-P22 and batch E0 1084 irradiated in experiment R2-K10. The results of the IMGA examinations revealed that batch E0 1232-1234 irradiated in sphere B2 of HFR-K1 had a failure fraction of $3.2 \times 10^{-2}$. The same fuel irradiated in compact 1-3 of FRJ2-P22 had a failure fraction of less than $1.8 \times 10^{-3}$. The difference in failure fraction results can be attributed to the five-times-higher accumulated fluence in experiment HFR-K1, $5 \times 10^{25}$ neutrons/m$^2$ ($E > 16$ fJ). Visual inspection of the failed fuel from batch E0 1232-1234 indicated the failure mechanism to be neutron-induced pyrocarbon cracking. The IMGA data from batch E0 1084 irradiated in sphere 3 of experiment R2-K10 was not of sufficient value to determine an accurate failure fraction. This was due to the nearly seven-year delay between reactor fuel discharge and IMGA examination.

A second set of irradiated fuels to be examined under this PWS was received at ORNL in August 1982. This set consisted of unbonded coated particles from experiments FRJ2-P23, FRJ2-P25, and DR-S6; in total about 10,000 unbonded particles were received. Postirradiation examinations of these fuels are scheduled to begin in August 1983.

## 2.6 EQUIPMENT DEVELOPMENT AND MAINTENANCE — M. J. Kania

The IMGA, the PGA, and the x-radiography facility are three important pieces of equipment in use in the PIE of HTGR fuels. Although they are used in routine PIE, we continue to maintain and upgrade their capabilities for more and better quality information.

### 2.6.1 Irradiated Microsphere Gamma Analyzer — M. J. Kania and G. A. Moore

During the past reporting period, the IMGA system has been available less than 30% of the time. Irradiated fuels from capsule HRB-15a were

examined for GA, and the initial examinations of fuel from capsule HT-35 were begun. These results are reported in detail in Sects. 2.3.4 and 2.3.1, respectively.

Major equipment failures were responsible for the unavailability of IMGA. Two components of IMGA (the pulse height analyzer system and the gamma-ray detector) were most seriously affected. Problems with the detector resulted in replacement of the lithium-drifted germanium crystal. This was essentially a new detector and required complete system recalibration. Unfortunately, the new crystal replacement was not explicitly pointed out and was not realized until weeks after the detector was put back into operation. No data loss occurred, however, as new detector efficiencies can easily be incorporated into all data analyses.

Failures with the pulse height analyzer and the data storage devices were not so easily rectified. Problems with the pulse height analyzer concerned the central processing core memory. Such problems required complete system shutdown until failed components could be isolated and replaced. Most failures occurred during IMGA examination runs and required a new run after system repair. The most serious problems were with the data storage devices used with the analyzer. Failure of these devices and subsequent operator error have resulted in the destruction of master disks containing operating system software and numerous IMGA examination runs. We were able to obtain the operating system from another storage device and transfer it to our disk system, but the data from the examination runs were not recovered. In several cases these examination runs covered over 100 h of continuous IMGA operation and represented the combined effort of several weeks of work. Such losses required a reexamination of fuel, provided it was still available.

Repairs to the pulse height analyzer and data storage devices were made to complete the examination of the HRB-15a fuel. However, before attempting to examine fuel from another experiment, the IMGA system will require a thorough maintenance period. We have obtained a second RK-05 disk drive, and this has helped reduce the work load on the original disk drive. The second drive was easily configured to the present operating system.

We also encountered a problem with the automated particle handler. A small number (3 to 10%) of the particles on which a gamma energy spectrum was acquired were not being deposited into the collector bins. Particles were being lost during their removal from the sample changer and loading into the proper collector bin. Although the particles were not retained, the gamma spectrometry data on each particle were preserved. The problem was identified as a missing roll-pin that served as a stop for the particle-unloading mechanism. Without the roll-pin, the unloading mechanism was not properly positioned, which resulted in misalignment of the particle drop-chute and the holes in the collector bin cover. Apparently this pin either was not replaced in the last particle handler servicing in 1979 or was broken during operations since that time (no evidence for the latter has been seen). The problem was eliminated by fabricating an alignment clamp, which attaches to the base of the particle handler and serves as a stop for the unloading mechanism.

Because IMGA plays an important part in our PIE effort, we decided to replace the present pulse height analyzer system. The IMGA is near the point at which a major operating system error or a major component hardware error would put the whole system out of operation until a suitable pulse height analyzer system could be obtained. This would virtually halt our postirradiation effort on HTGR fuels. Therefore, detailed specifications were prepared and submitted for acquisition of a new analyzer system.

### 2.6.2 Postirradiation Gas Analyzer — M. J. Kania and J. C. McLaughlin

During this reporting period a major upgrading of the PGA included significant changes in the system as follows:

- installation of a turbomolecular vacuum pumping system,
- automated operating valves to make all capable of being computer interfaced,
- installation of a capacitance manometer system to the cold breaking chamber for measuring increases in chamber pressure greater than 0.1 mPa ($1 \times 10^{-6}$ torr),
- installation of a new cold breaking chamber for increased radiation shielding, and

- installation of a quadrupole mass spectrometer and associated stainless steel high-vacuum system.

Each of the new additions will improve or extend the capabilities of the PGA system. The new turbomolecular pumping system replaces an original ion pump that was undersized for the system and quite inefficient. The new pumping system will speed up turnaround time for loading new samples into chambers. The installation of the automated calibration system and the new cold breaking chamber will reduce radiation exposure to operating personnel. After interfacing to the computer, the operator will be able to control calibrations without manual operation of components in the PGA glove box. The pressure-measuring system, a capacitance manometer, was installed to correlate gas content as measured by the spectrometer with breaking chamber pressure. Mass spectrometer systems are known to be extremely pressure sensitive, and, as our system pressure is dynamic during the actual gas content measurement, it may affect data collected. In the past we have also found that a system pressure measurement is a secondary check on whether all operations are functioning properly.

Acquisition of the quadrupole mass spectrometer will allow routine use of the high-temperature chamber. Previously, a time-of-flight spectrometer was connected to the high-temperature chamber, and the drift tube for this instrument was located outside the glove box. At high temperatures (>1000°C), volatile fission products like cesium are pumped through the system and plate out in the drift tube, causing a radiation hazard to operating personnel. By substituting a smaller quadrupole system for the time-of-flight instrument, we could incorporate the spectrometer head into the glove box, thus eliminating the hazard to personnel.

The installation of these components was completed and their operation checked in June 1982. The remaining tasks to be completed are the interfacing to the PDP 8/a minicomputer and the updating of software to automate the new equipment. The full interfacing will be accomplished in two steps, with the first step mainly transferring the digital data generated by the spectrometer directly into the computer memory. This first step will

require manual setup of the spectrometer; only the data acquisition will be computer controlled. The second step will include the actual spectrometer setup and control by the computer.

A method has also been developed to stretch the time interval of the gas pulse generated when a particle is broken. Two important consequences can result from stretching this pulse: (1) eliminate the rapid rise in pressure and uncertainty in data accumulation by the instrument in a rapidly changing pressure environment and (2) the longer time period provides for a more accurate measurement of the partial pressures of the gas species present. The method requires the use of an orifice of such size that the duration of the gas pulse can be extended from 1 to 2 s to 100 to 120 s. Calculations indicate this can be accomplished with an orifice having a diameter of 0.762 mm (0.030 in.) coupled with a butterfly valve.

Butterfly valves incorporating such an orifice have been fabricated and installed in the PGA facility. When the valve is open, the pumping speed for the system is not affected. When the valve is closed, the orifice is in place and the pumping speed is drastically reduced. This creates a pressure differential on the breaking chamber side of the orifice versus the spectrometer side of the orifice. With a mean gas content of about 70 nmol of gas released from a single particle, the time required for the pressure to equalize on each side of the orifice is about 115 s. By incorporating such a device, we hope to extend the performance and resolution capabilities of the PGA system.

### 2.6.3 X-Radiography Facility — M. J. Kania

During this reporting period the present system was upgraded by the acquisition of a new high-voltage power supply and console. This allows higher tube voltages and beam currents in addition to those now available with the system. The system can operate with either a high-voltage (16–160 kV)-low-current x-ray tube or a low-voltage (5–50 kV)–high current x-ray tube. The new power supply and console are necessary to provide shorter exposure times to allow greater resolution. With shorter exposure times the amount of "fogging" of the x-ray film caused by the sample inherent radiation is drastically reduced; therefore, increased resolution is possible. The new system was delivered in October 1982.

In addition to the new power supply, three new x-ray tubes were purchased for the facility: two low-voltage tubes (5–50 kV) and one high-voltage tube (16–160 kV). One of the low-voltage tubes is in use and the other serves as a spare. The high-voltage tube will not be used until the new system is installed.

## 2.7 REFERENCES

1. R. L. Senn, I. I. Siman-Tov, and R. E. Harper, "Capsule and Facility Design for an Irradiation Test of HTGR Fuel Rods with Controlled Moisture Injection," unpublished data, Dec. 31, 1982.

2. I. I. Siman-Tov, "Thermal Analysis of HTGR Fuel Rod Specimens Irradiated in Capsule HRB-16," unpublished data, Dec. 31, 1982.

3. T. N. Tiegs, I. I. Siman-Tov, and M. J. Kania, "Capsule HT-35," pp. 23–27 in *High-Temperature Gas-Cooled Reactor Technology Development Program Annual Progress Report for Period Ending December 31, 1980*, ORNL-5753, 1981.

4. E. L. Long, Jr., "Capsule HT-35," pp. 75–81 in *High-Temperature Gas-Cooled Reactor Base Technology Program Annual Progress Report for Period Ending December 31, 1979*, ORNL-5643, 1980.

5. M. J. Kania and T. N. Tiegs, "Capsule HT-35," pp. 16–21 in *High-Temperature Gas-Cooled Reactor Technology Development Program Annual Progress Report for Period Ending December 31, 1981*, ORNL-5871, 1982.

6. E. L. Long, Jr., and D. P. Stinton, "Capsule HRB-15b," pp. 105–09 in *High-Temperature Gas-Cooled Reactor Base Technology Program Annual Progress Report for Period Ending December 31, 1977*, ORNL-5412, 1978.

7. W. E. Thomas et al., *High-Temperature Gas-Cooled Reactor Experiment HRB-15b: Particle Loadings and Irradiation in the High Flux Isotope Reactor*, ORNL/TM-6892, December 1979.

8. T. N. Tiegs et al., "Capsule HRB-15b," pp. 95–97 in *High-Temperature Gas-Cooled Reactor Base Technology Program Annual Progress Report for Period Ending December 31, 1979*, ORNL-5643, 1980.

9. M. J. Kania and T. N. Tiegs, "Capsule HRB-15b," pp. 23–27 in *High-Temperature Gas-Cooled Reactor Technology Development Program Annual Progress Report for Period Ending December 31, 1981*, ORNL-5871, 1982.

10. T. N. Teigs and K. R. Thoms, *Operation and Postirradiation Examination of ORR Capsule OF-2*, ORNL-5428, February 1979.

11. M. J. Kania, B. A. Thiele, and F. J. Homan, *Irradiation-Induced Permeability in Pyrocarbon Coatings, Final Report of Work Conducted Under PWS FD-12*, ORNL/TM-8348, October 1982.

12. J. W. Ketter and R. E. Bullock, *Capsule HRB-15b Postirradiation Examination Report*, GA-A15940, General Atomic Company, San Diego, Calif., June 1981.

13. M. J. Kania, "Results of Postirradiation Examination Conducted at ORNL on HTGR Fuel Specimens Irradiated in Capsule HRB-15a," unpublished data, Dec. 31, 1982.

14. F. J. Homan, J. A. Conlin, and I. I. Siman-Tov, "Capsule HRB-16," pp. 82–98 in *High-Temperature Gas-Cooled Reactor Technology Development Program Annual Progress Report for Period Ending December 31, 1981*, ORNL-5871, 1982.

15. D. P. Stinton, "Dense UCO Kernel Development," pp. 48–49 in *High-Temperature Gas-Cooled Reactor Technology Development Program Annual Progress Report for Period Ending December 31, 1980*, ORNL-5753, 1981.

16. D. P. Stinton et al., *Production of Spherical $UO_2$-$UC_2$ for Nuclear Applications Using Thermochemical Principles*, ORNL/TM-7651, March 1981.

17. D. T. Young, *Status Report — 350 Micron UCO — 1981*, GA-906215, GA Technologies, Inc., San Diego, Calif., September 1981.

18. R. J. Lauf, T. B. Lindemer, and R. L. Pearson, "Out-of-Reactor Studies of Fission Product–Silicon Carbide Interactions in HTGR Fuel Particles," to be submitted for publication.

19. M. J. Kania, F. J. Homan, and A.-W. Mehner, *Comparison of U.S. and FRG Postirradiation Examination Procedures to Measure Statistically Significant Failure Fractions of Irradiated Coated-Particle Fuels*, ORNL/TM-8346, August 1982.

20. M. J. Kania and G. A. Moore, *Postirradiation Examination of HTR Coated Particle Fuels Under PWS FD-20: Set I — HTI Biso-Coated $(Th,U)O_2$ Fuels from Experiments HFR-K1, FRJ2-P22, and R2-K10*, ORNL/TM report in preparation.

# 3. STRUCTURAL COMPONENT DEVELOPMENT AND TESTING (WBS ORI309 and ORI411)

D. J. Naus

## 3.1 INTRODUCTION

The Structural Component Development and Testing research and development task consists of generic studies designed to provide technical support for ongoing prestressed concrete reactor vessel (PCRV)-related activities, to contribute to the technological data base, and to provide independent review and evaluation of the relevant technology. These studies are identified through direct communication with PCRV designers, participation in American Concrete Institute-American Society of Mechanical Engineers committee activities, literature reviews, and communications with researchers in other countries. The program involves four basic interrelated activities: (1) technology assessments, (2) analysis methods development, (3) materials studies, and (4) structural component testing. During this reporting period activities were conducted in three subtask areas: (1) analysis methods development, (2) concrete properties for reactor applications, and (3) structural component testing.

## 3.2 ANALYSIS METHODS DEVELOPMENT

The objective of the analytical effort is to develop techniques that can be incorporated into existing modern finite-element computer programs to improve their accuracy and efficiency. We are currently investigating finite-element computation of creep effects in concrete structures and an embedded-rebar modeling technique.

### 3.2.1 Finite-Element Computation of Creep Effects

The set of computer subroutines developed for finite-element computation of creep effects in reinforced concrete structures has been installed

on the IBM 3033 computer at Oak Ridge National Laboratory (ORNL). In developing the program, designated as CREEP80 (ref. 1), the creep law was considered to be linear, that is, to follow the principle of superposition. The program uses a rate-type creep law based on expanding the relaxation function of concrete into a series of real exponentials, called Dirichlet series. This creep formulation may be visualized by the Maxwell chain model, with the elastic modulus dependent on the concrete age. Material properties can be input either as empirical creep data or as the double-power law for creep. A step-by-step stable integration procedure is used in combination with iterations in each time step. The effects of temperature variations (limited to $\leq$80°C) on creep behavior are modeled by use of the activation energy concept, with different activation energies used for creep rate and the aging process. We defined shrinkage either by using formulas[2] or by specifying a set of experimentally observed values. The concrete is assumed to be homogeneous and isotropic with time-dependent properties and not to be susceptible to cracking.

A series of simple test problems and one large reactor problem were considered to illustrate program capabilities: an axially loaded thin cylinder, a radially loaded thin cylinder, an axially loaded standard concrete (152 mm in diameter by 305 mm) test cylinder, and a 40-m-diam by 36-m-high longitudinally and circumferentially prestressed concrete pressure vessel that undergoes a 55°C temperature increase 550 d after prestressing (concrete age of 730 d). Figure 3.1 presents exaggerated deformations obtained for the reactor vessel at various times.

### 3.2.2 Anchorage Zone Analysis by Use of an Embedded-Bar Concept

When conducting finite-element analyses of reinforced concrete structures, a correct representation of individual reinforcing bars with truss elements in most of the available codes is virtually impossible. The rebars are required to lie only along the edges of the continuum elements. To alleviate this difficulty, we developed a procedure that allows arbitrarily oriented rebars to be embedded in the isoparametric continuum elements.[3] This was accomplished through an algorithm that introduces both positional nodes to define the location of the rebar and an additional basis coordinate.

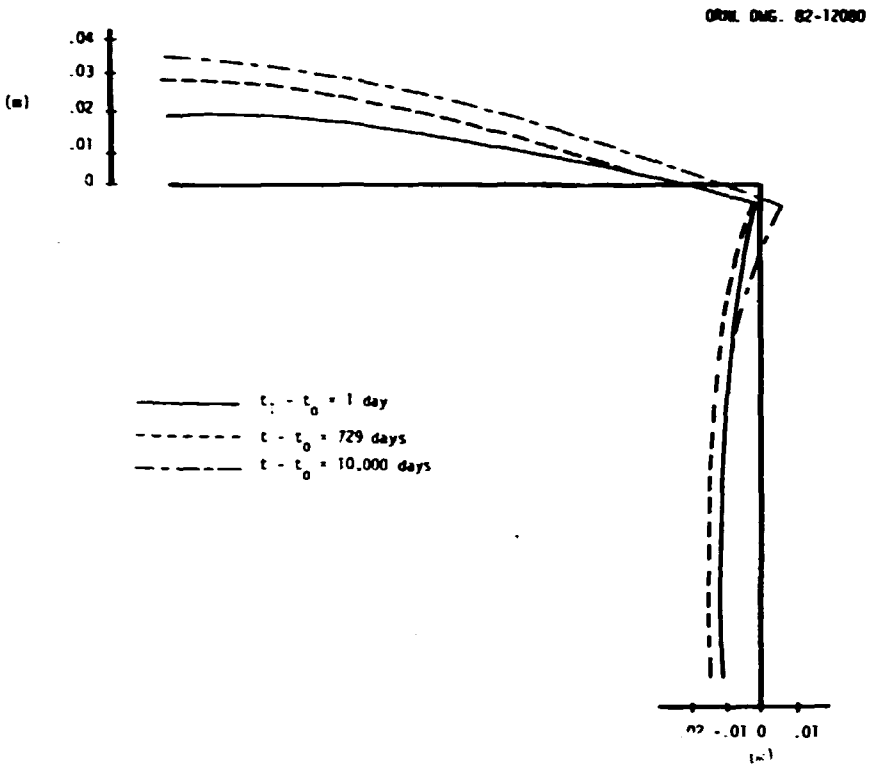


Fig. 3.1. Exaggerated deformations of large reactor vessel problem at various times.

After implementation of the concept into our two- and three-dimensional versions of the ADINA finite-element code, it was validated for simple test cases, that is, grouted tendon flexure elements. To verify the concept further, we performed analyses of end anchor test specimens simulating the anchorage zones of posttensioned tendons in secondary containment vessels of nuclear power plants. We obtained only general agreement between the experimentally determined strain values and those determined analytically (Fig. 3.2). We believe that this resulted from the lack of an unloading cycle in the analysis and the fact that the ADINA concrete model did not represent the material behavior accurately; that is, the concrete model was stiffer than the actual concrete being modeled. Further evaluation of the model requires the development of a more representative concrete model.

## 3.3 CONCRETE PROPERTIES FOR REACTOR APPLICATIONS

Objectives of the concrete properties for the reactor applications task are to develop a bank of highly reliable data and to provide the basic

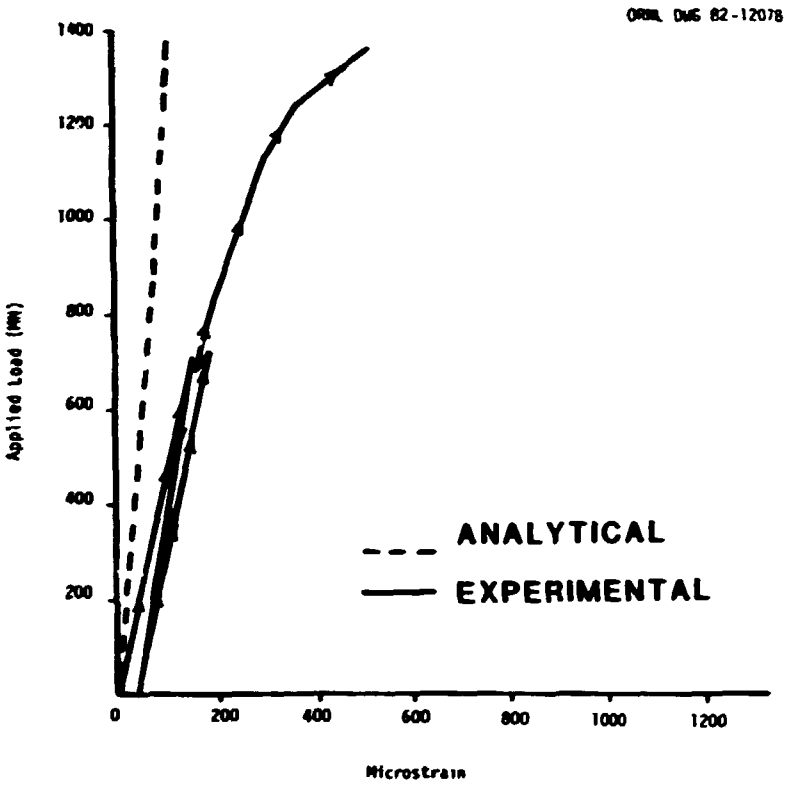


Fig. 3.2. Comparison of analytical and experimental strains for end anchorage block.

information required to support development of improved analysis methods. Current activities are related to evaluating aggregate sources for production of high-strength concrete and developing a performance specification for a concrete elevated-temperature multiaxial material testing system.

### 3.3.1 Review of Aggregate Sources and Impact on Production of High-Strength Concrete

Current PCRV designs incorporate the use of a high-strength concrete (55.2-MPa compressive strength) to effect lower costs through reduced vessel size requirements. A key ingredient in the production of concretes having suitable compressive strengths is related to aggregate quality. For an aggregate to be suitable for production of high-strength concrete, it should have a high compressive strength, good bonding potential with cement paste, and moderate absorption. However, aggregates meeting these requirements may not be available in all parts of the United States.

To identify the availability of suitable aggregate materials for production of 55.2-MPa concrete, a cursory survey was conducted.[4] Results of the survey indicate that (1) the availability of aggregate for concrete production is limited only by the cost of the end product because aggregate may be transported to any given site, (2) aggregates suitable for production of 44.8-MPa concrete should also be suitable for production of 55.2-MPa concrete, and (3) economic benefits derived from the use of higher strength concretes for PCRV construction would more than offset the incremental costs of qualifying a particular concrete mix.

### 3.3.2 Testing-Machine Development in Support of Concrete Property Determinations

Development of concrete models to provide improved analysis capabilities for concrete structures requires material property data. These data should be generated under multiaxial loadings that are representative of the mechanical and thermal loadings likely to be encountered in a PCRV. Although some data meeting these requirements are available, their use is somewhat limited because (1) a representative interface was not provided between the testing-machine platens and the specimen; (2) accuracy and resolution of the devices for determining specimen deformation were questionable; (3) the complete specimen stress-strain curve could not be obtained; (4) loadings in the $x$-, $y$-, and $z$-directions were not independent; and (5) data could be obtained only at room temperature.

Using information from a survey of the concrete multiaxial property data and the systems employed in obtaining the data, we developed a draft performance specification for an elevated-temperature multiaxial concrete testing system during the last reporting period.[5] Basic components of the specification included (1) general requirements (specimen configuration, fatigue, and static loading capabilities), (2) load frame assembly (stiffness and dimensional tolerances), (3) environmental system (heating requirements), (4) specimen development and instrumentation (102-mm specimen, actuator stroke, accuracy, and resolution), (5) interactive computer control and data acquisition (load and temperature control, data acquisition, data processing, and data display), and (6) computer program functional requirements (software specifications).

During this reporting period the draft performance specification and a preliminary request for comments were sent to potential vendors. After receipt of these comments, discussions were held with each of the potential vendors, following which the purchase specification was revised to incorporate vendor input.

## 3.4 STRUCTURAL COMPONENT TESTING

### 3.4.1 Model Testing Technique Development

As noted in the previous reporting period, should a PCRV model test be required for licensing, two areas that require additional development have been identified: wire-winding of the models and nonleak liner systems. Activities during this reporting period focused on fabrication of the approximately 1/30-scale PCRV models and ancillary equipment to demonstrate the techniques developed, that is, use of a prestressed concrete pipe manufacturer to prestress the models circumferentially and a 12-gage AISI 1008 drawing quality steel liner consisting of a flanged head to which a skirt section is joined.

Two PCRV models about 1 m high by 1 m in diameter (Fig. 3.3) were fabricated. The first model was fabricated from a plain concrete mix and will be used to demonstrate the techniques developed. The second model was fabricated from a fibrous concrete mix and will be used to provide an indication of the effectiveness of fibrous concrete for application to PCRV construction. Table 3.1 presents mix proportions for the plain and fibrous concrete mixes. Control specimens tested at a 56-d concrete age indicate that both the plain and fibrous concrete mixes meet current PCRV concrete property requirements for strength ($\geq$55 MPa) and modulus of elasticity ($\geq$38 GPa). About four months after casting, the models were shipped to the prestressed concrete pipe vendor's plant, where 123 turns of 6.35-mm-diam prestressing wire were applied to each model at a force of 31.1 kN. The models were then returned to ORNL.

All ancillary equipment for testing the models has been developed. This includes the pressurization system (hydraulic power supply, accumulators, servovalve, controller, intensifier and piping), which can provide

ORNL-PHOTO 8917-82

Fig. 3.3. Plain and fiber-reinforced prestressed concrete reactor vessel models after casting.

Table 3.1. Plain and fibrous concrete mix proportions

| Material | Type concrete ($kg/m^3$) | |
|---|---|---|
| | Plain | Fibrous |
| Cement (type II) | 529 | 530 |
| Flyash | 67 | 67 |
| Sand | 621 | 622 |
| Coarse aggregate[a] | 931 | 932 |
| Fibers (50 mm by 0.5-mm diam, hooked) | 0 | 88 |
| Water | 238 | 239 |
| Water-reducing agent | 794[b] | 796[b] |

[a]Maximum size for plain mix, 191 mm; maximum size for fibrous mix, 95 mm.

[b]$mL/m^3$.

closed-loop pressurization to the models at pressures up to 34.5 MPa; instrumentation systems; and a multichannel computer-controlled data acquisition system. Testing of the models will be completed during the next reporting period.

### 3.4.2 Structural Response Testing of Thermal Barrier Ceramic Pads

We are evaluating the candidate ceramic pad configurations that support the graphite posts in the bottom head region of the core outlet plenum of the PCRV for a high-temperature gas-cooled reactor (HTGR). The objective of the first phase of the program was completed during this reporting period, which included a determination of the ability of the pads to withstand mechanical loading conditions representative of those imposed on the pads by thermal gradients.

Hard ceramic materials investigated include 85 and 99.5% pure alumina. Test articles fabricated from these materials were right circular disks 216 mm in diameter and either 38 or 76 mm thick. Extending vertically through each disk was a 76-mm-diam hole as shown in Fig. 3.4. Two interface materials that are used with the hard ceramic materials to provide a

ORNL-PHOTO 8056-82

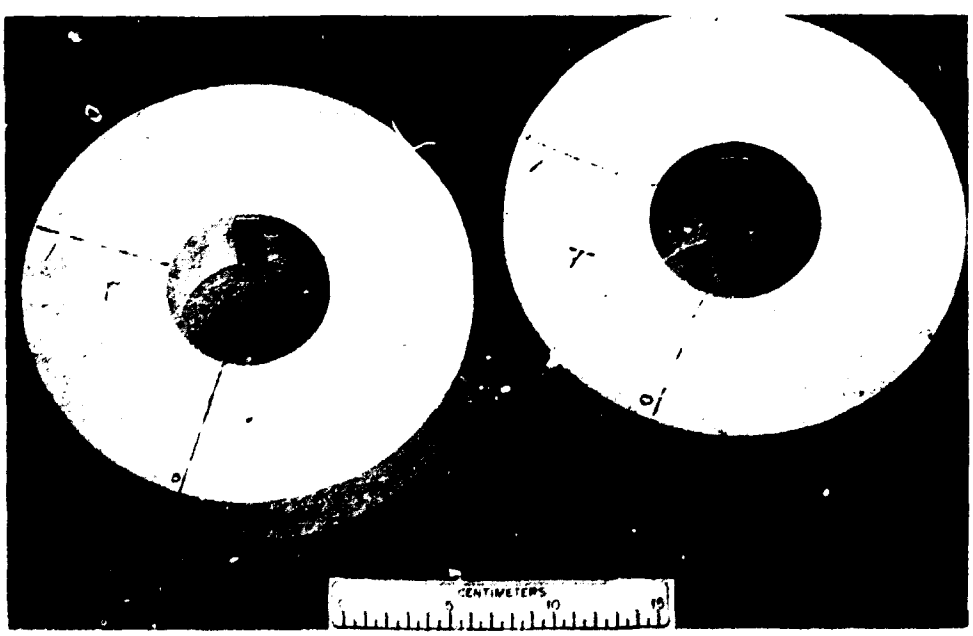


Fig. 3.4. Alumina thermal barrier hard ceramic pad test specimens.

more uniform loading environment and to permit more pad rotational freedom (reduce stresses) were also investigated: a woven silica fabric and a graphite cloth.

The pads and interface materials were investigated by a test developed at ORNL.[6] Loadings representative of those induced into the pads by thermal gradients were applied to the pads with the test fixture shown in Fig. 3.5, which incorporates conical platens so that the contact angle between the platens and pads can be changed. Data obtained as a function of applied load during a test included rotations, axial and circumferential strains, and acoustic emission. A total of 62 hard ceramic pad material structural tests was conducted in this evaluation.[7]

ORNL-PHOTO 8289-82

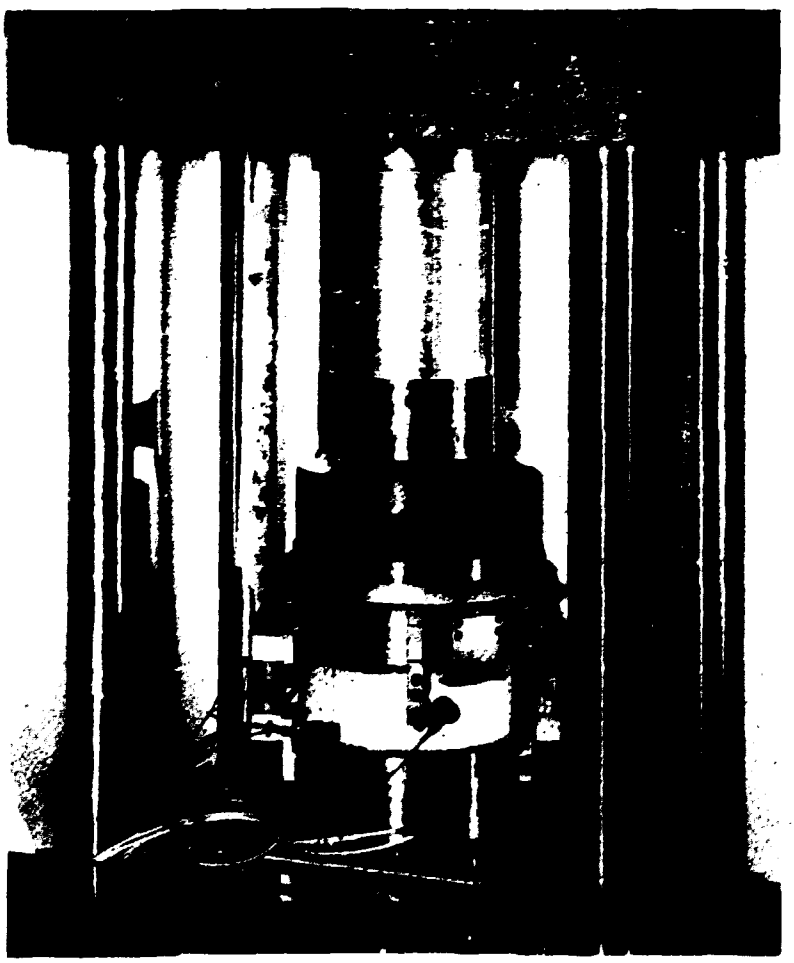

Fig. 3.5. Test fixture for applying representative loadings to hard ceramic pad specimens.

## 3.5 REFERENCES

1. Z. P. Bazant and E. C. Rossow, "CREEP80 Axisymmetric Finite-Element Program for Creep Analysis of Aging Concrete Structures at Variable Temperature," unpublished data, Dec. 31, 1982.

2. Z. P. Bazant and L. Panula, "Practical Prediction of Time-Dependent Deformations of Concrete," pp. 307–28 and 415–34 of vol. 2 and pp. 169–83 of vol. 12 in *Materials and Structures*, Reunion International des Laboratories, Paris, 1979.

3. J. R. Dougan and D. N. Fanning, "Anchorage Zone Analyses Using an Embedded Bar Concept," unpublished data, Dec. 31, 1982.

4. C. B. Oland, "Sources of Aggregates Available in the United States and the Impact of Aggregate Availability Relative to the Production of High-Strength Concrete," unpublished data, Dec. 31, 1982.

5. G. C. Robinson, *Purchase Specification for Elevated-Temperature Multiaxial Concrete Testing System*, Specification M-11926-RS-001-0, Oak Ridge National Laboratory, November 1980.

6. G. C. Robinson, "Plan for Conducting Structural Response Tests of Thermal Barrier Hard Ceramic Pads," unpublished data, Dec. 31, 1982.

7. C. B. Oland, D. J. Naus, and G. C. Robinson, "Structural Response Testing of Thermal Barrier Hard Ceramic Materials," unpublished data, Dec. 31, 1982.

# 4. HTGR STRUCTURAL MATERIALS (WBS 0R1201, 0R1201Ad, 0R1202, and 0R1501)

P. L. Rittenhouse

## 4.1 INTRODUCTION — P. L. Rittenhouse

Our work on structural materials is focused on design data needs that have been identified for the High-Temperature Gas-Cooled Reactor (HTGR) Steam Cycle-Cogeneration (SC-C) lead project. The programs in progress emphasize alloys and ceramics that have been selected as reference materials for critical components of the SC-C system, such as thermal barriers, heat exchangers, prestressed concrete reactor vessel (PCRV) liners and penetrations, reactor internals, and core support structure. Although we expect these reference materials to perform satisfactorily, additional information and data are needed for the detailed design of the SC-C and to ensure that the materials are suitable from all viewpoints, including ASME Code approval and long-term service.

The other principal participant in the U.S. effort on HTGR structural materials for the SC-C system is GA Technologies, Inc. (GA); a small effort related to SC-C alloys is performed by the General Electric Company (GE), but its major responsibility is alloys for advanced HTGRs. All the materials work is coordinated on a national basis through the activities of the HTGR Materials Working Group.

The activities of the Oak Ridge National Laboratory (ORNL) program on HTGR structural materials fell into the following six major areas during 1982:

- mechanical properties,
- corrosion and compatibility of alloys,
- joining technology,
- structural ceramics,
- fission product-materials interactions, and
- liner and penetration studies.

The various tasks within each of these areas are discussed in separate sections of this chapter.

## 4.2 MECHANICAL PROPERTIES OF HTGR ALLOYS, WELDMENTS, AND CERAMICS — C. R. Brinkman, K. C. Liu, J. F. King, H. E. McCoy, and J. P. Strizak

### 4.2.1 Creep and Tensile Properties of Alloys and Weldments — H. E. McCoy and J. F. King

Testing during 1982 involved a large number of materials, including Hastelloy X base metal (two heats), Hastelloy X weldments (two welding processes), Inconel 617 base metal (two heats), Inconel 617 gas tungsten arc (GTA) weldment, Inconel 618 base metal, Inconel 618 GTA weldment, HD556 base metal, HD556 GTA weldment, Hastelloy X–alloy 800H weldment (two welding processes), several heats of modified Inconel 617 with variations in chromium and titanium concentrations, Incoloy 802, Inconel 718, and 2 1/4 Cr-1 Mo steel (three heats). Creep test temperatures ranged from 482 to 871°C; test environments were air and HTGR-He.

Techniques were developed previously for making sound welds in Hastelloy X by both the GTA and shielded metal arc (SMA) welding processes. Short-term tensile strength of the weld metal was generally superior to that of the base metal, but the failure of creep specimens containing a transverse weldment occurred in the weld metal. Although the creep strength of Hastelloy X weld metal was inferior to that of Hastelloy X base metal, the difference was very small. Possible difficulties with Hastelloy X are (1) the fracture strain at ambient temperature decreases very significantly with elevated-temperature exposure and (2) the carburization that occurs during exposure to HTGR-He makes the reduction in fracture ductility even greater. Several creep tests on Hastelloy X are now approaching 50,000 h, and testing will continue into 1983.

Inconel 617 is readily weldable by the GTA process with Inconel 617 filler metal. The weld deposit is stronger than the base metal, and failure occurs in the base metal during tensile and creep rupture tests. Although the material carburizes during high-temperature exposures, we have detected no effect of carburization on creep properties. This alloy is considerably stronger than Hastelloy X, and its ductility at ambient temperature is greatly reduced by long-term exposure at elevated temperatures. However, the rate of ductility decrease for Inconel 617 at

a given temperature is less rapid than that for Hastelloy X. Ductility values after 20,000 h of exposure at 871°C are about the same for both. Inconel 617 also exhibits very low creep fracture strain (1–2%) in a temperature range around 650°C. Inconel 617 is no longer considered a reference alloy for the steam cycle HTGR, and our testing of this material is therefore being phased out in 1983.

Inconel 618 was welded with Inconel 618 filler metal by the GTA process. The weld deposit was stronger than the base metal under all conditions tested, so failure in a sample with a transverse weld occurred in the base metal. The creep strength of this alloy is similar to that of Hastelloy X. Impact samples of base metal and transverse welds are being aged in inert gas at 871°C; samples tested after aging in excess of 10,000 h showed remarkable retention of impact strength. Testing of this alloy is also in a phaseout period.

Several chemical modifications of Inconel 617 have also been evaluated. The modifications center around the reasoning (1) that chromium increases the tendency for carburization to occur and that the 20 to 23% Cr present in most commercial alloys is not needed for adequate oxidation resistance in HTGR-He and (2) that titanium or aluminum may proviue some strengthening through carbide or gamma prime dispersions and be effective in forming oxides that resist carburization. Test effort has been minimal for most of these alloys, but some results are available. The modified alloys are easily weldable and exhibit improved resistance to carburization. The alloys have creep strength in the range of that for standard Inconel 617. Those that are stronger contain sufficient aluminum and titanium to form gamma prime. Emphasis on these alloys will decrease even further during 1983 because of their lack of application to the steam cycle HTGR.

Incoloy 802 was welded satisfactorily with Inconel 617 filler by the GTA process. The short-term low-temperature creep strength of Inconel 617 is slightly less than that of Incoloy 802, so failure occurred in the Inconel 617 weld metal. Incoloy 802 contains 0.3% C, and the fracture strain is quite low. No further work on this alloy is anticipated.

The alloy HD556 is stronger than Inconel 617 and can be suitably joined with HD556 filler metal. The cast weld metal is relatively weak in this alloy, and failure therefore usually occurs in the weld metal.

Although fracture strains are quite high under creep conditions, the ductility at ambient temperature degrades rapidly with exposure at elevated temperature. Work on this alloy was terminated this year.

Hastelloy X and alloy 800H were joined with both Inco weld A [shielded metal arc welding (SMAW) process] and ERNiCr-3 (GTA process) filler materials. Alloy 800H has lower creep strength than the other materials involved, so failure consistently occurred in it. No additional work on these weldments is planned.

The creep strength of 2 1/4 Cr-1 Mo steel is lower than that of the other materials being studied. It is, however, a very important material for use in the cooler parts of the steam system. Three heats of material are being tested, and it appears that the material is carburized at 482°C but decarburized at all higher test temperatures. These changes in carbon content appear to have some small effects on the creep behavior. Some creep tests have reached 50,000 h and are continuing.

Tests have recently been initiated on Inconel 718, a candidate for use in the core lateral restraint structure and in the circulator bellows. This material can be heat treated to produce excellent creep strengths, but at about 650°C overaging occurs and the strength decreases.

As evidenced from the foregoing, a very large number of alloys and weldments were involved in our 1982 program. Most of these were carryovers from previously initiated studies; efforts next year will be devoted almost totally to Inconel 718, 2 1/4 Cr-1 Mo steel, and Hastelloy X.

4.2.2 Effect of Thermal Aging on Properties — H. E. McCoy

Most of the alloys being evaluated change properties as a result of exposure at elevated temperatures. A number of test samples are being exposed to determine the magnitude of these effects. Some of the changes are thermally induced, and some are the results of interactions with the HTGR-He environment. Thus, aging tests are being run in both inert gas and HTGR-He.

Samples of Inconel 617 and Hastelloy X base metal and weldments have been tested following 20,000-h exposure to inert gas and HTGR-He. Some strength changes occurred, but the observation of primary interest was

that the fracture strain at ambient temperature was reduced. The magnitude of the reduction was greater when aged in HTGR-He than when aged in inert gas. Some of these samples have now been aged 40,000 h. Samples of Inconel 618 base metal and weldments and modified Inconel 617 being aged in HTGR-He have accumulated 19,000 h of exposure. Samples of Inconel 718 have been aged for 3000 h.

4.2.3 Low-Cycle Fatigue and Creep-Fatigue Interactions — J. P. Strizak

Fatigue testing of Hastelloy X is under way at 760°C in air and HTGR-He environments. Results of continuous-cycling strain-controlled fatigue tests are given in Table 4.1. Figure 4.1 compares the resultant fatigue lives obtained in the two environments. A small beneficial effect of the helium environment is seen on fatigue life compared with data obtained in air. This behavior is similar to that observed previously[1] at 538 and 871°C.

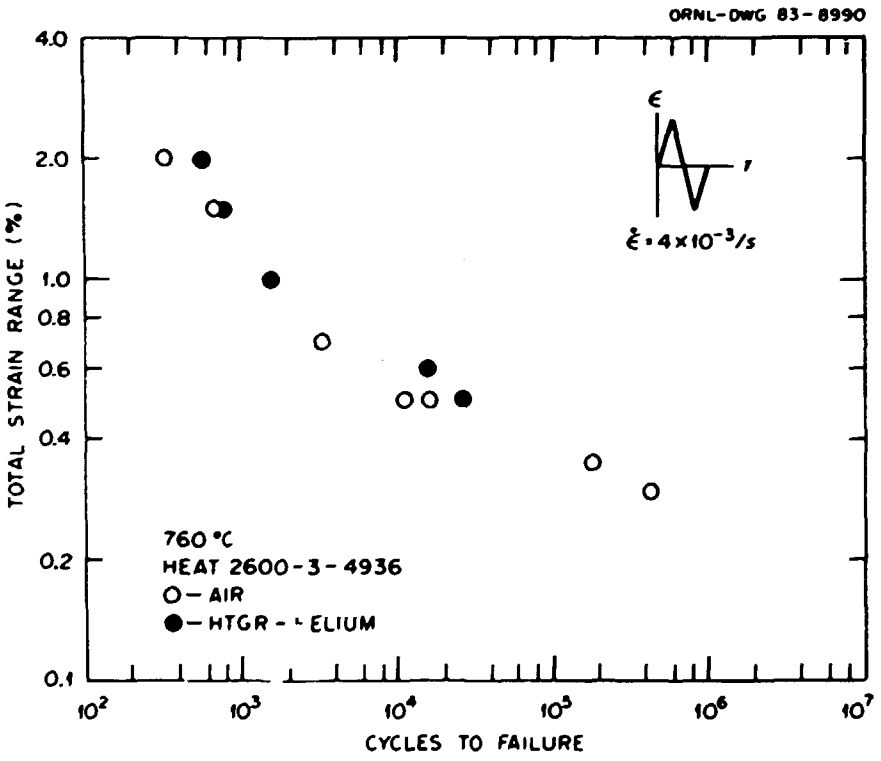


Fig. 4.1. Comparison of strain-controlled fatigue data generated at 760°C in air and HTGR-He for Hastelloy X.

Table 4.1. Low-cycle fatigue data for Hastelloy X at 760°C

| Specimen[a,b] | Total strain range[c] $\Delta\varepsilon_t$ (%) | Stress range $\Delta\sigma$ (MPa) | Stress amplitude[d] (MPa) | | Strain range[d] (%) | | Cycles to failure $N_f$ |
|---|---|---|---|---|---|---|---|
| | | | Tensile $\sigma_t$ | Compressive $\sigma_c$ | Elastic $\Delta\varepsilon_e$ | Plastic $\Delta\varepsilon$ | |
| *Tests conducted in air* | | | | | | | |
| HXL96 | 2.0 | | | | 0.58 | 1.42 | 331 |
| HXL50 | 1.5 | 800 | 396 | 404 | 0.50 | 1.00 | 598 |
| HXL2 | 1.0 | 684 | 339 | 345 | 0.47 | 0.53 | 1,582 |
| HXL17 | 0.7 | 655 | 323 | 332 | 0.45 | 0.25 | 3,351 |
| HX07 | 0.5 | 558 | 277 | 281 | 0.38 | 0.12 | 16,077 |
| X4701 | 0.5 | 584 | 288 | 296 | 0.40 | 0.10 | 11,155 |
| X4710 | 0.35 | 569 | 297 | 272 | 0.31 | 0.04 | 178,288 |
| X4704 | 0.3 | 517 | 247 | 270 | 0.28 | 0.02 | 457,234 |
| *Tests conducted in HTGR-He* | | | | | | | |
| HX15 | 2.0 | | 438 | 463 | 0.62 | 1.38 | 567 |
| HX20 | 1.5 | | 402 | 412 | 0.56 | 0.94 | 750 |
| HX18 | 1.0 | | 391 | 423 | 0.60 | 0.40 | 1,558 |
| HX19 | 0.6 | | 292 | 321 | 0.42 | 0.18 | 15,647 |
| HX17 | 0.5 | | 283 | 330 | 0.42 | 0.08 | 26,525 |
| X4201 | 0.5 | | 272 | 310 | 0.40 | 0.10 | 13,543 |

[a]Hourglass-shaped specimen, 5.35-mm minimum diameter, R:d ratio (radius:diameter) = 6.

[b]Specimen numbers with H prefix are heat 4936; X prefix, heat 4284. Material was solution annealed.

[c]Fully reversed strain control fatigue tests employing a triangular waveform with a strain rate of $4 \times 10^{-3}$/s.

[d]Values at $N_f/2$.

Results of creep-fatigue tests obtained to date are given in Table 4.2. The introduction of tension or compression strain hold periods resulted in lower fatigue lives compared with the continuous-cycle fatigue lives obtained in air and HTGR-He. In air, resultant fatigue lives of tests conducted at a strain range of 2% showed that compressive hold periods were somewhat more damaging than were the tensile hold periods. This was observed in both solution-annealed material and material (initially solution annealed) that was aged for 20,000 h at 704°C in argon before fatigue testing. Further, fatigue lives for creep-fatigue tests conducted at strain ranges of 0.5 and 2% on the preaged material were lower compared with results obtained for solution-annealed material. Similar behavior was previously reported[1] for continuous cycle data obtained at 538 and 871°C on preaged material. Results of 760°C creep-fatigue tests on specimens X2302 and 3310 indicated that preaging at 871°C was somewhat more damaging than was preaging at 704°C.

As shown in Table 4.2 the fatigue life of Hastelloy X at a strain range of 0.5% was reduced from about 16,000 to 1600 cycles when hold periods were introduced. Fatigue lives of tests with compressive hold periods were essentially the same as cyclic lives obtained in tests with tension hold periods. Increasing the hold period from 0.5 to 1.0 h had no apparent effect on cyclic life. It should be noted that tests with tension hold periods developed mean compressive stresses and that compressive hold period tests developed mean tensile stresses. The most damaging effect on fatigue life was obtained when tension and compressive hold periods were introduced during each cycle of the test. Creep-fatigue testing in both air and HTGR-He environments is continuing.

### 4.2.4 High-Cycle Fatigue — J. P. Strizak

In March 1982 a low-cycle fatigue test system was outfitted for high-cycle fatigue testing in air. Testing of Hastelloy X in air at 760°C is continuing; the objective is to obtain data for lifetimes of up to $10^8$ cycles. Limited data obtained to date are given in Table 4.3. Specifications are currently being developed for procurement of an environmental chamber and associated hardware. We expect a high-cycle fatigue system for testing in HTGR-He to be operational about the end of Fiscal Year 1983.

Table 4.2. Creep-fatigue data for Hastelloy X at 760°C

| Specimen[a,b] | Total strain range[c] $\Delta\varepsilon_t$ (%) | Hold period[d] (h) | Stress range $\Delta\sigma$ (MPa) | Stress amplitude (MPa) | | Strain range (%) | | Relaxed stress (MPa) | | Cycles to failure $N_f$ | Time to failure $t_f$ (h) |
|---|---|---|---|---|---|---|---|---|---|---|---|
| | | | | Tensile $\sigma_t$ | Compressive $\sigma_c$ | Elastic $\Delta\varepsilon_e$ | Plastic $\Delta\varepsilon_p$ | Tensile $\sigma_{tr}$ | Compressive $\sigma_{cr}$ | | |
| *Tests conducted in air* | | | | | | | | | | | |
| HXL96 | 2.0 | 0 | 852 | 416 | 436 | 0.58 | 1.42 | | | 331 | 0.92 |
| X2307 | 2.0 | 0 | 965 | 475 | 490 | 0.67 | 1.33 | | | 153 | 0.43 |
| HXL05 | 2.0 | 1.0T | 936 | 450 | 486 | 0.34 | 1.66 | 77 | | 214 | 214.59 |
| HXL97 | 2.0 | 1.0C | 912 | 456 | 456 | 0.37 | 1.63 | | 100 | 147 | 147.41 |
| HX06 | 2.0 | 1.0T + C | 921 | 456 | 456 | 0.11 | 1.87 | 81 | 86 | 195 | 390.54 |
| X2304 | 2.0 | 1.0T | 954 | 455 | 499 | 0.41 | 1.59 | 104 | | 121 | 121.34 |
| X2302 | 2.0 | 1.0C | 977 | 508 | 469 | 0.42 | 1.58 | | 105 | >101 | >101.28 |
| X3310 | 2.0 | 1.0C | 923 | 456 | 467 | 0.38 | 1.62 | | 104 | 88 | 88.24 |
| HX07 | 0.5 | 0 | 558 | 277 | 281 | 0.38 | 0.12 | | | 16,077 | 11.16 |
| HX13 | 0.5 | 0.5T | 457 | 189 | 268 | 0.23 | 0.27 | 62 | | 1,643 | 822.64 |
| HX09 | 0.5 | 0.5C | 586 | 359 | 232 | 0.31 | 0.19 | | 94 | 1,622 | 812.13 |
| HX10 | 0.53 | 0.5T | 562 | 218 | 344 | 0.28 | 0.25 | 71 | | 1,530 | 766.06 |
| HX11 | 0.5 | 0.5T + C | 549 | 269 | 280 | 0.12 | 0.38 | 84 | 95 | 1,286 | 1,286.89 |
| X2306 | 0.5 | 0.5C | 565 | 321 | 244 | 0.28 | 0.22 | | 89 | 1,573 | 787.59 |
| TC1 | 0.5 | 1.0C | 569 | 325 | 224 | 0.29 | 0.21 | | 94 | 1,606 | 1,607.12 |
| TC2 | 0.5 | 1.0T | | | | | | | | >381[e] | >381.76 |
| *Tests conducted in HTGR-He* | | | | | | | | | | | |
| HX17 | 0.5 | 0 | 613 | 283 | 330 | 0.42 | 0.08 | | | 26,525 | 18.42 |
| X4201 | 0.5 | 0 | 582 | 272 | 310 | 0.40 | 0.10 | | | 13,543 | 9.40 |
| HX16 | 0.5 | 0.5C | 659 | 366 | 293 | 0.32 | 0.18 | | 97 | >1,563[f] | 782.59 |
| X4203 | 0.5 | 0.5T | | | | | | | | >2,499[e] | >1,251.24 |

[a]Hourglass-shaped specimen; 5.35-mm minimum diameter, R:d ratio (radius:diameter) = 6.

[b]Specimen numbers with H prefix are solution-annealed heat 4936; X4 prefix, solution-annealed heat 4284; X2, heat 4936 aged 20,000 h at 704°C in argon; X3, heat 4936 aged 20,000 h at 871°C in argon.

[c]Fully reversed strain control fatigue tests employing a triangular waveform with a strain rate of $4 \times 10^{-3}$/s.

[d]T, tension hold period introduced each cycle at peak strain amplitude; T, compression hold period.

[e]Test in progress.

[f]Test terminated because of power interruption in laboratory.

Table 4.3. High-cycle fatigue data at 760°C in air for Hastelloy X

| Specimen[a] | Total strain range[b] $\Delta\varepsilon_t$ (%) | Stain rate $\dot{\varepsilon}$ (%/s) | Frequency[c] (Hz) | Stress amplitude (MPa) | | Stress range, $\Delta\sigma$ | Strain range (%) | | Cycles to failure $N_f$ |
|---|---|---|---|---|---|---|---|---|---|
| | | | | Tensile $\sigma_c$ | Compressive $\sigma_c$ | | Elastic $\Delta\varepsilon_e$ | Plastic $\Delta\varepsilon_p$ | |
| X4701 | 0.50 | 0.4 | | 286 | 293 | 579 | 0.40 | 0.10 | 11,155 |
| X4702 | 0.35 | 0.4 | | 297 | 272 | 569 | 0.31 | 0.04 | 178,288 |
| X4703 | 0.30 | 0.4 | | 247 | 270 | 517 | 0.28 | 0.02 | 457,234 |
| X4709 | 0.28 | 0.4 | 15 | 267 | 253 | 520 | 0.26 | 0.02 | 15,500,000 |
| X4708 | 0.27 | 0.4 | 10 | 248 | 248 | 462 | 0.27 | | 60,342,990 |
| X4712[d] | 0.285 | 0.4 | | | | | | | >1,891,000 |

[a]Heat 2600-7-4747, solution-annealed material. Uniform-gage specimen with 6.35-mm diam by 19-mm-long gage area.

[b]Fully reversed uniaxial push-pull tests with a triangular waveform.

[c]Changed from strain control to load control after reaching stable stress amplitudes.

[d]Test in progress.

### 4.2.5 Stress Relaxation of Ceramics — K. C. Liu

Time-dependent mechanical properties of structural ceramics in creep and stress relaxation are important data for the design and safety analyses of the HTGR core support pads that are likely to be constrained during thermal transients. A stress relaxation system capable of testing structural ceramics at high temperature by four-point bending in controlled HTGR-He atmosphere, developed at ORNL and reported previously,[2] has been checked out and is now in commission.

An exploratory test was performed on a silicon nitride specimen at nominally 750°C in an HTGR-He environment by four-point bending. The specimen was loaded to a bending strain of 0.25% and held constant to investigate the stress relaxation behavior as depicted in Fig. 4.2. The

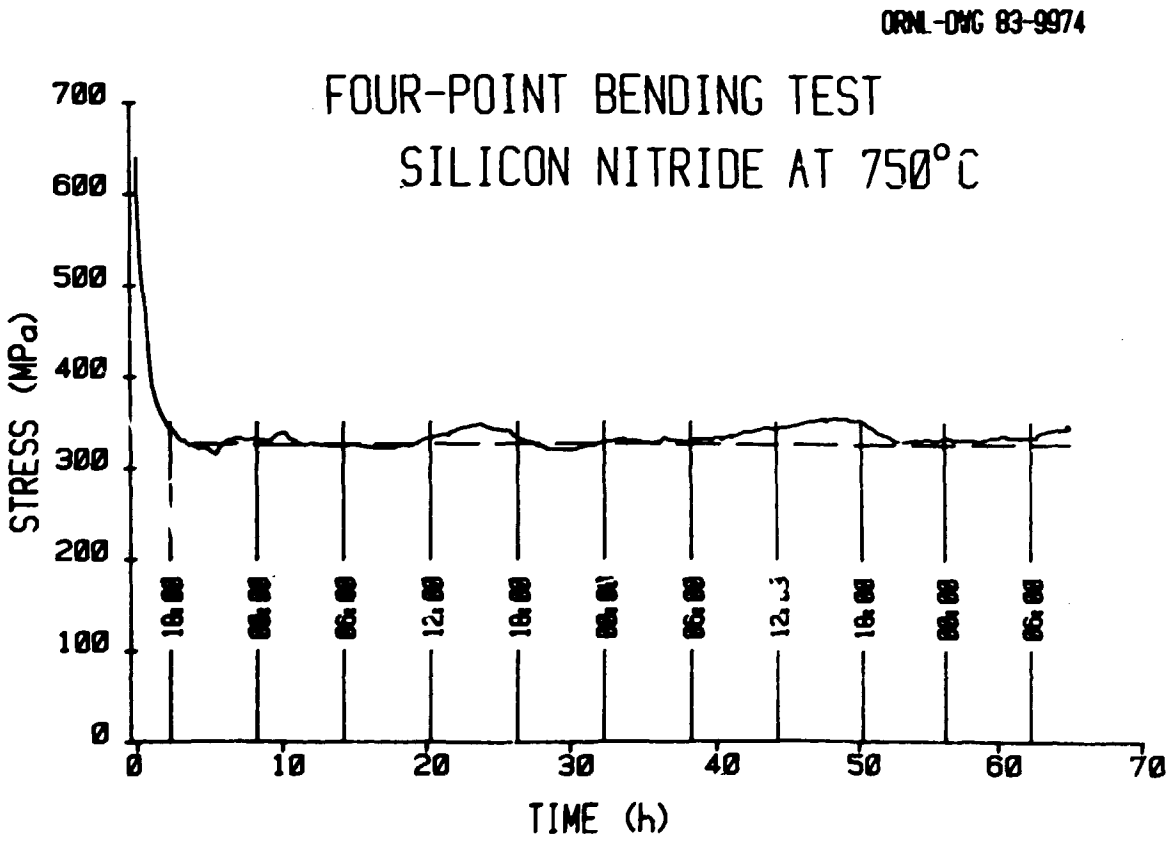


Fig. 4.2. Four-point bending test of silicon nitride at 750°C.

maximum stress at the onset of stress relaxation was 640 MPa (92,800 psi), decreased 23% to 492 MPa (71,400 psi) in the first 0.5 h, and 37% to 403 MPa (58,460 psi) and 43% to 365 MPa (52,900 psi), respectively, in the subsequent two 0.5-h periods. The stress was 324 MPa (47,000 psi) at the end of the 65-h test. Almost all (96%) the stress relaxation was accomplished in the first 5-h period. In theory, the stress response thereafter should decrease monotonically and remain flat as illustrated in Fig. 4.2 by the dashed line. However, the recorded stress response was somewhat incoherent. Examinations indicate that two stress risers occurred consistently between about 9:00 AM and 6:00 PM daily during weekdays. This observation suggests that the changes of the ambient temperature exerted a strong influence on the test results because the load application pull rod, although mostly enclosed in the environmental chamber, was a heat sink. Efforts are now being made to eliminate the anomalies by reinstalling the testing system in a more confined atmosphere, where the ambient temperature can be controlled reasonably.

The modulus of elasticity calculated on the basis of the beam equation was 260 GPa ($37.76 \times 10^6$ psi) at 750°C compared with 320 GPa ($46.47 \times 10^6$ psi) at room temperature, a decrease of about 20%.

In summary, the testing system is now apparently operational, provided that tests are conducted in a controlled atmosphere with a reasonably stable ambient temperature.

4.2.6 Creep Behavior of Ceramics — H. E. McCoy

Compressive creep tests were run previously on Corning grade 7941 $SiO_2$ from 816 to 927°C. However, Corning has not been able to manufacture the 7941 grade consistently, and we are now using a Thermo Materials $SiO_2$. Our more recent testing of $SiO_2$ was performed at 650°C, which is closer to the expected service temperature. Tests are also in progress on two grades of Coors $Al_2O_3$ (AD-85 and AD-995) at 750°C; these tests are now in excess of 5000 h. In addition to compressive creep, two four-point bending creep tests are in progress on the Thermo Materials $SiO_2$.

## 4.3 CORROSION AND COMPATIBILITY OF HTGR ALLOYS — J. H. DeVan, H. Inouye, and P. F. Tortorelli

### 4.3.1 Carburization of Alloys by HTGR-He — H. Inouye

The relationships of $\dot{S}(H_2O)$ (the supply rate of $H_2O$) and $\dot{S}(CH_4)$ (the supply rate of $CH_4$) to the carburization of Hastelloy X and alloy 800H are shown in Figs. 4.3 and 4.4, respectively. In Fig. 4.3 the carburization levels vary inversely with log $\dot{S}(H_2O)$. An oxide layer formed on the surfaces of Hastelloy X specimens when $\dot{S}(H_2O)$ exceeded about $1 \times 10^{-5}$ g/(cm$^2$·h) and on alloy 800H at values in excess of about $5 \times 10^{-7}$ g/(cm$^2$·h). Below these respective water supply rates, the surface reaction products consisted of carbides rather than oxides. Therefore, the intersections of the line segments appear to be the critical water supply rates that define the carbide-oxide formation boundaries. The displacement of the carbon increase $\Delta C$ versus the $\dot{S}(H_2O)$ plot for alloy 800H to the left of that for Hastelloy X is attributed to the effects of alloy composition on carburization and in particular to the influence of about 0.4 wt % each of titanium and aluminum on the oxidation of alloy 800H.

In contrast to the effect of $H_2O$, $\Delta C$ increased with log $\dot{S}(CH_4)$ in the manner shown in Fig. 4.4. At the lower $CH_4$ supply rates, surface carbide particles were observed on both alloys, but at the higher supply rates continuous carbide layers were formed. The inflections in the plots of Fig. 4.4 therefore appear to correspond to changes in the morphology of the surface carbides.

The parameter that describes the test gas conditions at the specimen surface is

$$\dot{S} = (Q_{He})(P)(M)/AV \ , \qquad (1)$$

where

$\dot{S}$ = impurity supply rate [g/(cm$^2$·h)],
$Q_{He}$ = helium flow rate at system pressure (cm$^3$/h),
$P$ = impurity partial pressure,
$M$ = impurity molecular weight (g/mol),
$A$ = specimen surface area (cm$^2$),
$V$ = molecular volume at 298 K (cm$^3$/mol).

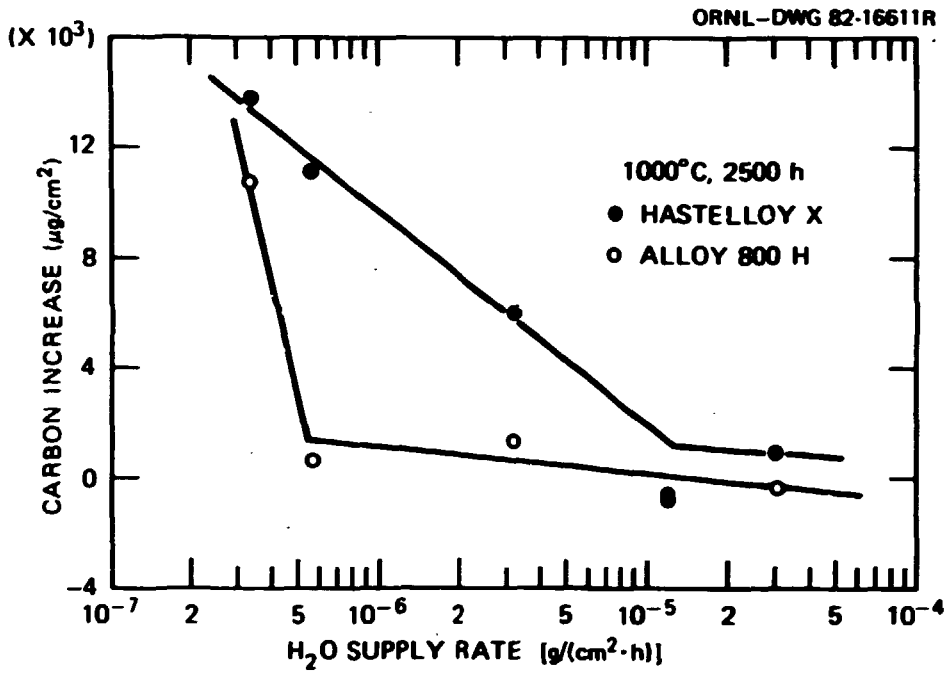


Fig. 4.3. Dependence of carburization on the water supply rate. Nominal test gas: 50 $H_2$/5 $CH_4$/5 CO/0.00–0.014 $H_2O$ (Pa) [500 $H_2$/50 $CH_4$/50 CO/0.0–1.4 $H_2O$ (μatm)]; HTGR-He flow: 1–10 L/min.

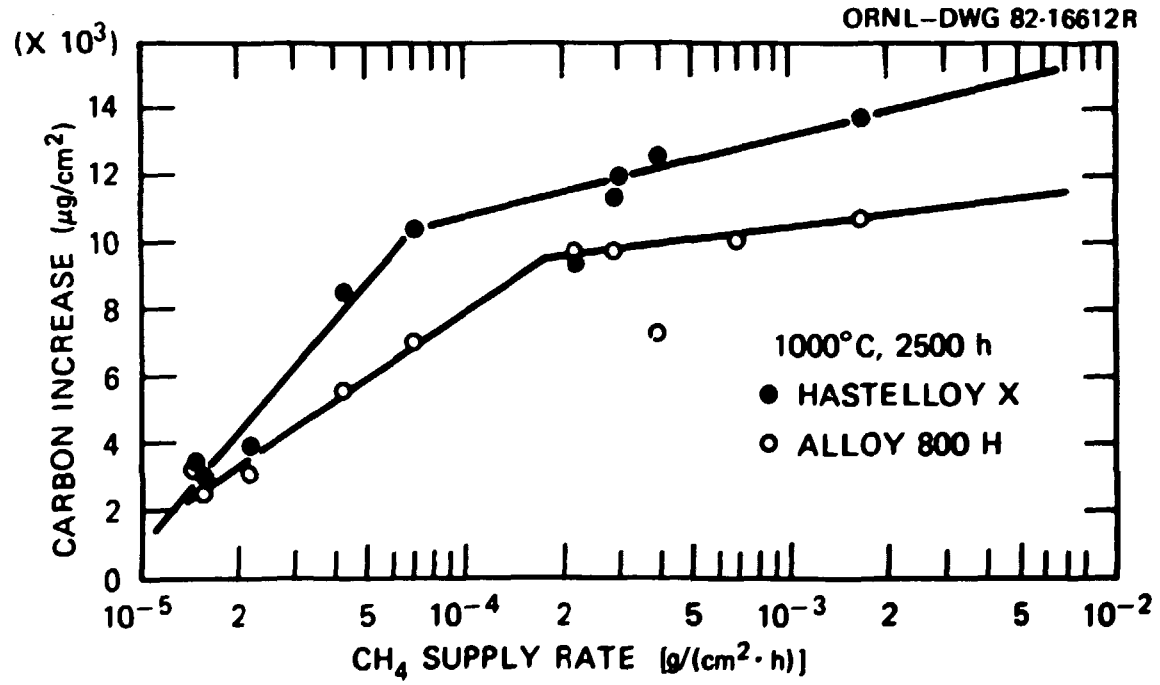


Fig. 4.4. Dependence of carburization on the methane supply rate. Nominal test gas: 50 $H_2$/5 $CH_4$/5 CO/0.00–0.014 $H_2O$ (Pa) [500 $H_2$/50 $CH_4$/50 CO/0.0–1.4 $H_2O$ (μatm)]; HTGR-He flow: 1–10 L/min.

Thus, a stringer of corrosion specimens in a retort is exposed to helium impurities, whose supply rates vary inversely with the surface area of the exposed specimens. Because the impurities react with the specimens, their concentration decreases at each succeeding downstream specimen position, and this depletion causes the carburization of alloys to depend highly on position in the gas stream, as shown in Fig. 4.5. The appearance of carburization maxima for specimens at the intermediate positions in the retort was caused by the depletion of $H_2O$ and $CH_4$ from the test gas.

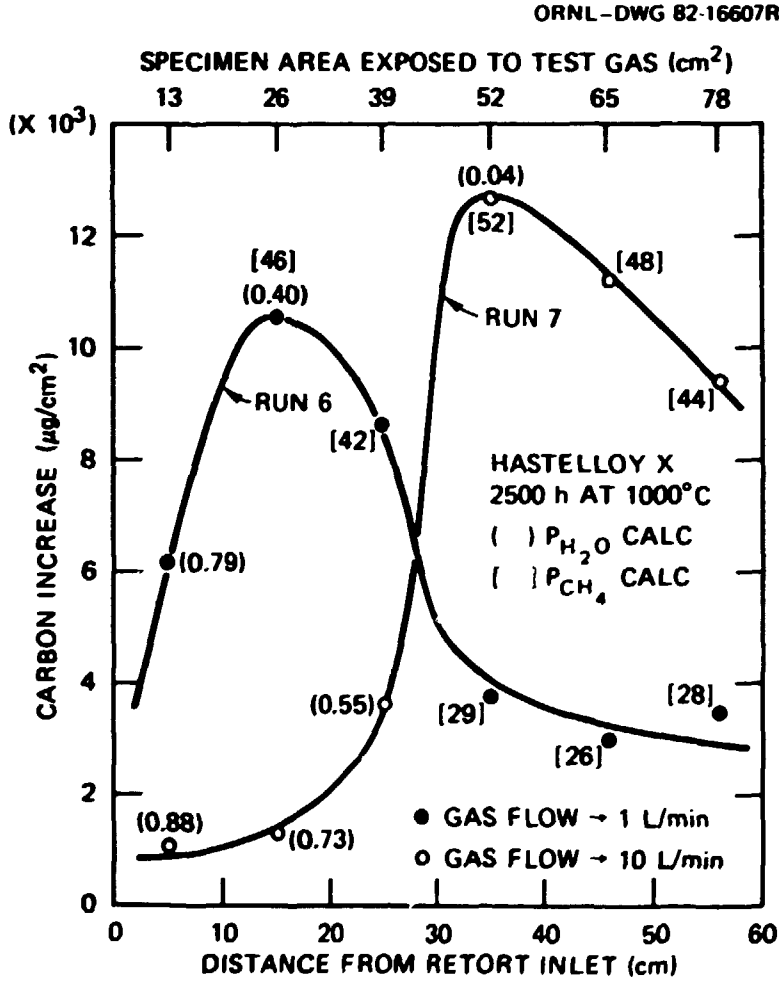


Fig. 4.5. Dependence of the carburization of Hastelloy X on HTGR-He flow rate and specimen position in the retort. Nominal test gas: 50 $H_2$ /5 $CH_4$/5 CO/0.091–0.096 $H_2O$ (Pa) [500 $H_2$/50 $CH_4$/50 CO/0.90–0.95 $H_2O$ (μatm)]; outlet-inlet gas composition, run 6: 3.9 $H_2$/2.1 $CH_4$/0.5 CO/0.096 $H_2O$ (Pa) [39 $H_2$/-21 $CH_4$/5 CO/-0.95 $H_2O$ (μatm)]; run 7: 1.4 $H_2$/0.6 $CH_4$/0.23 CO/0.091 $H_2O$ (Pa) [14 $H_2$/-6 $CH_4$/2.3 CO/-0.90 $H_2O$ (μatm)].

The extent of the depletion of these impurities at each specimen position can be estimated from the carburization levels as follows: the $\dot{S}(H_2O)$ corresponding to the measured carbon increase is determined from Fig. 4.3, and this value is used to calculate $P_{H_2O}$ from Eq. (1). The calculated $P_{H_2O}$ (shown in Fig. 4.5 by the number* enclosed in parentheses) indicates complete $H_2O$ depletion when exposed to 52 $cm^2$ or more of specimens. Hygrometer probes indicate inlet $H_2O$ levels of 0.095 Pa (0.95 μatm) for run 6 and 0.090 Pa (0.90 μatm) for run 7 but no $H_2O$ at the outlets.

The $P_{CH_4}$ at various positions in the retort was calculated as above but using Fig. 4.4 and Eq. (1) and are shown by the values enclosed within brackets in Fig. 4.5. Depletion of $CH_4$ in this case was not complete but was significant, especially for the run conducted at the lower flow rate of 1 L/min, and was confirmed by analyses of the test gases at the retort inlet and outlet. At the carburization maxima in Fig. 4.5, the $CH_4$ levels were calculated to be equal to the measured inlet levels, from which it can be concluded that the $CH_4$ levels upstream of the carburization maxima were also equal to the measured inlet level. The lower levels of carburization of the specimens upstream of the maxima can therefore be attributed to the inhibiting influence of $H_2O$ on carburization in the presence of $CH_4$ via oxide film formation.

4.3.2 Decarburization of 2 1/4 Cr-1 Mo Steel in HTGR-He - Y. Inouye

A test plan was made to determine the kinetics and the influence of the initial carbide morphology in 2 1/4 Cr-1 Mo steel on its decarburization by HTGR-He containing 10.1 $H_2$/1.0 $CH_4$/5.0 CO/1.5 $H_2O$/1.5 $CO_2$ (Pa) [100 $H_2$/10 $CH_4$/50 CO/15 $H_2O$/15 $CO_2$ (μatm)]. The test matrix consists of four exposure temperatures (427, 510, 580, and 650°C) and times (1000, 2000, 3000, and 7000 h) for alloy specimens in the annealed (ferrite plus pearlite) and normalized (bainite) conditions. The initial 1000-h exposure at the designated temperatures has been completed, and posttest evaluations are in progress.

---

*Partial pressures expressed as μatm.

### 4.3.3 Reaction of Boronated Graphite Compacts with HTGR Alloys — J. H. DeVan and P. F. Tortorelli

The reactor control rods of an HTGR consist of clad boronated graphite. It is therefore important to assess the compatibility of this graphite with the cladding material under typical HTGR environmental conditions. During 1982 experiments were initiated to assess the kinetics of the solid-state reactions between boronated graphite compacts and both type 316 stainless steel and alloy 800H. As shown in Fig. 4.6, stacks of alternating layers of polished $B_4C$-graphite, alloy 800H, and type 316 stainless steel were put under a compressive load of 4.14 MPa (600 psi) (by use of an air-driver ram) and held at 700 and 810°C in flowing HTGR-He. The experiments were designed so that specimens in the stacks could be removed at predetermined intervals (1000, 3000, 6000 and 15,000 h) and gas samples could be periodically taken from the helium stream and analyzed by gas chromatography. After removal, the specimens are to be analyzed by metallographic observation of polished and etched cross sections and

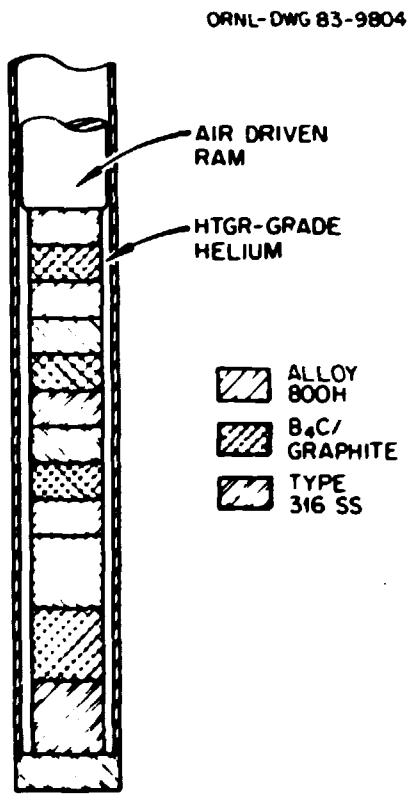


Fig. 4.6. Schematic of specimen stack held in compression in HTGR-He for compatibility testing.

by electron microprobe examination. Using such techniques, we will determine the extent of the reactions as functions of time and exposure temperature.

4.3.4 Research in Support of Core Support Performance Test — H. Inouye

This study was directed to determining the feasibility of measuring the oxidation of graphite in core support performance test (CSPT) helium containing 100 $H_2$/100 CO/50 $CO_2$/20 $H_2O$ (ppm in 71 atm He) when the test gas is heated to 700°C with molybdenum heaters. The principal objectives were to explore (1) whether the oxidation of the molybdenum by the helium impurities would cause failure of the heater wires and (2) whether molybdenum would vapor transport as volatile oxides onto the downstream graphite test piece and alter or obscure oxidation of graphite by the test gas. The main results and conclusions based on a pair of small loop tests of 1000-h duration with and without molybdenum in the upstream positions and graphite in the downstream positions were

1. Molybdenum was superficially oxidized to form an adherent oxide of $MoO_2$(s). The oxidation level was too low to affect the use of molybdenum as a heater.
2. Scattered molybdenum particles were present on the downstream graphite test pieces but had no measurable effect on the oxidation of the graphite.
3. A reverse water-gas reaction generated excessive levels of $H_2O$ in the test gas.

4.4 JOINING TECHNOLOGY — J. F. King and G. M. Goodwin

The HTGR Welding Development Program has evaluated the weldability of an alloy 800H forging that simulates a steam generator tubesheet. This prototypic HTGR tubesheet forging is the largest known alloy 800H forging ever produced. The much larger forging, 1.6 m in diameter by 0.53 m thick, needed for current designs requires the longest lead time and is considered to be one of the most highly critical components of the steam generators. About one-half of the 760-mm-diam 460-mm-thick prototype forging was obtained for use in the weld cladding evaluation. Welding concerns were raised because of the wide range of microstructures present

in this forging. The cladding surface and the interface bet n the cladding and base metal must be defect free for joining the st m generator tubes to the tubesheet by internal bore welding. This evaluation included cladding of the forging surface, metallographic examination of various regions, and tensile tests of the cladding metal, the base metal, and the interface between the two. The results of this work have been reported;[3] they are summarized in this progress report.

4.4.1 Weld Cladding of a Simulated Superheater Tubesheet — J. F. King

Current designs for using large alloy 800H forgings as superheater tubesheets require that the surface be clad with ERNiCr-3 weld metal. This clad layer must be relatively defect free, because the alloy 800H superheater tubing is joined to the tubesheet by internal-bore welding in this material as shown in Fig. 4.7. The presence of oxide inclusions in the clad layer or zones of hot cracking at the interface could lead to

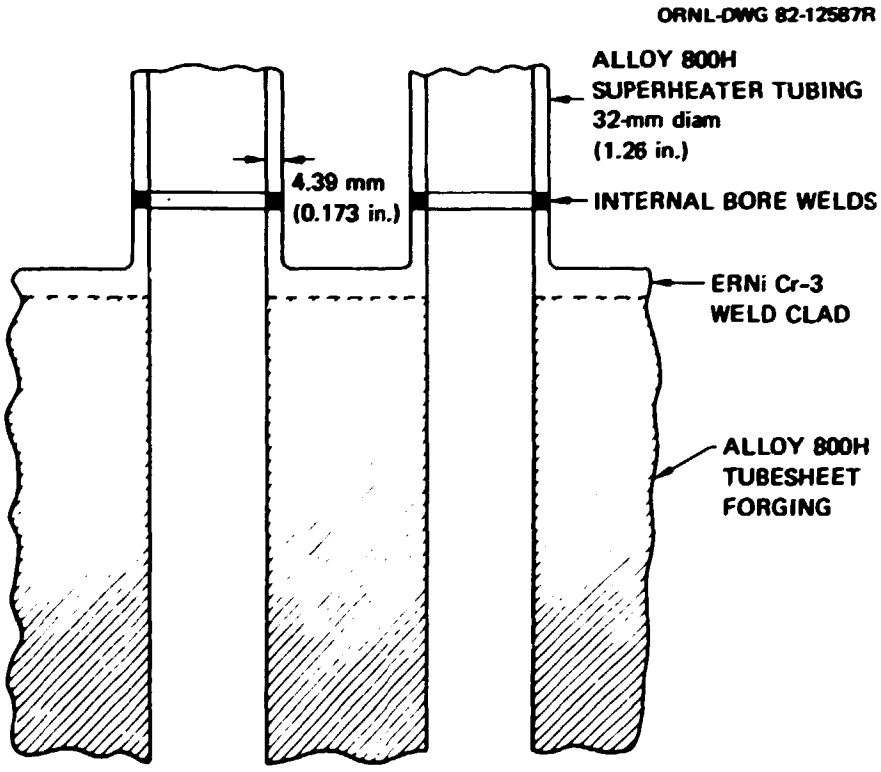


Fig. 4.7. Weld cladding of the superheater tubesheet forging required to provide material for joining tubes to the tubesheet by internal-bore welding.

failures in the relatively thin tube walls. To investigate the weldability of this forging surface and to evaluate the cladding mechanical properties, we clad the top surface.

Weld cladding was accomplished with the hot-wire GTA process. The clad deposit was American Welding Society Specification ERNiCr-3, commonly known as Inconel 82. This filler metal has a nominal composition of 67% Ni–20% Cr–3% Mn–3% Fe–2.5% Cb. A surface view of the completed first layer is shown in Fig. 4.8. Seven layers were deposited to complete the cladding to a depth of 19 mm. Welding parameters for this cladding are listed in Table 4.4. After welding, the top of the forging with the weld cladding was removed by sawing. An additional area was weld clad later with the same technique and welding parameters. This was the region near

CYN-4910

Fig. 4.8. Surface view of the first layer of weld cladding on alloy 800H forging. Seven layers were required to complete the cladding.

the center of the forging bottom identified as having large grains and as-cast structure. The top layer and this localized bottom section were used for the subsequent evaluations.

Table 4.4. Welding parameters for cladding alloy 800H forging

| | |
|---|---|
| Gas tungsten arc welding torch | |
| Current: | 250 to 375 A |
| Voltage: | 13 to 14 |
| Travel speed: | 0.6 to 0.85 mm/s |
| Shielding gas: | 75% He–25% Ar |
| Hot-wire filler addition | |
| Current: | 80 A, ac |
| Wire feed rate: | 85 mm/s |
| Wire diameter: | 1.14 mm |
| Oscillation | |
| Width: | 51 mm |
| Dwell time: | 2 s |
| Frequency: | 7 cycles/min |

### 4.4.2 Evaluation of Weld Cladding Tubesheet — J. F. King

Examination of the clad forging was conducted to determine if weldability problems existed and to evaluate the tensile properties of the weld cladding. A few creep tests are also in progress on this material, but these data are not yet available. From visual examination and observations during the weld cladding, no weldability problems were apparent. Side-bend test specimens containing one-half forging base material and one-half weld cladding were prepared and tested. After bending and examination we found that the specimens contained no gross defects and that the cladding fusion line had good ductility.

Twelve metallographic specimens were prepared from the forging top cladding surface. The specimens were selected to cover the wide range of

microstructures present in the forging. Neither fusion line defects nor evidence of hot cracking was found in any of the zones of different microstructures. Figure 4.9 is a typical photomicrograph of a fine-grained region of the forging with the ERNiCr-3 weld cladding, and Fig. 4.10 is from a typical coarse-grained region. The variable microstructures present at the forging top surface apparently had no detrimental effect on the weldability.

Metallographic examination of the clad bottom section of the forging having large grains and as-cast structure revealed different results. Six metallographic specimens were examined from the center of this region. The majority of the fusion line examined was sound and similar to that of the top section. The photomicrograph in Fig. 4.11 shows this fusion line with a zone of the as-cast structure in the large-grained base material.

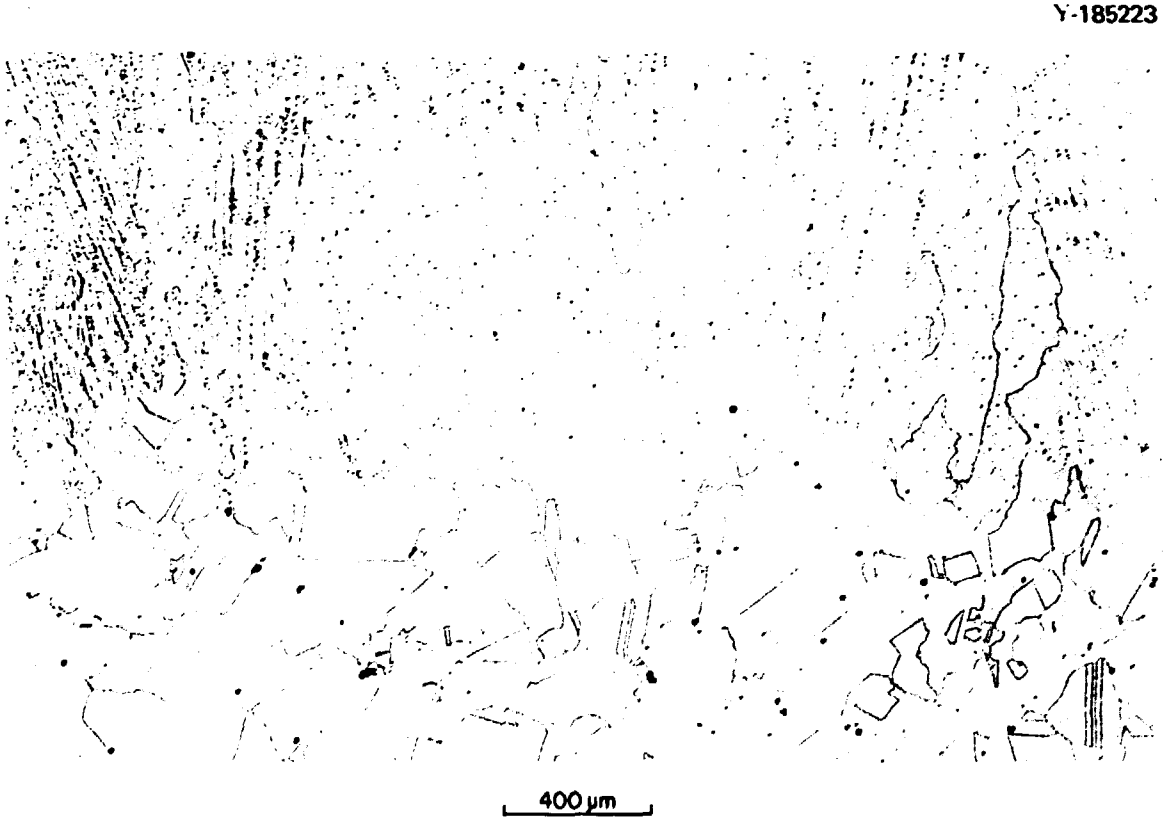


Fig. 4.9. Typical weld cladding fusion line photomicrograph from a fine-grained region of the alloy 800H forging.

Y-185226

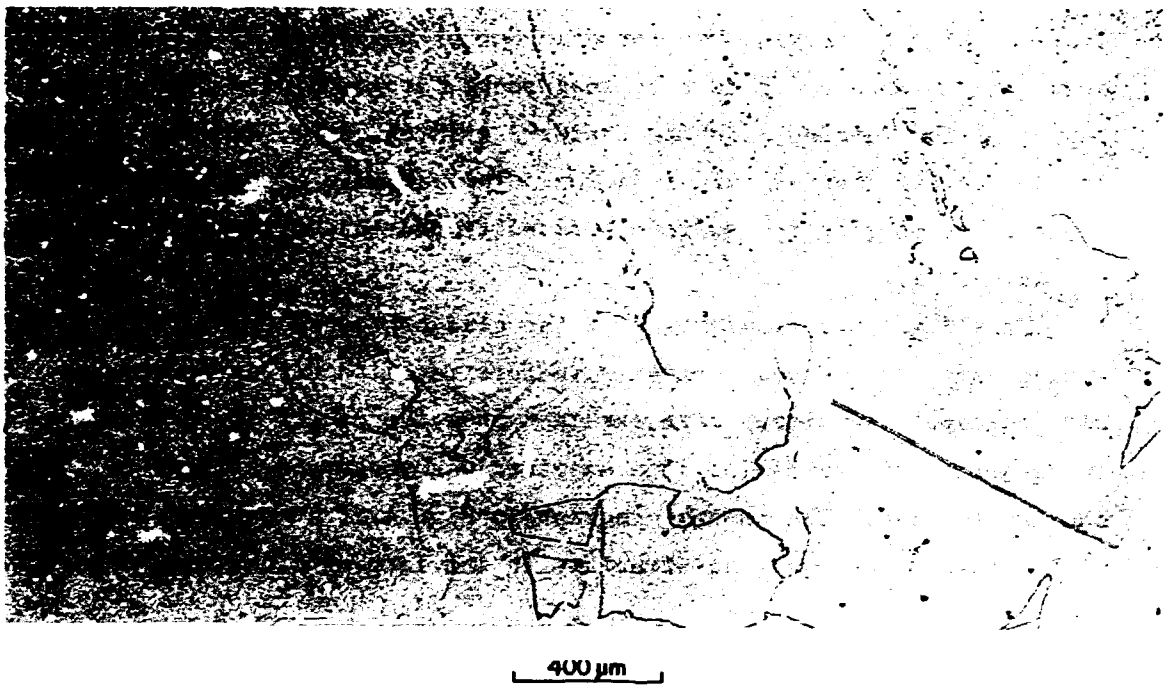


Fig. 4.10. Typical weld cladding photomicrograph from a coarse-grained region of the alloy 800H forging.

Y-185804


Fig. 4.11. Large-grained region containing as-cast structure from weld cladding bottom section of forging.

Microprobe examination of this as-cast zone revealed a high concentration of titanium. Heat-affected zone (HAZ) hot cracking in alloy 800 weldments has been associated with localized titanium enrichment.[4] A few fissures were found at or near the fusion line in the HAZ of the weld-clad bottom section, but these were not conclusively determined to be caused by the as-cast structure. Figure 4.12 shows one of the areas containing hot cracks, which could be a problem in a clad tubesheet.

Y-185806

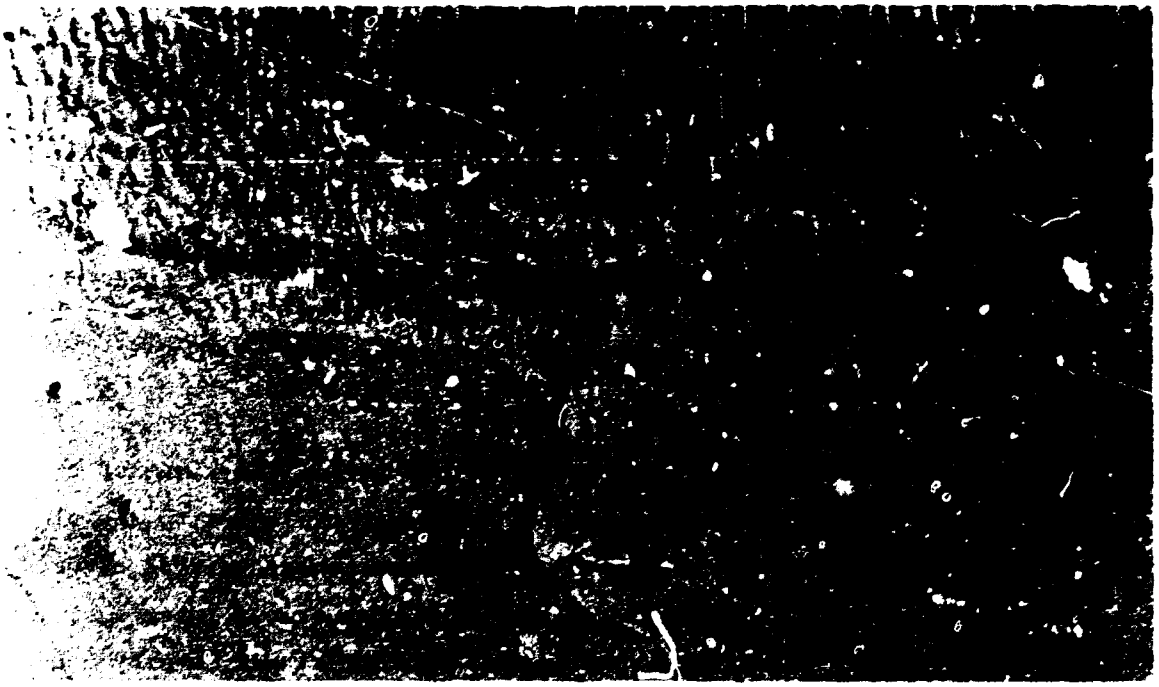


Fig. 4.12. Heat-affected zone hot crack found in the large-grained region near center of forging bottom.

4.4.3 Mechanical Properties of the Clad Tubesheet — J. F. King and H. E. McCoy

Test samples were taken in the manner shown in Fig. 4.13. The specimens designated WT and WL were entirely of weld metal; the test sections were 6 mm (0.25 in.) in diameter and 25 mm (1.0 in.) long. These two

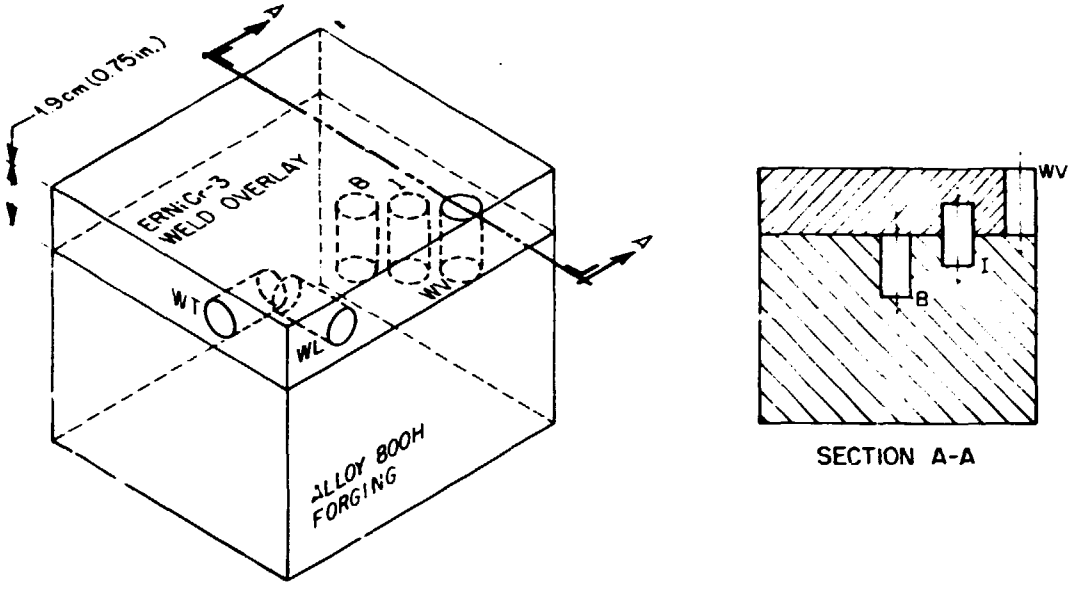


Fig. 4.13. Orientations of test samples from alloy 800H forging with approximately 1.9-cm weld overlay of ERNiCr-3. The abbreviations used are more fully described as WT = transverse sample of weld metal, WL = I = sample across weld overlay–base metal interface, and B = sample totally of alloy 800H base metal.

orientations are orthogonal to each other and are in the plane of the weld overlay. Samples were taken with their axes perpendicular to the plane of the overlay and machined so that their gage sections consisted of weld metal (WV), Incoloy 800H base metal (B), and of the weld interface, including the fusion line and small portions of weld metal and Incoloy 800H (I). These samples had gage sections 6 mm (0.25 in.) in diameter and 12.5 mm (0.5 in.) long.

The results of tensile tests on these samples are summarized in Table 4.5. The strength parameters (yield and ultimate tensile strengths) are compared in Fig. 4.14 with those reported in Huntington Alloy's literature for alloy 800H base metal and deposited ERNiCr-3 weld metal. Although the Huntington Alloy data indicate that the ERNiCr-3 weld metal is considerably stronger than alloy 800H, our test results did not show much variation between the properties of the two materials. Our alloy

Table 4.5. Tensile properties of alloy 800H–ERNiCr-3 samples

| Sample | Sample orientation[a] | Test temperature (°C) | Yield stress (MPa) | Yield stress (ksi) | Ultimate tensile stress (MPa) | Ultimate tensile stress (ksi) | Uniform elongation (%) | Total elongation (%) | Fracture location[b] | Reduction of area at fracture (%) | Reduction of area at interface[c] (%) |
|---|---|---|---|---|---|---|---|---|---|---|---|
| T-1 | WT | 25 | 332 | 48.1 | 608 | 88.2 | 65.0 | 67.4 | | 59.8 | |
| L-1 | WL | 25 | 354 | 51.3 | 612 | 88.8 | 55.0 | 59.4 | | 61.3 | |
| S-2 | WV | 25 | 300 | 43.5 | 579 | 84.0 | 62.0 | 80.0 | | 68.0 | |
| S-4 | B | 25 | 314 | 45.5 | 558 | 81.0 | 47.3 | 59.4 | | 60.8 | |
| S-1 | I | 25 | 332 | 48.2 | 565 | 82.0 | 51.3 | 66.0 | I | 67.3 | |
| S-9 | I | 25 | 348 | 50.5 | 567 | 82.2 | 51.7 | 63.4 | | 63.4 | 23.8 |
| S-15 | I | 25 | 337 | 48.9 | 566 | 82.1 | 54.8 | 63.8 | | 58.4 | 22.8 |
| S-21 | I | 25 | 337 | 48.9 | 574 | 83.2 | 56.7 | 67.7 | | 59.7 | 25.7 |
| S-28 | I | 25 | 318 | 46.1 | 569 | 82.6 | 55.1 | 70.1 | | 67.3 | 32.1 |
| S-33 | I | 25 | 339 | 49.1 | 576 | 83.5 | 52.4 | 66.6 | | 63.8 | 28.8 |
| T-2 | WT | 427 | 270 | 39.1 | 505 | 73.3 | 66.0 | 72.6 | | 55.6 | |
| L-2 | WL | 427 | 254 | 36.8 | 519 | 75.3 | 60.2 | 63.7 | | 50.7 | |
| T-3 | WT | 538 | 257 | 37.3 | 474 | 68.8 | 65.5 | 70.8 | | 61.8 | |
| L-3 | WL | 538 | 265 | 38.5 | 487 | 70.6 | 55.0 | 61.7 | | 56.8 | |
| S-5 | WV | 538 | 225 | 32.6 | 456 | 66.2 | | 82.4 | | 79.1 | |
| S-12 | B | 538 | 238 | 34.5 | 448 | 65.0 | | 63.4 | | 51.3 | |
| S-3 | I | 538 | 241 | 35.0 | 425 | 61.6 | | 44.2 | I | 47.0 | |
| S-29 | I | 538 | 241 | 34.9 | 454 | 65.8 | | 62.8 | I | 58.0 | |
| S-35 | I | 538 | 266 | 38.6 | 474 | 68.7 | | 66.4 | I | 54.4 | |
| T-4 | WT | 649 | 205 | 29.8 | 390 | 56.6 | 56.1 | 56.1 | | 59.5 | |
| L-4 | WL | 649 | 208 | 30.2 | 383 | 55.5 | 64.8 | 73.8 | | 56.5 | |
| S-27 | WV | 649 | 214 | 31.0 | 412 | 59.7 | 60.0 | 90.4 | | 70.1 | |
| S-14 | B | 649 | 245 | 35.6 | 368 | 53.4 | 38.0 | 45.2 | | 42.7 | |
| S-6 | I | 649 | 273 | 39.6 | 415 | 60.2 | 40.4 | 48.4 | I | 46.7 | |
| S-10 | I | 649 | 244 | 35.4 | 412 | 59.7 | 48.6 | 60.6 | | 45.2 | 29.9 |
| S-17 | I | 649 | 235 | 34.1 | 406 | 58.9 | 45.4 | 53.4 | | 40.5 | 23.8 |
| S-22 | I | 649 | 243 | 35.2 | 412 | 59.7 | 48.0 | 58.0 | I | 50.8 | |
| S-30 | I | 649 | 231 | 33.5 | 414 | 60.0 | 43.2 | 49.2 | I | 35.2 | |
| S-36 | I | 649 | 245 | 35.6 | 414 | 60.1 | 41.0 | 48.1 | I | 43.3 | |

[a]WT, transverse sample of weld metal; WL, longitudinal sample of weld metal interface; WV, weld metal sample perpendicular to weld interface; I, weld metal and Incoloy 800H; B, sample totally of alloy 800 base metal. Samples designated WT and WL had a gage length of 2.5 cm (1 in.) and were deformed at a strain rate of 0.2 m/s. Samples designated WV, B, and I had a gage length of 1.3 cm (0.5 in.) and were deformed at a strain rate of 0.2 m/s.

[b]I denotes that failure occurred at weld and base metal interface.

[c]If the sample orientation was such that it contained a weld and base metal interface (orientation I) and failure did not occur at the interface, the values in this column denoted the reduction in area at the interface.

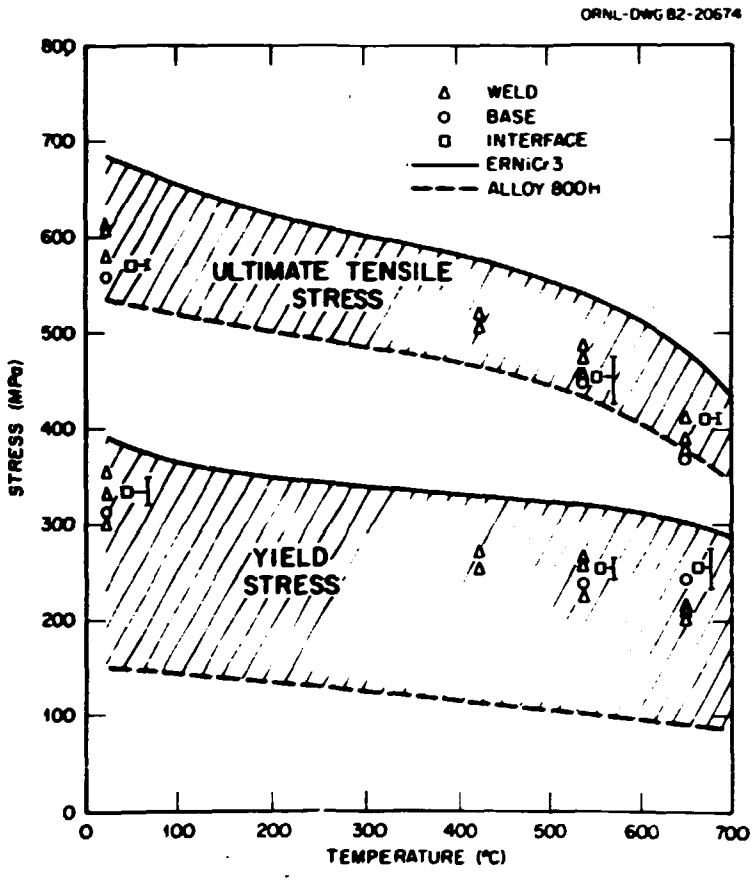


Fig. 4.14. Comparison of tensile properties of alloy 800H–ERNiCr-3 weldment samples with those for alloy 800H base metal and ERNiCr-3 weld metal from Huntington Alloy literature.

800H appears to be stronger than the vendor's data, and our deposited ERNiCr-3 appears to be weaker. The vendor's data for alloy 800H is for annealed 20.7-mm-thick (0.313-in.) plate, and our material was a rather large forging with very large grain size. The larger grain size of our material may account for the higher strength. The vendor's data for ERNiCr-3 is for weld deposits made in welding alloy 800H. Standard weld configurations would have involved considerably more intermixing between weld and base metals than would a 1.9-cm-thick (0.75-in.) weld overlay, so it is not surprising that the strengths do not agree exactly.

The elongation and reduction of area values in Table 4.5 show that the base and weld metals were ductile over the entire range of test temperatures. One interesting observation was that several of the samples

failed at the fusion line or alloy 800H-ERNiCr-3 interface (noted I). At a test temperature of 25°C, six samples had a fusion line in the gage length, and failure occurred at the fusion line in one sample. At 538°C, three samples had fusion lines in the gage length, and all three samples failed at the fusion line. At 649°C, six samples had fusion lines in the gage length, and failure occurred at this location in four samples. Thus, there may be a weakness at the fusion line. When failure did not occur at the fusion line, the diameter at the fusion line was measured and the reduction in area calculated (right column, Table 4.5). Considerable deformation occurred at the fusion line even when failure occurred elsewhere.

The various samples tested came from numerous locations in the fabricated part and represent obvious differences in grain size of the alloy 800H and other more subtle differences in working and other variables. The spread in experimental results is quite small, indicating that these variables had little effect on the properties.

### 4.4.4 Conclusions

1. The variable microstructure of the alloy 800H forging had no significant effect on its weldability related to weld cladding.

2. Sections from the forging bottom contained large grains, and some as-cast structures contained some microfissures after cladding.

3. A more uniform microstructure is desirable but not essential for weld cladding.

4. The test results indicate that tensile properties of all areas of the fabricated part are reasonable. The strength parameters are above minimum requirements for alloy 800H, the weaker component of the fabricated unit.

5. Fracture strains are high in all areas, indicating the lack of embrittlement due to the weld overlay process.

6. The tensile properties appear to be quite acceptable, but there is a strong tendency at elevated temperatures for failure to occur at the fusion line.

7. Fabrication variables that affected grain size and possibly other properties had no detectable influence on the tensile properties at various locations in the forging.

## 4.5 STRUCTURAL CERAMICS — A. J. Moorhead and R. J. Lauf

### 4.5.1 Structural Characterization of Core Support Ceramics — R. J. Lauf

#### 4.5.1.1 Fused Silica

Thermo Materials fine-grained fused silica was examined before and after creep testing. The microstructure consisted of large grains of glass surrounded by finer material containing some porosity. A trace of crystalline material was detected but not conclusively identified. After about 0.6% creep strain (35 MPa compressive stress for 1488 h at 538°C), some darkening of the $SiO_2$ indicated that the oxide was partially reduced by the simulated HTGR environment. No structural changes were observed microscopically, and no crystalline phases developed during creep testing.

#### 4.5.1.2 Alumina

Two grades of alumina were examined before creep testing: Coors AD-85 and AD-995. A full-size pad of AD-85 was sectioned for metallographic examination. The microstructure [Fig. 4.15(*a*)] consisted of tabular $Al_2O_3$ grains surrounded by a glassy phase. Transmission electron microscopy (TEM) [Fig. 4.15(*b*)] confirmed the presence of significant glassy material. The quantity of glass and its distribution suggest that the glass phase will control the creep behavior of AD-85 alumina. A small amount of porosity was observed metallographically. The pores typically did not exceed 25 μm and were randomly distributed. The overall microstructure was fairly uniform throughout the cross section of the pad.

Several pieces of a pad of AD-995 alumina were obtained and examined by optical microscopy and TEM [Fig. 4.16(*a*) and (*b*)]. Some porosity (about 1%) was observed; the pores were angular and about 25 μm across. The $Al_2O_3$ grains were equiaxed, and only a very small amount of glass was present, mostly at grain boundary triple points. A small amount of porosity within the $Al_2O_3$ grains was observed by TEM.

### 4.5.2 Fracture Toughness Testing of Ceramics — R. J. Lauf

The room-temperature fracture toughness $K_{IC}$ of Coors AD-995 alumina was measured by a short-rod geometry method. The $K_{IC}$ values ranged from 4.2 to 4.5 $MPa \cdot m^{1/2}$. The Coors AD-85 samples were also measured, giving

Y-189204


400X

E-41138


Fig. 4.15. Coors AD-85 alumina as received. (*a*) Optical micrograph showing $Al_2O_3$ grains surrounded by darker glassy phase. (*b*) Transmission electron micrograph.

Y-189721


200X

E-41145

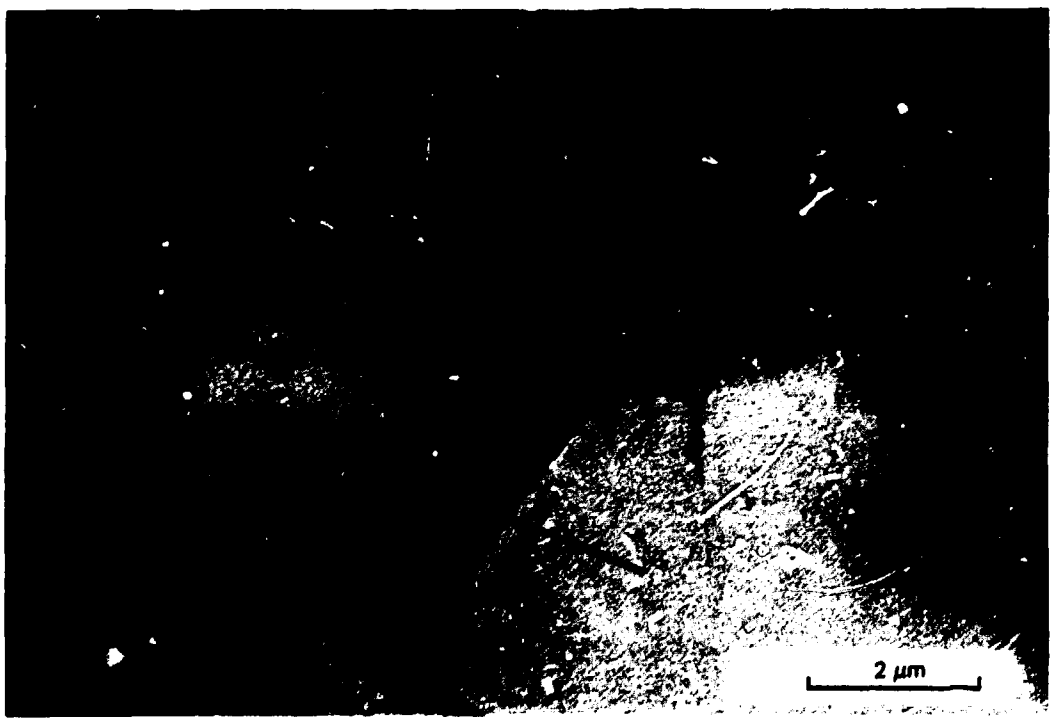


Fig. 4.16. Coors AD-995 alumina as received. (*a*) Optical micrograph showing angular $Al_2O_3$ grains, some porosity, and a small amount of glass. (*b*) Transmission electron micrograph. Arrows indicate glass at grain boundary triple points.

values of 2.4 to 3.0 MPa·$m^{1/2}$; however, we believe that moisture might have caused these values to be erroneously low. More AD-85 specimens will be machined, and the test will be repeated with oven-dried samples.

## 4.6 FISSION PRODUCT-MATERIALS INTERACTIONS — C. R. Brinkman and H. E. McCoy

The purpose of this study is to determine the susceptibility of nickel-base alloys to intergranular embrittlement by fission products such as cesium and tellurium. The initial experiments involved generating a test environment by passing helium through Cr-$Cr_2O_3$ to adjust the oxygen concentration, through molten cesium to pick up a small partial pressure of cesium, and over heated tellurium to pick up a small partial pressure of tellurium. This test gas was passed over alloy samples held at elevated temperatures. We were not successful in causing cracking by this method, likely the result of impurities in the system, which cause the cesium and tellurium to be present in the oxide form.

Granules of $Cu_3Te_4$ and $Cr_5Te_6$ in the bottom of a vessel of LiF-$BeF_2$-$ThF_4$ salt were used successfully to expose samples to tellurium. Samples of Hastelloy X, Inconel 617, Hastelloy N, and N-7 Cr-12 Mo-1 Nb were suspended in the salt up to 5000 h at 704°C. These samples were strained to failure at ambient temperature after exposure so as to fracture any embrittled grain boundaries. The deformed samples were then prepared metallographically to determine the extent of cracking. The first three alloys listed above were cracked intergranularly to a depth of about 0.1 mm. The samples of Ni-7 Cr-12 Mo-1 Nb had only occasional intergranular cracks. This agrees well with our previous observation that the addition of 1% Nb improved the resistance to intergranualar embrittlement by tellurium.

All work in this area was terminated late in the year because fission product deposition is not expected to be a significant problem for the steam cycle HTGR.

## 4.7 LINER AND PENETRATION STUDIES — D. O. Hobson and R. K. Nanstad

The several thick-section steel members that constitute the penetrations and closures of the PCRV are governed by rules for fracture toughness

defined by Div. 1, Sect. III, of the *ASME Boiler and Pressure Vessel Code*.[5] Those toughness requirements were developed, however, for materials used in light-water reactor (LWR) pressure vessels. Because PCRV steels differ from LWR steels, a need exists for developing realistic requirements for the PCRV ferritic materials and applications. Therefore, the objectives of the program are

1. to define a reference fracture toughness curve for ferritic components of the HTGR pressure boundary similar to the $K_{IR}$ curve in Appendix G of ref. 5,
2. to define a temperature-indexing procedure for this curve, based on standard materials qualification tests [e.g., Charpy V-notch (CV) and drop-weight] similar to the $RT_{NDT}$ procedures of ref. 5, and
3. to obtain a quantity of fracture toughness data large enough that a statistically meaningful evaluation of the data can be conducted to serve as a tool to help assess the probability of component failure.

Over the past several years, mechanical properties data have been obtained on different heats of PCRV plate and forging material and on weldments made from those materials. The testing program utilized $C_V$ and drop-weight impact tests, subsize and standard tensile and 1T compact specimens, as well as instrumented precracked Charpy specimens for static and dynamic fracture toughness testing. These tests were completed on the plate and forging materials (A 537, class 1; A 537, class 2; and A 508, class 1) and on various weldments fabricated with the submerged arc, shielded metal arc, and flux cored welding processes. These will be evaluated in a report to satisfy the third above objective.

This past year we have concentrated on the first two above objectives. Figure 4.17 illustrates fracture toughness data obtained for PCRV penetration steels with the tests mentioned above and provides a comparison of those data with the $K_{IR}$ curve.

The majority of these tests did not produce "valid" $K_{IC}$ values according to ASTM fracture toughness criteria because of specimen size or temperature limitations. All the data lie above the $K_{IR}$ curve but in some

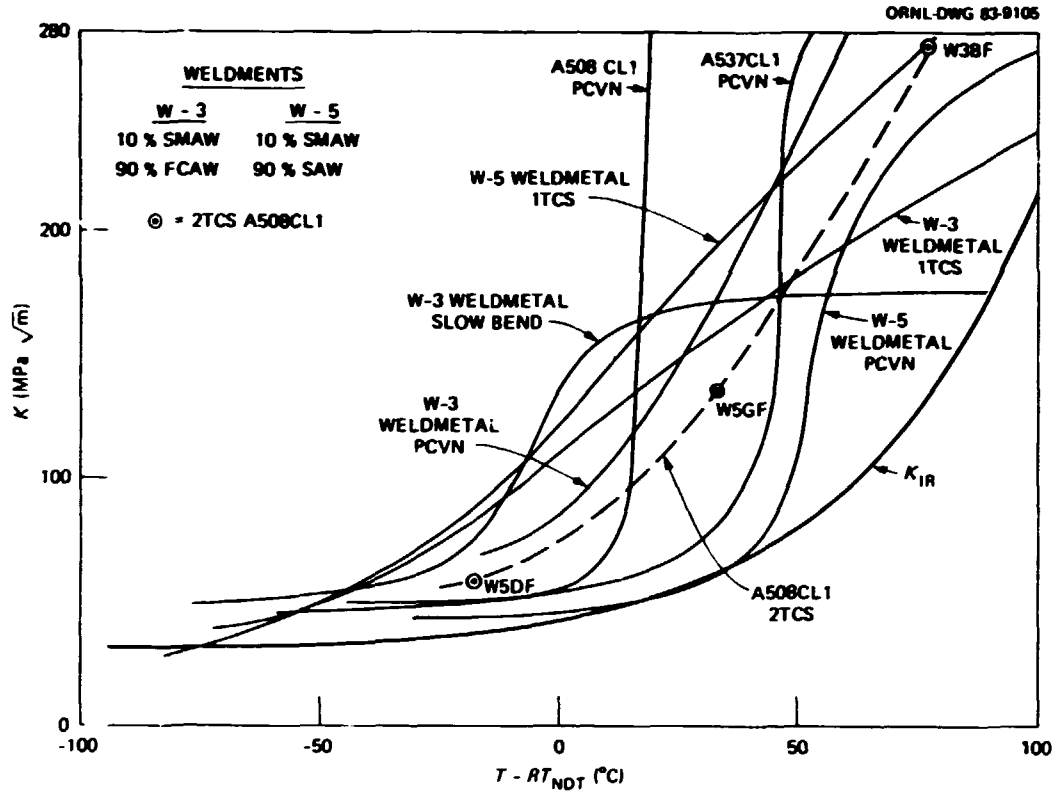


Fig. 4.17. Comparison of $K$ values for HTGR weldment materials with the $K_{IR}$ curve for pressurized water reactor materials.

cases are very close. One curve — labeled A 508, class 1 (2TCS) — was generated by high-strain-rate testing of 2T [5-cm-thick (2-in.)] compact specimens. Of the three tests on this curve, only the lowest (W5DF) was valid according to ASTM criteria.

The 2T compact specimens of A 508, class 1, forging material from the W3 and W5 weldments were tested at –75 and –25°C and at room temperature. These temperatures were, respectively, 18°C below and 32 and 77°C above the nil-ductility temperature (NDT) determined by drop-weight testing (–57°C).

Before specimen testing, the mechanical and electronic responses of the 100-metric-ton servohydraulic testing machine and the displacement of clip gages were examined to determine whether or not they could respond adequately to the dynamic test mode requirements. All the load- and displacement-measuring devices responded adequately during the load-deflection portion of the test. Some "ringing" was observed after fracture

took place. This occurred in the load cell and in the clip gage when the specimen broke, freeing the gage and causing it to vibrate like a tuning fork. A plot of strain versus time was analyzed in the ringing region and showed the free vibrational frequency of the clip gage to be approximately 522 Hz.

All data were recorded at intervals of 200 μs per data point on a digital storage oscilloscope. The testing machine was programmed to test with a square wave function, which means simply that the ram moved to the end of its preset stroke distance at the fastest rate it was capable of moving. The stress intensity rate for the −75°C test (straight-line slope) was $0.26 \times 10^4$ MPa $\sqrt{m}$/s. This is about a factor of 10 slower than similar 2TCS specimens used to develop the original $K_{IR}$ curve. The test results are shown in Table 4.6.

The single "valid" test (W5DF) produced a $K_{IC}$ toughness value 20 MPa $\sqrt{m}$ higher than the value of $K_{IR}$ at that temperature. Examination of the data from which the $K_{IR}$ curve was derived shows scatter well above the present data point. For this reason, the present $K_{IR}$ curve still appears to be an appropriate lower bound for HTGR materials toughness. Higher temperature testing would require thicker specimens to obtain valid tests.

Of special importance will be high-rate testing of W5 weld metal at $T$-$RT_{NDT}$ values of 10 to 40°C. The W5 weld metal curve in Fig. 4.6 was fitted to precracked Cv specimen test data, and it lies just tangent to the $K_{IR}$ curve over the above temperature range. During the next reporting period, two 3T [8-cm-thick (3-in.)] compact weld metal specimens of W5 weld metal will be tested at high strain rates near the tangency position. One specimen may be tested at $T$-$RT_{NDT}$ = 50 or 60°C. Current plans include testing of crack arrest specimens to measure crack arrest toughness, $K_{Ia}$.

Table 4.6. Results of high-rate two-thickness compact specimen fracture toughness testing of A 508, class 1, forgings

| Specimen | Test temperature (°C) | $K$ (J) (MPa $\sqrt{m}$) | $K$ (J) (ksi $\sqrt{in.}$) | Valid $K_{IC}$ |
|---|---|---|---|---|
| W3BF | Room | 274 | 250 | No |
| W5GF | −25 | 134 | 122 | No |
| W5DF | −75 | 58 | 53 | Yes |

## 4.8 REFERENCES

1. J. P. Strizak et al., *The Influence of Temperature, Environment, and Thermal Aging on the Continuous Cycle Fatigue Behavior of Hastelloy X and Inconel 617*, ORNL/TM-8130, April 1982.

2. K. C. Liu, "Stress Relaxation of Ceramics," pp. 149–54 in *High-Temperature Gas Cooled Reactor Technology Development Program Annual Progress Report for Period Ending December 31, 1981*, ORNL-5871, 1982.

3. J. F. King and H. E. McCoy, "Evaluation of Weld Clad Alloy 800H Tubesheet Forging," unpublished data, December 1982.

4. J. C. Lippold, "An Investigation of Heat-Affected Zone Hot Cracking in Incoloy 800," *Weld. J.* 62(1), 1–11-s (January 1983).

5. *ASME Boiler and Pressure Vessel Code*, Sect. III, Div. 1, American Society of Mechanical Engineers, New York, 1980.

# 5. GRAPHITE DEVELOPMENT (WBS OR1203 and OR1501)

W. P. Eatherly

## 5.1 GRAPHITE IRRADIATIONS — J. A. Conlin

### 5.1.1 Graphite Creep Irradiation Experiment OC-5 — R. L. Senn

Capsule OC-5, the fifth in a series of graphite creep irradiation experiments, began irradiation in core position E-5 of the Oak Ridge Research Reactor (ORR) on December 17, 1981, and was removed on March 8, 1982, after 64.6 full-power days (fpds) of a scheduled 110-fpd irradiation. The capsule was designed to irradiate graphite specimens previously irradiated in capsules OC-1 and OC-3. The specimens were irradiated at $900^{+20}_{-10}$°C while under a compressive stress of 13.8 MPa (20.7 MPa for selected specimens) for 46,521 MW(h) of irradiation, corresponding to a peak fast fluence of about $1.25 \times 10^{25}$ neutrons/m$^2$ ($E > 29.3$ fJ). Detailed descriptions of the design and operation of the graphite creep irradiation experiment series have been published.[1-6]

#### 5.1.1.1 Irradiation History

Several problems were encountered during the construction and irradiation of capsule OC-5. As previously reported,[6] the experiment was damaged during fit-up into the ORR mockup facility before installation in the reactor. The bent outer containment was replaced, but the cracked graphite specimen holder and sleeve were almost irreplaceable and were therefore reused. This decision was reached only after calculations were performed to show that the effect on heat transfer rates and resulting temperature changes would be negligible and that the cracked graphite would therefore not interfere with the test results.

Another problem encountered early in the irradiation period was the failure [as evidenced by gas leaking from the pneumatic electromechanical (PEM) cells to the control gas system] of both of the PEM cell bellows used to check the compressive forces being applied by the upper bellows to the specimen columns. Maintenance of the design pressure in these systems was impossible; therefore, the low-pressure alarms and related instrumentation were disabled, and the PEM systems were left to revert to the ambient gas pressure of the capsule. Although this failure was not expected to affect experimental operation, it did prevent ongoing measurements from showing that the compressive forces were being applied to the entire specimen columns during the irradiation. Except for one column in the first of these experiments (OC-1), no misalignment of the specimen columns was experienced. Dimensional changes were made to correct the interference problem in the first experiment; hence, the probability of compromising the data from OC-5 was small.

Early in the irradiation, an abnormally large number of the thermocouples in the graphite sleeve adjacent to the various specimens began to fail. The pattern seemed to show that failure occurred between reactor shutdown and startup periods, as if the rapid decrease in temperature from about 800 to about 70°C or the subsequent increase was contributing to the failure. Ultimately, 10 of the 23 graphite sleeve thermocouples failed. A detailed investigation continues to determine the reason for this abnormally high number of thermocouple failures so early in the irradiation. Some results of this ongoing investigation are reported below.

Satisfactory experimental operation was not compromised by the thermocouple failures, because there were two thermocouples in each heated zone and the central movable thermocouples continued to operate satisfactorily. When both thermocouples in a heated zone failed, the heater was operated manually on a day-to-day basis, with the central thermocouple used to verify proper specimen temperatures.

The experiment operated satisfactorily in other respects; the specimens were maintained at an operating temperature of $900^{+20}_{-10}$°C, and the design compressive stress was maintained. As noted earlier, however, the experiment was terminated after only 65 d of a scheduled 110-d irradiation. The decision to remove the experiment was prompted by a significant change

in the temperature difference between the two central movable thermocouples. This temperature difference was typically in the 30 to 50°C range during most of the testing period. A change was noted during the last week of February, which seemed to peak at an 85 to 90°C range during the first week of March. Such a large temperature difference between the two unstressed specimen columns was intolerable and would eventually result in the loss of meaningful data, because it could no longer be assumed that the same conditions were being maintained for both the stressed and unstressed columns.

We felt that the cracked specimen holder and sleeve[6] might have somehow shifted to one side and contributed to the temperature difference across the experiment. We also postulated that the difficulty with the thermocouples may have been due to excessive grain size in the thermoelements. A series of tests was conducted with the experiment in the reactor pool.

5.1.1.2 In-Pool Examination

A test was conducted to determine if the graphite specimen holder and sleeve were moving toward one wall of the capsule during operation at temperature with compressive forces on the specimen column, thus causing the temperature asymmetries along the specimen columns and prompting the early termination of the experiment.

A special thermocouple holder was devised to permit application of two thermocouples 180° apart at various elevations along the exterior wall of the capsule. A temperature of about 500°C was established along the length of the graphite specimen holder with the experimental electrical heaters. Measurements were made with the external thermocouples in the areas known to crack in the graphite pieces. Temperatures without pressure in the bellows system were 68.6°C (north side) and 61.6°C (south side). Pressure was then applied to the bellows system to duplicate the conditions of the capsule under irradiation. The external temperatures then measured 72.4°C (north side) and 60.4°C (south side). The temperature increased 3.8°C on one side and decreased 1.2°C on the opposite side, lending credence to our postulation that the internal portions of the capsule were actually shifting to one side during experimental operation.

### 5.1.1.3 Thermocouple Failure Investigation — R. M. Carroll

While capsule OC-5 was still in the ORR pool, special tests were conducted to determine the locations and possible causes of the excessive thermocouple failures during operation. Locating the positions of wire rupture for the thermocouples includes analysis of loop resistance, capacitance, and insulation resistance measurements. Time domain reflectometry could not be used because of the multiple connectors along the length of the thermocouples.

Fourteen of the original 30 thermocouples failed, including 10 of the 23 graphite sleeve thermocouples. Three failures involved the Chromel leg touching the sheath. One thermocouple failed in service (open circuit) about 200 mm above the junction but then reestablished contact. The other open circuits arose from failures at or near the junction. These conclusions are supported by the resistance measurements and, with less confidence, by capacitance measurements. Quite clearly, the specifications or the quality assurance program for nuclear quality thermocouples is faulty. This situation is currently under analysis by the Instrumentation and Controls Division in its thermocouple program.

### 5.1.1.4 Postirradiation Examination

Capsule OC-5 was moved to a hot cell and disassembled in September 1982. During disassembly, sooty deposits were found inside both the upper and lower portions of the experiment, including the graphite sleeves and the inside surface of the stainless steel containment vessel. All previous capsules in this series were bright and clean during disassembly. The presence of the soot was evidence that oxygen found its way into the capsule control gas region during operation. Although gases used for the control gas system pass through cleanup traps, gases used for pressurizing the bellows systems do not; early in the operation of this experiment, leaks were found in both of the lower bellows (PEM cell) systems. The bellows supply gas is batch analyzed and is expected to have less than 2 ppm O. However, it is possible that oxygen got into the system because of a higher than normal oxygen or water vapor content from the relatively uncontrolled helium supply system used for bellows pressurizing and control.

All the graphite test specimens were removed from the experiment without difficulty. They were identified, bottled, and transferred to Metals and Ceramics Division personnel for analysis, as reported elsewhere in this section.

The graphite sleeve and specimen holder were pushed out of the stainless steel containment vessel without undue difficulty. The cracked areas looked much the same as they had when the pieces were installed. No chipping or spalling was seen, although the crack was slightly more open on one side than on the other. We had no way of determining when this occurred, however.

Because of the unexpectedly large number of thermocouple failures during operation of this experiment, great care was taken during the postirradiation examination (PIE) to determine the locations and possible causes of the failures. All thermocouple sheaths, leads, and connections in the experimental lead tube were carefully examined. No defects or failures were noted, and the circuits were continuous down to the in-core portion of the capsule where the lead tube was cut off.

In the hot cell, the thermocouples were lifted out of their respective slots very carefully. The tips (sensing ends) of eight of the thermocouples (which were bent about 90° and inserted into a hole in the graphite sleeve adjacent to the various specimens) were already broken or broke off as we tried to remove them. The identities of the thermocouples were retained where possible. Some had fallen out of their slots during disassembly and could not be positively identified. Some of the broken tips were recovered for analysis, and all the identifiable thermocouple pieces were tagged and saved for analysis. The cause of the apparent embrittlement of the sheaths and wires has not yet been determined, but results from the ongoing investigation will be reported as they become available.

Nineteen of the 20 flux monitor capsules installed in the experiment were recovered and identified. They are now being analyzed and will be reported by others.

5.1.1.5 Summary

Graphite creep irradiation experiment OC-5 was irradiated in ORR core position E-5 for 64.6 fpds to a peak fast fluence of $1.12 \times 10^{25}$ neutrons/m$^2$

($E > 29.3$ fJ). The capsule contained graphite specimens previously irradiated in capsules OC-1 and OC-3. All were irradiated at a nominal 900°C specimen temperature while a compressive stress of 13.8 MPa (20.7 MPa for selected specimens) was applied to two columns. Two similar columns of specimens served as unstressed control specimens. Detailed analysis of the specimens, flux monitors, and other aspects of the PIE are reported elsewhere in this section.

### 5.1.2 High Flux Isotope Reactor (HFIR) Graphite Irradiation Experiments — R. L. Senn

#### 5.1.2.1 HFIR HTK Target Capsule Series

Two additional HFIR target capsules, HTK-5 and -6, were irradiated in this series of experiments conducted in cooperation with the Federal Republic of Germany (FRG). The general design for these experiments was reported previously.[7]

Irradiation of HFIR target capsule HTK-5, containing 64 graphite specimens, was completed as scheduled. The HTK-5 was an FRG priority experiment containing five FRG experimental graphites in comparison with H451 and POCO AXF graphites. The capsule was installed in HFIR outer target position B-1 on December 24, 1981, and removed on December 12, 1982, after an expected lifetime exposure of $3.8 \times 10^{26}$ neutrons/m$^2$ (15 HFIR fuel cycles) at 600°C.

The HFIR target capsule HTK-6, also containing 64 graphite specimens, was a High-Temperature Gas-Cooled Reactor (HTGR) priority experiment containing grades of H451 from two lots, an improved H451, and TS-1621, in comparison with selected FRG grades. The HTK-6 was installed in HFIR outer target position F-7 on July 18, 1982, and was removed on January 5, 1982, after an exposure to a fluence of $1.8 \times 10^{26}$ neutrons/m$^2$ (seven HFIR fuel cycles) at 900°C.

Results from the HTK series of irradiation experiments are reported elsewhere in this section.

#### 5.1.2.2 High Flux Isotope Reactor Target Fracture Capsule Series

A parametric study was completed for the irradiation of standard 12.7-mm-diam (1/2-in.) premilled fracture mechanics (FM) specimens of various graphites in HFIR target capsules similar to previous target capsule designs described above. The experiments have been designated HTF-1,

-2, -3, and so forth for a series of HFIR target fracture (HTF) mechanics irradiation capsules. The study included heat transfer calculations for irradiation at specimen surface temperatures of 400, 700, and 900°C. Because of the nature of the FM specimens and their fixed 12.7-mm (0.500-in.) outside diameter, the wall thickness of the aluminum containment tube was varied to achieve the necessary gas gap changes required to adjust specimen temperatures rather than change the specimen diameters, which is normal with these experiments.

A conceptual design for the experiment is shown in Fig. 5.1. Each graphite specimen is designed so that two 12.7-mm-OD (0.500-in.) by 19.05-mm-long (0.750-in.) FM specimens with premilled slotted ends can be cut from the irradiated piece. About 4.76 mm (3/16 in.) of additional length is provided to permit cutting-off and squaring the ends of each FM specimen. A silicon carbide temperature monitor may also be inserted in the center of each double specimen. Graphite centering devices similar to those used in our present target capsules will be keyed on the premilled slots in each end of the double specimens. Note that the overall length of such a double specimen and a centering spacer is 47.625 mm (1.875 in.); thus, ten double specimens can be accommodated in a standard target capsule having about 495 mm (19 1/2 in.) of active core length available for specimens.

The thermal analysis was performed with the standard GENGTC one-dimensional heat transfer program used for all the recent HTK graphite target capsules. The same gamma heat profile was used as that proved for recent HTK experiments. The calculations used an average gamma heat for each of the four quadrants in one-half of the experiment, which is assumed to be symmetrical. The results are shown in Table 5.1 and Fig. 5.2. The data in Fig. 5.3, taken from the initial (HT-1) target capsule questionnaire, show permissible conditions of the capsule wall thickness.

As shown in the table and figures, all the proposed operating conditions fell within permissible ranges except the upper quadrant of the 900°C neon case, in which the required wall thickness was too thin. The maximum heat conduction to the coolant water is $3.66 \times 10^9$ W/m$^2$ [<116,000 Btu/(h·ft$^2$·°F)] for these unfueled experiments, so there is no problem from that standpoint.

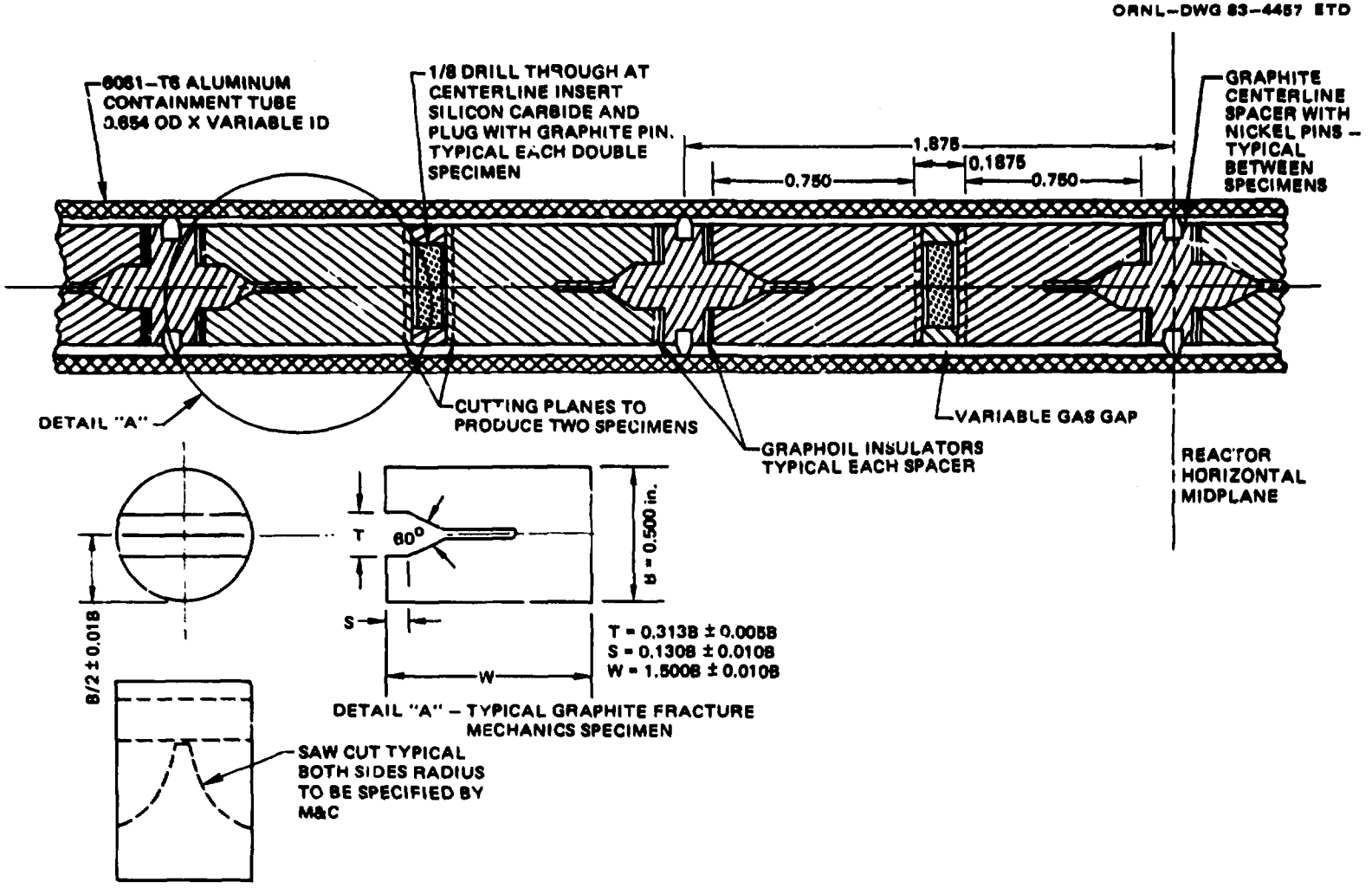


Fig. 5.1. Conceptual design for graphite fracture mechanics High Flux Isotope Reactor target fracture series capsule irradiation experiments. Dimensions are in inches; 1 in. = 2.54 cm.

Table 5.1. Thermal analysis for High Flux Isotope Reactor target fracture series test capsules

| Specimen position[a] (quadrant) | Assumed average gamma heat[b] (W/g) | Required gas gap | | Resulting wall thickness[c] | | Specimen surface temperature (°C) | |
|---|---|---|---|---|---|---|---|
| | | (mm) | (in.) | (mm) | (in.) | Initial | Final[d] |
| | | *For 900°C argon fill gas* | | | | | |
| 1st (upper) | 24 | 0.521 | 0.0205 | 1.435 | 0.0565 | 901 | 915 |
| 2d | 35.5 | 0.254 | 0.0100 | 1.702 | 0.0670 | 901 | 956 |
| 3d | 41.6 | 0.203 | 0.0080 | 1.753 | 0.0690 | 904 | 982 |
| 4th | 45.5 | 0.178 | 0.0070 | 1.778 | 0.0700 | 904 | 995 |
| | | *For 900°C neon fill gas* | | | | | |
| 1st | 24 | 1.384 | 0.0545 | 0.572 | 0.0225 | 900 | 903 |
| 2d | 35.5 | 0.635 | 0.0250 | 1.321 | 0.0520 | 902 | 924 |
| 3d | 41.6 | 0.483 | 0.0190 | 1.473 | 0.0580 | 898 | 929 |
| 4th | 45.5 | 0.432 | 0.0170 | 1.524 | 0.0600 | 906 | 941 |
| | | *For 700°C neon fill gas* | | | | | |
| 1st | 24 | 0.572 | 0.0225 | 1.384 | 0.0545 | 715 | 740 |
| 2d | 35.5 | 0.330 | 0.0130 | 1.626 | 0.0640 | 708 | 761 |
| 3d | 41.6 | 0.267 | 0.0105 | 1.689 | 0.0665 | 704 | 770 |
| 4th | 45.5 | 0.241 | 0.0095 | 1.714 | 0.0675 | 706 | 783 |
| | | *For 400°C helium fill gas* | | | | | |
| 1st | 24 | 0.572 | 0.0225 | 1.384 | 0.0545 | 398 | 420 |
| 2d | 35.5 | 0.356 | 0.0140 | 1.600 | 0.0630 | 397 | 432 |
| 3d | 41.6 | 0.305 | 0.0120 | 1.651 | 0.0650 | 404 | 447 |
| 4th | 45.5 | 0.267 | 0.0105 | 1.689 | 0.0665 | 400 | 446 |

[a]Graphite specimens were assumed to be H451 graphite with 12.7-mm (0.500-in.) OD, a density of 1.72 g/cm$^3$, and a thermal conductivity of 31.15 W/(m·K) [18 Btu/(h·ft$^2$·°F)].

[b]The average gamma heat for an experiment in a High Flux Isotope Reactor outer target position, divided into four quadrants. The fourth quadrant is just above the midplane. The gamma heating profile is assumed to be symmetrical about the midplane.

[c]The standard 6061T6 aluminum tube used as the containment for target capsules has a 16.6-mm (0.654-in.) OD with a nominal (for previous experiment) inside diameter of 13.5 mm (0.532 in.), giving a nominal wall thickness of 1.55 mm (0.061 in.).

[d]The final surface temperature calculation assumed an irradiation resulting in not more than a 1% linear shrinkage of the graphite specimens and the resultant increased gas gap between the specimen and the containment wall.

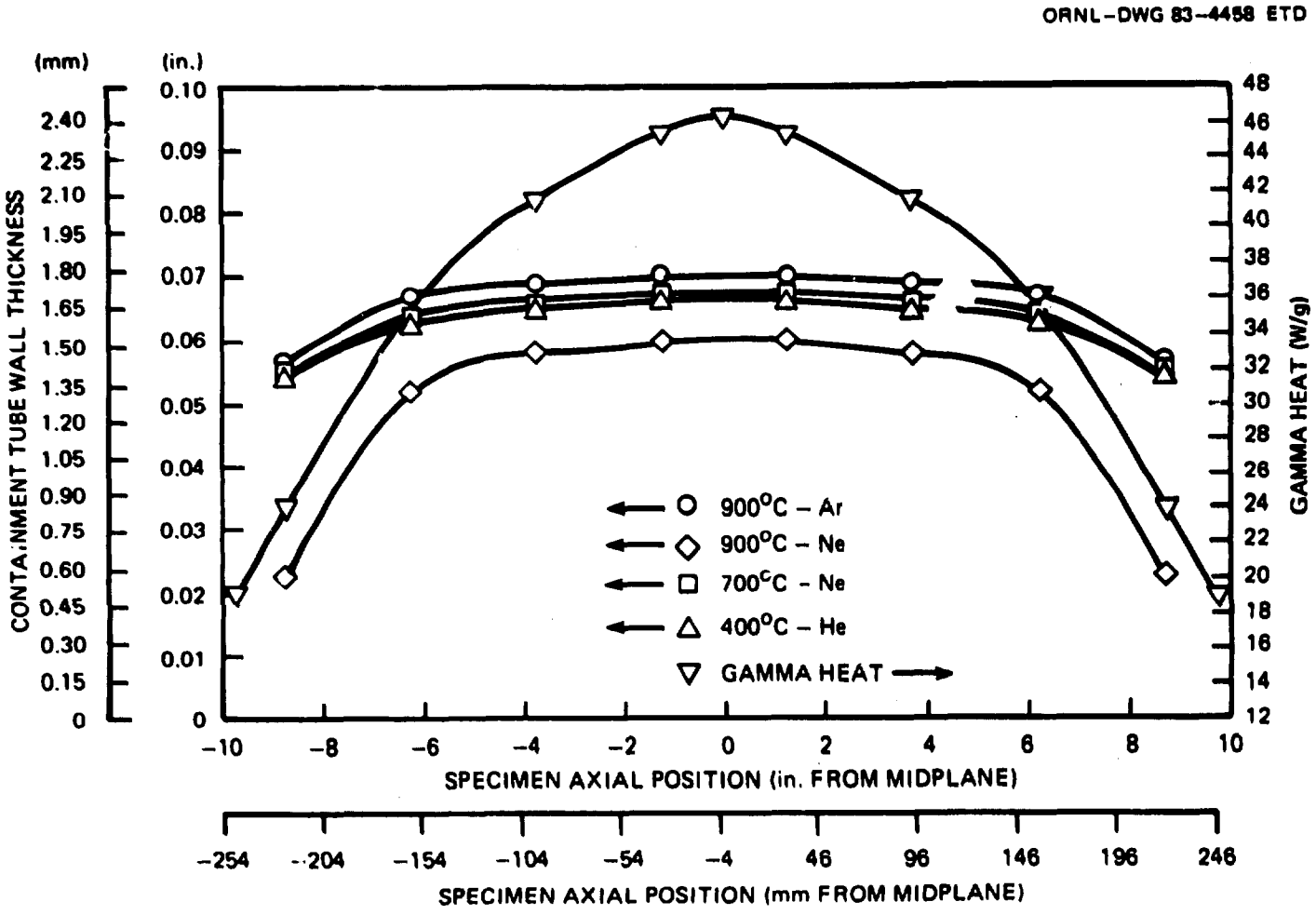


Fig. 5.2. High Flux Isotope Reactor (HFIR) target fracture capsule containment tube wall thickness and HFIR gamma heat versus specimen axial position.

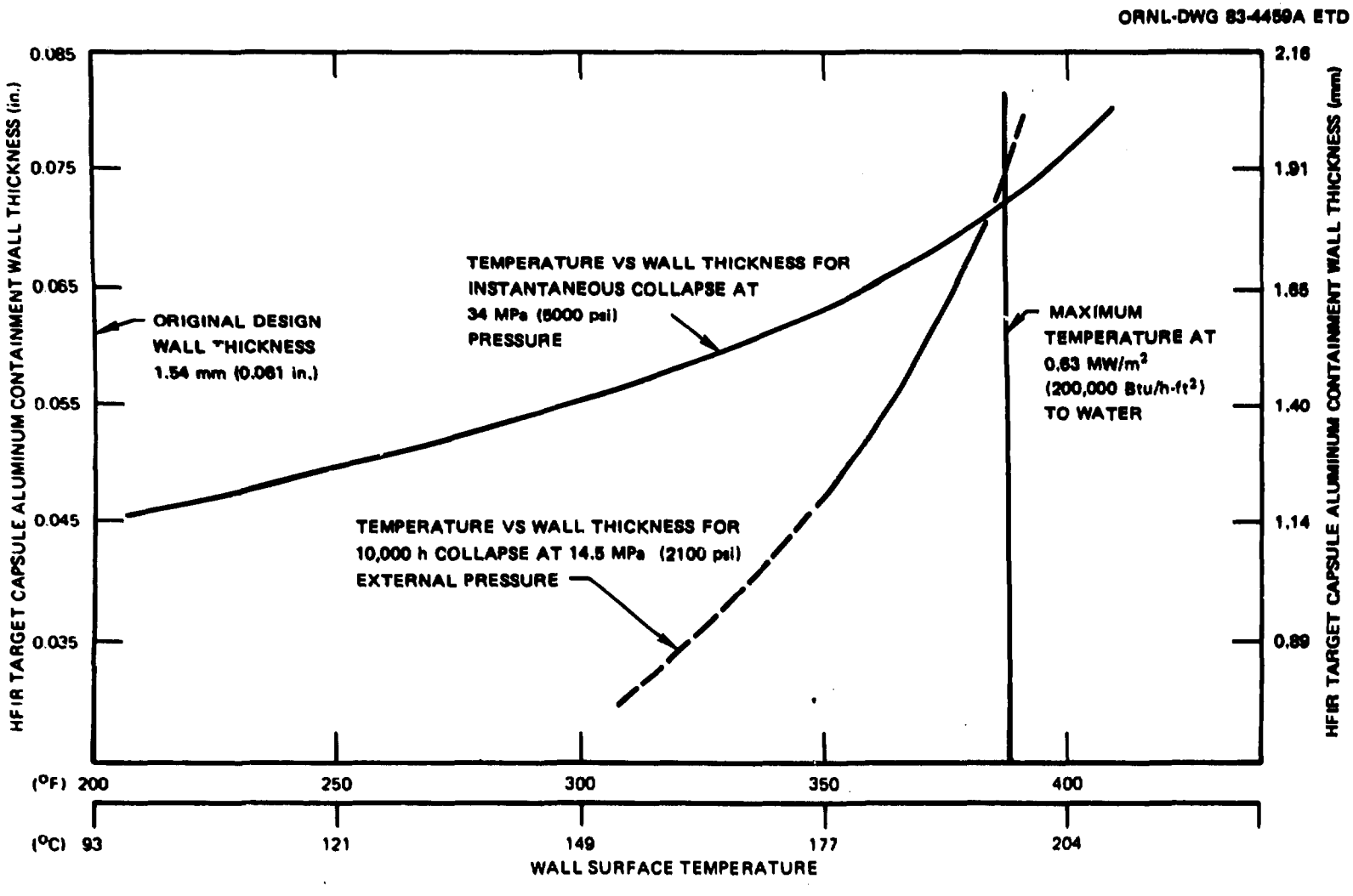


**Fig. 5.3. High Flux Isotope Reactor target capsule wall thickness required versus wall surface temperature.**

Several design aspects will be considered in making the final parameter decisions. Note the very small 0.178-mm (7-mil) gas gap at the fourth (midplane) quadrant for the 900°C argon case and the resultant approximately 90°C temperature increase toward the end of the irradiation period. Extreme precision in building the parts is required for such small gas gaps (although we believe it is feasible); of course, the specimen surface temperatures become very sensitive to shrinkage and the resultant gas gap increase.

These effects are considerably mitigated for the 900°C neon case, in which the midplane specimen has a comfortable 0.43-mm (17-mil) gas gap and shrinkage will cause an estimated 35°C specimen surface temperature increase during irradiation. However, the upper quadrant specimens (at both ends of the capsule) in this design would have to be abandoned, operated at a different temperature, or designed with a smaller specimen diameter, because the external wall temperature of about 100°C limits the wall thickness to 1.19 mm (0.047 in.), which is considerably more than the 0.57 mm (0.0225 in.) calculated for these conditions.

At the end of this reporting period, a design order was implemented, and engineering design was under way to provide drawings for the HTF series of target capsules described above. Three such capsules have been planned, encompassing two FM target capsules, HTF-1 and HTF-2, to be irradiated for 7 HFIR fuel cycles at 600 and 900°C, respectively, and HTF-3, to be irradiated at 600°C for 15 cycles. The various capsules will contain specimens from H451, graphNOL N3M, and ASR-1R graphites.

### 5.1.3 Irradiation Creep Results — C. R. Kennedy

Preliminary studies of creep experiment OC-5 at 900°C now extend the results to a fluence of $50 \times 10^{24}$ neutrons/m$^2$, with creep strains to almost 4%. In general, the new data are an extension of previous results, with an indication of a slowly decreasing creep rate. The results for H451 are shown in Fig. 5.4.

The initial experiment in this series, OC-1, forced an overload on half of the specimens. The overloaded specimens have also been recycled into OC-3 and OC-5, with design stresses of 13.8 and 20.7 MPa. The previously overloaded 13.8-MPa specimens yielded the same creep coefficient

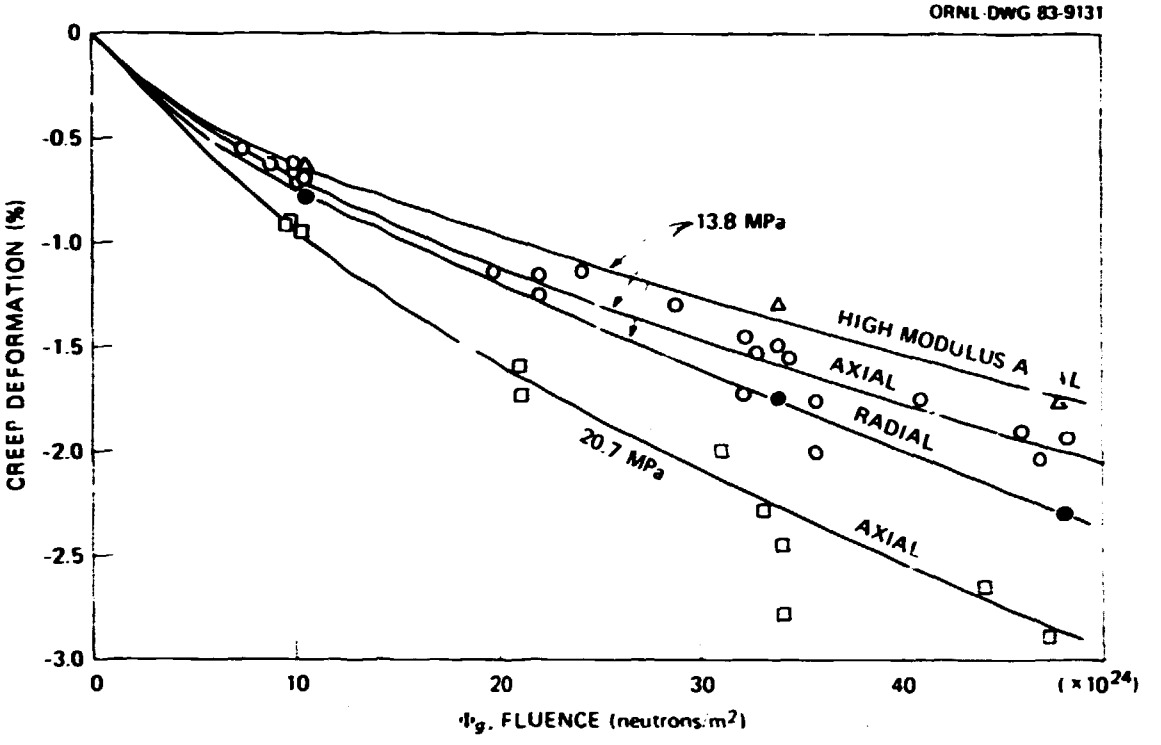


Fig. 5.4. Irradiation creep of H451 at 900°C in compression.

as did the specimens with a normal history, even though they have been overstrained by about 0.5%. Conversely, the 26.7-MPa specimens with 1 to 1.5% overstrain have shown a reduced creep rate coefficient of $0.92 \times 10^{-35}$ $MPa^{-1} \cdot (neutrons/cm^2)^{-1}$. This implies a relaxation of the overload strain, as might be expected.

5.1.4 German Irradiation Program — C. R. Kennedy

Experiments HTK-5 (620°C) and HTK-6 (900°C) were removed from HFIR, and the specimens were extracted and measured. Although the results are still preliminary, several relevant conclusions have become evident. We now have a reasonable number of various grades that have been irradiated past their maximum densification fluence at temperatures from 600 to 900°C. It was observed previously that the damage rates resulting in dimensional changes do not vary appreciably over this temperature range, but, as the irradiation temperature increases, the life expectancy from loss of density occurs much sooner at the elevated temperatures. The maximum densification that occurs with temperature is shown in Fig. 5.5.

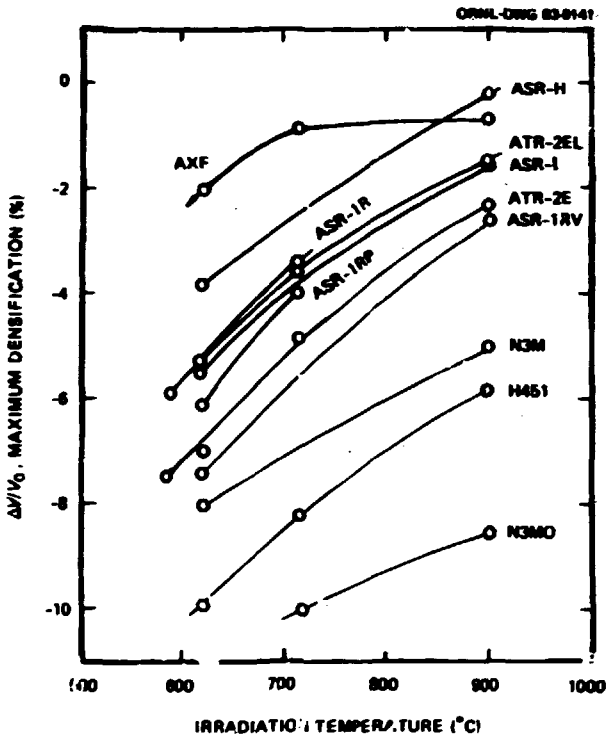


Fig. 5.5. Maximum densification of various graphite grades as a function of temperature for recent High Flux Isotope Reactor irradiations.

All the graphites clearly have essentially the same reduction in the maximum densification with increasing temperature. This suggests that the structural accommodation of the anisotropic growth in the *c*-axis and *a*-axis shrinkage by irradiation is reduced by increasing the temperature of irradiation; that is, the internal volume to accommodate the irradiation growth is reduced, thus causing the growth to increase the internal shear stresses actively at the interparticle boundaries and to initiate fracturing and structural degradation at lower fluences. The loss of the internal accommodating void volume can be a result of simply heating the graphite to the irradiation temperature as anisotropic crystallographic thermal expansion coefficients fill in the accommodating void volume.

The accommodating void volume is largely a result of cooling the graphite in the final stages of graphitization. The anisotropic *c*-axis shrinkage and the relatively stable *a*-axis generate the necessary cracking between the layer planes to generate the void volume to accommodate the irradiation growth. The extent of this accommodation can be measured by comparing the volumetric coefficient of thermal expansion to theoretical.

The difference between the two is a measure of the void volume created by the final stages of fabrication. Therefore, a graphite with a large volumetric coefficient of thermal expansion (CTE) will not densify greatly under irradiation, but one with a small volumetric CTE will densify greatly. However, we also know that, if the graphite has higher initial density, it will also not densify as much under irradiation. Therefore, the total densification under irradiation can be considered to be a function of the volume created by the anisotropic CTEs and the overall porosity:

$$(\Delta V/V_0)_I = f[(\Delta V/V_0)_{CTE}, (\Delta V/V_0)_D] ,$$

where

$(\Delta V/V_0)_I$ = maximum densification under irradiation,

$(\Delta V/V_0)_{CTE}$ = 2000 $(27 \times 10^{-6} - CTE_V)$, the void volume created by cooling down from 2000°C,

$(\Delta V/V_0)_D$ = (2.05 − initial bulk density)/2.05 = the void volume within the structure accessible to helium, and 2.05 is the apparent helium density.

Now that we have irradiated a reasonable number of grades with a range of $(\Delta V/V_0)_I$, it would be relevant to examine the data to determine the relative significance of $(\Delta V/V_0)_{CTE}$ to $(\Delta V/V_0)_D$. This should also allow the prediction of the maximum densification of future materials. As a first approximation and for simplicity, we assume a linearized function for a sensitivity calculation in the form

$$(\Delta V/V_0)_I = A + B(\Delta V/V_0)_{CTE} + C(\Delta V/V_0)_D .$$

A multiple linear regression analysis yields the coefficient values $A = -0.0825$, $B = 2.85$, and $C = 0.85$ at 620°C irradiation temperature. Considered as a type F1 functional fit, the standard deviation on $(\Delta V/V_0)_I$ is 0.0076. However, it is interesting to note that, as a type S1 statistical fit, the correlation coefficient is $r^2 = 0.90$. In other words, the linearized fit to the data is quite a good representation. Measured and computed values are compared in Table 5.2.

Table 5.2. Comparison of actual and calculated maximum densification $\Delta V/V_0$

(Irradiation temperature = 620°C)

| Grade | Actual $\Delta V/V_0$ (%) | Calculated $\Delta V/V_0$ (%) |
|---|---|---|
| V356 | 9.6 | 9.2 |
| V483 | 9.1 | 8.1 |
| ATR-2R | 7.0 | 7.1 |
| ATR-2E | 7.1 | 7.1 |
| ATR-2EL | 6.5 | 8.0 |
| ASR-1R | 5.3 | 5.9 |
| ASR-1RP | 6.7 | 7.4 |
| ASR-1RS | 7.1 | 7.8 |
| ASR-2R | 8.5 | 8.4 |
| UKAEA-11 | 5.3 | 5.2 |
| AXF | 1.6 | 1.4 |
| H-451 | 9.9 | 9.3 |

We conclude that at 620°C the thermal expansion voids are three times ($B$ = 2.85) more effective than their intrinsic volume in controlling the irradiation-induced densification, whereas the helium-accessible voids are effective on a one-to-one ratio ($C$ = 0.85). We also note that each of the three terms in the equation are of comparable magnitude $O(10^{-1})$; hence, the densification is equally sensitive to both types of voids.

We also note that the quantity $(\Delta V/V_0)_I$ changes by 3 to 4 vol % as the irradiation temperature changes from 620 to 900°C. This suggests that the coefficient $B$ should be about 10 rather than the 2.85 we calculate at 620°C. Quite clearly, the linearized sensitivity equation we have fitted successfully at 620°C must at the very least have temperature-dependent coefficients. Unfortunately, we do not yet have sufficient property data to perform a sensitivity calculation at 900°C.

In summary, virtually all the data appear to be self-consistent in implying that the decrease in life expectancy of graphite with increasing temperature is only mildly related to growth-rate changes. The major

cause of the lifetime reduction is the loss of void volume by thermal expansion to accommodate the differential anisotropic growth of irradiation. The thermal expansion is between three and ten times as effective in reducing the potential densification by irradiation.

The resistance of graphite to irradiation damage must also depend on the ability of the graphite to withstand internal strains due to anisotropic irradiation growth. Thus, graphites with high strain energy release rates might be expected to be more resistant to the internal shearing and to exhibit greater resistance to neutron-induced damage. To evaluate this possible interrelation, a number of graphites used in our irradiation program have been fracture-toughness tested. The results of testing 19.05-mm-diam specimens are given in Table 5.3.

Table 5.3. Results of fracture toughness testing of various graphites

| Grade | Crack orientation[a] | $K_{IC}$ (MPa $\sqrt{m}$) | | $G_{IC}$ (Pa·m)[b] | $\sigma_f$[c] (MPa) | $a$[d] (μm) | Lifetime ($10^{22}$ neutrons/cm$^2$) at | | |
|---|---|---|---|---|---|---|---|---|---|
| | | | | | | | 620°C | 715°C | 900°C |
| ASRI | RL | 1.21 | 0.04 | 137 | 41.2 | 275 | 3.6 | | 1.4 |
| V356 | RL | 1.38 | 0.06 | 169 | 37.4 | 434 | 3.1 | | |
| V483 | RL | 1.42 | 0.06 | 191 | 33.8 | 562 | 3.1 | | |
| ASR-1R | RL | 1.58 | 0.05 | 231 | 26.6 | 1124 | 2.8 | 2.3 | |
| ASR-2R | RL | 1.40 | 0.06 | 207 | 20.2 | 1528 | 2.7 | | |
| ATR-2E | RL | 1.57 | 0.08 | 266 | 20.0 | 1962 | 4.1 | 3.0 | 1.8 |
| ATR-2R | RL | 1.73 | 0.10 | 289 | 25.1 | 1512 | 2.8 | | |
| ASR-1RP | RL | 1.54 | 0.07 | 219 | 27.3 | 1112 | 3.3 | 2.8 | |
| ASR-1RS | RL | 1.50 | 0.04 | 212 | 28.4 | 888 | 3.9 | | |
| ASR-1RV | RL | 1.53 | 0.02 | 214 | 31.3 | 760 | 3.6 | | 1.6 |
| H451 | RL | 1.39 | 0.04 | 212 | 28.0 | 784 | 4.15 | 3.0 | 2.1 |
| H451 | CR | 1.44 | 0.07 | 241 | 28.0 | 820 | 4.15 | 3.0 | 2.1 |
| H451 | LR | 1.54 | 0.06 | 247 | 30.7 | 800 | 4.15 | 3.0 | 2.1 |
| H451I | RL | 1.54 | 0.03 | 250 | 29.5 | 868 | 4.15 | | 2.1 |
| M3M | RL | 1.70 | 0.05 | 255 | 61.4 | 244 | 4.7 | | 3.6 |
| AXF | RL | 1.78 | 0.02 | 236 | 87.8 | 131 | 4.1 | 3.1 | 2.4 |

[a]Orientation symbols: R, radial; L, longitudinal; C, circumferential. The first letter is the direction normal to crack, the second letter is the diraction the crack is propagating.

[b]We use the relationship: $G_{IC} = K_{IC}^2/E$.

[c]Flexure strength.

[d]We use the relationship: the effective half-length $a = \frac{1}{\pi}(K_{IC}/\sigma)^2$.

The results of this comparison do not demonstrate a simple relationship. It should be realized, however, that the first-generation graphites such as AGOT had $K_{IC}$ values of only 0.6 to 1.0 MPa $\sqrt{m}$, with lifetimes of about 25% less than those more advanced grades in Table 5.2. It does demonstrate that lifetime depends not only on the graphite's ability to withstand the internal shears mechanically but also on its ability to accommodate the shearing, with internal flaws and porosity reducing the internal strains.

These results furnish good agreement between the calculated flaw (defect) size and the pore structure evident from the microstructure. It is also quite apparent that lifetime and particle size are not interrelated.

## 5.2 GRAPHITE CORROSION

### 5.2.1 Corrosion Experiments — C. D. Bopp

A number of steam-oxidation runs have been made with our two 0.1-MPa (1-atm) steady-state loops. These experiments have generally used the brittle-ring specimens to permit comparison between various graphite grades and have been conducted at 900°C, which necessitated runs of several weeks' duration. Only the inner surfaces of the rings were oxidized. Monitoring at intervals showed that steady-state conditions were generally realized within the first day of loop operation as determined by the reaction products and the demand rate for new water-vapor-containing helium gas.

These experiments were directed to a number of objectives: establishing better data on Stackpole 2020 graphite at 900°C, determining the effects of interrupted oxidation, and establishing the sensitivity of oxidation rate to billet locations and heat treatment temperatures. These last questions are, of course, involved with chemical catalysis.

### 5.2.2 Microstructural Measurements — D. A. Lee and J. M. Keller

Surface area BET measurements are continuing on various grades of graphite of interest to the HTGR program. The most extensive data taken recently (Table 5.4) pertain to H451 graphite. These data include a number of points beyond those previously reported.

Table 5.4. Measurements on H451 graphite rod segments

| Rod and segment | He $H_2O$ saturation temperature (°C) | Oxidation temperature (°C) | Oxidation time (h) | Weight loss (%) | Surface area ($m^2/g$) | Standard deviation (goodness of fit) |
|---|---|---|---|---|---|---|
| 2-1 | 20 | 1000 | 343 | | 5.048 | 0.0115 |
| 2-7 | 20 | 1000 | 343 | | 6.026 | 0.0052 |
| 2-13 | 20 | 1000 | 343 | | 5.158 | 0.0025 |
| 2-16 | 20 | 1000 | 343 | | 4.861 | 0.0011 |
| 3-1 | 20 | 1000 | 168 | 4.77 | 4.769 | 0.0048 |
| 3-7 | 20 | 1000 | 168 | 4.77 | 4.934 | 0.0021 |
| 3-13 | 20 | 1000 | 168 | 4.77 | 5.346 | 0.0037 |
| 3-16 | 20 | 1000 | 168 | 4.77 | 5.169 | 0.0038 |
| 5-1 | 20 | 900 | 504 | 6.7 | 3.735 | 0.0020 |
| 5-4 | 20 | 900 | 504 | 6.7 | 4.136 | 0.0015 |
| 5-7 | 20 | 900 | 504 | 6.7 | 4.205 | 0.0021 |
| 5-10 | 20 | 900 | 504 | 6.7 | 4.107 | 0.0023 |
| 5-13 | 20 | 900 | 504 | 6.7 | 4.756 | 0.0024 |
| 5-16 | 20 | 900 | 504 | 6.7 | 3.633 | 0.0036 |
| 9-1 | 10 | 900 | 504 | 3.61 | 4.378 | 0.0058 |
| 9-4 | 10 | 900 | 504 | 3.61 | 4.210 | 0.0112 |
| 9-7 | 10 | 900 | 504 | 3.61 | 4.410 | 0.0076 |
| 9-10 | 10 | 900 | 504 | 3.61 | 4.139 | 0.0048 |
| 9-13 | 10 | 900 | 504 | 3.61 | 3.712 | 0.0019 |
| 9-16 | 10 | 900 | 504 | 3.61 | 4.012 | 0.0027 |
| 11-2 | 10 | 900 | 672 | 2.13 | 2.539 | 0.0049 |
| 11-3 | 10 | 900 | 672 | 2.13 | 3.451 | 0.0100 |
| 11-7 | 10 | 900 | 672 | 2.13 | 2.592 | 0.0145 |
| 11-12 | 10 | 900 | 672 | 2.13 | 3.428 | 0.0146 |
| 11-15 | 10 | 900 | 672 | 2.13 | 3.414 | 0.0191 |
| 11-18 | 10 | 900 | 672 | 2.13 | 2.574 | 0.0160 |
| 11-19 | 10 | 900 | 672 | 2.13 | 2.864 | 0.0015 |
| 14-7 | 10 | 1000 | 336 | 2.3 | 3.043 | 0.0270 |
| 14-13 | 10 | 1000 | 336 | 2.3 | 3.918 | 0.0230 |
| 15-7 | 5 | 900 | 504 | 2.9 | 3.917 | 0.0141 |
| 15-13 | 5 | 900 | 504 | 2.9 | 3.924 | 0.0248 |

The apparatus has been modified to permit gas porosimetry measurements in the 1- to 100-nm range. Measurements are now in progress on both Great Lakes H451 and Stackpole 2020 graphites.

## 5.3 GRAPHITE PHYSICAL PROPERTIES

### 5.3.1 Fracture Toughness Testing — C. R. Kennedy

Fracture of graphite components in the HTGR will not occur if the material and loading conditions are according to specifications. The concern is the off-specification material or an unanticipated loading situation that may initiate fracture of the graphite components. Therefore, the effect of the largest anticipated flaw or the largest possible stress concentration must be considered. This requires a study of the fracture toughness characteristics of the material to relate permissible stress to flaw size. This study must obviously include the effects of irradiation and oxidation on the base material characteristics.

The short-rod specimen with a chevron notch is used. This specimen, with diameters of 12.7, 19.05, and 25.4 mm, is compatible with present oxidation and irradiation specimen sizes and is economic in specimen preparation time and material. However, fracture toughness testing or any crack propagation study must consider the effect of the specimen geometry and the material characteristics in altering the notch stress concentration factor. Most methods of fracture toughness testing do not consider the effect of plastic deformation in crack propagation. The short-rod specimen testing procedure does include this particularly important characteristic of graphite, which is so well known from the tensile stress-strain curve. With the same notch geometry but with varying diameters, the method allows determination of the effective width of the notch as modified by plastic deformation. Thus, the effective stress concentration can be calculated for more exact estimations of the critical stress intensity factor. To confirm these procedures for graphite, grades of GraphNOL N3M, POCO AXF, H451, and 2020 (as received and heat treated to 2800°C) were tested with specimen diameters of 12.7, 19.05, and 25.4 mm. The results of this testing with approximately five specimens for each point are given in Fig. 5.6. There seems to be some variation with size; however, in most

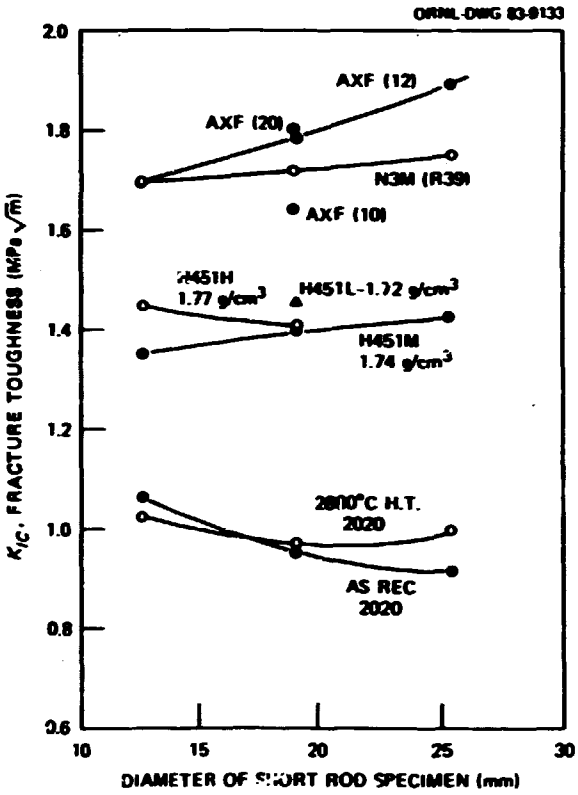


Fig. 5.6. Fracture toughness results of testing short-rod specimens with diameters of 12.7, 19.05, and 25.4 mm.

cases, it is not statistically relevant. The POCO AXF appears to be size dependent, which is in agreement with past results for experiments using notched bars in bending. The other graphite grades do not show a significant difference between 25.4- and 19.05-mm-diam specimens and only slight variations in the 12.7-mm results. It thus appears that the most consistent data were obtained from testing the larger specimens.

A major question in the study of the mechanical properties of oxidized graphite is whether the oxidation causes a reduction in strength greater than that expected by the porosity increase. To resolve this question, a group of experimental graphites with controlled porosity differences created by fabrication were fracture-toughness tested. These graphites were fabricated at ORNL by use of advanced green-cake technology and are well characterized from other studies. The results of this series are given in Fig. 5.7, which demonstrates an exponential relationship between fracture toughness and porosity.

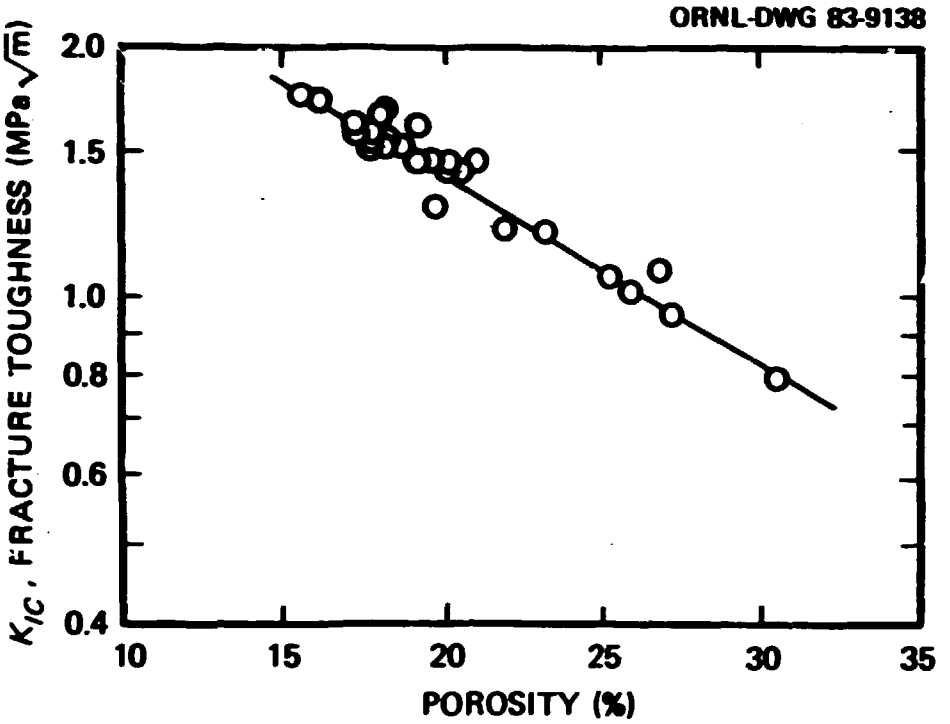


Fig. 5.7. The fracture toughness of experimental GraphNOL N3H graphites with different densities.

Specimens of H451 and 2020 oxidized in steam at 900 and 1000°C were also fracture-toughness tested, with the results given in Fig. 5.8. Again, although with more scatter, the results tend to follow an exponential relationship with porosity. It is also interesting that not only does grade 2020 have a significantly lower $K_{IC}$ value but that the value is also reduced more by oxidation. These results are significant in that they emphasize the importance of assuring the quality of 2020 and demonstrating that it is free of disparate flaws.

The strain energy release rate $G_{IC}$ can also be calculated from the fracture toughness values by

$$G_{IC} = (K_{IC}/E)^2 ,$$

where $E$ is Young's modulus. The calculated $G_{IC}$ values are given in Fig. 5.9. The value of $G_{IC}$ can be compared with the energy required to create two new surfaces. Those graphites with higher $G_{IC}$ values have

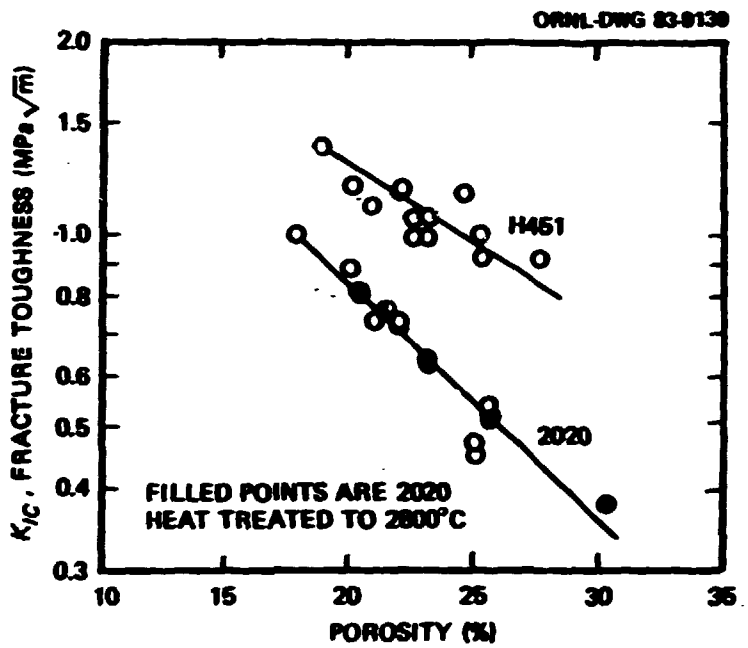


Fig. 5.8. The effect of steam oxidation on the fracture toughness of H451 and 2020 graphite.

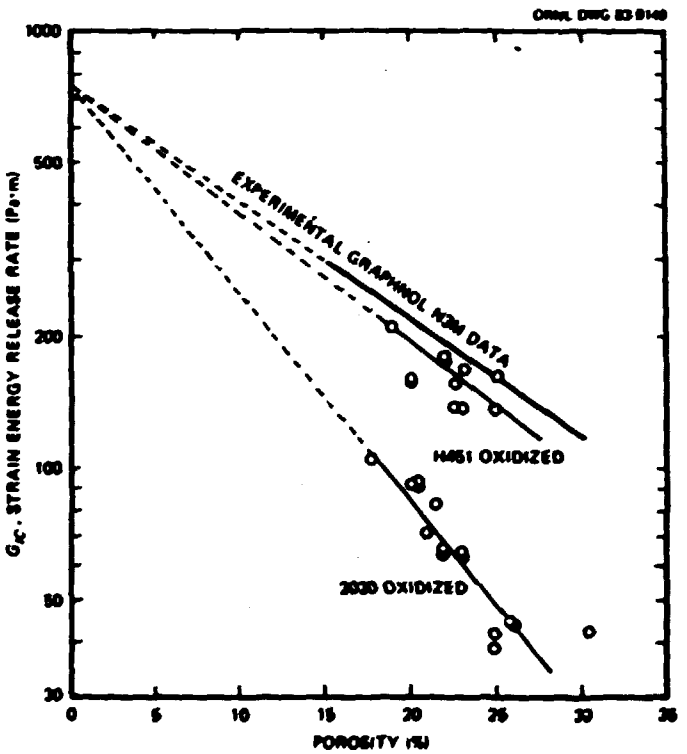


Fig. 5.9. The effect of oxidation on $G_{IC}$ of H451 and 2020 compared with the GraphNOL N3M fabrication data.

structures that are more resistant to fracture; however, they may have lower strength values because of larger internal flaws. Such a contrast was exhibited between grades 2020 and H451. Also, graphites with higher $G_{IC}$ values are probably a result of more effective use of the binder. Note that the values of $G_{IC}$ for H451 and 2020 both extrapolate to a common value for "zero" porosity. From this we infer that graphites with no porosity and with a contiguous structure may have a common $G_{IC}$. The loss in $G_{IC}$ with porosity is greater than expected by a simple loss in cross-sectional area. This implies that binding in some graphites is considerably more effective than in others, as indicated again by the difference between 2020 and H451. The implication is that a graphite more resistant to the effects of oxidation would result from increased effectiveness of the binder, yielding not only higher $G_{IC}$ values but a $G_{IC}$ that is less sensitive to oxidation.

The size of an equivalent critical defect with a length of $2a$ can be calculated from

$$2a = 2(K_{IC}/\sigma_f)^2/\pi ,$$

where $\sigma_f$ is the fracture strength. The result of these calculations for the oxidized graphites are shown in Fig. 5.10. The large defect size for unoxidized H451 is in very good agreement with the flaws evident in the microstructure. However, the microstructure of 2020 does not indicate flaws greater than about 100 to 150 μm, or five times smaller than the calculated value for the unoxidized material. Also, although the defect size increases with oxidation for H451, it does not increase for either as-received or heat-treated 2020 graphite. The only observable defect in the 500- to 600-μm 2020 is the agglomerates of high-Z material evident in the microradiographs of as-received material. These are not directly visible in the optical microstructure of the graphite or in the radiography for 2800°C heat-treated material. It appears that the critical defect in 2020 is associated with these agglomerates even though the 2800°C heat treatment has volatized or diffused these agglomerates. The relic structure created by the agglomerations remains. During oxidation

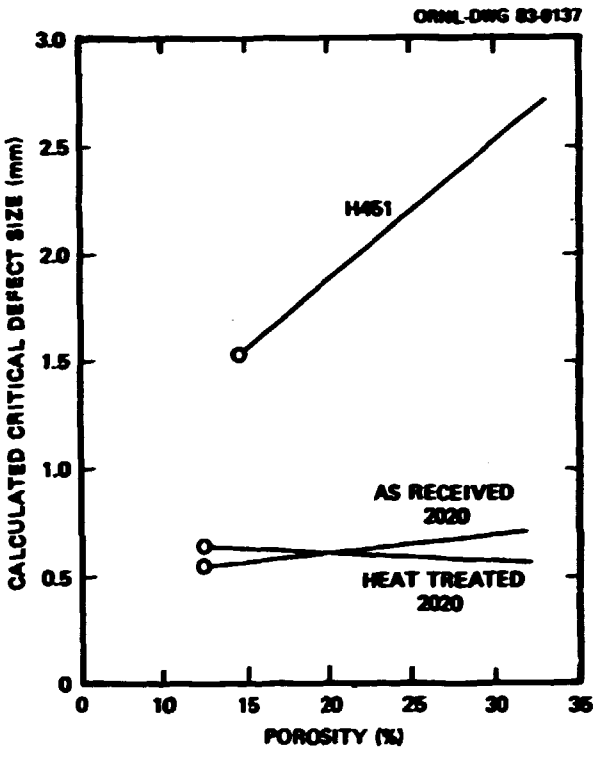


Fig. 5.10. The effect of steam oxidation on the calculated critical defect size of H451 and 2020 graphite.

of the as-received 2020, the carbon within the agglomerate appears to be oxidized preferentially by catalytic oxidation, with little increase in the overall size of the agglomerate. In the case of the heat-treated 2020, the oxidation is not concentrated but uniformly attacks the whole structure. The oxidation is almost certainly increasing the size of the smaller flaws, but the relic flaw size is so large it still controls fracture. The same thing may also be occurring in the as-received material as well, but to a smaller extent.

### 5.3.2 Statistical Analysis of Tensile Strengths for H451 Graphite — W. P. Eatherly

The design engineer faced with the structural application of graphite must ensure that the material will withstand the forces placed upon it. In the normal course of events this leads to a definition of a minimum acceptable strength and the subsequent imposition of a suitable safety factor to make it extremely unlikely that that minimum strength is

actually reached. It then becomes the materials engineer's job to produce such a material. Actually, a series of compromises is made between the design engineer and the materials engineer.

Ideally, the safety factor is replaced by complete knowledge of the statistical properties of the graphite coupled with a complete description of how graphite fails under given stress conditions. We are concerned with both of these aspects, but here we wish to consider the statistical problem only. This has been the subject of intensive study during the past year. The mathematics involved is straightforward but both conceptually complex and structurally abstruse. It seems worthwhile to summarize the procedures used and their results to date on a purely conceptual basis, with the objective of providing a coherent account unencumbered with mathematical obscurities.

The story starts with very high-quality aerospace graphites having such good structures that they are relatively transparent to sound. These materials may therefore be searched sonically and their flaw characteristics determined nondestructively. This has led to a somewhat idealized dichotomization of flaws into two types, background and disparate. One visualizes background flaws to be quasi-continuously present and characteristic of the raw materials and their particulate form. Disparate flaws are generally introduced during fabrication, are much larger in size, and occur as isolated defects. From the general nature of graphite manufacture, one would expect this picture, provable for the sonically transparent materials, to be a general situation. On this basis, we began our statistical search in the H451 tensile data for the occurrence of disparate flaws and the extreme penalty they impose on strength.

### 5.3.2.1 Tolerance Limits and Variance Analysis

From the viewpoint of the design engineer, the probability of a structural failure is couched in terms of a statistical property called a "tolerance limit." This leads to a statement of the form, "I am 95% confident that 99% of the material is above my minimum acceptable strength." We might translate this expression into the form, "If I build 100 reactors, I will expect 1% or less of the graphite fuel blocks to fail in 95 of the reactors, but 1% or more in the other five reactors." This statement may

seem weak, but it is precise and literally requires thousands of data points, for one must have a very well-defined knowledge — not of all the data but, rather, of the lowest 1% of the data. And on the basis of that knowledge, we reject all graphite having strength properties that lead to the occurrence of the lower 1% of the data.

This rejection (truncation) must obviously be made on a billet-by-billet basis. One can hardly obtain enough data on a single billet to determine whether or not to reject it. Not only would the cost be prohibitive but we would destroy the billet in the process. Thus, we must reach a decision to keep or reject a given billet by pooling our knowledge of many billets and assuming that they have certain similar statistical properties and then rejecting a given billet on the basis of very few data points on that billet. The key words are "certain similar statistical properties," and this reduces to the hope that variability within a billet is a common property of all billets regardless of their average strength.

These considerations lead us to a variance analysis procedure: we assume that the billets have a common variability characterized by a standard deviation $\sigma_w$ ($w$ = within billet) but with billet mean strengths that are also variable and characterized by a standard deviation $\sigma_b$ ($b$ = between billets). To apply this procedure requires that we show that a common $\sigma_w$ does exist over all billets (variance homogeneity), and for the case of H451 we find this is true, specifically

$$\sigma_w \approx 1.38 \text{ MPa } (200 \text{ psi}),$$

$$\sigma_b(\text{axial}) \approx 2.28 \text{ MPa } (331 \text{ psi}),$$

$$\sigma_b(\text{radial}) \approx 1.03 \text{ MPa } (149 \text{ psi}),$$

with mean strengths of about 12.8 MPa (1860 psi) axial and 16.1 MPa (2340 psi) radial.

But these results would apply only to the material if it were free of disparate flaws, and these present quite a different problem.

5.3.2.2 Skewness; Disparate Flaws

We have argued above that we must accept and reject billets on the basis of an individual billet characteristic only and have concluded that, if variance homogeneity exists within billets, such a goal is attainable. If we look at each data subset representing an individual billet, we find that homogeneity does not exist and quickly recognize that homogeneity fails because frequently one or more "too low" values of strength occur. This is exactly the data characteristic we would expect to be introduced by the disparate flaw, an occasional very weak specimen. Such a distribution is termed "negatively skewed" (i.e., it has too many values occurring in the negative tail of the distribution).

We must now dichotomize the strength measurements into two categories, those characteristic of the background flaw field and those characteristic of the disparate flaw, but we must also recognize that such a dichotomization is artificial. We accomplish all this by use of the Nair criterion at the 5% level. That is, if a very low (or very high) strength value exists in the data subset that is very unlikely for the number of measurements that exist, we classify it as a disparate and define this by accepting a 5% risk that the point we so classify is incorrectly classified; one time in twenty it does indeed represent a true low point from the background flaw field.

This method of classification is statistically sound and leads to two very important results. First, it homogenizes the variances (i.e., after truncating the data within billets, all billets are found to behave as though they possess a common standard deviation $\sigma_w$). Second, it ties the disparates directly to the billet mean strength; in other words, we may eliminate the dangerous disparates on the basis of the relatively few measurements necessary to define the billet average strength.

In summary, we find that the disparate flaws occur about 3.8% of the time for the specimen size employed, lie on the average about 5.03 MPa (730 psi) below the billet mean, and are themselves characterized by a standard deviation of about 1.07 MPa (155 psi).

### 5.3.2.3 Characterizing the Tolerance Limit

We now see that the tolerance limit is completely dominated by the disparate flaws. At the mean value for the strength within the disparate distribution, the background flaw field contributes only about 0.1% of the total distribution below that mean, whereas the disparate flaw field contributes 1.9% of the distribution. If we desire 99% of the population to lie above our minimum acceptable strength, then we must require that only about 75% of the disparate strengths lie above this minimum. This is, in a sense, a most happy result in that we do not need to know well the tails of the disparate distribution because we must reject a large fraction of it. Only relatively crude estimates of its mean and standard deviations are required. We can indeed make the statement that we are 99% confident that 99% of the population will lie above 6.62 MPa (960 psi) tensile strength radial and 9.93 MPa (1440 psi) axial.

The above analysis also indicates where material improvement must be sought. Improving the mean strength will tend to move the disparate distribution upward and decrease its contribution to the effective tail. But obviously the key improvement is to decrease the occurrence of disparate flaws. The problem in the end is an economic one: a higher price for a better quality graphite versus the economic penalty of severe truncation in a lower quality graphite.

### 5.3.2.4 Problems and the Future

The above results are still open to revision, although the general conclusions will stand. The key error is the severity of the truncation; it has removed too much of both tails leading to a so-called platykurtic distribution. The result is an underestimate of the within-billet variance $\sigma_w$, and this error threads through all aspects of the calculation. The error will probably be largely eliminated if the upper tail is not truncated.

A more basic problem exists in that we postulate the occurrence of disparate flaws as characteristic of graphite in general. We find that a statistical analysis of an aerospace graphite confirms the results of sonic testing and that compressive strengths in a fibrous composite graphite also indicate a mild negative skewness, as might be expected for

compression rather than for tension. It will be most interesting to see if the above statistical analysis applies equally well to Stackpole 2020 graphite, and here we may foresee the development of an adequate data base over the next year.

### 5.3.3 Improved Moderator Graphite — C. R. Kennedy

A development program to obtain a moderator graphite with improved mechanical properties has been initiated by GA Technologies, Inc. (GA), and Great Lakes Research Corporation (GLRC). The primary activity at Oak Ridge National Laboratory (ORNL) on this project was to assist in evaluating the experimental materials. This was done primarily with nondestructive techniques, with the objective of eventual use of these techniques to evaluate full-scale billets for reactor use. We also included as controls in these evaluations representative materials from our fracture mechanics and HFIR irradiation programs.

The nondestructive characterization (NDC) procedures were in two steps: (1) inspection of the subsize experimental billet as a whole, as received from GLRC, and (2) inspection of smaller cut-up sections. The initial NDC of the whole block was to gain experience for valid evaluations of future full-scale blocks. The NDC of the sections was to determine the variability within the billet and to have a more direct comparison of the NDC to destructive tensile test results performed at GA. Inspection of the blocks included

1. bulk density,
2. measurement of longitudinal and shear wave velocities in both the axial and radial directions,
3. measurement of the ultrasonic attenuation of the longitudinal wave in the block,
4. measurement of the eddy current response, and
5. low-voltage radiograph of a 19.05-mm-thick center slab cut from each block.

All the measurements were referenced to a 25.4-mm grid scribed on the ends of each block at 25.4-mm intervals as 0, 90, 180, and 220° down the sides from top to bottom. After the full billet was examined, it was sectioned and reexamined.

A central 19.05-mm slab was removed from each block and radiographed. The resulting radiographs, contact printed for ease of overall examination, gave clear indications of concentrations of high-Z contamination within the blocks. They also gave clear indications of structural irregularities due to preferred orientation of pores from working as well as evidence of density gradients both from impregnation and, on a finer scale, from mix-ball retention. The radiographs yield a quick overall relative estimate of block quality.

Sonic measurements of velocity to obtain the Young's modulus $E$ and the sonic attenuation $\alpha$ for estimating defect size can be used to predict the tensile strengths, as outlined in previous studies on oxidation and irradiation.[8] The parameter $(E/\alpha)^{1/2}$ is shown to be a relatively good estimate of the tensile strength in Fig. 5.11. Not only do the means compare well, but the coefficients of variation also compare well, as shown in Fig. 5.12. These plots demonstrate the potential of these sonic measurements to estimate both the mean value of strength and the variability. We recognize that these billets are subsize and that continued development will be required to extend these principles to full-scale blocks. The ability to establish dependable NDC techniques significantly

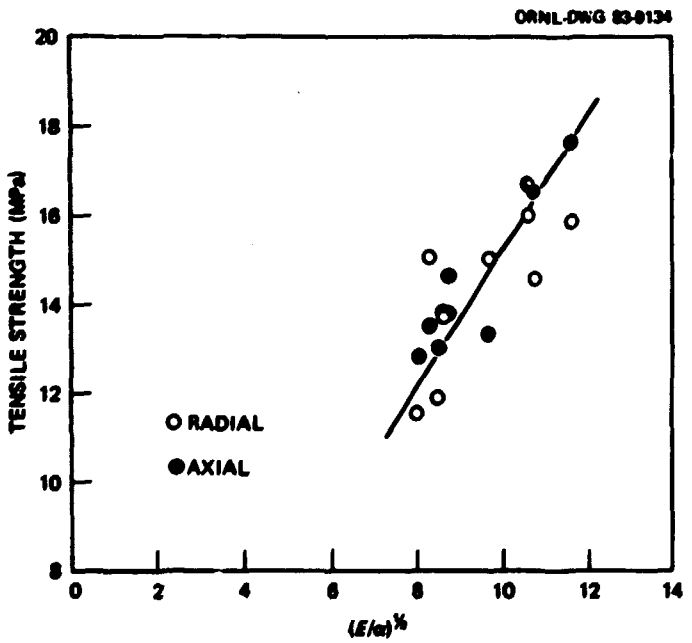


Fig. 5.11. Tensile strength of H451I as a function of $(E/\alpha)^{1/2}$.

## Table 5.5. Analysis of $(E/\alpha)^{1/2}$ data from segments

[The symbols $\bar{x}$ and $s$ represent means and standard deviations of $(E/\alpha)^{1/2}$]

| Group and block number | Segments | | | | | | Grand average | | Bartlett test | Within | Between | F-ratio | Comments | |
|---|---|---|---|---|---|---|---|---|---|---|---|---|---|---|
| | 1 | | 2 | | 3 | | | | | | | | Variance homogeneity | Means |
| | $\bar{x}$ | $s$ | $\bar{x}$ | $s$ | $\bar{x}$ | $s$ | $\bar{x}$ | $s$ | $K_2$ | $s_w$ | $s_b$ | | | |
| III | | | | | | | | | | | | | | |
| MB1-1 | 8.88 | 0.90 | 9.10 | 0.69 | 9.20 | 0.55 | 9.06 | 0.73 | 5.99 | 0.73 | 0.80 | 1.21 | Homogeneous | No difference |
| MB1-2 | 8.44 | 0.90 | 8.09 | 0.70 | 8.53 | 0.58 | 8.35 | 0.75 | 4.76 | 0.74 | 1.12 | 2.31 | Homogeneous | No difference |
| MB1-3 | 9.13 | 0.68 | 8.65 | 0.65 | 9.03 | 0.46 | 8.94 | 0.63 | 5.06 | 0.61 | 1.24 | 4.21 | Homogeneous | No difference |
| MB2-1 | 9.37 | 0.70 | 9.41 | 0.58 | 9.70 | 0.48 | 9.49 | 0.60 | 2.41 | 0.59 | 0.90 | 2.31 | Very homogeneous | No difference |
| MB2-3 | 9.86 | 0.59 | 9.31 | 0.48 | 8.82 | 0.66 | 9.33 | 0.71 | 1.98 | 0.58 | 2.54 | 19.02 | Very homogeneous | One end very low |
| MB3-1 | 8.36 | 0.85 | 8.09 | 0.59 | 8.92 | 0.49 | 8.46 | 0.74 | 7.22 | 0.66 | 2.11 | 10.17 | Borderline | Center low |
| IV | | | | | | | | | | | | | | |
| MB4 | 6.40 | 0.21 | 6.19 | 0.28 | 6.64 | 0.21 | 6.41 | 0.30 | 5.19 | 0.24 | 1.09 | 20.94 | Homogeneous | Center low |
| MB5 | 6.64 | 0.32 | 6.23 | 0.31 | 6.57 | 0.35 | 6.49 | 0.37 | 1.59 | 0.33 | 1.05 | 10.45 | Very homogeneous | Center low |
| MB9 | 8.29 | 0.63 | 8.08 | 0.44 | 8.65 | 0.76 | 8.35 | 0.66 | 7.88 | 0.63 | 1.36 | 4.61 | Questionable | |
| MB10 | 7.92 | 0.63 | 7.72 | 0.59 | 8.03 | 0.74 | 7.90 | 0.66 | 2.03 | 0.66 | 0.72 | 1.21 | Very homogeneous | No difference |
| V | | | | | | | | | | | | | | |
| MB14-1 | 8.50 | 0.94 | 8.14 | 0.55 | 8.48 | 0.68 | 8.38 | 0.75 | 6.54 | 0.74 | 1.00 | 1.85 | Questionable | |
| VII | | | | | | | | | | | | | | |
| MB19-3 | 13.08 | 1.02 | 9.95 | 0.84 | 0.67 | 0.91 | 1.24 | 1.63 | 1.43 | 0.93 | 8.03 | 75.21 | Very homogeneous | Center low |
| MB20-2 | 12.70 | 0.91 | 0.53 | 1.12 | 0.98 | 1.45 | 1.51 | 1.50 | 2.52 | 1.16 | 5.36 | 21.35 | Very homogeneous | One end low |
| MB20-3 | 12.58 | 0.90 | 0.46 | 0.87 | 0.55 | 0.61 | 1.20 | 1.26 | 4.91 | 0.81 | 5.87 | 53.32 | Homogeneous | One end high |
| VIII | | | | | | | | | | | | | | |
| M1B-21 | 0.58 | 0.54 | 5.90 | 0.42 | | | 5.74 | 0.50 | 0.72 | 0.48 | 1.11 | 5.30 | Very homogeneous | No difference |
| M1B-22 | 5.67 | 0.56 | 5.81 | 0.41 | | | 5.74 | 0.49 | 2.06 | 0.49 | 0.49 | 0.98 | Very homogeneous | No difference |
| M1B-24 | 9.39 | 0.43 | 8.59 | 0.65 | 9.05 | 0.39 | 9.04 | 0.58 | 9.03 | 0.51 | 1.70 | 11.25 | Questionable | Center low |
| M1B-25 | 9.67 | 0.58 | 8.89 | 0.75 | 9.11 | 0.53 | 9.22 | 0.68 | 3.07 | 0.63 | 1.96 | 10.54 | Very homogeneous | Center low |
| IX | | | | | | | | | | | | | | |
| MWB26-1 | 9.27 | 0.58 | 8.47 | 1.11 | 8.57 | 0.80 | 8.77 | 0.92 | 8.09 | 0.85 | 2.12 | 6.15 | Questionable | One end high |
| MWB26-2 | 8.95 | 0.99 | 8.23 | 0.69 | 8.30 | 0.67 | 8.49 | 0.85 | 5.16 | 0.80 | 2.41 | 9.15 | Homogeneous | One end high |
| X | | | | | | | | | | | | | | |
| MAB27-1 | 9.86 | 1.08 | 9.80 | 0.90 | 0.23 | 0.84 | 9.96 | 0.95 | 0.79 | 0.94 | 1.92 | 4.14 | Very homogeneous | No difference |
| MAB27-3 | 9.63 | 1.22 | 9.12 | 0.71 | 9.62 | 0.57 | 9.45 | 0.90 | 4.82 | 0.88 | 2.56 | 8.57 | Lacks homogeneity | |
| MAB28-1 | 9.92 | 1.16 | 9.62 | 0.70 | 9.94 | 0.72 | 9.83 | 0.99 | 8.61 | 0.89 | 0.89 | 1.01 | Questionable | No difference |
| MAB28-3 | 10.18 | 1.16 | 9.27 | 1.18 | 9.90 | 0.77 | 9.78 | 1.11 | 4.32 | 1.05 | 2.78 | 4.66 | Homogeneous | No difference |
| I | | | | | | | | | | | | | | |
| 2179-8 | | | | | | | | | | | | | | |
| II | | | | | | | | | | | | | | |
| 2179-14EB | | | | | | | | | | | | | | |
| 2179-14EC | 8.95 | 1.18 | 0.26 | 0.85 | | | 9.60 | 1.21 | 2.58 | 1.05 | 4.53 | 19.42 | Very homogeneous | One end low |
| 2179-16EB | 8.24 | 1.32 | 7.95 | 1.04 | | | 8.10 | 1.19 | 2.20 | 1.20 | 0.97 | 0.67 | Very homogeneous | No difference |

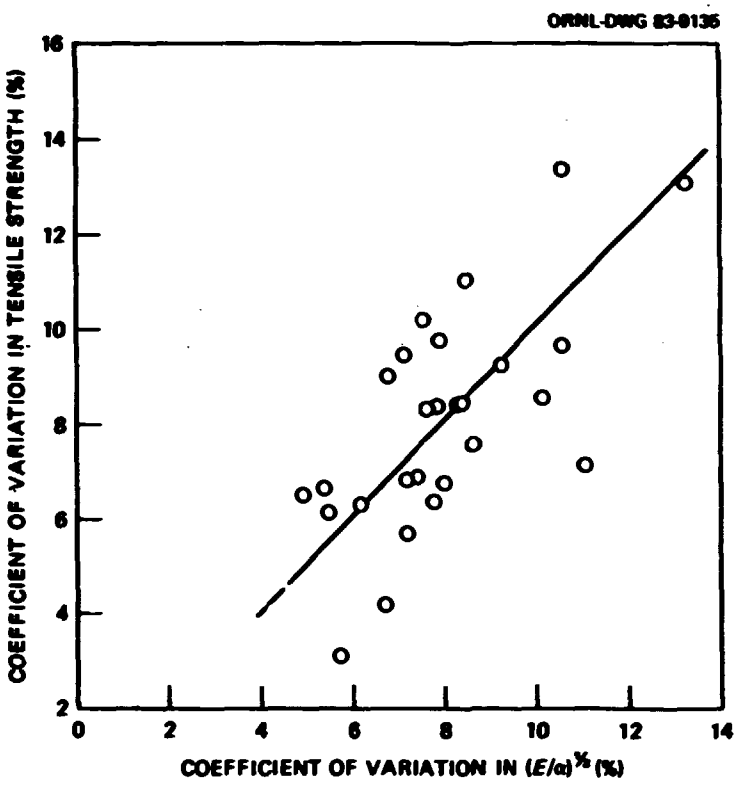


Fig. 5.12. Comparison of the coefficients of variation in axial tensile strength with $(E/\alpha)^{1/2}$ from each segment.

increases the confidence in the performance of the material. It is important to realize that these techniques evaluate essentially all the block volume, whereas sampling the end of a block really evaluates only that end of the block.

The sonic evaluations were also used to evaluate structural uniformity. The $(E/\alpha)^{1/2}$ results were initially compared for homogeneity of variances by the Bartlett test. Given in Table 5.5 are the calculated values of the Bartlett test parameter $K^2$, which are to be compared with percentage points of the $\chi^2$ distribution. For values of $K^2$ greater than 7, the hypothesis of homogeneity must be questioned. For $K^2$ greater than 10, the variances lack homogeneity, and any further comparisons are also in doubt. The within- and between-group standard deviations are given; the $F$-ratio for groups with the same means would have a very low value of less than 5. Billets having $F$-ratios greater than 10 definitely imply differences in the means. It should be recognized, however, that this test must be

preceded by a test of homogeneity for validity. Therefore, the data obtained from several of the blocks that failed the Bartlett test cannot be compared on the basis of the F-statistic.

The billets in group III all passed the Bartlett test and were insensitive to the dry cores in billets MB1-1, MB1-3, and MB2-1. Billets MB2-3 and MB3-1 indicated a difference due to the dry core in MB2-3 and a weak center in MB3-1 (confirmed by tensile testing). The billets in group IV indicate weak centers in MB4 and MB5. There is no other test to corroborate these differences; however, the sensitivity levels in these data are very high, and these small differences may not be relevant. Billets MB9 and MB10 indicated a high level of uniformity, confirmed by other evaluations as well as by tensile testing. Group V, represented by billet MB14-1, was in good agreement with other evaluations, including tensile testing. Group VI was not evaluated. Group VII billets all indicated good homogeneity but low values of $(E/\alpha)^{1/2}$ at the ends or centers. These billets were tensile tested and did not confirm the differences in the means. In each case in which the top of the billet was indicated to be very strong, this result was actually confirmed by tensile testing, but the differences were not as large as projected. The parameter $(E/\alpha)^{1/2}$ in these blocks appears to be more sensitive to the structure than the tensile strength. The remainder of the billets in groups VIII, IX, and X, except for MAB27-3 (which did not indicate homogeneity), had slightly higher values of $(E/\alpha)^{1/2}$ at one or both ends.

In all, these billets are very uniform, considering that they were made from small experimental batches. Larger production batches should be expected to possess improved uniformity even with a scaleup in billet size.

Although strength is very important in evaluating graphite, it is exceedingly important that the fracture toughness is not reduced in the process. Therefore, selected billets were fracture-toughness tested by use of short-rod specimens in comparison with grade H451. The results given in Table 5.6 with available tensile test results are very encouraging. All except MIB-25 had a fracture toughness value greater

Table 5.6. Fracture toughness testing results

| Block | $K_{IC}$ (MPa $\sqrt{m}$) | $G_{IC}$ (Pa·m) | Critical defect size (mm) | Radial tensile strength (MPa) |
|---|---|---|---|---|
| MB2-1 | 1.54 | 250 | 8.68 | 13.3 |
| MB-10 | 1.41 | 115 | 7.81 | 12.84 |
| MB-14-1 | 1.54 | 236 | 7.15 | 14.66 |
| MB-20-3 | 1.60 | 244 | 5.34 | 17.62 |
| MIB-25 | 1.19 | 153 | 3.06 | 17.29 |
| H-451 | 1.39 | 218 | 8.69 | 12.0 |

[a]Defect size, $2/\pi(1-\mu^2)K_{IC}{}^2\sigma_f{}^2$.

than H451. In that flaws and defects are bound to exist in the core structure graphite, it is more important to have a high fracture toughness than a high strength. These results are very promising indications that both improved strength and fracture toughness can be obtained.

It is also important that the radiation damage data base not be lost by these relatively minor changes in fabrication procedures to confirm that the continued irradiation resistance specimens from a selected billet, MB2-1, were directly compared with H451 in capsules HTK-5 and -6. The results (Fig. 5.13) give the volume changes with fluence. It is

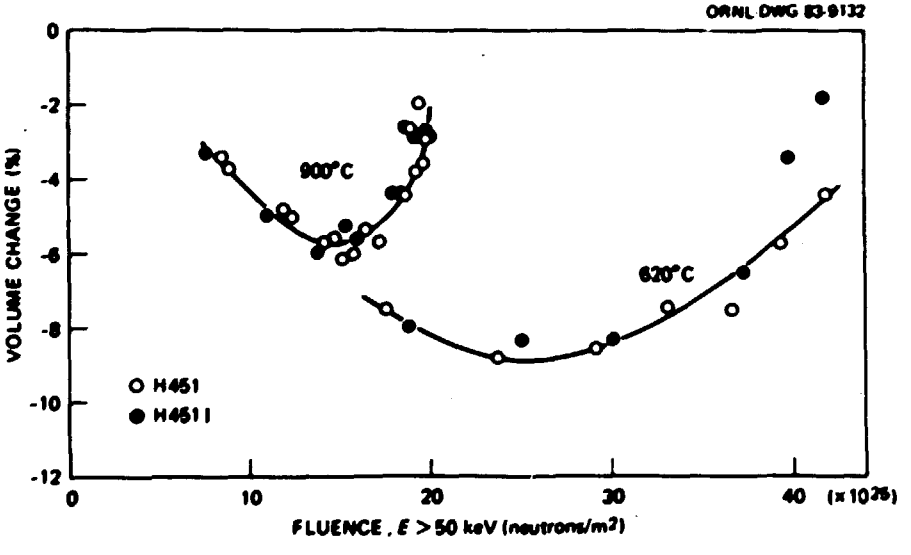


Fig. 5.13. Comparison of irradiation resistance of H451I with that of H451.

obvious that the expected lifetimes are identical. The only difference is that H451 shows a mild extrusion texture while H451I (MB2-1) exhibits a mild molded texture. In all, it seems quite realistic and probable that a new moderator graphite with significantly improved mechanical properties can be produced without a loss in the high texture toughness or irradiation resistance inherent in H451.

## 5.4 REFERENCES

1. R. L. Senn et al., *Design, Operation, and Initial Results from Capsule OC-1, the First of a Series of Graphite Creep Irradiation Experiments*, ORNL/TM-5798, May 1977.

2. R. L. Senn et al., "Characterization and Standardization of Graphite," pp. 476–84 in *High-Temperature Gas-Cooled Reactor Base-Technology Program Progress Report for Period January 1, 1974–June 30, 1975*, ORNL-5108.

3. R. L. Senn, J. A. Conlin, and W. P. Eatherly, "Graphite Creep Experiment OC-1," pp. 373–89 in *High-Temperature Gas-Cooled Reactor Base-Technology Program Progress Report for Period July 1, 1975–December 31, 1976*, ORNL-5274.

4. R. L. Senn, J. A. Conlin, and W. P. Eatherly, "Creep Experiments OC-2 and OC-3," pp. 323–27 in *High-Temperature Gas-Cooled Reactor Base-Technology Program Annual Progress Report for Period Ending December 31, 1977*, ORNL-5412.

5. R. L. Senn, J. A. Conlin, and W. P. Eatherly, "Creep Capsule OC-4," pp. 205–09 in *High-Temperature Gas-Cooled Reactor Technology Development Program Annual Progress Report for Period Ending December 31, 1980*, ORNL-5753.

6. R. L. Senn, J. A. Conlin, and W. P. Eatherly, "Capsule Irradiations," pp. 189–99 in *High-Temperature Gas-Cooled Reactor Technology Development Program Progress Report for Period Ending December 31, 1981*, ORNL-5871.

7. R. L. Senn, J. A. Conlin, and W. P. Eatherly, "KFA Graphite Irradiations," pp. 327–30 in *High-Temperature Gas-Cooled Reactor Base-Technology Program Progress Report for Period Ending December 31, 1977*, ORNL-5412.

8. C. R. Kennedy, J. A. Conlin, and W. P. Eatherly, "Strength Testing on Oxidized Graphite," pp. 49–52 in *High-Temperature Gas-Cooled Reactor Technology Development Program Progress Report for Period Ending December 31, 1981*, ORNL-5871.

# 6. HIGH-TEMPERATURE REACTOR PHYSICS STUDIES (WBS ORI304 and ORI501)

D. E. Bartine

## 6.1 INTRODUCTION

The reactor physics studies performed this past year under the High-Temperature Gas-Cooled Reactor (HTGR) Analysis effort were concerned mainly with performance of the prismatic HTGR. The thermal-hydraulic effort extended previous work so that the use of one-dimensional (1-D) flow in a three-dimensional (3-D) neutronics problem became available for routine use in our analysis. Fuel temperature distributions and averages were included in the outputs to allow meaningful comparison between cases. Options on coolant flow orificing were studied and made available to the code user.

The depletion-perturbation theory was tested further for use in sensitivity and optimization studies. Results from 1-D models of the small-core modular sector are encouraging. Benchmarking of low-enriched uranium cross sections was initiated under an agreement between Oak Ridge National Laboratory (ORNL) and GA Technologies, Inc. (GA). The thermal-hydraulic modeling of a continuously fueled pebble-bed reactor (PBR) was upgraded to calculate fuel temperature distributions under various fueling conditions.

## 6.2 HIGH-TEMPERATURE REACTOR METHODS DEVELOPMENT

### 6.2.1 Thermohydraulic Model — D. R. Vondy

The development of thermal-hydraulic methods for the prismatic HTGR continued this past year, with emphasis on enhancing compatability with our 3-D neutronics code system, the accounting and calculation of meaningful temperature averages and distributions, and the treatment of coolant orificing. We now make routine use of the code in our analysis, and formal documentation for application is in progress.

The local high-temperature reactor (HTR) thermal-hydraulic capability was extended to permit results by use of power density data for 1-D, 2-D, and 3-D neutronics problems. The 1-D coolant flow treatment in a 3-D core may be used to model an $x,z$ problem given $x$ neutronics data or a $tri,z$ problem given $tri$ neutronics data for a plane traversing the hexagonal assemblies. The third axial coordinate is added by specifying the number of mesh points and an axial power density distribution function. Also, $r,z$ geometry is treated directly with certain limitations, and of course the coding was primarily to treat 3-D problems directly.

An option in our modeling is that the coolant flow can be controlled with orifices to satisfy some objective function. Defining the coolant outlet temperature as the average of the temperatures of the coolant exiting channels associated with each orifice, the outlet temperatures might be made equal, recognizing that this should be a practical mode of operation. In preparing the documentation, care was taken to explain that this solution is highly idealized. Considering that measurements are necessary and are certainly subject to interpretation as well as failure, this ideal state cannot be achieved in practice because of imperfect association of orifice, coolant flow, and temperature. However, this condition is desired as a solution for a basic analysis. The procedures were added to produce a second solution routinely as a perturbation from the reference so that additional information is always generated. This second solution is obtained with a lower limit placed on the orifice resistances, generating information of a practical nature. This condition is also desired as a solution for a basic analysis.

### 6.2.2. Neutronics Models — D. R. Vondy

We continue to upgrade our basic analysis system, including the neutronics code VENTURE (ref. 1). Special procedures are sometimes necessary to treat large thermal reactors, and within our HTGR analysis effort we have made improvements in our basic capability.

The VENTURE neutronics code allows treatment of the equilibrium $^{135}Xe$. In the neutron balance equations, this code allows a nonlinear loss term that depends on the local fission rate and the $^{135}Xe$ decay, chain yield

fraction, and microscopic cross sections. Treating equilibrium $^{135}Xe$ is useful to prevent a false spatial oscillation of the flux when the history of a large core is treated in discrete exposure time steps.

A difficulty was identified in estimating the optimum overrelaxation coefficients. The spectral radius of the space problem at each energy is estimated with iteration without acceleration on the nonsource problem by use of an $\ell_1$ norm. A simple extrapolation scheme has been in use to attempt to extract an error contribution from this estimate. Examination of the results for a number of HTR problems showed that this extrapolation procedure frequently failed. With the overrelaxation coefficient seriously underestimated, the solution process is often very slow. A new procedure was tested and adopted, which extracts two eigenvalue contributions from the estimate of the dominant one.[2] An example of the results for a many-meshpoint problem is shown in Table 6.1. Here the eigenvalue is the square of the spectral radius. Extracting a value becomes more difficult as the eigenvalue approaches unity. Note that the extracted data shown tend to an asymptotic value, as does the related overrelaxation coefficient. The final value (1.787) was judged to be acceptable for use in this case, sufficiently close to the optimum. The extracted value after 20 iterations is more accurate than the reference estimate after 60 iterations.

Table 6.1. Example of the results for a many-meshpoint problem

| Iteration | Norm estimate | | Extracted estimate | |
|---|---|---|---|---|
| | Eigenvalue | Over-relaxation coefficient | Largest of a pair of eigenvalues | Over-relaxation coefficient |
| 20 | 0.9567 | 1.656 | 0.9811 | 1.758 |
| 40 | 0.9702 | 1.706 | 0.9846 | 1.779 |
| 60 | 0.9788 | 1.746 | 0.9859 | 1.787 |

In modeling the HTGR, good results were obtained with a 3-D model consisting of an axial traverse and pieces of four fuel blocks representing four ages associated with 1/4 core refueling. This model reduced calculations to problems that were solved at an acceptable cost compared with the prohibitively expensive full-core representations, yet use of the model gave useful information about fissile loading, burnable poison, control rod positioning, power density, and fuel temperatures.

## 6.3 HIGH-TEMPERATURE GAS-COOLED REACTOR ANALYSIS

### 6.3.1 Depletion Perturbation Analysis — B. A. Worley and J. O. Johnson

This work follows last year's successful demonstration of the applicability of depletion-perturbation theory (DPT) to HTGR analysis. The emphasis this past year was on extending the applicability to understand the potential of DPT better. A modest effort was undertaken to calculate response in time to changes in beginning-of-cycle (BOC) nuclide densities for the 1250-MW(t) modular reactor design under study in the United States.[3]

Calculations have been completed for the BOC and end-of-cycle (EOC) $k_{eff}$ (effective reactivity) response to changes in BOC nuclide densities. Furthermore, BOC and EOC zone power fraction sensitivites to changes in BOC number densities were calculated for the 4-2-2 zoning scheme of a 1-D benchmark problem. An investigation has been initiated to determine the proper equilibrium xenon treatment for depletion-perturbation analysis.

The results presented in Table 6.2 depict the change in $k_{eff}$ ($\Delta R$) for a positive 1% change in the BOC number densities. Thus, an increase in the bottom fuel zone $^{232}Th$ BOC number density of 1% will result in a 0.0026 decrease in the BOC $k_{eff}$ and a 0.0013 decrease in the EOC $k_{eff}$. Note that the system appears to be undermoderated at BOC because of the positive $k_{eff}$ response obtained by increasing the carbon number density in the fuel regions. Also, changes in the carbon number density in the reflectors have a small effect on $k_{eff}$. The $^{232}Th$ and $^{238}U$ responses shift from negative to positive in proceeding from BOC to EOC in the top and middle fuel regions because of the shift in the power distribution for the 4-2-2

Table 6.2. Energy-integrated change in $k_{eff}$ for a positive 1% change in the beginning-of-cycle number densities

| | Change in $k_{eff}$ | |
|---|---|---|
| | Beginning of cycle | End of cycle |
| | *Top reflector* | |
| $^{12}C$ | 2.07337 E-06 | 5.79986 E-06 |
| | *Top fuel zone* | |
| $^{12}C$ | 7.44008 E-05 | -3.33367 E-05 |
| $^{232}Th$ | -1.31901 E-04 | 4.54854 E-05 |
| $^{238}U$ | -1.10975 E-06 | 1.95148 E-07 |
| $^{10}B$ | -5.71190 E-05 | 6.82528 E-05 |
| | *Middle fuel zone* | |
| $^{12}C$ | 3.82517 E-04 | -2.11274 E-04 |
| $^{232}Th$ | -6.15682 E-04 | 3.72184 E-04 |
| $^{238}U$ | -7.32630 E-06 | 2.88723 E-06 |
| $^{10}B$ | -2.39625 E-04 | 2.17332 E-04 |
| | *Bottom fuel zone* | |
| $^{12}C$ | 1.81472 E-03 | 1.25406 E-03 |
| $^{232}Th$ | -2.59708 E-03 | -1.27624 E-03 |
| $^{238}U$ | -5.10583 E-05 | -3.67246 E-05 |
| $^{10}B$ | -1.03214 E-03 | -2.19863 E-04 |
| | *Bottom reflector* | |
| $^{12}C$ | 3.23881 E-05 | 6.63457 E-05 |

loading scheme. Note that in the bottom zone where $^{238}U$ is heavily loaded, the $^{238}U$ and $^{232}Th$ responses decrease and remain negative. The small positive $^{10}B$ response for EOC $k_{eff}$ in the top and middle fuel zones is a result of the small power shifts caused by the $^{10}B$-graded loadings.

6.3.2 Continuously Fueled Reactor Analysis — B. A. Worley, D. R. Vondy, and M. A. Savage*

The thermal-hydraulic modeling of the continuously fueled PBR was upgraded in the treatment of coolant flow under normal operating conditions. The local code PEBBLE (ref. 4) was enhanced to calculate conditions for which peak fuel temperatures occur. Pebble surface temperatures are now recalculated to adjust for local power peaking and for pebble recycles through the core. Local coolant mass flow is also adjusted to model local power peaking in 1-D axial models.

Additional information on fuel temperatures within the core was added through an accounting of the cumulative fraction of the core above reference temperatures at 25°C intervals between the maximum and minimum fuel temperatures. We feel that this addition is a valuable aid for the analyst in understanding complicated numerical modeling. An example is the distribution of fuel versus temperature for two simple situations, coolant upflow and coolant downflow. Figure 6.1 is a plot of the cumulative fraction of the fuel above several reference temperatures. For example, about 28% of the fuel is above 700°C with coolant downflow. Only 2 or 3% of the fuel is hotter with upflow. We conclude that a much more complete picture of core performance is now available.

This work on the continuously fueled core, for which we had already developed a local thermal-hydraulic code, was a valuable testing and modeling aid for our HTGR prismatic-core thermal-hydraulic development.

Heat removal by radial conduction and convection is also a concern in the analysis of accident conditions involving little or no coolant flow. Under separate funding, a 1-D finite difference heat transfer code is being written to calculate fuel temperature distributions in pebble-bed or prismatic-fueled HTGRs under conditions of loss of coolant and loss of pressure. Of particular interest is the incorporation of the dependence of the thermal conductivity of graphite on temperature and neutron fluence. A 1-D steady-state code has been written, which has the capabilities of using temperature-dependent thermal conductivities and heat generation

*Pennsylvania State University, University Park.

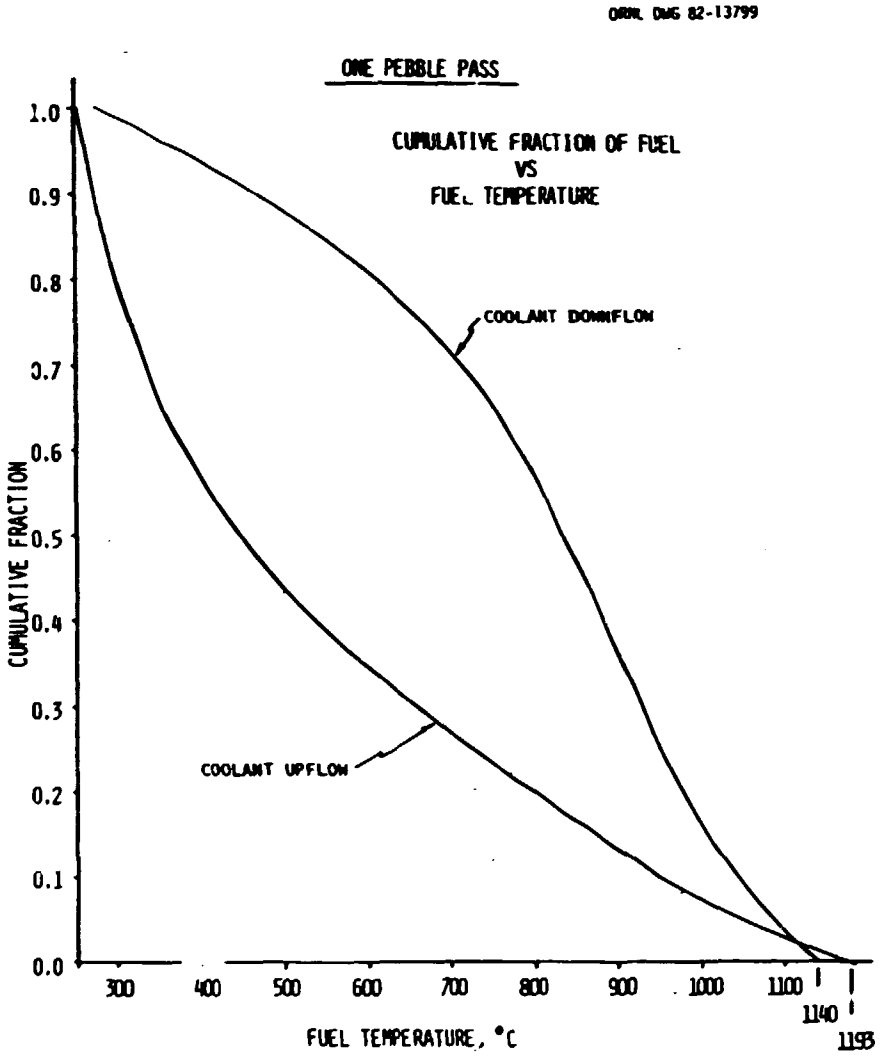


Fig. 6.1. Cumulative fraction of fuel above reference temperatures versus temperature.

rates and of treating a multiregion problem in either rectangular or cylindrical geometries with convective and/or radioactive boundary conditions. The code has been tested fairly extensively against the HEATING6 computer code with very favorable results (<0.4% difference). Features to be incorporated into the code include the consideration of radiation as well as conduction effects within the core for the pebble bed, the temperature and fluence dependence of the graphite thermal conductivity, and the capability of solving transient as well as steady-state problems.

## 6.4 REFERENCES

1. D. R. Vondy, T. B. Fowler, and G. W. Cunningham III, *The Bold Venture Computation System for Nuclear Reactor Core Analysis, Version III*, ORNL-5711, June 1981.

2. D. R. Vondy, "A Double Error Mode Extraction Procedure," *Nucl. Sci. Eng.* 80, 198–201 (1982).

3. General Electric Company, *HTGR Modular Reactor System (MRS) Design Status Reports*, Advance Reactor Systems Department, Sunnyvale, Calif., October 1982.

4. D. R. Vondy, *PEBBLE: A Two-Dimensional Steady-State Pebble-Bed Reactor Thermal Hydraulics Code*, ORNL-5698, September 1981.

# 7. HIGH-TEMPERATURE REACTOR SHIELDING STUDIES (WBS OR1417)

C. O. Slater and D. T. Ingersoll

## 7.1 INTRODUCTION

The High-Temperature Gas-Cooled Reactor (HTGR) shielding work continued the 1981 efforts to design a two-phase experiment to examine neutron streaming in the HTGR lower regions. As with previous experiments performed under other programs, the need for this experiment was confirmed on the basis of detailed design analysis, and the experimental design was evolved by use of the design results. The following sections review the design results and show how they were incorporated into the experimental design.

## 7.2 THE HTGR BOTTOM REFLECTOR AND SUPPORT BLOCK NEUTRON STREAMING EXPERIMENT

From the inception of the program, the two major objectives of the HTGR bottom reflector and support block neutron streaming experiment were to determine (1) both the shielding effectiveness of the boron pins and a near optimum number per block and (2) the extent of neutron streaming in the large coolant holes in the bottom reflectors and support blocks. Because of the size and complexity of the configurations and funding limitations, the experiment was split into two segments. These naturally fell along the lines of the experimental objectives. Thus, we have the boron pin effects experiment to be performed in fiscal year 1983 and the neutron streaming experiment to be performed in fiscal year 1984. The pre-analysis and design of these experiments are discussed in later sections.

### 7.2.1. Final Experimental Design

The final experimental design for the full configuration is shown in Fig. 7.1. Following a mockup of the Tower Shielding Facility Reactor and

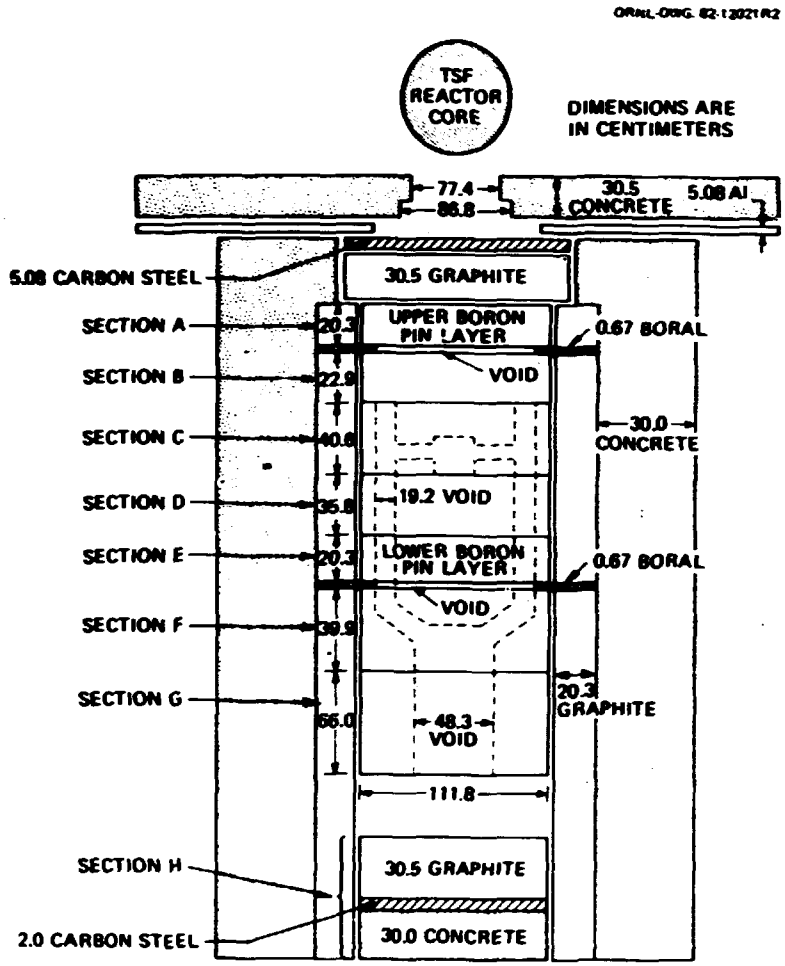


Fig. 7.1. Plan view of the full configuration for the High-Temperature Gas-Cooled Reactor bottom reflector and support neutron streaming experiment.

its concrete collimators is a spectrum modifier made up of 5.08 cm of carbon steel followed by 30.5 cm of graphite. The spectrum modifier will be discussed further in Sect. 7.2.4.3. Following the spectrum modifier are seven test sections (sections A–G), which represent various portions of HTGR lower support structure. Section A is the upper boron pin layer. Each of the simulated seven reflector blocks may contain up to 216 boron pins, which are inserted among an array of small coolant holes. Section B continues the small coolant holes of section A up to the point at which the large coolant holes begin in the outer reflector blocks in section C. Section C also contains small coolant holes in the center column. These small holes funnel into the 16.8-cm-diam center hole, which in turn funnels

into the six 19.2-cm-diam outer coolant holes through six 7.62-cm-diam coolant holes. Section D contains only the six 19.2-cm-diam outer coolant holes. The lower boron pin layer is section E. As with section A, section E is followed by a 0.67-cm-thick boral slab to prevent thermal neutrons from circumventing the boron pin layer by transversing a region outside the seven-reflector-block pattern. Sections F and G are mockups of the support blocks, with section F being the transition portion where the large coolant holes in the outer six reflectors merge into the single large coolant hole in the support block. Section H was included to provide neutron reflection to section G in the approximate proportion that the support posts, bottom liner, and prestressed concrete reactor vessel (PCRV) provide neutron reflection in the HTGR design. A prototypic mockup of the support post region was impractical because the large voids among the support posts meant significant coupling among the seven-column regions within the reactor. This would have required a much larger mockup than the reactor source, funds, or available materials would allow. Even a proposed experiment to measure the neutron streaming effects among the support posts alone was found to be impractical because it taxed available resources and because a system to suspend the posts in front of the Tower Shielding Reactor was not readily apparent. The other sections of the experimental configuration (sections A–G), however, appear to represent the corresponding HTGR lower support structure adequately.

### 7.2.2. Fabrication

After the conceptual design for the experiment was formulated, the next task was to consider fabrication and its costs. The more nearly ideal arrangement of a seven-column pattern fabricated within large graphite blocks (2.4- × 2.4-m cross section) was rejected as being too costly because of the large amount of graphite required and the machining necessary to square the graphite blocks. Instead, efforts were centered on the fabrication of the experimental configuration test sections within 112- by 112-cm graphite blocks (made up of four 55.9- × 55.9-cm blocks) and the use of material on hand for the spectrum modifier, the core support post-PCRV mockup, and the reflector surrounding the test sections.

A contract was negotiated with GA Technologies, Inc., to provide the fabrication drawings and to fabricate the components because it had experience in such fabrication. It was also the only one that would fabricate the boron pins needed in the experiment. Others were hesitant because of the possible contamination of their graphite works by small amounts of boron. With a tight fabrication schedule, we were able to get all components fabricated and delivered by the end of the first quarter of fiscal year 1983.

### 7.2.3. Measurements

The experimental configuration of Fig. 7.1 was separated into sections, not only for ease of fabrication but for provision that measurements could be taken behind each section. In some cases, measurements will be made within the large coolant holes. With such measurements, we expect to determine where the calculations and measurements begin to disagree. Primarily, measurements will be made with the bare cadmium-covered and 5-in. Bonner balls at specified distances behind and/or within a configuration. At selected locations, differential flux measurements will be made with the NE213 and the hydrogen counter spectrometers and with the 3-, 6-, and 10-in. Bonner balls. Count rates at these locations serve as checks on the spectrometer results. Details of the measurement program have been given in Appendix B of an internal document.[1]

### 7.2.4 Preanalysis

The preanalysis of the experiment actually began with the analysis of the HTGR design, because the results from that analysis were used in the design of the experiment. Thus, results of the design analysis are reviewed in this report before presentation of results from the preanalysis of the experimental configurations. Detailed results from the design analysis have been published.[2,3]

#### 7.2.4.1. Neutron Streaming Factors for the HTGR Reference Design

Calculations for the HTGR reference design showed very large streaming-correction factors for the lower support structure for all

energy ranges. The streaming of fast and intermediate energy neutrons had a great influence on the thermal neutron flux at the bottom of the support block, because the boron pin layers were very effective in lowering the emergent thermal neutron flux level with respect to the incident thermal neutron flux. Fast- and intermediate-energy neutrons provided a secondary source of thermal neutrons through thermalization in the graphite between the two boron pin layers and in the support block below the bottom boron pin layer.

The streaming calculations were performed with the two-dimensional discrete ordinates transport code DOT (ref. 4) and the Monte Carlo code MORSE (ref. 5). The approximate streaming factors for the bottom reflectors and support block are summarized in Table 7.1, and the streaming factors for the support post region for radiation levels at the sidewall are shown in Table 7.2. The streaming-correction factors were obtained by ratioing MORSE results to results from a DOT calculation in which the source was corrected for bottom reflector and support block neutron

Table 7.1. High-Temperature Gas Cooled Reactor bottom reflector and support block neutron streaming factors

| Energy range | Average factor (DOT) | Average factor (MORSE) |
|---|---|---|
| Fast ($E$ > 0.1 MeV) | 150 | 2000 |
| Intermediate (3.05 eV < $E$ < 0.1 MeV) | 480 | 7000 |
| Thermal ($E$ < 3.05 eV) | 125 | 1610 |

Table 7.2. High-Temperature Gas Cooled Reactor support post streaming-correction factors for neutron fluxes at the sidewall

| Energy range | Factor |
|---|---|
| Epithermal ($E$ > 3.05 eV) | 5.0 |
| Thermal ($E$ < 3.05 eV) | 2.5 |

streaming, but the geometry included a homogeneous mockup of the support posts. Epithermal neutron streaming factors at the bottom of the support post region were from 20 to 100% higher than were those at the side of the support post region. The thermal neutron factors were about the same at the side and bottom, being slightly higher at the side.

#### 7.2.4.2 Neutron Fluence at the Lower Sidewall Class B Thermal Barrier Cover Plate

An initial design survey calculation was made on a homogeneous mockup of the HTGR lower and side regions. From this calculation we obtained a maximum value of $10^{16}/cm^2$ for the thermal neutron fluence to the sidewall thermal barrier cover plate, this value being found at the core level. The thermal neutron fluence to the sidewall cover plate beneath the core support block level was about $6 \times 10^{14}/cm^2$. Subsequent calculations in which the streaming factors of Sect. 7.2.4.1 were applied led to a maximum thermal neutron fluence of $1.05 \times 10^{18}/cm^2$ at the sidewall thermal barrier cover plate (beneath the core support block level), this value exceeding the design constraint by a factor of 10.5. Thus, the overall streaming-correcting factor at the sidewall for thermal neutrons was about 1750. Certainly, there is a margin for error in this value. Even if it were smaller by a factor of 10, the shield design would still have problems. The value of the experiment was made evident on the basis of the need to get a firm handle on the thermal neutron streaming factors.

#### 7.2.4.3. Spectrum Modifier for the Tower Shielding Facility

For the results of the experiment to be relevant to the design, certain similarities should exist between the design and the experimental mockup. Along with the physical similarity, the similarity of spectra is a most important consideration. Consequently, significant effort was devoted to finding a suitable spectrum modifier that would alter the incident Tower Shielding Reactor neutron source spectrum and give an emergent neutron spectrum very similar to that leaving the bottom of the HTGR core. Rather than the spectrum modifier of 5.1 cm of carbon steel followed by 20.3 cm of graphite, which was reported in the 1981 annual progress report,[6] the final design is one consisting of 5.1 cm of carbon steel followed by 30.5 cm of graphite. The improvement in the agreement

between e design and experimental spectra can be seen by comparing the new results in Fig. 7.2 with the old results in Fig. 7.3. Although the old results showed better structural agreement in the epithermal neutron range, the spectrum was very deficient in thermal neutrons. The new results improve the thermal neutron fraction of the spectrum and give a nearly flat flux distribution in the epithermal energy range below 900 keV.

#### 7.2.4.4 Poisoning Requirements for Reflector Surrounding Boron Pin Layers

One of the problems with the limited mockup of the HTGR lower regions was the possibility of a significant number of thermal neutrons being able to go around the boron pin layers, scatter back into the test sections beyond the pin layers, and make substantial contributions to radiation levels below the support block. This contrasts with the HTGR design, in which neutrons must pass through the boron pin layers of the seven-column region in which it originates or through those of one of the surrounding seven-column regions before reaching the bottom of the support block. The chances that the thermal neutron originating above the top boron pin layer will reach the bottom of the boron pin layer are much less if it has to traverse the two boron pin layers than if it could circumvent one or both of the layers. Hence, ways were sought in which to poison the graphite reflector regions surrounding the boron pin layers to prevent these problems.

The obvious solution to these problems was to extend the boron pin pattern considerably beyond the seven-column mockup of the design. However, this solution was rejected because of much greater costs and the time involved in fabricating and installing the large number of boron pins. The second choice was to cover a large region surrounding the seven-column pattern with a slab of poisonous material like boral to prevent thermal neutrons from circumventing the boron pin layers. Several thicknesses and arrangements of boral slabs were tried and examined for their effects on radial and axial Bonner ball count rate traverses and indirectly on the radial and axial neutron flux profiles. The final arrangement is that shown in Fig. 7.1, where 152- by 152-cm, 0.67-cm-thick boral slabs with the seven-column pattern cut from the center are placed at the end of

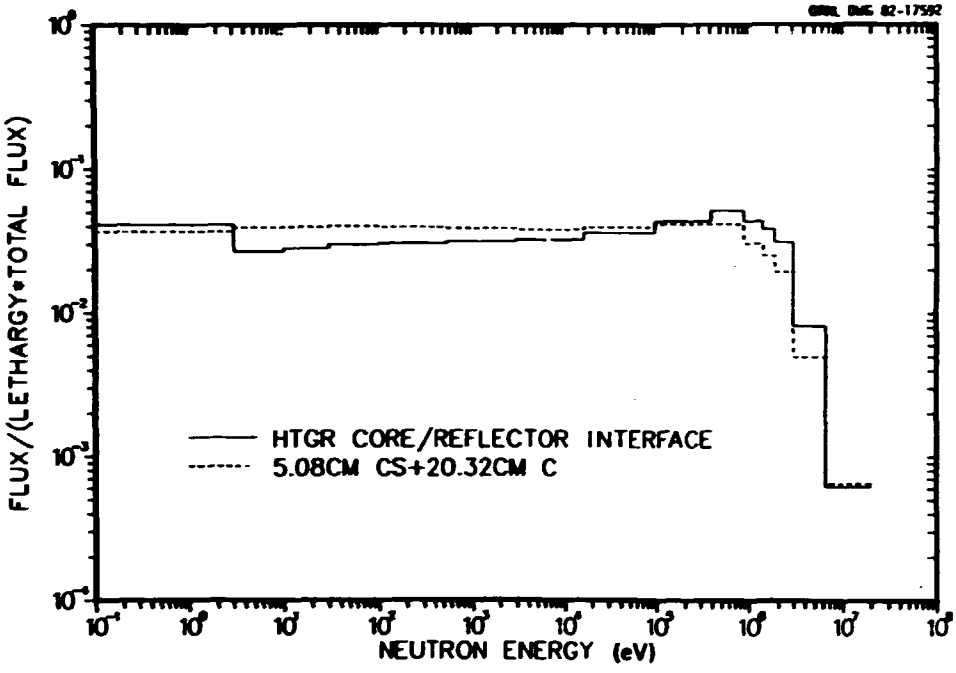


Fig. 7.2. Comparison of the neutron spectrum at the High-Temperature Gas-Cooled Reactor core-bottom reflector interface with a Tower Shielding Reactor modified spectrum through 5.08 cm of steel plus 20.3 cm of graphite in a spectrum modifier consisting of 5.08 cm of steel and 30.5 cm of graphite.

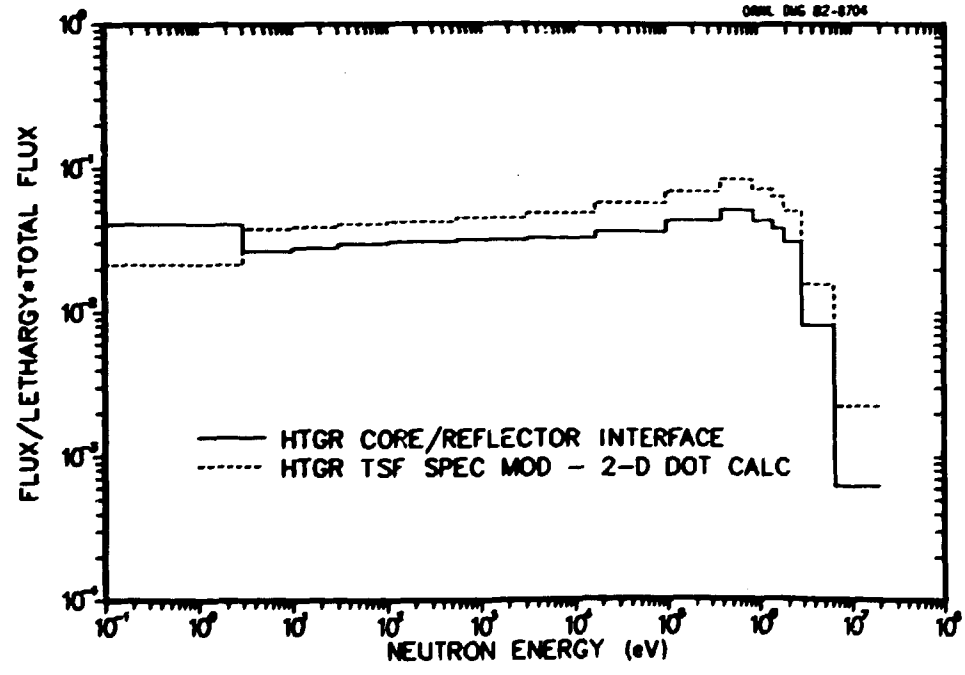


Fig. 7.3. Comparison of the neutron spectrum at the High-Temperature Gas-Cooled Reactor core-bottom reflector interface with a Tower Shielding Reactor modified spectrum for a spectrum modifier consisting of 5.08 cm of carbon steel and 30.5 cm of graphite.

each boron pin layer. This arrangement greatly improved the results over those from earlier arrangements, which contained thicker boral slabs at each end of each boron pin layer but which covered only the 112- by 112-cm test section and not the graphite side reflector. Calculated radial traverse curves all show outward gradients and consequently no net gain of neutrons from the side reflector region.

7.2.4.5. Peripheral Reflector Requirements

Inherent in the limited mockup of the HTGR lower core support structure was the loss of the nearly flat radial traverses across a given region. The reactor design contains a semi-infinite array of regions so that there is little loss or gain of neutrons between regions. With the experimental mockup, there are no identical regions surrounding the mockup, and the source drops off considerably beyond the seven-column region. Therefore, one can expect significant leakage from the region. To conserve neutrons, it was proposed that the test sections be surrounded with additional layers of graphite for neutron reflection and of concrete for additional reflection and shielding. The peripheral reflectors were to be constructed from the 10.2- by 10.2-cm by 122-cm-long graphite posts available at the Tower Shielding Facility. Therefore, reflector thicknesses studied were multiples of 10.2 cm. One, two, and three layers of posts were studied. Figure 7.4 shows a two-dimensional model of a mockup containing the first boron pin section and the small coolant hole section. Shown also are parameters $a$, $b$, and $c$, which are varied to give the five cases indicated. Three boral thicknesses $a$ and graphite reflector thicknesses $b$ were considered. The concrete thickness $c$ was fixed after the initial choice of graphite and concrete thicknesses (cases A, B, and C) by increasing its thickness by the amount that the graphite thickness $b$ was decreased (cases C and D). The boral slabs are shown at both ends of the boron pin section and extend only to the outer boundaries of the test sections.

For the calculational model shown in Fig. 7.4, Fig. 7.5 shows a comparison of radial traverses for the bare Bonner ball detector at the end of the small coolant hole section for the design and the five exprimental cases. The bare Bonner ball measures mostly thermal neutrons. Of interest

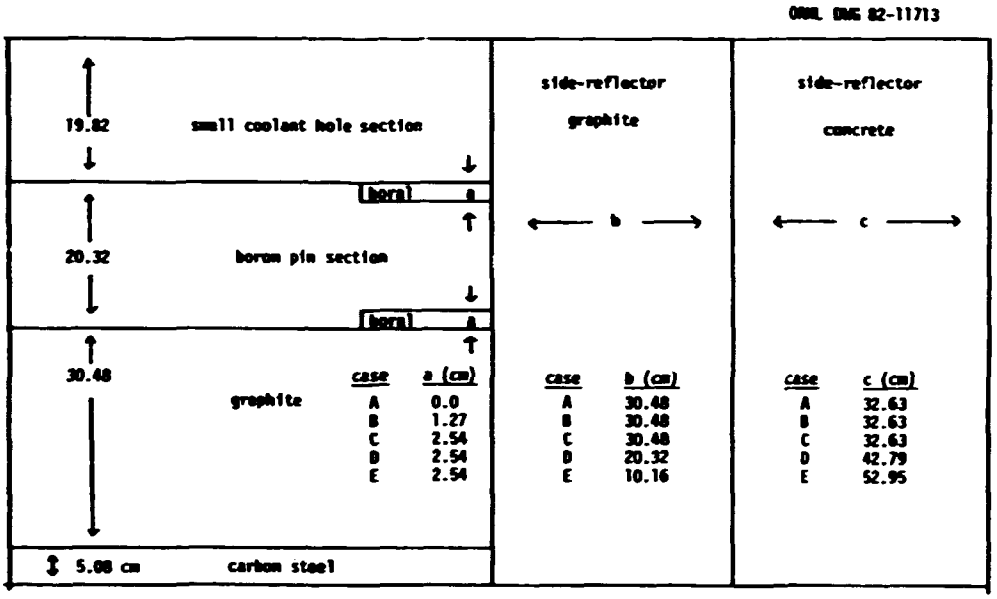


Fig. 7.4. Parametric two-dimensional R-Z model for the High-Temperature Gas-Cooled Reactor shielding experiment configuration containing the boron pin and small coolant hole sections. The parameters are $a$, the boral thickness; $b$, the graphite side reflector thickness; and $c$, the concrete side reflector thickness.

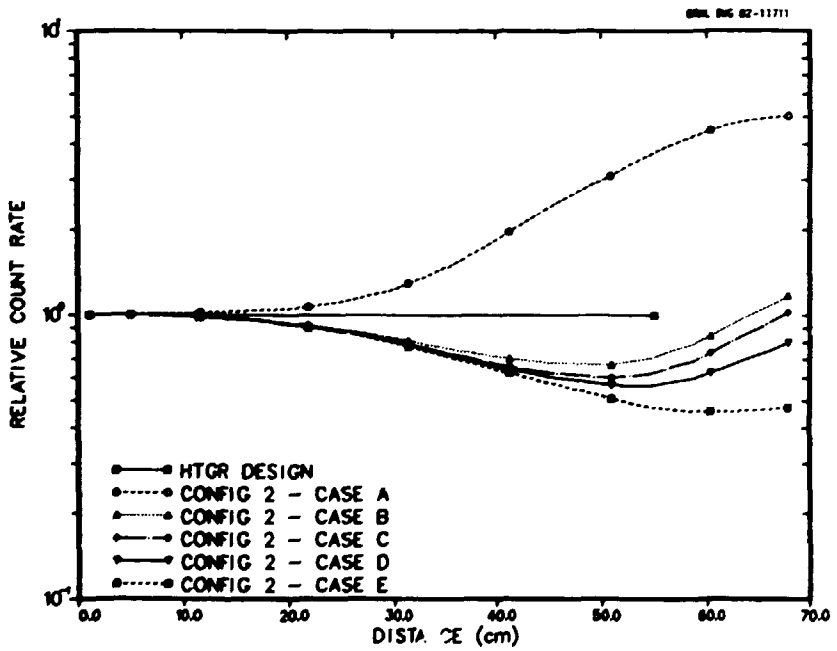


Fig. 7.5. Comparison of the bare Bonner ball radial distribution for the High-Temperature Gas-Cooled Reactor design and the proposed experiment. (The equivalent cylindrical radius of the seven-column cell is about 50 cm.)

for the peripheral reflector requirements are cases C, D, and E. As indicated, the equivalent cylindrical radius for the seven-column region is about 50 cm. The figure shows that the count rate of 50 cm compared with that on the centerline increases with increasing graphite thickness. Much thicker graphite reflectors could possibly have made the radial traverse nearly flat from 0 to 50 cm. However, the number of graphite posts available at the Tower Shielding Facility was limited. Thus, the 20.3-cm-thick peripheral reflector was chosen because the results obtained with it at the 50-cm radius were not much different from those obtained with the 30.5-cm reflector at 50 cm and because fewer graphite posts would be required.

From Fig. 7.5, one can also see the difficulties (Sect. 7.2.4.4) with the boral slab arrangement shown in Fig. 7.4. With no boral (case A), many thermal neutrons circumvent the boron pin section and would have a great influence on the thermal neutron flux levels in the test sections that follow the small coolant hole section. For the other cases (B, C, and D) with thick graphite reflectors, the boral maintains the outward thermal neutron leakage out to a point near the edge of the test section, but the leakage is inward beyond that point because the thermal neutrons circumvent the boron pin section by traversing the graphite side reflector. Extending the boral to cover the side reflector eliminates that problem, as stated above.

### 7.2.4.6. Comparison of Calculated Neutron Responses for the Experiment and the HTGR Reference Design

The degree to which the experiment successfully models the design depends on the success achieved in matching neutron responses for the experiment to those of the design. An integral part of the experiment preanalysis was the identification of changes in certain parameters, which would lead to neutron spectra similar to those of the design. The three parameters that could be controlled were (1) the spectrum modifier (Sect. 7.2.4.3), (2) the peripheral reflector poisoning (Sect. 7.2.4.4), and (3) the peripheral reflector thickness (Sect. 7.2.4.5). Certain of these parameters were fixed before detailed comparisons were made with the measured spectra.

Calculations were made on two-dimensional R-Z models of the experiment and design lower core support structure mockup by use of a 150-direction biased quadrature set. The quadrature set has 115 directions (many nearly straight ahead) away from the core or the Tower Shielding Reactor source. Calculations were made for three experimental designs. The geometry for the first calculation performed included 2.54-cm-thick boral slabs surrounding each of the boron pin sections as shown in Fig. 7.4 for the first boron pin section. The peripheral reflector thickness was 30.5 cm. This calculation is labeled HET3 in subsequent discussions. The second calculation was performed on the same model except that a single 0.64-cm-thick slab of boral was placed at the end of each boron pin section and that the boral slabs were extended outward to cover the peripheral reflectors. This calculation is labeled HET1. In the HET2 calculation, the HET1 geometry is modified to include the large coolant hole in the center reflector column in the model.

Calculated relative bare and 5-in. Bonner ball count rates along the axis of the geometry models are shown in Figs. 7.6 and 7.7, respectively. The design results have been normalized in Fig. 7.6 to the HET2 results at a common point below the upper boron pin section. The design results appear to undergo a much steeper depression in the thermal neutron flux (bare Bonner ball count rate mostly due to thermals) in the upper boron pin section than do the experimental results. Beyond that first boron pin section, the agreement between the experimental and design results appears to be good. The agreement is also good for the 5-in. Bonner ball count rate as shown in Fig. 7.7. The departure of the design and HET2 results from the HET1 and HET3 results at 75 cm results from the inclusion of the large coolant hole in the central column in the former two calculations and the absence of the hole in the latter two calculations. It is interesting that the HET2 results return to agreement with the HET1 and HET3 results following the second boron pin section. This is attributed to differences in the temperature used in processing the thermal neutron scattering cross sections used in the design calculation versus that used for processing cross sections used in the experimental calculations. The boron and graphite thermal neutron scattering cross sections for the design

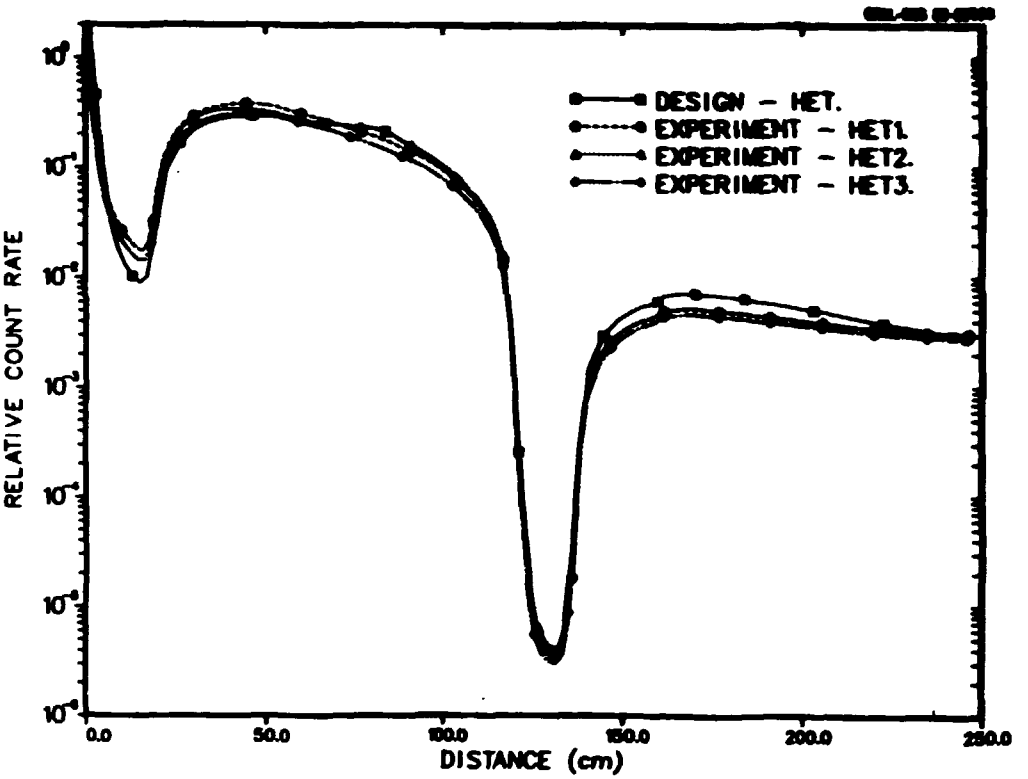


Fig. 7.6. Comparison of the relative bare Bonner ball count rate axial traverses for the High-Temperature Gas-Cooled Reactor design and three experimental configuration designs.

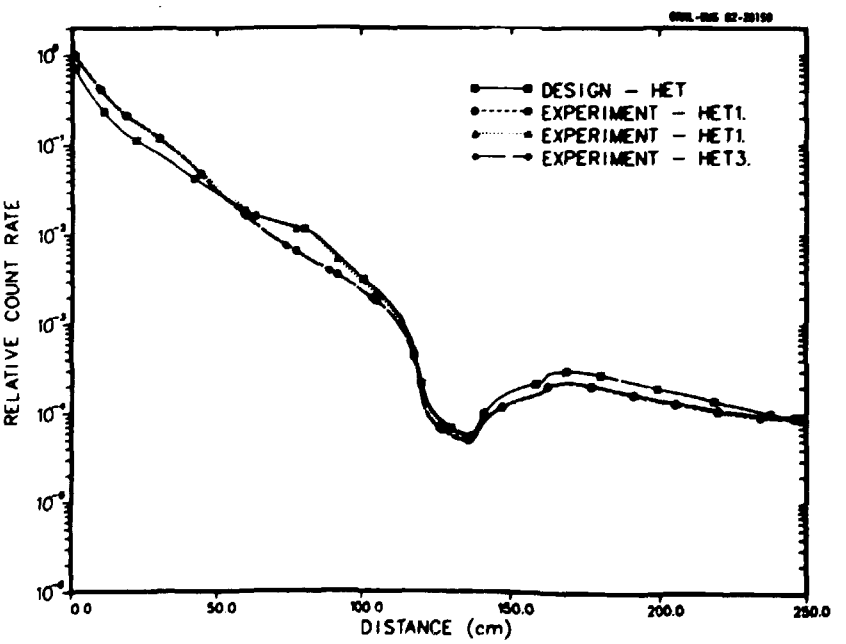


Fig. 7.7. Comparison of the relative 5-in. Bonner ball count rate axial traverses for the High-Temperature Gas-Cooled Reactor design and three experimental configuration designs.

were processed at 550 and 1200 K, respectively, whereas those for the core were processed at 293 K. The thermal neutron flux should recover at a higher level in the support block with the higher temperature graphite cross sections than with the room-temperature graphite. Because the thermal neutron flux becomes dominant in the support block region, it has a great influence on the 5-in. Bonner ball count rate. So, if the thermal neutron flux recovers to a higher level in the support block when the high-temperature-processed cross sections are used, the 5-in. Bonner ball count rate should also recover to a higher level when the same cross sections are used.

Relative bare Bonner ball count rates for radial traverses at the end or bottom of the support block are compared in Fig. 7.8. The design and experimental results all show a relatively flat response across the large 48.26-cm-diam (24.13-cm-radius) coolant hole and a drop-off behind the graphite block. The experimental results continue to drop because of the

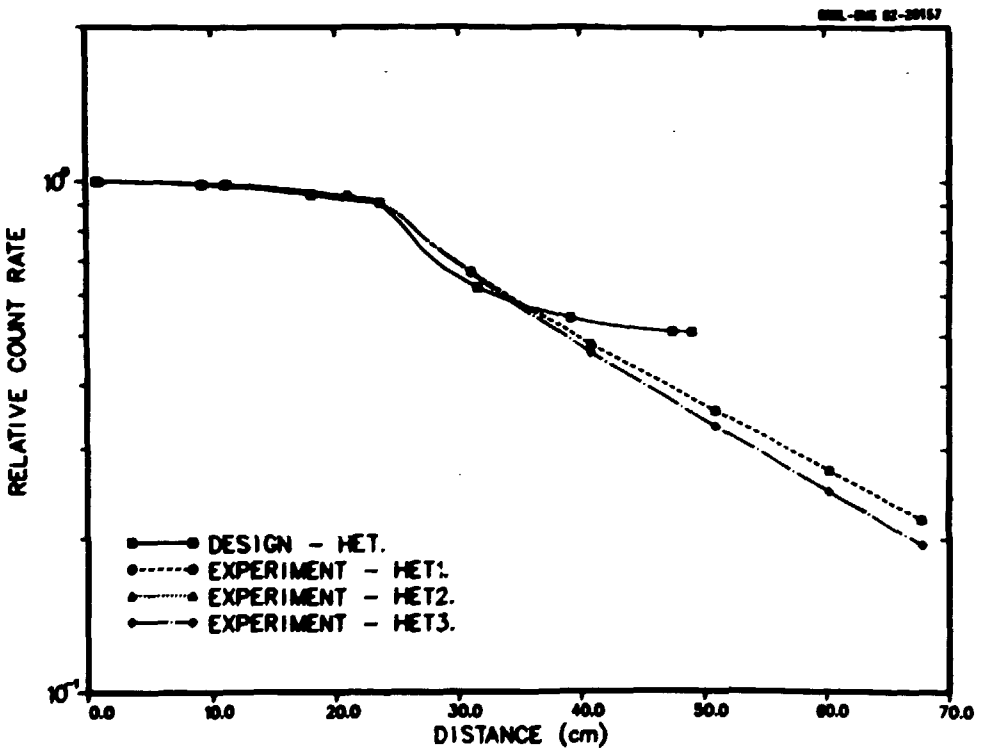


Fig. 7.8. Comparison of the relative bare Bonner ball count rate radial traverses behind the support block for the High-Temperature Gas-Cooled Reactor design and three experimental configuration designs.

finiteness of the configuration, but the design curve levels off at the cell boundary (50 cm) to about 45% of the value at the centerline. The design curve levels off because of the reflective boundary condition used in the calculation to simulate an infinite array of such cells. The radial distributions in Fig. 7.8 were averaged over the 50-cm radius of the cell, and we found that the average for the design calculation was about 5% higher than were the averages for the experimental calculations. For the 5- and 10-in. Bonner balls, the design results were about 10% higher. These small differences between the design and experimental results are not expected to contribute to significant differences in the calculated streaming-correction factors for the two because the homogeneous calculations should partially compensate for those differences.

With regard to streaming-correction factors for the experiment, Table 7.3 shows some results obtained for the HET3 experimental mockup compared with a homogeneous model of that mockup. Absolute Bonner ball count rates are compared, as are streaming correction factors, at the center of the cell and at the edge of the cell. Streaming-correction factors on the centerline vary from 125 to 204, but at the periphery of the cell they are constant at about 40 for all the Bonner ball count rates. The bare Bonner ball count rate is a strong indicator of the thermal flux behavior.

Table 7.3. Comparison of Bonner ball count rates at the end of the support block for homogenous and heterogeneous calculations of the High-Temperature Gas-Cooled Reactor bottom reflector and support block neutron streaming experiment

(HET3 heterogenous model used)

| Bonner ball | Count rate (counts/(min·W) | | | | | |
|---|---|---|---|---|---|---|
| | Centerline | | | Periphery | | |
| | Homogeneous | Heterogeneous | Heterogeneous: Homogeneous ratio | Homogeneous | Heterogeneous | Heterogeneous: Homogeneous ratio |
| Bare | 1.1850 E+1 | 1.4853 E+3 | 125.3 | 7.3152 | 2.8984 E+2 | 39.62 |
| 2-in. Cd-covered | 3.7181 E-1 | 4.8682 E+1 | 130.9 | 2.2919 E-1 | 9.0865 | 39.65 |
| 5-in. | 1.3265 | 2.330 E+2 | 175.9 | 8.0536 E-1 | 3.2025 E+1 | 39.76 |
| 10-in. | 1.4174 E-1 | 2.8885 E+1 | 203.8 | 8.4080 E-2 | 3.3397 | 39.72 |

Thus, one would expect a thermal neutron flux streaming-correction factor of 125 along the cell centerline. This is almost the same result as the average streaming-correction factor, which was calculated for thermal neutrons for the design by use of the two-dimensional geometry model. The influence of the epithermal neutrons is felt in the other Bonner ball count rates, where part of the thermal neutron influence is eliminated by the cadmium cover over the Bonner balls.

The comparisons of calculated responses for the experiment with those for the design showed that reasonable agreement between the distributions of the responses can be achieved and that similar streaming-correction factors can be expected. Close agreement between the two will certainly make the task of applying the experimental results to the design much easier.

## 7.3. SUMMARY

The HTGR bottom reflector and support block neutron streaming experiment configurations were designed, preanalyzed and modified, and fabricated and delivered. Because of funding limitations, the experiment was divided into (1) the boron pin effects experiment and (2) the neutron streaming experiment. The experiment was preanalyzed so that certain components could be modified to make calculated neutron spectra within the experimental mockup similar to calculated spectra for the design. This helps to ensure the relevance of the experimental results to the design shielding analysis. The preanalysis results indicated that we can expect to obtain neutron spectra and Bonner ball count rates from the experiment very similar to those calculated for the design. And since it is impractical to mock up the support post region at the Tower Shielding Facility, we must continue to rely on calculations for the streaming factors for the support post region.

## 7.4. REFERENCES

1. C. O. Slater and D. T. Ingersoll, "ORNL Response to General Atomic Company's Requirements for HTGR Lower Reflector and Core Support Neutron Streaming Experiment," unpublished data, Dec. 31, 1982.

2. C. O. Slater and S. N. Cramer, *Survey Analysis of Radiation Levels in the HTGR Lower Regions*, ORNL/TM-8141, February 1982.

3. C. O. Slater and S. N. Cramer, "High-Temperature Reactor Shielding Studies," pp. 259–68 in *High-Temperature Gas-Cooled Reactor Technology Development Program Annual Progress Report for Period Ending December 31, 1981*, ORNL-5871, June 1982.

4. W. A. Rhoades et al., *The DOT-IV Two-Dimensional Discrete Ordinates Transport Code with Space-Dependent Mesh and Quadrature*, ORNL/TM-6529, January 1979.

5. M. B. Emmett, *The MORSE Monte Carlo Radiation Transport Code System*, ORNL-4972, February 1975.

6. C. O. Slater and S. N. Cramer, "Bottom Reflector and Support Block Neutron Streaming Experiment," pp. 264–67 in *High-Temperature Gas-Cooled Reactor Technology Development Program Annual Progress Report for Period Ending December 31, 1981*, ORNL-5871, June 1982.

# 8. HIGH-TEMPERATURE REACTOR COMPONENT FLOW TEST LOOP STUDIES (WBS OR1417 and OR1428)

J. P. Sanders, A. G. Grindell, and W. P. Eatherly

## 8.1 INTRODUCTION — J. P. Sanders

The Component Flow Test Loop (CFTL) is a large high-pressure high-temperature test facility capable of circulating helium with controlled levels of impurity through primary system High-Temperature Gas-Cooled Reactor (HTGR) components. The loop can be used to obtain engineering studies and to verify performance of these components under steady-state or transient operating conditions that represent normal, upset, or emergency operation.

Outstanding features of the loop include three gas-bearing circulators with individual variable-frequency power supplies, vortex shedding flowmeters, a 5-MW power supply for heating the helium, and a data acquisition system (DAS) with an analogue-to-digital converter (ADC). The gas-bearing circulators permit operation without contamination from a lubricant, such as oil or water, on the shaft. The three 250-kVA power supplies for the circulators provide an output of 440 V at controlled frequencies from 0 to 400 Hz. Commercial vortex-shedding flowmeters were modified and calibrated to provide flow measurements in both 4- and 6-in. pipe with an accuracy of ±1% of full-scale reading over a flow range of 1 to 150.

Transformers at the site provide a total power of 6.75 MW at a secondary voltage of 440 V. The primary voltage of 13,800 V is supplied by a 40-MW substation at the perimeter of the building. Of this total capacity, one 1-MW transformer provides power for the three variable-frequency power supplies, a 0.75-MW unit provides all utility power for the loop, and two 2.5-MW units provide power to heat the circulating gas to the desired

temperature. At present, one 0.5-MW motor-driven induction regulator controls power to an installed helium heater. Two additional 0.5-MW regulators are in place but have not been connected with appropriate cable.

The DAS is a PDP-11/34 system with two disks, two tape drives, and an on-line printer-plotter. The RSX-11M operating system is capable of multitasking so that data can be stored and reduced concurrently. The 640 channels of the ADC can be interrogated in any order and at any frequency up to 10,000 data points per second under control of the computer.

### 8.1.1 Background

Construction of the CFTL was initiated in August 1977 under the Gas-Cooled Fast Reactor (GCFR) program. Financial support from that program was continued through September 1981. The total contribution from this funding for the actual construction was about $9.6 million. In June 1981 the facility was transferred to the national HTGR program, and about $825 thousand was made available through September 1982 to perform appropriate modifications to the facility.

Because of this shift in the planned application of the facility, significant modifications had to be made in the major characteristics of the loop. For example, the proposed test structure for the GCFR was a symmetrical segment of a core fuel or blanket assembly. These assemblies were to be electrically heated to simulate their thermal performance. The heat, added to the helium by the test structure, was to be removed in an air-cooled heat exchanger. For the HTGR application, the heat needed to bring the helium to the required temperature at the test structure must be added in a heater separate from the test unit.

The normal operating pressure for the HTGR of 7.2 MPa (1050 psia) can easily be accommodated by the design for a nominal GCFR operating pressure of 10.6 MPa (1540 psia). The required maximum temperature for HTGR testing of 1000°C (1830°F) can be included in the loop operation in the same manner as the maximum test temperatures of 600°C (1100°F) for the GCFR. These temperatures are confined to the interior volume of a test vessel, and the temperature of the pressure boundary is limited by an internal attemperation flow of helium at the circulator discharge temperature. This attemperation flow mixes with the hot gas before it exits the vessel.

The planned tests for the core assemblies for the GCFR required rapid and precisely controlled transients in both power and flow. Testing for the primary system components for the HTGR requires either steady-state testing or testing with relatively slow transients that can be controlled manually. As a consequence, some power control features have been temporarily bypassed, and another small PDP-11/03 computer that was to be used as a direct digital controller has neither been programmed nor installed in the loop.

### 8.1.2 Status

Funding provided by the GCFR program provided completion of the loop to a designated "Stage Alpha." This configuration closed the circulating loop by replacing the test vessel with a section of 4-in. pipe. It provided no connections to the DAS and no electrical heaters.

The construction for Stage Alpha was completed in September 1981, and all three circulators were operated at 17,000 rpm. Problems with the position indicators for the gas-bearing surfaces were alleviated, and operation of the three units at the design speed of 21,000 rpm was attained in December 1981.

At that time, all operation was suspended so that modifications could be made for the Core Support Performance Test (CSPT) series for the HTGR. These tests required fabrication and installation of a test vessel to contain the test structure and the helium heater and the procurement and installation of an impurity measurement system (IMS) and an impurity control system (ICS). The loop configuration with the test vessel installed is shown in Fig. 8.1.

By December 1982 the vessel had been fabricated and installed. This vessel used many components that had been ordered and received but not installed during the previous construction effort for the GCFR testing. The ICS had been designed and installed, and the IMS had been ordered but not received. To permit an orderly schedule for testing, an interim IMS with manually operated equipment was in place at this time.

In December 1982 after the loop had been closed, a TEST P-1 series was initiated to determine the loop characteristics without the installation of the test structure. This series initially determined the leak rates at varying pressure levels and the overall system volume.

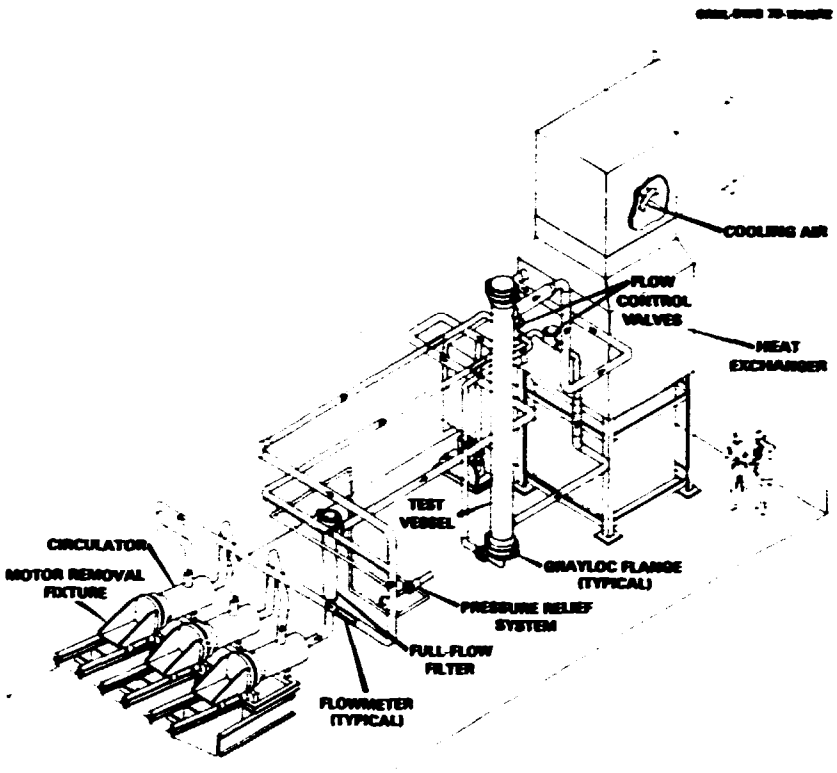


Fig. 8.1. Isometric of the Component Flow Test Loop modified for the Core Support Performance Test.

This TEST P-1 was inserted in the CSPT series after it was determined in small loop experiments that the material from which the loop was constructed could promote a reaction among the chemically active components in the helium at the initial composition, temperature, and pressure proposed for the experiment. TEST P-1 will subsequently determine the ability to maintain the required composition in loop, and this series of tests will determine whether or not the effect of the loop surface will be passivated with time. The series will also explore the kinetics and dynamics of the gas-phase reactions in the circulating stream.

After TEST P-1 is completed, a column of graphite pieces fabricated from off-the-shelf Stackpole 2020 graphite will be placed in the test vessel. This right circular test column will then be exposed to helium with controlled levels of impurities to establish the accelerated corrosion rate. This series of tes conditions has been designated as TEST ZERO.

Following these initial tests, the actual test of a simulated segment of the core support structure will begin. This subsequent test sequence has been designated as TEST ONE.

### 8.1.3 Core Support Performance Test Application

The initial application proposed for the CFTL was a test to determine the performance of the core support structure for an HTGR. The core support structure (Fig. 8.2) consists of a graphite slab supported by three graphite posts. At the contact point between the post and the slab is a graphite insert called the "post seat" (Fig. 8.3) and at the bottom of the post, a similar post and seat configuration.

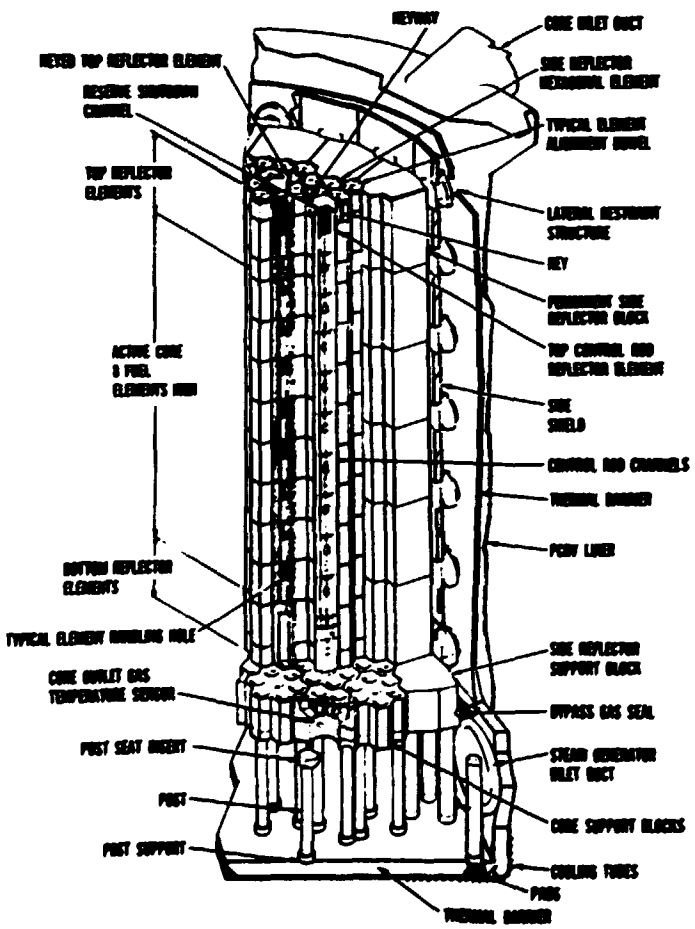


Fig. 8.2. High Temperature Gas-Cooled Reactor core and support structure. Drawing provided by the GA Technologies, Inc., and used with its permission.

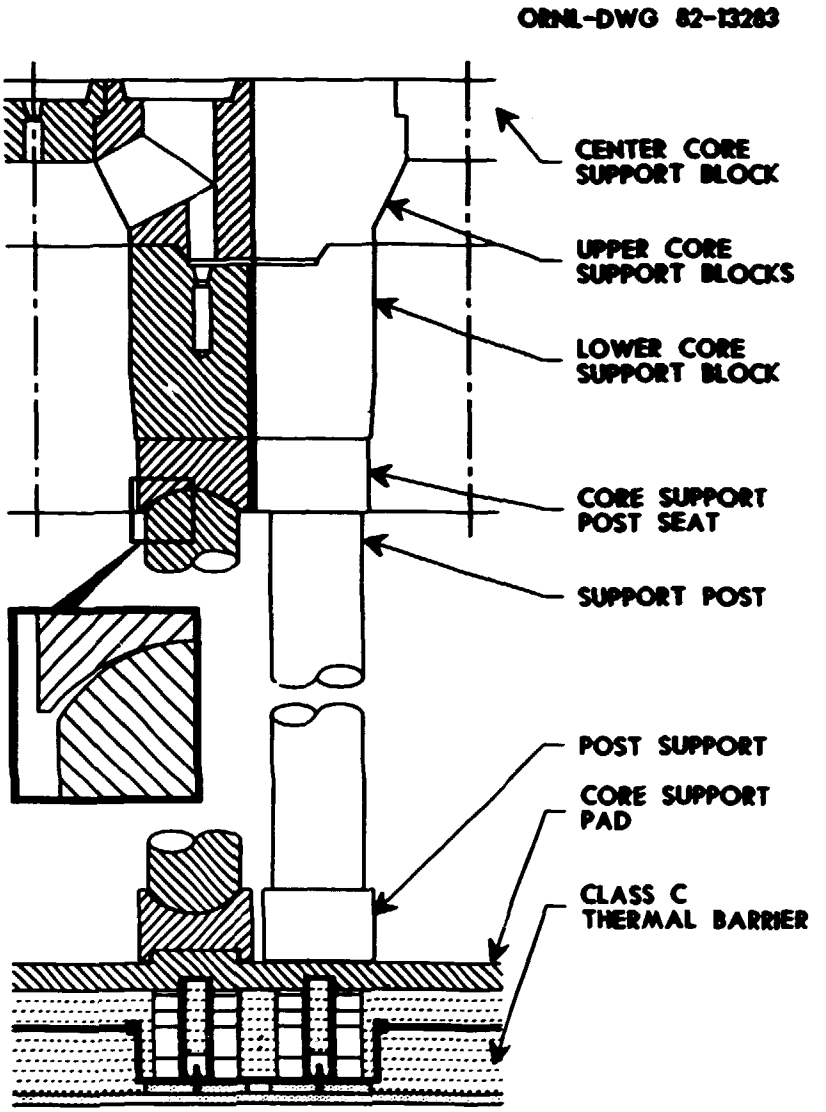


Fig. 8.3. Details of High-Temperature Gas-Cooled Reactor core support structure.

To permit relative movement at the junction of the post and the seat during a seismic event, both the end of the post and the dish of the seat have a spherical curvature. The radius of curvature of the post end is less than the radius of the seat so that, in effect, there is a point contact at this interface. In application, the graphite at this point will elastically and inelastically deform and generate an area of contact sufficient to sustain the load under a finite stress state believed to be below the fracture strength of the graphite. The concentration of stress in this area is usually denoted as Hertzian stress.

The geometry of the core support structure thus presents an area of stress concentration at the apex of a narrow slit between the spherical surfaces. The degradation in the strength of the graphite due to long-term corrosion could result in loss in the required structural performance characteristics. A seismic event could result in a shift in the area of stress concentration to either a degraded or deformed area and produce a failure of a post or its seat.

The importance of the reliability of the structure is emphasized by the fact that it is installed for the operating life of the core, which is assumed to be 40 actual years or 32 full-power years. Although the current design of the core support structure permits replacement of the components during the operating life of the core, this replacement can only be accomplished during an extended period of nonavailability of the reactor. In addition, failure of the core support structure during operation has implications concerning the safe operation of the reactor.

### 8.1.4 Other Applications of the Loop

In general, the CFTL can be used to evaluate the engineering performance of any of the major primary loop components of the HTGR plant. The test for some of these components falls more easily within the loop characteristics than it does for others. During the past year, the major effort was an evaluation of the loop as a test bed for the performance characteristics of the core auxiliary heat exchanger (CAHE). This unit is a component of the core auxiliary cooling system (CACS) and is therefore part of the safety system of the reactor. The performance of this unit must be determined under a variety of operating conditions.

The CFTL provides the flow of gas at the controlled composition, temperature, and pressure needed for the test. It has the power supply necessary to provide the required input of heat, and it has a DAS appropriate to the needs of the test. A circulating water system with an appropriate heat dump to remove the heat from the secondary side of the CAHE would have to be added.

The CFTL circulators, which are connected in series, will not now provide the required volumetric flow for the test of a 19-rod full-length CAHE bundle. It would be possible to provide approximately the required

flow if the piping at the circulators were modified to provide parallel flow from the three units. Preliminary cost estimates indicated that this piping revision would be expensive, however, and alternative methods of meeting the test requirements are being investigated.

Other primary system components that have been considered for evaluation in the CFTL include a section of the primary steam generator, a section of an intermediate heat exchanger for intermediate loop in an HTGR, a reformer, the thermal barrier, and the flow control devices at the inlet to each region.

## 8.2 CORE SUPPORT PERFORMANCE TEST REQUIREMENTS

The general attributes and the importance of testing the core support structure have already been outlined. The important attributes of this test are that the actual size and geometry of the post-seat interface will be represented and that a structural load will be applied to simulate the structural loading. Since the structure cannot be tested for its actual lifetime of 32 full-power years, we must simulate the amount and the nature of the corrosion in a shorter period of time. The ability to simulate this corrosion in the shorter test interval is vital to the validity of the testing.

### 8.2.1 Status of the Study — W. P. Eatherly

During 1987 the preliminary calculations of oxidation behavior and material compatibility in the loop, particularly in relationship to the actual reactor, were critically examined, and a number of preliminary experiments were performed. To summarize, the ability to perform meaningful experiments on the graphite support structure remains unquestioned, although the knowledge of the graphite oxidation behavior in any detail remains uncertain.

The initial tests in the CSPT series will establish the loop behavior and the anticipated graphite behavior in the loop. These tests, however, do not provide information on the pressure-dependent behavior of the oxidation of Stackpole 2020 graphite. This dependence must be obtained by laboratory-scale tests. A major objective of the continuing work is to

establish this data base, at least in outline form. To this end, experiments have been defined to be performed in the high-pressure loop HOVA at KFA, Jülich, or in the loop at GA Technologies, Inc. (GA). These experiments are specified to determine the pressure dependence of the oxidation of graphite. In addition, experiments at 100 kPa (1 atm) will be conducted at GA in its microbalance systems to determine the coefficients of the rate equations as they reflect the inhibiting effects of water vapor and hydrogen. The comparative oxidation rates of Stackpole 2020 graphite versus other grades will be determined at Oak Ridge National Laboratory (ORNL).

Although the results obtained in the past year leave open many details of the CSPT series, results of a definitive nature will be available before the first test simulating the post-seat geometry is initiated.

8.2.2 Basis for Selection of Accelerated Test Conditions — R. A. Strehlow

Accelerated graphite corrosion tests are based on the assumption that the rate of corrosion follows the kinetic expression

$$\text{Rate} = kP(H_2O)/[1 + k_1P(H_2) + k_2P(H_2O)] .$$

This relation indicates that at high-water or hydrogen partial pressures, the rate is not proportional to the partial pressure of water $P(H_2O)$; that is, there is an impedence by either hydrogen or water. Since the permeation or penetration of water into the pores of the graphite is proportional to the pressure of water vapor, it should be possible to select concentrations of both water vapor and hydrogen to duplicate at a markedly enhanced rate the degree of penetrating corrosion in a reactor environment.

Earlier calculations predicted the conditions to simulate a six-month test of the corrosion expected in a reactor environment in 32 full-power years.[1] Because of the need in the CSPT series to provide corrosion protection for the molybdenum heaters used in the CPTL, it was necessary to increase the ratio of hydrogen to water vapor to 10 from the value of 5 chosen earlier. This does not appear to affect either the expected degree of penetrating corrosion or the extent of corrosion significantly.

The assumptions still include the premise that there will not be a significant catalytic effect at the extrapolated temperature, which would mitigate the applicability of the rate expression. Other assumptions, including the question of applicability of the rate expression and the precision obtained with extrapolation, might affect the exact conditions chosen for the accelerated tests but not the conclusion that conditions for conducting an accelerated test can be chosen. The preliminary TEST ZERO will assist in determining more exactly the optimum conditions for subsequent tests.

8.2.3 Material Compatibility Studies — J. H. DeVan

Chemical interactions among materials selected for use in the CSPT are being examined for their possible effects on loop performance and on graphite reactivity. Those reactions stemming from impurities in the helium coolant are reviewed in Sect. 4.3.1, and reactions occurring at the interface of mating structural materials are reviewed below.

Aluminum oxide ($Al_2O_3$) is incorporated into the internal structure of the CSPT to support the high-temperature (HT)-molybdenum heating elements; it is also one of the possible barrier materials between the graphite test structure and the loading post. As described previously,[2] we have conducted compatibility tests to determine the extent of contact interactions between $Al_2O_3$ and relevant mating materials. Test specimens consisted of 6.4-mm-OD (1/4-in.) HT-molybdenum rods placed in tight-fitting 6.4-mm semicircular grooves in Coors (>99.9%) $Al_2O_3$ and in Stackpole 2020 graphite blocks. The block and rod assemblies were supported on a Coors $Al_2O_3$ plate. Duplicate assemblies of each material combination were placed in a vacuum furnace (pressure $<1.3 \times 10^{-4}$ Pa) and heated to 1370°C.

After 3000 h, both the $Al_2O_3$ and graphite had bonded to the molybdenum rods. The assemblies were cut normal to the axis of the rod, and the cut sections were examined metallographically. The reaction between the $Al_2O_3$ and HT-molybdenum was extremely superficial; there was no evidence of significant material transport into the $Al_2O_3$ or of oxide or aluminide phase formation in the molybdenum. In contrast, at the contact surface between the molybdenum and graphite, a continuous carbide phase had grown

into the molybdenum to a maximum depth of 2.4 mm (0.093 in.). An unexpected finding in this test was the decomposition of $Al_2O_3$ produced by contact with graphite. Depressions about 1.5 mm deep formed in the $Al_2O_3$ support plate directly under the graphite blocks. No bonding occurred between the graphite and $Al_2O_3$, and the weight loss of graphite was insignificant compared with the loss of $Al_2O_3$ associated with the depressions. The results of this test were assessed as follows:

1. No degradation of the HT-molybdenum heater elements should result from contact with $Al_2O_3$ insulators even at a maximum element temperature of 1370°C.
2. The rapid carburization of HT-molybdenum in contact with graphite at 1370°C indicates that data on the reaction of molybdenum with carbon-containing impurities in CSPT helium will be needed before an operating temperature of 1370°C for the heater element can be considered practicable.
3. The reaction between graphite and $Al_2O_3$ was sufficiently rapid at 1370°C to require further testing at the lower contact temperature (<1000°C) proposed for these materials in the CSPT.

The above test results led us to conduct a second series of compatibility tests involving $Al_2O_3$, graphite, and HT-molybdenum. The specimen assemblies, exposure times, and furnace atmosphere were identical with those of the first series, but the temperature was reduced to 1000°C. After 3000 h, the HT-molybdenum rods had again bonded to the underlying $Al_2O_3$ and graphite grooves. However, lowering the test temperature totally eliminated the reaction between the $Al_2O_3$ support plate and graphite blocks. The results of this latter test indicated that the use of $Al_2O_3$ to separate the graphite test specimen from the loading post will neither pose engineering difficulties nor otherwise affect the graphite oxidation measurements at a gas temperature up to 1000°C. The carburization of HT-molybdenum at 1000°C in contact with graphite is still being evaluated.

8.2.4 Specification of Graphite — W. P. Eatherly

The graphite selected for the core support posts and seats is Stackpole 2020, a choice dictated by its commercial availability in the

required size, fine texture, and high tensile strength. As produced commercially, this material is a special graphite targeted for metallurgical applications. For this use, purity is neither required nor controlled. Tests at ORNL also suggest that the graphitization temperature ranged from 2400 to 2500°C.

For nuclear applications, the relatively high impurity levels, low graphitization temperature, and resultant unnecessary variability in properties are undesirable characteristics. Meetings were held jointly by GA and ORNL with the vendor, and a special run of controlled manufacture was defined. This run involves the traceability of raw materials and processing steps, controlling raw material, and increasing the graphitization temperature to 2600°C, all aimed at higher purity and reduced variability.

Some difficulties were encountered by the vendor in fabricating this special lot of 2020 graphite, particularly in reaching or exceeding the desired minimum graphitization temperature. The difficulties now appear to have been surmounted, and delivery of the material is expected in February 1983.

Whatever the final properties of this material, we are assured of two results for the CSPT experiments: The test graphite pieces will have been manufactured under traceable conditions and will definitely represent a material improved chemically over the routinely produced grade 2020. Although normal ash levels run from 1200 to 2500 ppm by weight, every indication is that this special "nuclear-quality" material will run below 1000 ppm.

8.2.5 Basis for Selecting the CSPT Conditions — R. A. Strehlow

One significant reaction in the planned CSPT is the reversible "water-gas shift reaction":

$$H_2O + CO \rightleftarrows H_2 + CO_2 \ .$$

This reaction has a temperature-dependent equilibrium constant, given by the expression:

$$K(t) = \frac{[H_2][CO_2]}{[H_2O][CO]} \ ,$$

where the brackets represent the partial pressure of the indicated compounds. The issue for the CSPT series in this reaction and its equilibrium constant is that the position of the equilibrium (i.e., the relative amounts of the gaseous species) is significantly temperature dependent. Consequently, as a volume of gas is circulated around the loop, first heated to the test temperature of 700°C and then cooled to perhaps 400°C, the value of the equilibrium constant will change significantly.

8.2.5.1 Basis for TEST P-1

The rate at which the partial pressures of the various species approach these equilibria depends on both the kinetics of the reaction and the mass transfer rates of the various gaseous species involved in the reaction. We expect that, because of the high flow of gas through the system, equilibrium will not be reached at all points. Consequently, although small differences in composition may occur at the various temperatures, we expect a single composition that might reflect the equilibrium constant at some effective temperature, which is less than the test temperature.

The value of the equilibrium constant increases as the temperature is lowered; the corrosion product carbon oxides might therefore contain a high proportion of carbide dioxide, which would increase the corrosion rate of both the graphite specimens and the molybdenum heaters. Because the position of the equilibrium cannot be calculated from literature data, experimental determination of the position of the equilibrium is required. Thus, this is a principal chemical purpose of the preliminary TEST P-1.

The results of the TEST P-1 series will be the demonstrated ability to control the concentrations of the intended impurities $H_2O$ and $H_2$ and the corrosion products CO and $CO_2$. In addition, the proper operation of the IMS will be determined.

8.2.5.2 Basis for TEST ZERO

All the testing to be performed in TEST P-1 will be without graphite in the loop. The carbon will be introduced into the gas phase by injection of carbon monoxide or carbon dioxide in the presence of the corrodent

water-hydrogen mixture in the helium carrier. The TEST ZERO series will include graphite specimens exposed to the gas phase containing the corrodent mixture. The purpose of TEST ZERO is to demonstrate the ability to oxidize graphite and to calculate the oxidation rates as determined by the gas analysis data in combination with the flow of feed and vent stream in the ICS and to measure the agreement between these calculated rates and those determined in postexperiment examination of the graphite specimens.

TEST ZERO will provide data to compare with the pretest estimates based on the character and extent of oxidation calculated from other experimental results. The use of laboratory data in making estimates for the rate and character of the resulting oxidation (i.e., the extent of oxidation in the internal pores of the graphite) presents serious uncertainties as a result of the following:

1. Rate data are obtained generally at significantly higher temperatures and require extrapolation to the test conditions for the CSPT.
2. Extrapolation of rate data from the customary 100-kPa (1-atm) pressure to the CSPT conditions of about 7.2 MPa (71 atm) involves making assumptions about the pore structure of the graphite and the way in which the pore structure changes with oxidation.
3. Catalysis of oxidation is not now well understood and can affect the rate expression as well as the nature of the resultant pore structure.

As a consequence of the uncertainties introduced by these factors, one of the principal purposes of TEST ZERO is to assess the quality of the estimates made for the present series of tests. The basis for estimating accelerated corrosion tests is described in Sect. 8.2.2. The specification of conditions for TEST ZERO is designed to permit analysis of the possible role of some of these factors.

## 8.3 DESIGN MODIFICATIONS FOR THE CSPT — C. J. Claffey and A. G. Grindell

At the beginning of 1982, projected expenditures indicated that the budget would not support completion of the test vessel internals as shown in Fig. 8.4 or the installation of a 1.5-MW helium heater and its power supply and controls. As a result of the budgetary restrictions and the

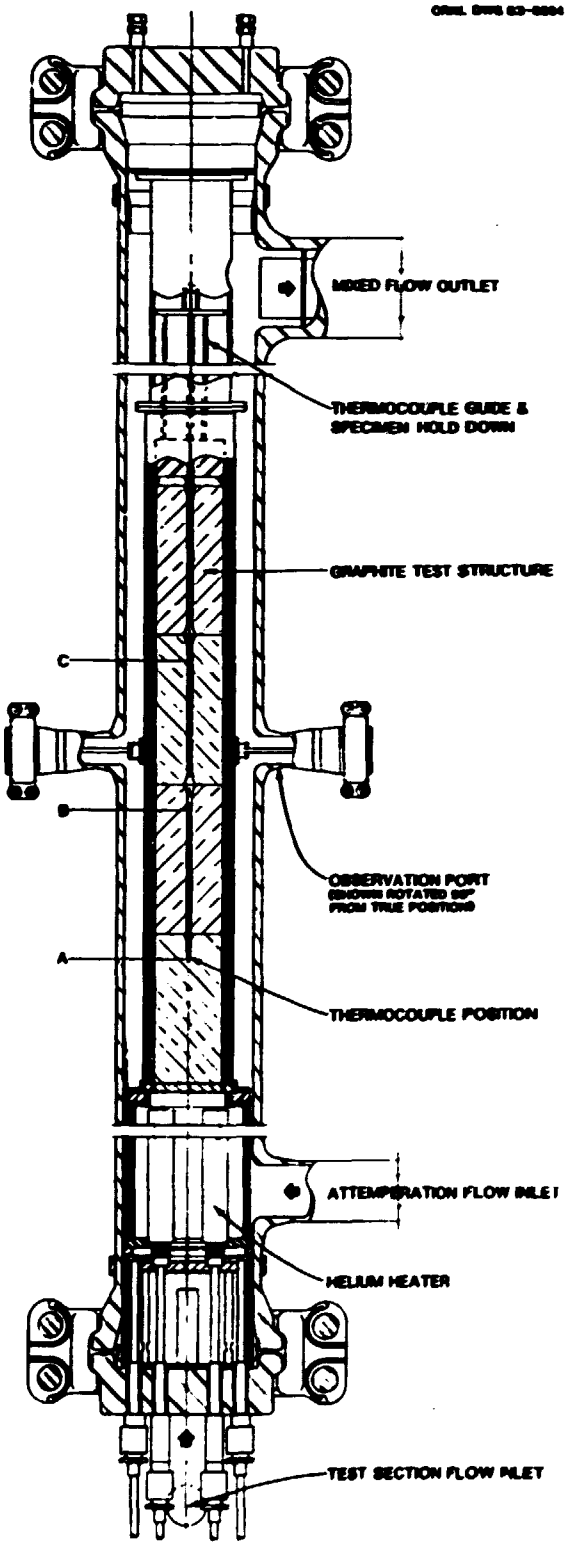


Fig. 8.4. Core Support Performance Test vessel and internals for TEST ZERO.

need to perform TEST P-1 and TEST ZERO before the initial TEST ONE, the design of the CSPT as shown in ref. 3 was modified to reduce costs and to accommodate these test needs. The ongoing designs of the recuperative heat exchanger, the 1.5-MW helium heater and associated power supply and controls, and the loading device for the graphite test structure were brought to an orderly halt, from which they may be completed as required.

The principal modifications needed to the CSPT vessel to accommodate the additional tests include installation of a 0.5-MW helium heater and connection of an existing 0.5-MW power supply and control system, an entry for the test helium flow through the bottom vessel closure, installation of a simplified vessel liner, and elimination of the recuperative heat exchanger and the device for loading the graphite test structure.

The principal modifications needed to the CFTL piping to accommodate the additional tests include installing two flow control valves equipped with actuators in the helium heater and the attemperation flow lines, installing a third flowmeter to measure the attemperation flow, and changing the piping to supply the helium heater flow to the bottom vessel closure.

The principal modifications needed to CFTL instrumentation and control systems to accommodate the tests include installation of an ICS and an IMS to control and measure the concentrations of hydrogen, moisture, oxygen, carbon monoxide, and carbon dioxide in the CSPT helium. In addition, appropriate temperature, pressure, flow, and power measurement sensors need to be added to both the test vessel and the loop and its components and connected to both the DAS and the requisite recording and protective logic instrumentation and controls.

The progress made in completing the modifications is summarized below and elucidated more fully in Sects. 8.3 through 8.7. The planning for and the initial operation of TEST P-1 is treated in Sects. 8.8 and 8.9.

By the end of 1982, all the design, procurement, fabrication, and installation activities for the mechanical and electrical tasks that are part of the modifications had been completed, and a large part of the instrumentation and control task had also been completed.

The CSPT piping modifications were fabricated as subassemblies and, along with the two flow control valves, were installed in the CFTL. The

construction of the CSPT test vessel was completed, and · vessel was installed and weld-connected to the modified piping. The ıbrication and assembly of the ceramic and molybdenum components for the helium heater were completed, and th. heater has been installed in the test vessel. Grayloc flange assemblies were installed as closures at the top and bottom ends of the vessel and at two observation ports. The completed piping system has satisfactorily sustained the pressure test required by the *ASME Boiler and Pressure Vessel Code*.

The existing 0.5-MW power supply, consisting of an induction voltage regulator and a special transformer having a 15-tap secondary, was connected to the helium heater. Appropriate equipment to protect the power supply from damage by overcurrent, ground short, and ground leakage was installed. The installed power supply was subjected to preoperational checkout and satisfactorily sustained a load test of about 40% of design.

A large portion of the instrumentation and control activities was completed at the end of the year. A third vortex shedding flowmeter was installed in the attemperation line. Thermocouples were installed in the test vessel and on the loop components and were connected to the DAS. Actuators for the two helium flow control valves were installed and connected to the instrument air supply and to a main board in the control room. The specification for the IMS was completed, and the work was awarded to Beckman Instruments, Inc. The installation of the ICS and an interim IMS was nearly completed. The interim IMS will serve during TEST P-1; we anticipate delivery of the IMS from Beckman and its installation in time for use with TEST ZERO. Work on the instrumentation and control systems remaining to be completed at the end of the year included the design and installation of interlock and protective circuits in the program logic controller and the checkout of several instruments, controls, and associated readouts.

The test specification for the TEST P-1 was prepared and a series of static proof tests was performed in December. This was practical because sufficient equipment for these static tests was already installed and because the tests could be performed without hindrance to the ongoing instrumentation and control work.

At the end of the year we were also considering the feasibility of operating CSPT TEST ONE, the first test with nuclear-grade graphite, in this modification of the CFTL; initial indications were favorable.

### 8.3.1 Test Vessel

The test vessel shell is a 5.44-m-long (214-in.) section of 16-in. pipe designed to contain 8.3 MPa (1200 psi) internal pressure plus anticipated piping and mechanical loads at 570°C (1050°F). The top and bottom closures for the vessel are Grayloc flange assemblies, both of which are removable for access to the vessel internals. The attemperation flow inlet and the mixed flow outlet nozzles are made with Sweepolet forged fittings. The helium heater flow inlet also utilizes a Grayloc flange assembly. Two observation ports are provided to permit inspection of the graphite test structure inside the vessel. The ports are closed with 4-in. (nominal) Grayloc flange assemblies. The vessel is made entirely of type 304H stainless steel except the Grayloc assemblies, which are of type 316 stainless steel. All the material is certified as acceptable by the requirements of the *ASME Boiler and Pressure Vessel Code*, Sect. III, Class 1. The vessel design and most of the fabrication conformed to these rules.

Modifications to the 16-in. Grayloc blind flanges used as test vessel closures were completed. The lower blind flange supports the helium heater and accommodates both the heater power electrodes and instrumentation feed-throughs and the test helium flow inlet nozzle. The flange for the upper end contains instrumentation feed-throughs only.

Three stainless steel rings were welded to the exterior of the test vessel for fabrication and assembly purposes. The finish machining of several surfaces in the vessel interior required supporting one end of the vessel in a steady rest with the other end supported in and driven by the spindle of a large engine lathe. A ring was required near each end of the vessel to provide the steady rest. An additional ring was required near the bottom end to mount an alignment fixture for installing the helium heater in the vessel.

### 8.3.2 Helium Heater

Since TEST P-1 and TEST ZERO do not require the 1.5-MW helium heating capacity originally planned for the CSPT, we decided to install only 0.5 MW

of capacity. This was accomplished by installing two 250-kW subassemblies in the heater mount, which can accomodate six subassemblies. Each subassembly consists of a heating element with a shroud and appropriate alumina plates and metal fasteners for mounting the subassembly onto the top of the bottom Grayloc closure and for simultaneously isolating the element electrically from the metallic closure.

The heating element is a helically wound coil of HT-molybdenum wire mounted on a grooved alumina mandrel and surrounded with an alumina shroud. The annular clearance between the heating element and the shroud is sized to provide adequate heat transfer between the element and the helium flowing in the annulus. Each end of the element is connected to solid rods of TZM-molybdenum that serve as power electrodes and penetrate the bottom closure flange. The electrode penetrations are sealed to the closure with Conax bulkhead fittings.

### 8.3.3 Test Vessel Internals

The test vessel and internals for TEST ZERO are shown in Fig. 8.4. The internals for TEST P-1 are identical except that the graphite test structure is not installed. The TEST ZERO vessel liner has been simplified, the helium heater capacity has been reduced to 0.5 MW from the previously envisioned 1.5 MW, and the recuperative heat exchanger and the loading device for the graphite structure have been eliminated.

The simplified liner separates the upward flow of high-temperature helium that traverses the surface of the graphite test structure from the upward flow of the cooler attemperation helium in the annulus between the liner and the outer vessel wall, the pressure boundary. The attemperation flow maintains the pressure boundary below the vessel design temperature. The two flows join in the upper end of the vessel and are mixed in the mixing section located in the vessel outlet nozzle. The lower two sections of the three-section liner have corrugated metallic insulation to reduce the radial outward flow of heat from the high-temperature helium to the cooler attemperation helium.

The design of the graphite test structure for TEST ZERO was completed, and drawings for its fabrication were issued in late December 1982. The

design of a stainless steel load post, which rests on the top of the test structure, was also completed and issued for fabrication. The load post is equipped with tubes used to guide the thermocouples into the graphite structure during their insertion. The preliminary design of tools and fixtures for handling the graphite during fabrication and transportation and during installation in and removal from the test vessel was essentially complete by the end of the year.

### 8.3.4 Loop Piping

The piping system of the Stage 1 CFTL was modified to accomodate the CSPT as shown in Fig. 8.1. The modification equips the piping system with a third vortex shedding flowmeter to measure attemperation helium flow and with two flow control valves and actuators to regulate the test helium and the attemperation helium flows. A pipe to deliver helium flow to the bottom closure of the test vessel was added to the piping system. The design of adequate support and thermal insulation for the piping and components was completed. A work platform with access ladders was designed to provide a safe working area during the installation and removal of the graphite test structure and test vessel internals as required at the top of the test vessel.

The elimination of the recuperative heat exchanger required the use of an upward flow of the test helium in the test vessel. The attemperation helium flow in the test vessel was already in the upward direction.

Sufficient CFTL piping was reclaimed to provide all the material needed for the piping modifications. The design also permitted substantial prefabrication of the piping subassemblies at the ORNL Plant and Equipment shops.

The design and fabrication of the piping was according to both the *ORNL Controlled Manufacturing Manual* and the *ASME Boiler and Pressure Vessel Code*, Sect. III, Class 2.

## 8.4 ELECTRICAL MODIFICATIONS — T. L. Hudson and E. M. Lees

Wireways and cabling were installed to connect the existing 0.5-MW power supply and control equipment to the CSPT helium heater; heater power

measurement and protective devices were also installed. The heater power supply was then operated satisfactorily at partial load. The control equipment for two additional 0.5-MW power supplies was set in place. The three variable-frequency power supplies (VFPS) for the helium circulators were restarted after having been unused for a year; they were load-tested satisfactorily to supply the circulators.

The existing 0.5-MW power supply installed for the Stage Alpha CFTL was modified from ten circuits of 50 kW each to two 250-kW circuits to match the power requirements for the two CSPT helium heaters of the larger size.

Figure 8.5 is a schematic of the installed 0.5-MW power supply, including the control equipment and its protective and power measurement devices. Circuitry to protect each of the two helium heaters from overcurrent and ground leakage was installed and checked functionally. A 45-kW water-cooled dummy load was used to check the operation of the power supply and control system before connecting it to the heaters. The power supply was operated satisfactorily at about 40% of design load.

Two of the three VFPSs failed to function properly when initially restarted after a one-year shutdown; the third VFPS functioned properly. The two VFPSs supplied less than half of full-power capacity and thus could not bring the circulators to minimum starting speed. A failed diode in one supply was replaced with a higher rated unit, and a silicon controlled rectifier gate control circuit was replaced in the other supply. Normal operation of the supplies and the circulators was subsequently obtained.

## 8.5 IMPURITY CONTROL AND MEASUREMENT SYSTEMS — P. G. Herndon and R. E. Harper

In the planned CSPT, the graphite test structures will be exposed for six months to a controlled environment that will result in an amount of corrosion equivalent to 40 years of HTGR operation. This environment is created by the elution of constituents from the circulating gas stream and by the addition of appropriate replacement gas of controlled composition. To maintain the impurity concentrations at the required levels, the amount of each component must be measured and controlled over the ranges of concentrations shown in Table 8.1.

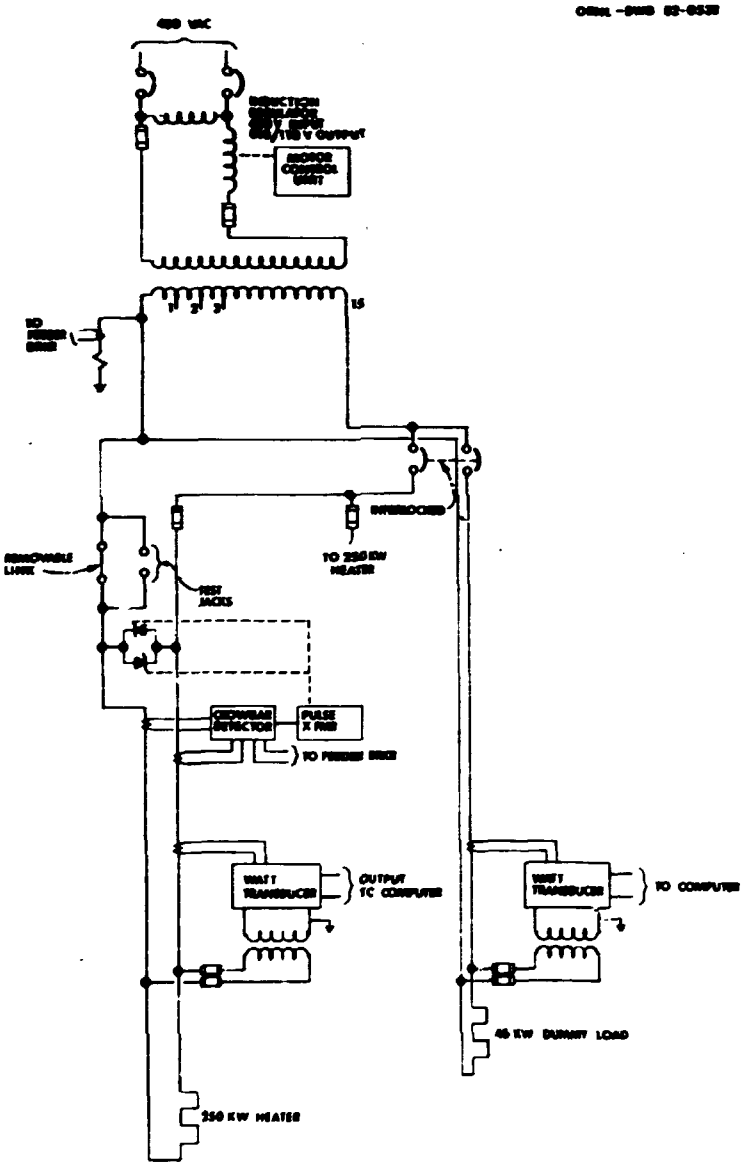


Fig. 8.5. Schematic of 0.5-MW power supply for the Core Support Performance Test.

The reliability of the measurement and control systems is vital to the success of the test because long-term performance results are to be extrapolated from short-term tests. Gaps in the recorded data of impurity concentration could result in questionable conclusions. Therefore, after an extensive survey of available analytical measurement techniques, an automated process gas chromatograph was chosen as the prime component of

Table 8.1. Core Support Performance Test impurities measurement system performance specifications

| Component | Range (vol ppm) | Accuracy (% of full scale) |
|---|---|---|
| | *CSPT measurement requirements* | |
| $H_2$ | 12–30,000 | |
| CO | 12–30,000 | |
| $CO_2$ | 10–10,000 | |
| $CH_4$ | 3–30 | |
| $O_2$ | 0.4–200 | |
| $H_2O$ | 1–1,000 | |
| He | Balance | |
| | *Gas chromatograph specifications (analysis cycle time: 10 min)* | |
| $H_2$ | 0–300, 0–30,000 | ±4, ±1 |
| CO | 0–300, 0–30,000 | ±4 |
| $CO_2$ | 0–100, 0–10,000 | ±10 |
| $CH_4$ | 0–30 | ±10 |
| $O_2$ | 0–200 | ±10 |
| | *Electrochemical trace oxygen analyzer (response time: 1 min)* | |
| $O_2$ | 0–2, 0–20, 0–200 | ±2 |
| | *Electrolytic trace moisture analyzer (response time: 1.5 min)* | |
| $H_2O$ | 0–10, 0–30, 0–100, 0–300, 0–1,000 | [a] |
| | *Capacitance trace moisture analyzer (response time: 5 s)* | |
| $H_2O$ | 0.001–20,000 | ±50 at 0.01[b]<br>±36 at 1.0[b]<br>±25 at 70[b]<br>±10 at 5,000[b] |

[a] ±5% of reading or ±1 vol ppm, whichever is greater.

[b] Percent of reading.

the IMS. The system provides the best solution to the conflicting requirements of accuracy, speed of response, reliability, wide measurement range, and acceptable cost. The complete system utilizes a combination of chromatographic, electrolytic, electrochemical, and capacitance techniques to make the required measurements.

### 8.5.1 Impurity Measurement System

Specifications were written for an assembled and packaged gaseous impurity analysis and measurement system that automatically detects and measures the impurity components in the circulating gas. After a lengthy bid and award procedure, an order was placed with the Beckman Instrument Company in the latter part of June 1982, with a promise of delivery in seven months. This measurement system is shown diagrammatically in Fig. 8.6; it consists of the following subsystems:

1. a sample conditioning and stream selecting system,
2. an automated process gas chromatographic system,
3. an electrolytic trace moisture analyzer,
4. a six-channel capacitance trace moisture analyzer, and
5. an electrochemical trace oxygen analyzer.

The sampling system draws samples from three points in the helium system operating at pressures to 7.69 MPa (1100 psig) and temperatures to 1040°C (1900°F). The sample streams are the test structure environment, the impurity injection line, and the calibration gas line. Each stream is filtered and reduced in pressure and temperature to 450 kPa (50 psig) and 27°C (80°F) or less before being delivered to the analysis measurement instruments. The gas chromatograph, which is automated for continuous unattended operation, sequentially samples the three streams on a cycle time of about 10 min. The performance capabilities of the instruments of the IMS are also shown in Table 8.1.

The analytical section of the chromatograph consists of a 2-m Chromosorb 102 column and a 2-m molecular sieve 5A column, with another 2-m Chromosorb 102 column serving as a moisture stripper. This latter column is periodically back-flushed to remove the accumulated moisture. The detection device is a filament-type thermal conductivity detector having a dynamic range of about $10^4$. The repeatability specifications of the chromatograph (Table 8.1) represent the maximum error observed in 95% of the readings taken on a sample gas of constant composition over a 24-h period as determined by a thorough quality control testing procedure.

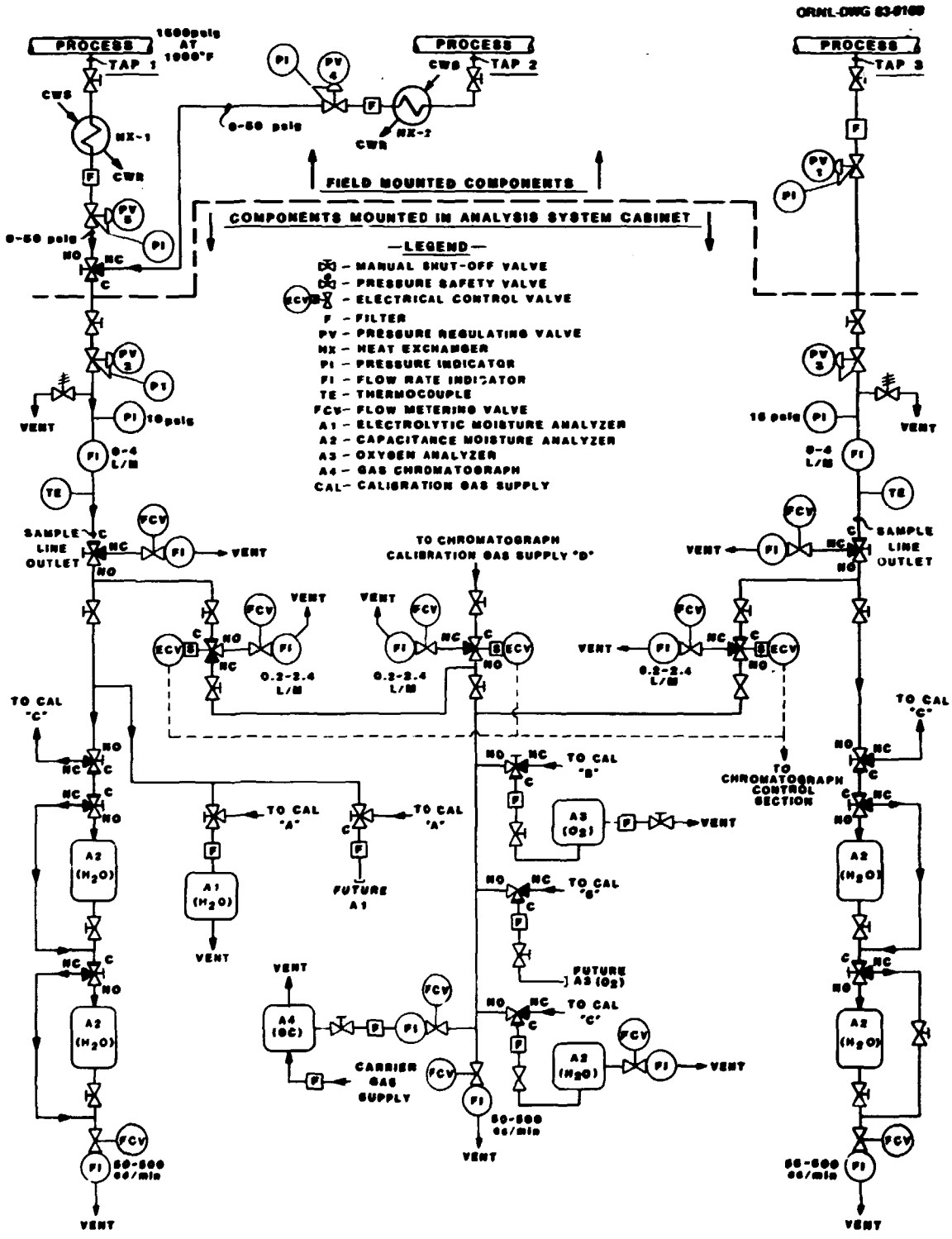


Fig. 8.6. The impurity measurement system for use on the Core Support Performance Test.

The results of the analysis and system status information are presented on a printer and simultaneously transmitted to an on-site PDP-11/34 minicomputer for recording. Data can also be recorded on a magnetic tape cassette. Chromatographs are presented on a strip chart recorder, and a six-pen recorder displays the results of the chromatographic analysis as concentration trend data.

Not all impurities of interest to the CSPT lend themselves to chromatographic analysis. Of particular experimental interest are trace quantities of $H_2O$ and $O_2$. Sudden influx of either of these components from an equipment malfunction or leak could seriously jeopardize the experimental results by increasing the oxidation rate of the graphite above the required value. Therefore, continuous measurement and rapid transient detection of the concentration of these components is necessary. In addition, problems exist in chromatographic analysis of $H_2O$ and $O_2$. Moisture is fairly intractable with a sorption method; good quantitative chromatographic peaks are the exception rather than the normal event. Coincident elution of $O_2$ with amounts of argon, which tends to be present in the makeup helium, interferes with the accurate detection of trace amounts of $O_2$.

For these and other considerations, separate analyzers were specified for both $H_2O$ and $O_2$. For accurate trace measurements of $H_2O$, flow-through electrolytic analyzers are used, which typically have accuracies of ±5% of reading. To provide a relatively rapid indication of $H_2O$ transients, capacitance sensors are used. These capacitance devices suffer from reduced accuracy at trace concentration levels, but their installation in the process stream yields quick response for this important measurement, and they are highly reliable.

Trace $O_2$ measurements are performed with flow-through open-cathode electrochemical fuel cells. These instruments have a lower range of 2 ppm full-scale with a sensitivity of ±0.01 ppm.

To avoid delay in the startup of TEST P-1 as a result of the delivery time quoted for the IMS, an interim IMS was designed, fabricated in the ORNL shops, and installed in the CFTL control room. This system includes a gas chromatograph and an electrochemical trace oxygen analyzer (both borrowed temporarily from another project) and an electrochemical trace

moisture analyzer previously purchased for use in the GCFR CFTL. This system provides a limited impurity measurement capability.

### 8.5.2 Impurity Control System

The design, procurement, and installation of the impurity control system (Fig. 8.7) were completed. The system consists of flow regulation lines for an oxygen-free helium supply and controlled loop venting, a gaseous impurity supply with injection control, and a moisture generation with injection control. The system functions automatically to maintain a specified impurity concentration by adding the gaseous impurities and removing the circulating gas at controlled rates.

The impurity cylinder manifold stations, the moisture generator pressure vessels, and the injection control valves are located in the loop area close to the point of injection. These are remotely controlled from two instrument panels located in the auxiliary control room, as shown in Fig. 8.8.

The method used to control the impurity concentrations is determined primarily by the need to vent the loop inventory continuously to limit the concentration of hydrogen produced by the reaction of water vapor with the graphite. Purified helium is also added continuously to maintain the system pressure constant at 7.24 MPa (1050 psia). For operation at a loop temperature of 700°C, the maximum vent flow, and consequently the helium makeup rate, is about 0.57 $m^3/h$. This action depletes all other impurities, and, to maintain the required composition, these constituents must be added continuously.

The helium supply system (Fig. 8.7) consists of the helium supply trailer and its backup cylinder bank, an oxygen adsorber, pressure regulators, and flowmeters. Helium from the trailer or bottles is automatically reduced from 12.5 MPa (1800 psig) to the loop operating pressure. The oxygen adsorbers are sampling cylinders with a capacity of about 0.0038 $m^3$ (1 gal) filled with OXISORB (chromous hydroxide on silica gel). The capacity of the adsorbent was determined by tests to be 56 std $cm^3$ of oxygen per gram of adsorbent. This means that 100 g (~4 oz) of OXISORB can purify (at room temperature) 1870 std $m^3$ He containing an initial oxygen concentration of 3 vol ppm or less. The adsorbent capacity is increased

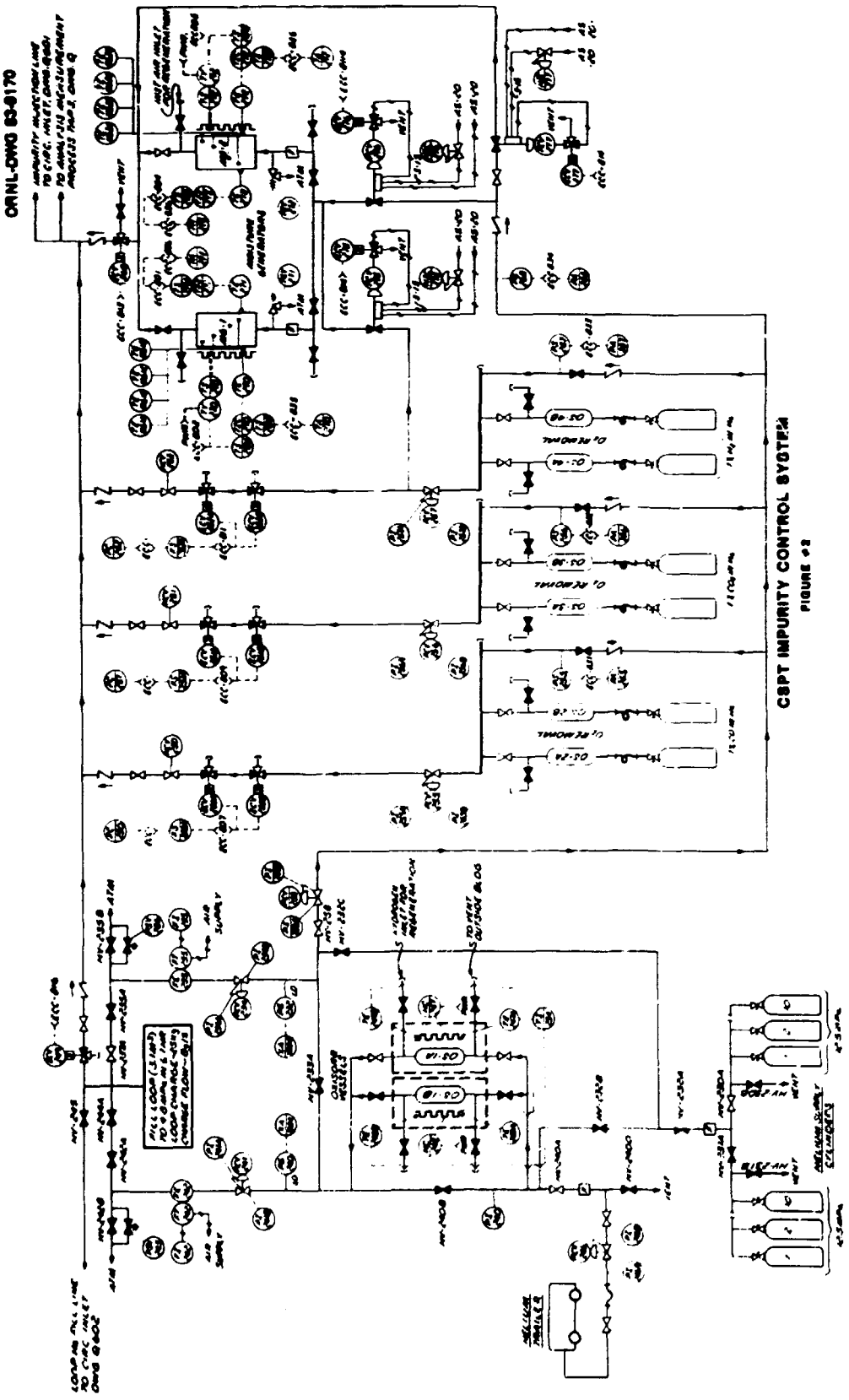


Fig. 8.7. Core Support Performance Test impurity control system.

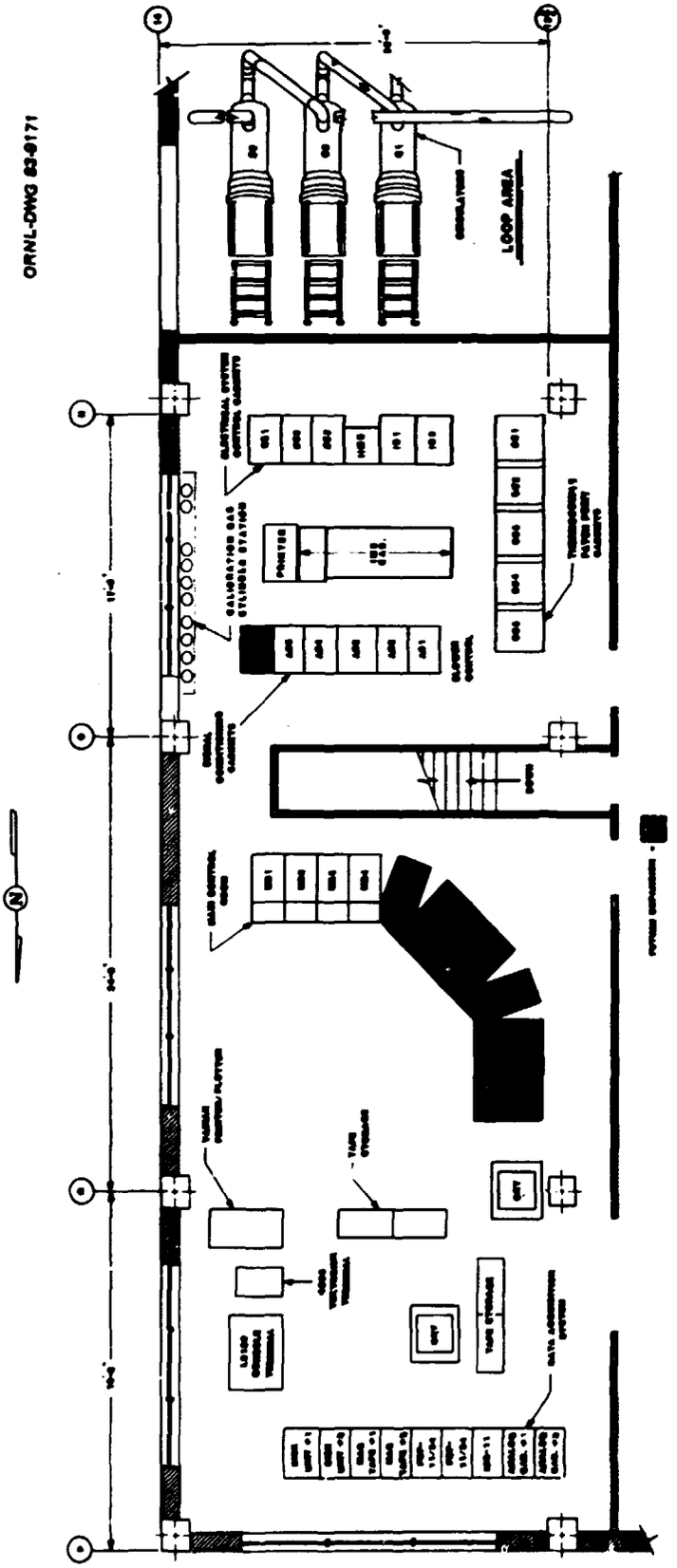


Fig. 8.8. Core Support Performance Test control room plan.

significantly if the adsorbent temperature is increased to 40°C. Low-watt wrap-on-type heating elements are installed on the vessels for this purpose. The OXISORB adsorbent can be regenerated for repeated use by flowing hydrogen through the material. The tests also determined that the amount of hydrogen required to regenerate the OXISORB material is less than the volume in one standard gas cylinder [5.66 std $m^3$ (200 std $ft^3$)]. The oxygen concentration of the purified helium will be 0.1 vol ppm or less.

All impurities except moisture are supplied from three separate high-pressure cylinder manifolds containing the impurities CO, $CO_2$, and $H_2$ diluted in helium. Each of these impurities is injected into the loop as a 1% mixture in helium. The moisture impurity is generated by the reaction of hydrogen with a matrix of copper oxide and is injected as a mixture of helium saturated with moisture at 100°C.

Control of the impurity injection rates presented some special problems because of the extremely low flows [0.03–0.23 std $m^3/h$ (1–8 std $ft^3$) at 7.24 MPa (1050 psia)] required. Conventional globe-type throttling valves with bellows stem seals and micrometering trim were rejected for all the applications except moisture and the loop letdown valve because of the minute port sizes required and the high cost. The method selected features time-proportioned pulse injection through two solenoid valves piped in series. This method utilizes a flow controller having an adjustable time-proportioned ON/OFF output signal that alternately opens and closes the two solenoid valves. It provides a wider range of control, can be operated in either the manual or automatic mode, and is less expensive.

The technique of reacting hydrogen with copper oxide to produce moisture relies on the reduction of a hot (650°C) copper oxide bed by a hydrogen-bearing stream of helium. This technique is one of the few that is not strongly dependent on temperature for control. Moisture injection is controlled by varying the inlet hydrogen concentration and the ratio of bypass helium flow to that of the water-bearing effluent from the copper oxide matrix. The reduced oxide can be regenerated in place by passing air over the hot bed to reoxidize the copper.

Among the disadvantages of the CuO reduction method is the obvious expense of building vessels to operate at the high loop pressure and 650°C temperature. All impurities are delivered to the loop through the same

line that transports the clean makeup helium so that the impurity mixture is injected rapidly into the loop at a point immediately upstream from the circulators. This same mixture is also piped to the IMS for analysis.

## 8.6 LOOP INSTRUMENTATION AND CONTROL — P. G. Herndon and S. C. Rogers

A number of additions and modifications to the existing loop instrumentation and control systems were required to accommodate the 500-kW helium heater and the revised configuration of the loop piping. The additions and revisions completed are described in the following sections.

### 8.6.1 Flow Measurement and Control

The installation of two 4-in. bellows-sealed helium flow control valves and one additional vortex shedding flowmeter was required in the main loop of the CFTL. One of the valves is installed in the line supplying the flow to the helium heater, and one, in the line supplying the attemperation flow. The valves purchased earlier for the GCFR program were on hand. Although a hydraulic actuator system was purchased with these valves, it is too complex for the CSPT requirements, and the system would have been much more costly to install and operate than would conventional pneumatic type actuators.

Two pneumatically powered cylinder actuators were procured and installed on these valves. Because the actuators and valves were not supplied by the same manufacturer, adapter hardware was required to connect the actuator mounting yoke to the bonnet of the flow control valves. This adapter was designed and fabricated in the ORNL shops.

The actuators, capable of stroking from fully open to fully closed in 1.5 s, provide the capability for operating the loop in both steady-state and fast-transient flow modes at a reasonable cost. The actuators can be configured to fail closed, open, or in position. The valve actuators are also equipped with manually adjustable mechanical stops that limit stem travel. Computer simulations of loop dynamics identified the valve stem positions to provide the required range of helium flows for both the helium heater and the attemperation path to ensure that the circulators

would never operate in a surge condition. The mechanical stops were set accordingly. Each valve was connected to an existing remote manual operating station on the main control board.

One 4-in. vortex shedding flowmeter was installed in the attemperation flow line. The pulse output signal from the meter was connected to a recorder on the main control board through an existing frequency-to-voltage converter. A low-flow-limit switch was added to the output signal from the helium heater flowmeter (FE-4) for use in the protective interlock circuits.

### 8.6.2 Temperature Measurement and Control

The design and installation of a system that provides automatic temperature control for the helium heater outlet gas and that also measures the voltage and power input to the heater were completed. Both temperature and power are recorded by existing instruments located on the main control board. Adjustable limit switches are included in both systems to initiate alarms and shutdown actions for out-of-limits conditions.

Revision of the heat exchanger (HX-1) control system was not required except for the addition of a speed measurement for the air blower supplying cooling air to the heat exchanger. A low-speed-limit switch is included in this system to initiate protective actions when an out-of-limit condition exists.

### 8.6.3 Loop Protection

The design of a protective interlock system for the helium heaters and the loop piping system was completed, and the necessary modifications were made in the system. High-temperature switches that initiate both alarms and shutdown actions were installed to monitor the helium gas temperatures at the inlet and outlet of the HX-1. The protective interlock logic for the helium heater is shown in Fig. 8.9. The logic was implemented by using the spare input-output (I-O) components for the existing programmable logic controller (PLC).

Additional PLC utility software that provides the capability for logic program development and documentation was purchased and installed on

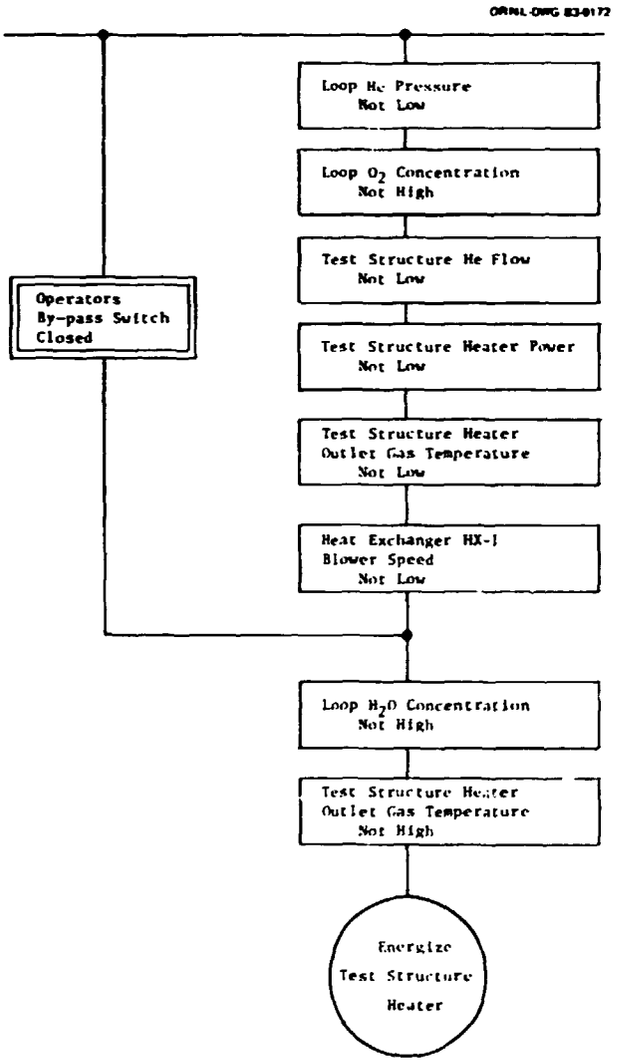


Fig. 8.9. Core Support Performance Test structure heater protective interlock logic.

both the CFTL PDP-11/34 DAS and the MACES NET PDP-11/34 computer. This software allows existing PLC programs to be modified and documented easily and quickly. It also provides other useful features such as I-O table mapping and automatic contact labeling.

### 8.6.4 Instrumentation of the Test Structure

The fabrication and installation of thermocouples to measure temperatures in the test vessel and the associated signal cables connecting them to the data acquisition system as required for initial tests was

completed. Thirty-two thermocouples were installed on the liner and on the heater assembly. Ten thermocouples were installed on the outside of the test vessel. Surplus material, tested and certified to the Reactor Development and Technology Standards by ORNL Instrumentation and Controls Division's thermometry group, was used for fabrication of these assemblies. Fabrication of six additional assemblies containing 12 thermocouples, custom designed to be inserted into the graphite test structure for TEST ZERO, was also completed.

The cable and connector assemblies that transmit measurement signals from the graphite test structure and from the loop to the DAS contain a total of 112 shielded cable pairs. The cables were laid in existing cable trays and connected to the DAS input terminals.

### 8.6.5 Reduction of emi Noise

Modifications and improvements were made to cables, chassis covers, filters, and electrical ground connections to eliminate or to reduce satisfactorily the electromagnetic interference (emi) noise that has appeared previously on the instruments that measure bearing film thickness, speed, and power for the helium circulators. The noise is generated by the solid-state variable-frequency power supplies.

The circulator displacement monitors were relocated to reduce the length of cable run from about 30 to about 9 m. The present twisted shielded pair cables were replaced with coaxial cables and connectors. Appropriate filters were installed on the output from the circulator power transducers. A separate insulated electrical grounding bus was installed for the signal cable shields. Thus, the ground for the signal cables will be completely separated from the ground for the power systems.

## 8.7 CONSTRUCTION PROGRESS FOR PRELIMINARY TESTS — H. C. Young and A. G. Grindell

The major construction efforts involved modification of the CFTL piping from the Stage Alpha configuration and the installation of the CSPT vessel.

### 8.7.1 Piping Modifications

The shakedown operation of the three helium circulators in the CFTL Stage Alpha piping configuration was completed in December 1981 (ref. 4). A fixed orifice in the loop piping was used to simulate the pressure loss of test vessel and flow control valves not installed in Stage Alpha.

The CFTL configuration for the CSPT is shown schematically in Fig. 8.1. The design of piping modifications to accommodate the CSPT vessel, two 4-in.-pipe-size helium flow control valves at the test vessel inlet and the attemperation flow inlet, and a third vortex shedding flowmeter to measure the attemperation flow was completed in March 1982.

Thirteen sections of 4- and 6-in. pipe and fittings were removed from the Stage Alpha piping and reclaimed for use in fabricating six new piping subassemblies for the CSPT. All piping required for these modifications was on hand except two 4-in. Grayloc flanges, which were purchased and delivered by May 1982.

A manufacturing plan was prepared, and fabrication of the piping subassemblies was completed by the ORNL Plant and Equipment shops and delivered to the CFTL site in June 1982. An installation plan was prepared, and field installation of the subassemblies was initiated in June 1982. Although fabrication problems delayed completion of the CSPT vessel, an overhead work platform and ladders were installed to provide access at the top of the test vessel for installing the vessel liner and graphite test structure as required. On completion of fabrication of the test vessel, it was installed and weld-joined to the loop piping in September 1982. The Grayloc blind flanges that form the vessel closures were installed at the top and bottom of the vessel liner, and the entire loop primary piping system was pneumatically pressure-tested satisfactorily on October 4, 1982.

The Flexitallic gaskets, which seal valve bonnet to valve body, leaked for both flow control valves during the pressure test. The gaskets were replaced. However, because of severe space restrictions, it was impractical to apply the specified 1000 N·m (800-lbf·ft) torque to the valve bonnet bolting to seat the gasket with existing tools. A special

device with an available hydraulic cylinder was designed, fabricated, and calibrated against a standard torque meter. It was used to tighten the bolts to the specified torque satisfactorily.

To change the loop pressure rating from 10.34 to 7.24 MPa (1500–1050 psia) and to satisfy the ASME Code requirements, the setting of the existing relief valve for the primary piping system was changed from 11.72 to 8.27 MPa (1700 to 1200 psia). A new rupture disk was installed to change the disk rating from 11.03 to 7.99 MPa (1600 to 1160 psia).

The Y-12 Plant Health and Safety Readiness Review Committee approved the piping modifications.

### 8.7.2 Vessel Manufacture and Installation

#### 8.7.2.1 Test Vessel

Design of the CSPT vessel was completed in the fall of 1981. The manufacturing plan was approved, and fabrication in the ORNL Plant and Equipment shops was initiated in early January 1982. Fabrication delays ensued when the welding of Sweepolet nozzles and Grayloc butt-weld hubs to each end of the test vessel resulted in distorted section circularity and excessive loss of concentricity among the parts. After making adjustments in the plan, the fabrication was completed, and the vessel was delivered to the test site on September 8, 1982. The vessel attemperation inlet and the vessel outlet nozzles were welded into the loop piping, and the helium heater inlet pipe was connected to the vessel with a Grayloc flange union. During completion of the fabrication of the vessel liner and an installation fixture for the helium heater, the two 16-in. Grayloc blind flanges that form the vessel closures were installed with appropriate flange clamps, and the entire vessel and piping system was subjected satisfactorily to the requisite ASME pneumatic pressure test. Figures 8.10 and 8.11 show side and top views of the test vessel and some of the loop piping that had been subjected to the pressure test.

Except for the purchase of a 3.66-m (12-ft) length of pipe for the central section of the vessel, all the material for fabricating the vessel was available from the original GCFR construction program. The type 304H stainless steel pipe was 0.4 m (16 in.) in outside diameter with a wall thickness of 22 mm (7/8 in.).

ORNL-PHOTO 8864-82

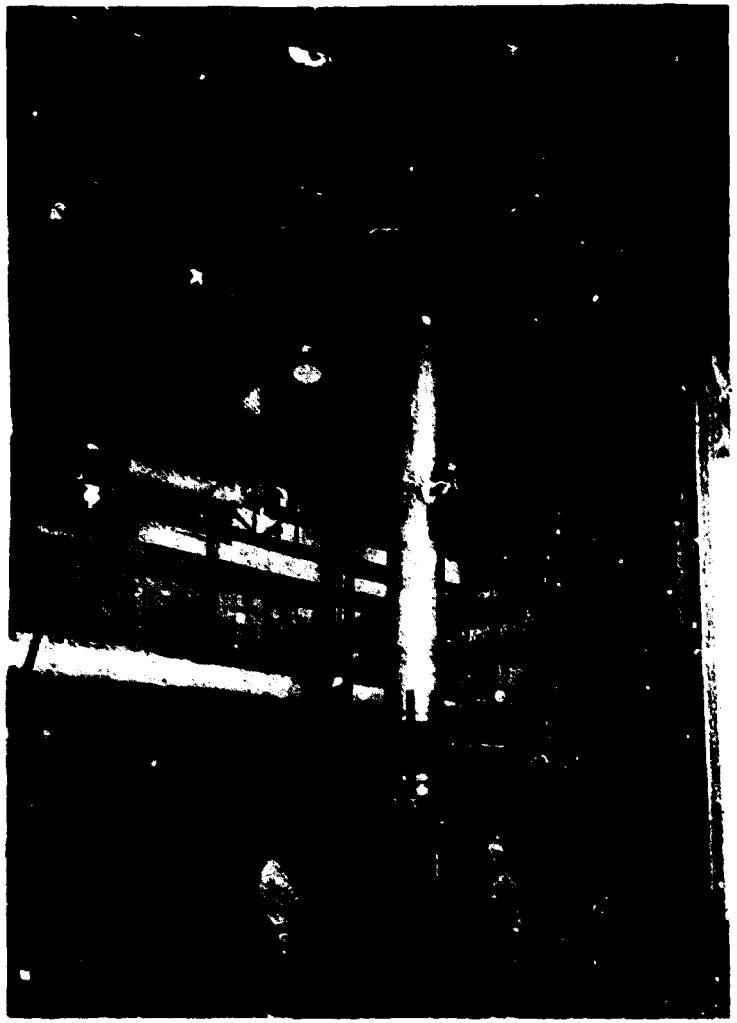

Fig. 8.10. The installed Core Support Performance Test vessel.

ORNL-PHOTO 8865-82

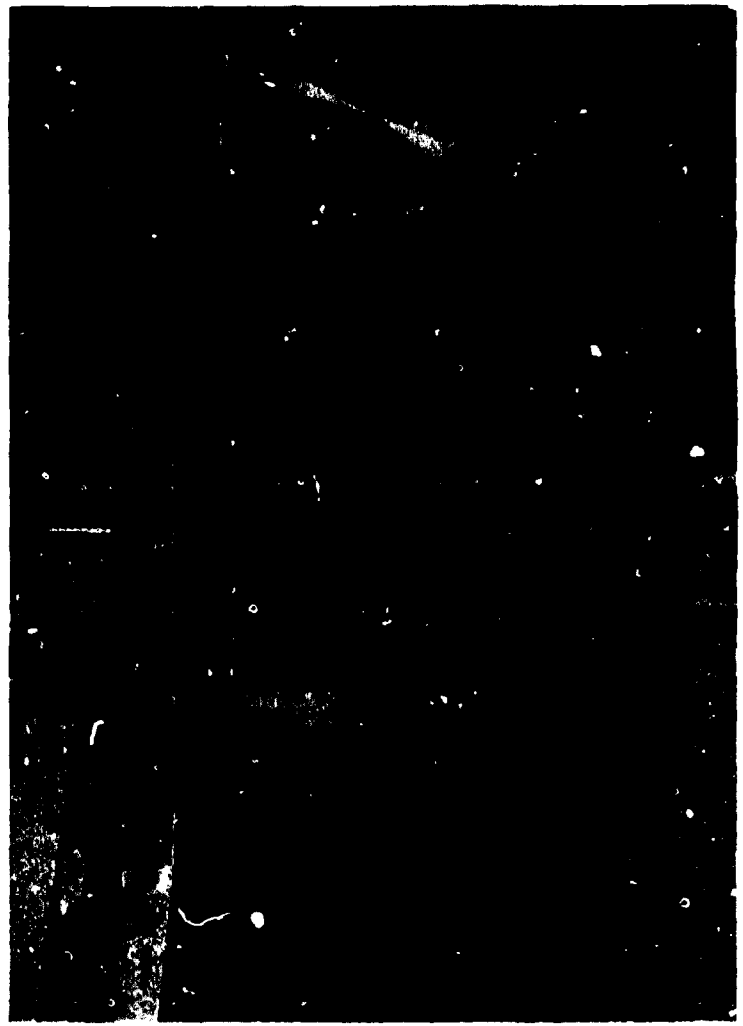

Fig. 8.11. Top head of the Core Support Performance Test vessel.

The vessel design drawings specified very close concentricity and squareness tolerances between the finish machined surfaces in the vessel interior and the finish machined register and seal surfaces in the Grayloc hubs at each end of the vessel. The tolerances were necessary to ensure proper mating between the liner seal ring and the vessel interior and between another liner seal ring and the helium heater near the bottom of the vessel. The proper fit of internal labyrinth seals would eliminate or minimize the bypass of helium heater flow into the attemperation flow and the bypass of helium around the helium heater, respectively. The tolerances would also ensure proper alignment of the force acting between the graphite test structure within the liner and the loading device to be installed later at the top of the vessel for CSPT TEST ONE. The vessel drawings also permitted fabrication of the top and bottom ends of the vessel as separate pieces while awaiting the delivery of the center course of the vessel. The top end consisted of a short piece of pipe of the same diameter as the vessel, butt-welded to a Grayloc hub and weld joined to a 10-in. Sweepolet nozzle. The bottom end was identical except for a 6-in. Sweepolet nozzle.

During joining, weld distortion of the Sweepolet nozzles caused the faces of the previously welded Grayloc hubs to move about 5 mm (0.200 in.) out of square with the vessel centerline. The out-of-squareness at the top of the vessel could be accommodated later by making adjustments in the structure that joins the loading device to the top Grayloc flange closure. However, the squareness and concentricity requirements for the lower end of the liner at the helium heater, which is mounted on the lower Grayloc flange closure, would not permit acceptance of this large distortion. Although the out-of-squareness was reduced to about 1.2 mm (0.050 in.) after separation and rewelding of the flange, we decided to refinish the face and seal surfaces of the Grayloc hub to make it square and concentric to the machined surfaces in the vessel interior. Both vessel ends were furnace stress relieved at 510°C (950°F). Although this stress relief would sensitize the type 304H stainless steel materials, this sensitivity was considered to be acceptable for the helium environment of the CSPT tests.

Also during the manufacture of the test vessel, we noted that external steady-rest surfaces would be required to permit finish machining the interior surfaces in the vessel to the required tolerances. Additional external surfaces would be needed to mount and center an alignment fixture for installation of the helium heater in the bottom of the vessel. Three rings were designed and weld joined to the exterior of the vessel.

In summary, the rewelding of the Grayloc hub to the bottom vessel end, the stress relief heat treatment of the two vessel ends, the weld joining of the two ends to the vessel center segment, and the addition of the three exterior rings resulted in the satisfactory completion of vessel fabrication, leaving only finish machining to be performed.

The vessel was transported to the Oak Ridge Gaseous Diffusion Plant and mounted in the large lathe shown in Fig. 8.12. All the surfaces in the vessel interior and on the three external rings were finish machined satisfactorily. However, it was not practical to obtain a satisfactory finish on the face and sealing surfaces of the Grayloc hubs in this lathe. The activity was supervised by a representative of the Gray Tool Company, Houston, the manufacturer of the Grayloc hubs and blind flange closures.

The seal surface was subsequently built up with weld metal at the ORNL Plant and Equipment shops, where the seal surfaces for both Grayloc hubs were refinished by a representative of Gray Tool Company, who may be seen in Fig. 8.13 using the portable machine constructed for this purpose.

The final vessel fabrication activity of weld joining two 3-in. Sweepolet nozzles and Grayloc blind flange closures to make observation ports at the vessel midsection was completed. Strongbacks fitted inside the vessel prevented distortion of the vessel during weld joining the two nozzles. The ports will permit making in situ observations and measurements of a portion of the CSPT graphite structure inside the vessel and liner.

The finished vessel was transported to the CFTL site in the Y-12 Plant for completing the installation and pressure test activities.

To reduce the construction period by an estimated 12 to 15 working days, we decided to forego the pneumatic pressure test of the test vessel

K/PH82-2813

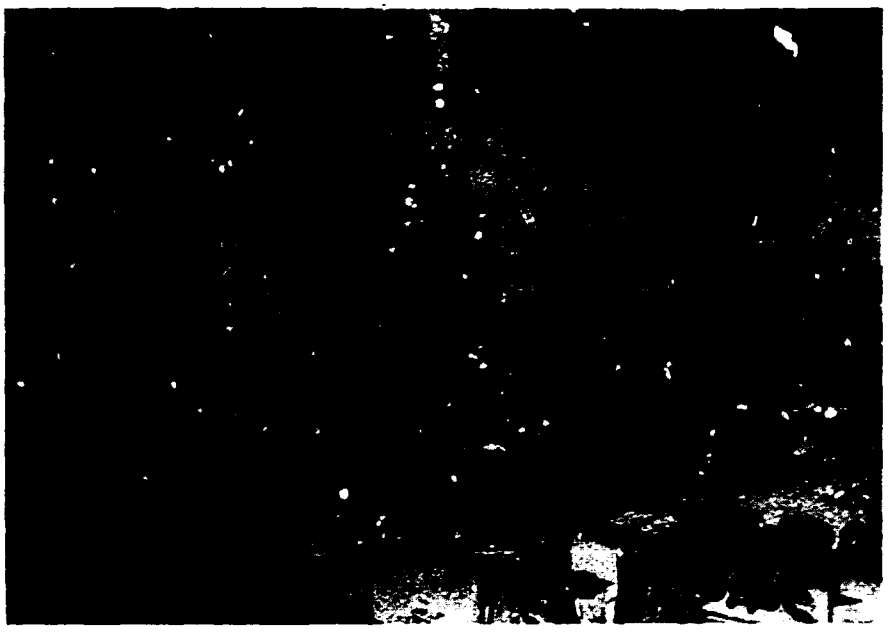

Fig. 8.12. Core Support Performance Test vessel mounted in large lathe.

ORNL-PHOTO 3748-82

Fig. 8.13. Refinishing seal surfaces of Grayloc hubs.

at the ORNL Plant and Equipment shops and to subject it to the same pressure test required for the completed vessel and piping system at the Y-12 Plant site of the loop. Although the vessel was constructed to all the requirements of the ASME Nuclear Code, the price of improving the schedule by foregoing the pressure test in the Plant and Equipment shops, which have an authorized N-Stamp, was the withholding of the stamp by the authorized inspector. The weld installation of the vessel, the piping subassemblies, and the flow control valves, which form the CPTL, was accomplished at Y-12 with qualified welding procedures and qualified weldors having a score or more years of experience in assembling high-temperature systems. However, the Y-12 Plant does not have and has not had an ASME N-Stamp authorization. Thus, the ASME N-Stamp was withheld for both the vessel and the piping system.

8.7.2.2 Test Vessel Liner

The stainless steel vessel liner shown in Fig. 8.14 is composed of three sections. The section with largest diameter separates the helium heater and its discharge flow of high-temperature helium from the attemperation helium flow. The other two sections guide the helium flow along the outside of the graphite test structure and separate it from the attemperation flow. The flow of attemperation helium in the space between the

ORNL-PHOTO 8844-82

Fig. 8.14. Three sections of the Core Support Performance Test vessel liner joined together. The lower section surrounds the helium heater, and the middle and upper sections contain the graphite test section and a loading device. The closures for the two inspection ports are in the middle section.

outside diameter of the liner and the inside diameter of the vessel protects the vessel pressure boundary from the high-temperature helium. The test and attemperation helium flows are mixed in a mixing section installed in the test vessel discharge, a length of 10-in. pipe. The discharge nozzle is connected to a 6-in. pipe to transport the mixed helium flow to the inlet of the helium-to-air HX-1.

The two lower sections of the liner contain corrugated metal insulation to reduce the heat transfer between the high-temperature and the attemperation helium flows. Twelve thermocouples are inserted at various elevations in the insulation to permit calculation of the radial heat transfer.

The liner, fabricated in the ORNL Plant and Equipment shops, was installed in the test vessel at the CFTL. The head room between the face of the top Grayloc hub of the vessel and the maximum lifting height of the overhead hoist in the CFTL would just accommodate the longest liner section.

### 3.7.3 Helium Heater Construction and Installation

The two helium heater subassemblies, each rated for 250 kW at 300 V, were fabricated, assembled, and installed in the test vessel with a special installation fixture. Figure 8.15 shows the two subassemblies mounted on the Grayloc blind flange that forms the bottom vessel closure. The helium flows through a 3.0-mm (1/8-in.) radial annulus between the outer surface of the heating element and the inner surface of a 0.063-m-ID (2 1/2-in.) by 0.91-m-long (3-ft) alumina shroud. One shroud has been removed to reveal the heating element.

Figure 8.16 shows the major components of a heater subassembly and support plates. The heating element consists of 140 turns of 5.4-mm-diam (0.214-in.) HT-molybdenum wire mounted onto a threaded alumina mandrel. The HT-molybdenum was selected for the heating element because its recrystallization temperature is above the calculated maximum operating temperature of the element. The two subassembly electrodes are made of arc cast TZM-molybdenum 22 mm (7/8 in.) in diameter. The diameter of the lower portion of the electrodes was reduced to 19 mm (3/4 in.) to pass through similarly sized Conax bulkhead fittings in the vessel closure.

ORNL-PHOTO 8890-82

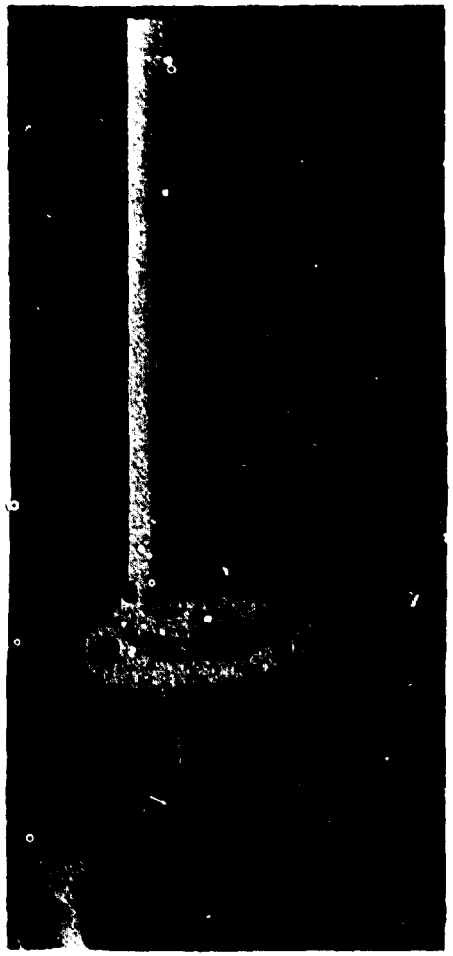

Fig. 8.15. Core Support Performance Test helium heater with two subassemblies installed on Grayloc blind flange closure.

ORNL-PHOTO 8874-82

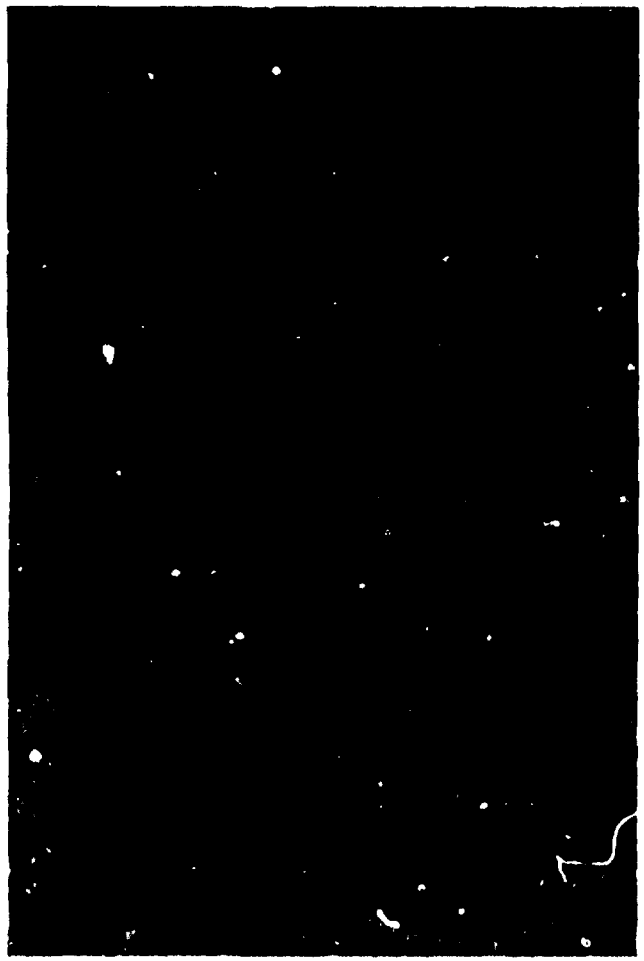

Fig. 8.16. Major components of the heater subassembly and support plate.

The resulting shoulder is supported on a ceramic insulator to transfer the axial pressure load to the Conax fitting. The heating element is supported from a large support plate, and the shroud tube is supported from a small plate in a position that is as concentric about the element as practical.

Because brazing or welding the HT-molybdenum would cause recrystallization and room-temperature embrittlement, the electrical conduction path between the heating element and the electrodes is provided by mechanical connections. The short electrode is connected to the lower end of the heating element with a compression ferrule and threaded fastener. A TZM disk located at the top of the subassembly joins the element to a threaded central electrode. The disk greatly reduces electrical heat generation compared with a pigtail connection originally proposed and also serves as the anchor point for the heating element.

The support plates for the heating elements and the shroud and mandrels for mounting the heating elements, all made of alumina, were fabricated by Coors Porcelain Company, Golden, Colorado. The shroud was produced by McDanel Refractory Company, Beaver Falls, Pennsylvania. All the molybdenum material was purchased by Thermal Electron Corporation (TECO) of Wilmington, Massachusetts, which also wound the heating elements and mounted them on the alumina mandrels.

Coors experienced difficulty producing the long slender alumina mandrels. The first ten, made by a wet-casting process, cracked during firing. The material was changed from 99.8 to 99.5% alumina to permit use of a dry isostatic pressing technique. Problems were then encountered in machining the long unfired mandrels and attempting to remove them from a metal mandrel. The matter was successfully resolved by making two equal lengths of starting material that are fastened together subsequent to firing with the aid of appropriate precision-ground threads to form the mandrel. Later, it was necessary for TECO to regrind the helical grooves on the outer diameter of the mandrel to obtain the accuracy necessary to thread the heating element on the mandrel.

With receipt of the support plates from Coors in mid-October 1982, all the parts were available at ORNL for assembly of the helium heater.

The two 250-kW subassemblies were assembled and mounted on the top side of the Grayloc blind flange that forms the bottom closure of the vessel.

Fabrication of a fixture for installing the heater in the test vessel was completed about the time of the heater assembly. The fixture consists of two assemblies: a fixed upper guide assembly and a movable lower table assembly on which the heater-blind flange assembly is mounted. Controlled vertical motion of the table is provided by three hardened ground rods attached mechanically to the table and slide-in bushings located in the guide assembly. The locations of six bushings in the guide (the two bushings for each rod are located at two elevations about 0.6 m (2 ft) apart to provide guidance) and of the three attachment holes in the table form three congruent equilateral triangles. This configuration requires the table to move vertically with respect to the guide along a fixed path. The guide, in turn, is mounted on machined surfaces on the vessel exterior in a machine design that ensures concentricity between the sealing surfaces on the heater flange assembly and matching sealing surfaces in the vessel. The entire table-flange-heater assembly is lifted with two hydraulic jacks supplied from a single hand-operated pump.

Figure 8.17 shows the heater-flange being installed in the test vessel during a trial demonstration of satisfactory fixture performance.

## 8.8 PLANNING FOR TEST P-1 — R. A. Strehlow and A. G. Grindell

### 8.8.1 Objectives — R. A. Strehlow

TEST P-1 was designed to achieve satisfactory operation of the CFTL and to obtain needed chemical data for later tests. The mechanical objectives include the demonstration of satisfactory loop operation and control over an extended period of four to six weeks. Proper helium flows, pressures, temperatures, and impurity concentrations must be maintained in subsequent tests. These factors are therefore the focus of attention in TEST P-1.

Since later tests of the oxidation of graphite will require knowledge of flows into and from the system, it was necessary to show that the system is leak-tight under several operating conditions. It was also necessary to determine several physical constants of the system, including volume and

ORNL-PHOTO 8694-82

Fig. 8.17. Installation of the heater-flange assembly.

time of response to changes in operating variables such as temperature and the addition of impurities to the system. Temperature control of the gas in the system and satisfactory operation of the heaters constitute the final mechanical objective.

Because of the need to protect the molybdenum heaters from corrosion while permitting corrosion of the graphite to occur at a selected rate, careful attention must be given to the oxidation potential as set by the hydrogen-to-water vapor ratio. This requirement was the principal constraint imposed by chemical considerations. Consideration of the phase relations for molybdenum oxides led to the requirement that the hydrogen-to-water vapor ratio not be less than 10 when the molybdenum heaters are at elevated temperatures.

The principal chemical objective for TEST P-1 is to determine the steady-state values of the components involved in the water-gas shift equilibrium. These values must be determined under conditions distinct enough that the characteristics of the system in this reaction will be known well enough to permit specifying the conditions for subsequent CSPT tests.

### 8.8.2 Procedures for TEST P-1 — A. G. Grindell

The test specifications for TEST P-1 were prepared by the loop operation personnel according to these objectives. The specifications were reviewed by GA personnel and issued as an internal document.

The initial portion of the specifications was used in December 1982 to perform several static tests. The tests, performed at ambient temperature without operation of the helium circulators, provided information on the evacuation characteristics of the CFTL helium system, the leak rates from the system for both evacuated and pressurized conditions, and the volume of the CFTL helium system (Sect. 8.9.3).

## 8.9 INITIAL OPERATION OF TEST P-1 — H. C. Young and A. G. Grindell

The initial test requirements in the test specifications for TEST P-1 were performed during early December 1982 with the components, equipment, and systems installed in the CFTL without disrupting the ongoing Instrumentation and Controls installation work. The test performed provided data on the time required to evacuate the system, the rate of pressure rise from the evacuated state, the rate of pressure loss from the pressurized condition, and the volume of the loop. The remaining tests in the TEST P-1 series involving thermal-flow and thermochemical characteristics will be performed after completion of the Instrumentation and Controls work.

### 8.9.1 Conditions

A pneumatic test of the CFTL primary piping system was completed during a prior testing at 10.34 MPa (1500 psia) with nitrogen as the pressurizing gas. The system contains a number of compression-type static

seals. Each of the three circulators has a 381-mm-diam (15-in.) fluorocarbon Omniseal. The test vessel contains two 406-mm (16-in.) Grayloc flange seal rings, three 102-mm (4-in.) Grayloc flange seal rings, and Conax fittings for the heater electrodes and thermocouple leads. The full-flow helium filter has a 254-mm (10-in.) Grayloc flange, and there are Flexatallic gaskets, which had to be replaced, in the two Copes-Vulcan flow control valves. The Conax seal glands were leak checked with the loop under positive helium pressure with a helium mass spectrometer and a sniffer probe and were retightened satisfactorily.

### 8.9.2 Operations

The system was evacuated with the installed mechanical vacuum pump (Hyvac 150) having a pumping speed of about 1275 L/min at 1-mm Hg pressure. The vacuum pump is closely connected to the CFTL primary system by about 1.83 m (6 ft) of 4-in. pipe. Two 4-in ball valves in series normally isolate the vacuum pump from the primary piping. A quick-closing slide valve would isolate the vacuum pump from the loop if the electrical supply to the vacuum pump were interrupted. A Hastings thermocouple-type vacuum gage with a range of 0 to 1000 μm Hg and a Wallace and Tiernan precision compound gage with a range of 0 to 800 mm Hg were used to measure the pressure during this operation.

The initial rate-of-pressure-loss tests were conducted by pressurizing the primary piping system with helium from a helium trailer, valving off the supply system, and measuring the rate of pressure loss on two calibrated digital pressure indicators with a range of 0 to 10 MPa. The graduations on these indicators were given to 0.001 MPa (0.145 psi).

The volume of the CFTL primary piping system with all components, circulators, test vessel, heat exchanger, filter, and piping was measured by initially pressurizing the CFTL to a pressure just above ambient. A pressurized, standard helium cylinder of known volume was then connected to the loop. The pressure and temperature of the loop and cylinder were permitted to come to equilibrium, and the initial and final pressure were measured with calibrated gages. The volume of the standard cylinder was determined by filling it with water and measuring the change in weight.

### 8.9.3 Results

The static tests were completed and reported internally in December 1982. Dynamic segments of the TEST P-1 series will be initiated in January 1983.

During the evacuation test, the rate of evacuation was initially reduced by valving with one 4-in. ball valve to protect the vacuum pump. When the system pressure was reduced to 145 mm Hg, the ball valves were fully opened. The pressure then dropped from 145 mm Hg to 1000 μm Hg in 14 min, to 30 μm Hg in 25 min, and to 21 μm Hg 2 h later. After valving off the vacuum pump, the rate of pressure rise was 10 μm Hg in 3 min.

The static leak rate with the CFTL filled with helium was determined by pressurizing with helium to 2.89 MPa (420 psig), valving off the supply, and noting the decrease in pressure during a 63-h period. The pressure decay rate was 42.7 kPa (6.2 psi) for a 24-h period. Prorated to the 7.24 MPa (1050 psia) operating pressure for the CSPT series and assuming molecular flow in the leaks, the pressure decay would be 103 kPa (15 psi) per 24 h. A pressure decay rate of 6.9 kPa/h (1 psi) was specified as acceptable.

The system volume was measured with the system initially pressurized to 104 kPa (15.1 psia). A standard helium cylinder having a volume of 0.0-3 $m^3$ (1.532 $ft^3$) and initially pressurized to 11.98 MPa (1738 psia) was connected to the loop and the pressure equalized at 274 kPa (39.8 psia). The barometer was 750 mm Hg, and the ambient temperature was 24°C. The CFTL system volume was determined to be 3.009 $m^3$ (106.3 $ft^3$).

## 8.10 REFERENCES

1. C. D. Bopp and W. P. Eatherly, "Test Operating Conditions," pp. 288–92 in *High-Temperature Gas-Cooled Reactor Technology Development Program Annual Progress Report for the Period Ending December 31, 1981*, ORNL-5871, June 1982.

2. J. H. DeVan, "Compatibility of HT-Molybdenum with $Al_2O_3$ and Carbon" pp. 322–24 in *High-Temperature Gas-Cooled Reactor Technology Development Program Annual Progress Report for Period Ending December 31, 1981*, ORNL-5871, June 1982.

3. W. R. Clark, "Design of Test Vessel and Internals," pp. 296–309 in *High-Temperature Gas-Cooled Reactor Technology Development Program Annual Progress Report for Period Ending December 31, 1981*, ORNL-5871, June 1982.

4. H. C. Young, "Circulator Operation," pp. 324–34 in *High-Temperature Gas-Cooled Reactor Technology Development Program Progress Report for Period Ending December 31, 1982*, ORNL-5871, June 1982.

# 9. APPLICATION AND PROJECT ASSESSMENTS (WBS OR03.1, OR31, and OR41)

P. R. Kasten

Three areas are covered in this chapter: (1) determining the potential market for High-Temperature Gas-Cooled Reactors (HTRs)* by evaluating HTR applications, (2) reviewing economic ground rules and cost factors to be used in assessing the economic performance of HTRs, and (3) evaluating modular-type HTRs. The work performed on HTR application assessments covers fossil conversion processes that could utilize HTRs as an energy source, a review of the experience obtained by industry on the occurrence of steam-methane-reformer fires and explosions (pertinent to HTR reformer applications), and an assessment of the national need for HTRs. The work on economic ground rules and cost factors helps to establish the economic bases used in the national HTR program for estimating the economic performance of HTRs.

The work on modular HTRs evaluates the technical and economic performance of such systems. Modular HTRs are proposed as a means of obtaining an inherently very safe reactor system. The basic approach is to design a system that, even under such extreme conditions as loss of reactor pressure and loss of forced convection cooling of the core, the fuel temperature will always remain below temperatures at which fuel retains nearly all the fission products and actinides. Because of the high heat capacity and heat conduction of the core materials, we can use a low power density and a small reactor core diameter to design an HTR with fuel temperatures that are inherently limited to relatively low values. Such a design leads to relatively low reactor power levels of about 250 MW(t), which tends to give

*The term HTR is used here rather than HTGR to indicate that either prismatic-fueled HTGRs or pebble-bed-fueled Pebble-Bed Reactors (PBRs) are considered.

high unit costs for power production. An important item is to determine how such a high degree of safety might impact both equipment and plant requirements and plant construction time. It might be possible that such small reactors when used in modular systems are relatively economic in comparison with a large single power unit; achieving such a degree of safety in an economic plant would be very desirable. Further, HTRs are well suited for generating high-temperature process heat, and small units might mesh into process heat applications and provide a broader application of nuclear energy than that achieved to date. Therefore, modular HTR studies are being conducted under the U.S. national HTR program, with GA Technologies, Inc. (GA), and General Electric Company (GE) developing a design for a High-Temperature Gas-Cooled Reactor (HTGR)(with prismatic fuel elements) and with GE developing a design for a pebble-bed reactor (PBR) (with pebble-bed fuel elements). Oak Ridge National Laboratory (ORNL) is serving as the peer reviewer of the relative technical and economic merits of these design studies and evaluations.

## 9.1 MARKET DEFINITION AND ASSESSMENT — W. R. Gambill

### 9.1.1 HTR Application to Fossil Conversion Processes

Based on 11 economic assumptions, the financial present values (PV) of avoided fossil fuel feedstock costs were calculated for 11 cases of HTGR application [both steam cycle-cogeneration (SC-C) and very high temperature reactor (VHTR)] to fossil conversion processes. The processes considered were ECCG (Exxon Catalytic Coal Gasification), H-Coal (standard and modified), and SRC (Solvent Refined Coal)-II for coal conversion; TOSCO-II and Paraho-Indirect for shale oil production; and steam reforming of natural gas to produce $H_2$ or synthesis gas ($CO + H_2$) for chemicals production (e.g., methanol). Using the ratio of PV to HTGR thermal power in units of $\$10^6$/MW(t) as an index of merit, we found that the most promising application is the reforming of natural gas for chemicals production, followed by surface retorting of oil shale to produce pipelineable oil and by coal conversion (catalytic and noncatalytic direct coal liquefaction and catalytic coal gasification).

For the various feedstocks, the average ratio of PV to thermal power was 2.00 for natural gas, 1.68 for oil shale, and 0.66 for coal. This work was reported in a paper[1] presented at the British Nuclear Energy Society conference on Gas-Cooled Reactors Today at Bristol, England, in September 1982.

### 9.1.2 Steam Methane Reformer Fires and Explosions

A survey was made of the frequencies of explosions and fires in operating steam-methane reformers (SMRs). The salient conclusions were as follows:

- There appears to have been only one SMR explosion in recent times, that at the SASOL-I plant in South Africa on April 14, 1975, which killed seven employees and injured seven others.
- Over the past 30 years, Exxon (worldwide, not just USA) has experienced two SMR fires but no explosions. It appears that with proper design such incidents will be very rare.
- HTGR reformers differ qualitatively from current fired SMRs because there is no hot-side flame combined with excess oxygen and because the heat source (helium) is inert. These differences appear to lead to a lower probability for occurrence of an internal reformer explosion or fire and to a higher probability for a combustible vapor cloud to be released by leakage or pressure-boundary failure, followed by an unconfined vapor cloud explosion (UVCE).
- Electric Power Research Institute (EPRI) work concerning light water reactor (LWR) safety[2] has shown that the presence of steam provides a mitigating effect on maximum $H_2$ combustion overpressures and that water sprays or water fog has a dramatic limiting effect on combustion pressures in dynamic hydrogen injection experiments.
- In two broad surveys of UVCE incidents,[3-4] none appear to have been caused by SMRs.

### 9.1.3 HTGRs and National Needs

A study was performed to relate HTGR applications of various types to national needs and to project the relationship to approximately the year 2025. The following is a brief summary of work performed to date.

Conventional energy projections nearly always indicate that growth rates decrease monotonically with time; consequently, historically observable fluctuations in energy growth are ignored. An alternative projection methodology has been described by Stewart in his book about transitional energy policies[5] and in two papers.[6-7] His approach is based on the observation that both total energy and electrical energy consumption rates in the United States (since 1850 for the former and 1905 for the latter) have exhibited a cyclic variation about a median logistic growth curve.

Stewart has applied the cyclic pattern of energy growth to projections of future energy consumption according to what he calls the cycle-adjusted-logistic (CAL) growth. The result[6] indicates a relatively flat total energy consumption until about the year 2000, with electrical energy growing at about 2% per annum during the same period. This CAL projection, however, forecasts a very rapid energy growth rate between the years 2000 and 2025, which will more than make up for the relative stagnation between 1980 and 2000.

9.1.3.1 Electrical Energy and the HTGR

The CAL projections indicate increasing electrification, the portion of energy used for electricity generation increasing from the present level of about 34% to almost 50% by 2000 and to about 63% by 2025. Stewart produced growth projections for U.S. nuclear energy[7] by combining the total energy growth projected by the CAL methodology with the results of Marchetti's energy substitution data for fractional market penetration.[8-9] A revised and updated version is presented in Table 9.1, in which:

- base year data are for 1982,
- average nuclear plant load factors are taken as 55% through 1990 and as 65% for later years,
- all additional LWRs are 3800-MW(t) reactors [currently ~1260 MW(e)], and
- the number of HTGRs represents 5% of nuclear additions (because of application to arid areas and siting features) after the year 2000.

Table 9.1 projects the use of 48 power-producing HTGRs over the next 47 years even with a minimal nuclear market penetration of 5%. An additional

Table 9.1. Electrical energy growth projections for the United States

(A partial revision of Stewart's 1981 projection[a])

| Year | Total energy[b] | | Fractional energy[c] (%) | | Generating capacity [GW(e)] | | Number LWRs[f] | Number HTGRs[g] |
|---|---|---|---|---|---|---|---|---|
| | (TW years) | (quads) | Electricity input | Nuclear input | Total[d] | Revised nuclear[e] | | |
| 1990 | 2.24 | 67 | 42 | 7 | 700 | 94 | 99 | 1 |
| 2000 | 2.41 | 72 | 49 | 10 | 930 | 132 | 129 | 2[h] |
| 2010 | 3.28 | 98 | 57 | 24 | 1490 | 434 | 371 | 14 |
| 2020 | 4.41 | 132 | 61 | 34 | 2270 | 876 | 725 | 32 |
| 2030 | 4.88 | 146 | 64 | 43 | 2770 | 1288 | 1055 | 48 |

[a]*Source:* H. B. Stewart, "Economic Growth as Affected by Technologies," presented at Gas-Cooled Reactor Associates Utility/User Conference on the HTGR, San Diego, Calif., Sept. 10-11, 1981.

[b]1981 projection.

[c]Percent of total energy.

[d]Assumes total system load factor of 45% and an average thermal efficiency increase from 33% in 1990 to 40% in 2030.

[e]With average nuclear load factors stated previously and thermal efficiency as in footnote *d*.

[f]If all nuclear reactors were light water reactors (LWRs) [3800 MW(t) each for additions]; 60 GW(e) and 72 LWRs in 1982.

[g]For 5% of nuclear additions being High-Temperature Gas-Cooled Reactors (HTGRs) beginning in 2001; 3300 MW(t) each.

[h]Fort St. Vrain Reactor (FSVR) + one new unit.

factor that could lead to a much higher HTGR market share is related below to an extensive study of precursors to potential severe core damage in LWRs, as reported by Cottrell[10] and by Minarick and Kukielka.[11-12] In these studies, the probability of severe core damage (SCD) of the Three Mile Island (TMI)-2 type was estimated to be $1.7 \times 10^{-3}$ to $4.6 \times 10^{-3}$ per reactor year. Table 9.2 results when an SCD $p = 0.0017$ per reactor year is combined with column eight of Table 9.1.

On the basis of the results in Table 9.2, a post-TMI-2 reduction by at least an order of magnitude would appear to be necessary, that is, to

Table 9.2. Estimate of number of severe core damage events

| Year | Severe core damage events[a] | |
|---|---|---|
| | Number/year[b] | Cumulative number[b] |
| 1990 | 0.2 | 1.3 |
| 2000 | 0.2 | 3.2 |
| 2010 | 0.6 | 7.4 |
| 2020 | 1.2 | 16.7 |
| 2030 | 1.8 | 31.9 |

[a]For case of only light water nuclear reactors. Rounded to nearest tenth.

[b]For $p = 0.0017$ per reactor year.

$p = 0.00017$ per reactor year or lower. This apparently can be accomplished in LWRs either by changes already incorporated into or by future changes in design and operation. However, another way of attaining this or a greater reduction would be to use HTGRs, which are characterized by several inherent safety features not shared by LWRs. Use of HTGRs for this purpose would increase the market share of HTGRs.

9.1.3.2 Nonelectrical Energy and the HTGR

Because of its high core-exit coolant temperature, the HTGR permits the application of nuclear energy to processes now using fossil fuels. These processes encompass resource recovery (tar sands and heavy crude oil), synthetic fuels production (from coal and oil shale), chemicals production (e.g., $H_2$, ammonia, and methanol by initially steam reforming natural gas), and delivery of process heat, primarily as high-temperature-high-pressure process steam (either directly by pipeline or indirectly by on-site generation with pumped molten salt). In each of the above four categories, the useful production rate per unit of fossil fuel consumption is enhanced by HTGR use compared with the alternative of fossil fuel use as the energy source.

Low and high estimates were made of the number of HTGRs that might suitably be applied by 2020 to 2025 in each of the four categories. An HTGR load factor of 70% was assumed for these nonelectrical applications. The resulting energy totals were then compared with projected nonelectrical energy needs derived by the CAL methodology.

### 9.1.3.3 Projected Totals

Summation of the sectoral projections gave the following totals for approximately the year 2020:

| Case | Total HTGR [GW(t)] | Total number 1170-MW(t) HTGRs | Electrical power (%) | Nonelectrical [GW(t)] |
|---|---|---|---|---|
| Low | 195.4 | 167 | 54 | 90.1 |
| High | 885.7 | 757 | 59 | 359.2 |

### 9.1.3.4 Comparison with Cycle-Adjusted-Logistic-Growth Projection for Nonelectrical Energy

The CAL methodology projects the nonelectrical energy component to remain fairly constant to the year 2025, at about 1.84 TW years/year (~55 quads/year). The nonelectricity uses include transportation, comfort heat, and industrial process heat. About 90% of these demands are currently met by oil and natural gas. We assumed, as did Stewart[6] in 1980, that the available supply of economically recoverable (conventional) gas and oil will be reduced by 50% by the year 2025. Although somewhat arbitrary, this projection is similar to that of the U.S. Department of Energy (DOE) for the United States and to that of the International Institute for Applied Systems Analysis for the world.[13] The latter organization, for example, has forecast that in 2025 about 50% of the total global oil consumption will be conventional petroleum. Given this projection, about 0.84 TW year/year (25 quads/year) of energy for nonelectrical uses now supplied by oil and gas must, by 2025, be supplied by alternative energy sources such as nuclear, coal, and solar energy.

The total HTGR nonelectrical capacity of 90.1 GW(t) (low case) corresponds to a 7.6% share of the substituted 0.84 TW year/year (25 quads/year)

and to only 3.4% of the 1.84 TW years/year (55 quads/year) of total nonelectrical energy. The high-case HTGR nonelectrical capacity of 359.2 GW(t) represents a 30.1% share of the substituted 0.84 TW year/year (25 quads/year) and 13.7% of the 1.84 TW years/year (55 quads/year) total.

## 9.2 REVIEW OF ECONOMIC GROUND RULES TO BE USED IN FUEL COST AND ALTERNATIVE ENERGY COST ESTIMATES — H. I. Bowers

The economic ground rules and assumptions developed by Gas Cooled Reactor Associates (GCRA) for the HTGR program have been reviewed throughout the year. An active part was taken in the workshop held at GCRA on December 15–16, 1982, to develop the fiscal year 1983 ground rules. Subsequently, we reviewed the December 22, 1982, Revision 1, economic ground rules distributed by GCRA and made the following comments.

In general, the values of the economic parameters recommended by GCRA fall within the range of values recommended in DOE/NE-0044, Version 1, *Nuclear Energy Cost Data Base*,[14] which was developed at ORNL for the DOE Nuclear Energy Division of Plans and Evaluations. As an overall observation, GCRA recommends higher coal costs and lower oil, natural gas, and $U_3O_8$ costs. Fossil fuel cost projections are those reported by Data Resources, Inc. (DRI), in the autumn 1982 *Energy Review*.[15] The DRI forecasts are based on assumptions of no new nuclear plant orders before the year 2000, no disruption of world oil supplies, and moderate economic recovery. These assumptions result in high coal prices, low oil and gas prices, and low uranium ore prices, compared with the forecasts reported in the DOE-EIA 1981 Annual Report to Congress, which have been used and summarized in DOE/NE-0044, Version 1. The DRI forecasts were about a year later, and the Energy Information Agency's (EIA's) 1982 forecasts will not be available until April 1983. However, the fuel cost projections are all within an acceptable range, and there is considerable uncertainty in all the values.

Thus, it is recommended that all economic comparisons include sensitivity analyses of the principal cost drivers. As a minimum, cost-sensitivity analyses should be performed for capital investment costs and fuel costs for both nuclear and fossil plants.

## 9.3 MODULAR REACTOR STUDIES — P. R. Kasten

The review work reported here covers efforts on reactor physics, fuel cycle costs, and fuel temperatures; fuel performance and permissible maximum temperatures; evaluation of pressure vessels; and review of maintenance and in-service inspection requirements, construction schedule, and balance of plant design and costs.

### 9.3.1 Reactor Physics, Fuel Cycle Costs, and Fuel Temperatures — B. A. Worley

The continuously fueled PBR was investigated under the U.S. Modular Reactor Study as an alternative to the prismatic, fixed-fueled HTGR core design. We recognize that the incorporation of a PBR might induce plant and/or reactor design changes, but, under the limited scope of this study, the reactor core size was kept identical to the reference 250 MW(t) HTGR core.

The core cavity of the modular reactor design being investigated in the United States[16] can accommodate a PBR core with a diameter of 3.49 m and a height of 6.34 m. For the reference core power of 250 MW(t), the resulting power density is 4.12 MW(t)/m$^3$. The fuel is uranium and thorium with a uranium mass enrichment of 0.20. The core inlet and outlet temperatures for the PBR were picked to be 250 and 950°C compared with 525 and 950°C for the HTGR core. The lower inlet temperature for the PBR is consistent with plant temperatures for process heat applications of the PBR from German design studies. The objective of the work reported here is to summarize the neutronic and thermal hydraulic characteristics of the reference 250 MW(t) PBR modular reactor.

An interesting option in using a PBR is the number of times a pebble can be passed through the core for a given fuel residence time. For example, for a residence time of 1168 full-power days, the pebbles can pass once through the core in 1168 days, twice through the core in 584 days per pass, and so on. The number of passes affects the core neutronic and thermohydraulic characteristics. With pebbles flowing from the top of the core to the bottom and with coolant downflow, passing the pebbles once through the core results in optimum reactor performance.[17] However, the

reference modular core design has coolant upflow to enhance decay-heat removal following accidental loss of main coolant circulation.

Coolant upflow affects fuel temperatures to the extent that immediate recycle of the fueled pebbles from the core discharge path to the pebble feed stream is desirable. We found that five pebble passes through the core considerably reduce the peak power density and lower the axial position of the peak so that fuel temperature peaking is reduced. More than five passes improve the performance, but only slightly. Subsequent analysis was performed for five pebble passes.

The core design of the 250 MW(t) PBR are summarized in Table 9.3, and the neutronic and thermal hydraulic characteristics for both the four- and five-year cases, in Table 9.4. For the continuously fueled modular PBR, a longer pebble residence time in the core reduces the $^{235}U$ feed rate up to a five-year core residence time (four full-power years at a 0.8 load factor). Coolant and fuel temperatures calculated for normal flow conditions gave a peak temperature of less than 1200°C. The pebble graphite thermal conductivity decrease as a function of neutron exposure was modeled by separate accounting of pebble fluence as the pebbles were recycled through the core. Also, the pebble surface temperatures were

Table 9.3. Design parameters of 250-MW(t) modular pebble-bed reactor

| Reactor design parameter | Value |
|---|---|
| Reactor power, MW(t) | 250.00 |
| Core diameter, m | 3.49 |
| Core height, m | 6.34 |
| Average core power density, MW(t)/m$^3$ | 4.12 |
| Top reflector thickness, m | 1.0 |
| Bottom reflector thickness, m | 1.0 |
| Side reflector thickness, m | 1.0 |
| Top gas gap thickness, m | 1.0 |
| Number of pebbles in core | 327,120 |
| Average inlet coolant temperature, °C | 250.0 |
| Average outlet coolant temperature, °C | 950.0 |
| Inlet pressure, MPa (atm) | 4.0 |
| Pebble diameter, mm | 60.0 |
| Pebble fueled region diameter, mm | 50.0 |
| Heavy metal (U + Th) per pebble, g | 8.26 |
| Number of pebble passes through core | 5 |

**Table 9.4. Results of performance calculations from two-dimensional representation of 250-MW(t) modular pebble-bed reactor**

| Case | Five-Year | Four-Year |
|---|---|---|
| Uranium enrichment, % | 20.0 | 20.0 |
| Pebble (C/U + Th), atom ratio | 450.1 | 450.1 |
| Pebble C/Th, atom ratio | 1033.6 | 841.0 |
| Fuel residence time at full power, d | 1460.0 | 1168.0 |
| Average fuel burnup, TJ/kg [MW(t)-d/kg] | 11.68 (135.2) | 9.37 (108.4) |
| *Core neutronic characteristics* | | |
| Conversion ratio | 0.52 | 0.54 |
| Fission product loss, % | 9.03 | 8.47 |
| Loss from core | | |
| Leakage loss, % | 6.37 | 6.66 |
| Absorption loss in top reflector, % | 1.16 | 1.15 |
| Absorption loss in bottom reflector, % | 0.19 | 0.22 |
| Absorption loss in side reflector, % | 2.71 | 2.88 |
| Total loss from core, % | 10.43 | 10.91 |
| Fissile inventory in core, kg | 145.94 | 131.31 |
| Peak pebble-averaged power, kW per pebble | 3.29 | 3.17 |
| Core-average peak power density, W(t)/cm$^3$ | 7.48 | 7.35 |
| *Feed rates (grams per full-power day)* | | |
| $^{235}U$ | 211.0 | 217.1 |
| $^{238}U$ | 843.9 | 868.4 |
| $^{232}Th$ | 795.2 | 1221.6 |
| *Discharge rates (grams per full-power day)* | | |
| $^{233}U$ | 20.2 | 28.4 |
| $^{234}U$ | 3.7 | 5.0 |
| $^{235}U$ | 17.4 | 21.5 |
| $^{236}U$ | 30.0 | 30.8 |
| $^{238}U$ | 752.2 | 789.5 |
| $^{237}Np$ | 3.3 | 2.8 |
| $^{232}Th$ | 736.4 | 1143.6 |
| $^{233}Pa$ | 0.8 | 1.6 |
| $^{239}Pu$ | 7.5 | 7.6 |
| $^{240}Pu$ | 5.3 | 4.9 |
| $^{241}Pu$ | 3.7 | 3.4 |
| $^{242}Pu$ | 3.3 | 3.9 |
| *Thermal-hydraulic and temperature characteristics* | | |
| Pressure drop, MPa (atm) | 0.274 (0.270) | 0.278 (0.274) |
| Coolant mass flow rate, kg/s | 68.8 | 68.8 |
| Peak outlet coolant temperature, °C | 1088.8 | 1100.3 |
| Core-average, volume-averaged fuel temperature, °C | 609.6 | 618.4 |
| Core-average, power-weighted fuel temperature, °C | 678.8 | 676.7 |
| Peak pebble surface temperature, °C | 1110.7 | 1120.3 |
| Peak fuel temperature averaged over pebble fuel, °C | 1145.8 | 1150.7 |
| Peak fuel temperature in pebble fuel, °C | 1174.6 | 1176.9 |
| *Cumulative fraction of the fuel above reference temperatures* | | |
| Temperature (°C) | | |
| 1200 | 0.0 | 0.0 |
| 1175 | 0.0 | 0.00003 |
| 1150 | 0.00094 | 0.00119 |
| 1125 | 0.00349 | 0.00447 |
| 1100 | 0.00826 | 0.00987 |
| 1000 | 0.05805 | 0.06169 |
| 900 | 0.16697 | 0.16845 |
| 800 | 0.28551 | 0.29510 |
| 700 | 0.38047 | 0.29360 |
| 600 | 0.47598 | 0.49184 |
| 500 | 0.58349 | 0.60089 |
| 400 | 0.71708 | 0.73382 |
| 300 | 0.91232 | 0.92163 |
| 200 | 1.0 | 1.0 |

adjusted to reflect local power peaking within zones. However, local peaking that may occur as a result of local flow blockage (i.e., random pebble packing) was not taken into account.

Fuel cycle costs for the reference U.S. modular HTGR and the modular four- and five-year PBR cases were calculated on the basis of the reference economic assumptions given in Table 9.5. Table 9.6 summarizes the costs and shows the lower fuel cycle cost of the PBR, the five-year fuel exposure being most economical of all. The HTGR is batch-refueled every four years. Current work under the U.S. Modular Reactor Study is an investigation of a batch two-year HTGR, which will lower the HTGR fuel cycle cost but probably at the expense of a lower availability.

Table 9.5. Reference cost and economic assumptions

| | |
|---|---|
| Startup date | 1995 |
| Capacity factor | 0.8 |
| Inflation rate, % | 8.0 |
| Ore escalation above inflation, % | 2.5 |
| Tails array, % | 0.2 |
| Discount rate, no inflation, % | 5.5 |
| Discount rate, with inflation, % | 14.0 |
| Interest rate, no inflation, % | 8.5 |
| Interest rate, with inflation, % | 21.2 |
| Fuel costs (1995 $) | |
| $U_3O_8$, $/kg ($/lb) | 88.18 (40.0) |
| Enrichment, $/kg | 140.0 |
| Conversion, $/kg | 6.0 |
| Handling charges, HTGR (1982 $)[a] | |
| Fabrication, low-enriched uranium | 8880/fuel element |
| Fabrication, high-enriched uranium | 7900/fuel element |
| Shipping | 3650/fuel element |
| Waste storage | 9350/fuel element |

[a]For the Pebble-Bed Reactor (PBR), the unit handling charges were taken to equal High-Temperature Gas-Cooled Reactor (HTGR) handling charges in terms of mills/kWh(e) for a given volume of fuel elements. This is valid for shipping and waste storage costs; it tends to penalize the PBR with regard to fuel fabrication costs but not significantly.

Table 9.6. Fuel cycle costs for 250-MW(t) High-Temperature Gas-Cooled Reactor (HTGR) and Pebble-Bed Reactor (PBR)

| | Levelized 30-year costs [mills/kWh(e)] | | | | | |
|---|---|---|---|---|---|---|
| | Constant dollar | | | Inflated dollar | | |
| | HTGR-4[a] | PBR-4[a] | PBR-5[b] | HTGR-4 | PBR-4 | PBR-5 |
| Fuel | 13.21 | 7.57 | 7.30 | 78.41 | 45.06 | 45.78 |
| Fabrication | 2.59 | 3.20 | 2.74 | 15.49 | 19.15 | 16.75 |
| Shipping | 0.69 | 0.69 | 0.52 | 2.63 | 2.63 | 2.63 |
| Waste | 1.85 | 1.85 | 1.40 | 7.79 | 7.79 | 7.79 |
| Total | 18.34 | 13.31 | 11.96 | 104.32 | 74.63 | 72.95 |

[a]Four-year fuel residence time; HTGR reload cycle is every four years.

[b]Five-year fuel residence time.

### 9.3.2 Permissible Fuel Temperatures Under Accident Conditions for Modular HTR — F. J. Homan and P. R. Kasten

This section summarizes pertinent information available on permissible maximum fuel temperatures under extreme accident conditions, which still leads to the long-term retention of fission products, the maximum temperature that we judge should be specified, and the bases for that value. The pertinent data utilized follow.

Out-of-reactor heating of previously irradiated particles to study kinetics of fission product attack of the SiC coatings and fission product release as given in refs. 18 and 19; core heatup experiments in which previously irradiated particles were heated from temperatures of about 1100 to about 2800°C at controlled rates (for the data presented in ref. 20 the heatup times ranged from 8 to 80 h); thermal cycling of cell 1 in capsule P13S. Fuel in this cell was cycled 24 times to temperatures of 200 to 400°C higher than the nominal irradiation temperature of 1200°C for these two capsules. Fission gas release measurements were compared with measurements taken on fuel irradiated in cell 1 of capsule P13R, which contained identical fuel but was not thermal cycled.[21]

As evaluated here, the selection of a maximum permissible fuel temperature for the modular reactor system (MRS) is aimed at having a system that can sustain a core heatup accident, recover from the accident, and continue operating in the normal mode. The temperatures reached in the core during the accident would not be high enough to damage the fuel to the extent that activity after restart would be above acceptable levels.

9.3.2.1 Evaluation of Existing Data

Information in ref. 20 indicates that Triso-coated fuel particles begin to fail at temperatures of about 1300°C but that the fraction of failed fuel is less than 1% at temperatures below about 1600°C; above 1700°C, the failure fraction increases significantly with temperature. Thus, maximum temperatures during accident conditions in the 1500 to 1600°C range are emphasized below.

9.3.2.2 Fission Product–SiC Interactions

The attack rate of SiC coatings by the rare earth fission products, presented in ref. 18, is a strong function of temperature. The attack rate of 1600°C is about 3.3 times higher than the attack rate at 1500°C, and this is significant if the transients are expected to be of long duration (several days). In 24 h, less than 1 μm of attack is predicted at 1600°C. Palladium attack of SiC occurs in both oxide and carbide fuels. Moreover, palladium attack is somewhat more rapid than is rare earth attack at temperatures above 1400°C (ref. 22). Available data suggest that about 1.2 μm of palladium attack can be expected in 24 h at 1600°C.

9.3.2.3 Thermal Cycling Data

The pertinent data are given in ref. 21. Cell 1 of capsule P13S was thermal cycled 24 times at temperatures ranging from 1400 to 1600°C from the base operating temperature of between 1100°C and 1200°C. Compared with release-to-birth (R:B) values of $^{85m}Kr$ obtained from specimens not thermally cycled, the thermally cycled specimens had $^{85m}Kr$ R:B values about a factor of 10 higher than those not cycled. These performance differences were the result of repeated thermal cycling, with each thermal

cycle lasting an hour; about half an hour was taken to increase the temperature to 1600°C, and ¿ h was taken to reduce the temperature to the base value. If the fission product SiC attack rates discussed in refs. 18 and 22 are applied, as much as 20 μm of attack could have occurred in some particles as a result of the thermal cycling. However, no significant fission product attack of the SiC was noted during metallographic examination of the fuel.[21]

In other tests,[21] increasing fuel temperatures from 1100 to 1600°C (in steps) and back to 1100°C during TRIGA reactor exposure testing gave $^{85m}$Kr R:B values three orders of magnitude higher than that expected if no additional fuel failures occurred during the cycling.

9.3.2.4 Conclusions

More damage clearly occurs to the fuel during temperature excursions to 1600°C than during excursions to 1500°C, so the decision as to the maximum temperature to use for safety design is based on the trade-off between the conservatism associated with improved fission product retention and the economic penalties due to that conservatism. The penalty for selecting too high a maximum temperature is that either too many fission products are released, which impacts licensing requirements on the plant, or that the fuel is so damaged by an accident that it subsequently cannot operate within the technical specifications and must be replaced.

It is probable that temperatures higher than 1600°C can be tolerated for short periods. The temperature level decision should be revieved after the transient durations are better known and more information on the trade-offs mentioned earlier is available. To indicate the kind of change that might take place, we estimate that the 1600°C value might increase to about 1700°C. However, at this time, we recommend a maximum design temperature of 1600°C, considering that exposed fuel will be utilized after an accident. The permissible temperature would be higher if exposed fuel were replaced with fresh fuel following severe accidents and probably could increase to perhaps 2000°C, although a specific analysis has not yet been performed.

### 9.3.3 Evaluation of Pressure Vessels for Modular HTRs — D. J. Naus and H. I. Bowers

Small MRSs offer potential advantages over larger HTGR-SC-C systems currently under investigation. Some of these potential advantages include complete replacement of individual units, assured shutdown cooling, high availability, reduced technical risks, and competitive capital investment costs and economics. As a part of the overall assessment of MRSs being performed at ORNL, an evaluation of pressure vessel concepts for application to these systems has been conducted.

In comparing the various pressure vessel concepts, several study parameters were utilized. They included modular reactor systems, with each module having a core thermal power of about 250 MW(t), a core inlet temperature of 425°C, a core outlet temperature of 950°C, a core geometry 6.34 m high by 3.5 m in diameter, and a design pressure of 4.8 MPa. The primary system of each module was based on the in-line reactor-reformer design, which included a core, a steam reformer, a steam generator, and a helium circulator. The entire primary coolant system was enclosed in a pressure vessel.

Three candidate pressure vessel concepts were considered in the study: prestressed concrete, prestressed cast iron, and steel. Each of these concepts was reviewed with respect to (1) general description; (2) materials and fabrication; (3) design and analysis; (4) experience; (5) advantages and limitations; (6) requirements for quality assurance, structural integrity testing, and in-service inspection; and (7) failure modes and repair considerations. Designs for each of the concepts for a 250-MW(t) reactor system were either obtained from background material [prestressed concrete reactor vessel (PCRV) and steel vessel] or were developed [prestressed cast-iron vessel (PCIV)]. A qualitative comparison between each of the concepts relative to technical, safety, and economic issues was also made. Study results indicate that both steel and prestressed concrete are viable as pressure vessel concepts for MRSs (ref. 23).

Cost estimates were developed for a PCRV and for a steel reactor vessel for application to an MRS. The study indicates that, for comparable systems, the installed direct costs will be about $17 million for

the PCRV system and about $29 million for the steel vessel system. These costs should be considered only as indicative of relative costs, with lesser confidence in their absolute values.

There are considerations that should be evaluated in addition to direct costs. For example, the different pressure vessel configurations being used suggest important differences in the plant structures. The PCRV is about 12 m in diameter and 27 m high, and the steel vessel is 6 m in diameter and 35 m high. Also, clearances must be provided for the PCRV wire-winding and tensioning machines, and seismic restraints may be required for the steel vessel. Further, use of a PCRV may affect the overall plant construction schedule adversely, because the PCRV may have to be built in series with the building structure, whereas the steel vessel can be fabricated offsite on a parallel schedule.

Another consideration is the integrity of the cooling lines used with the ultimate heat sink. For the steel vessel, any leakage of water from the cooling lines is maintained outside the reactor vessel; for the PCRV, any such coolant leakage would introduce water within the pressure vessel, and this would be a disadvantage. However, the integrity of the coolant lines can be made very high, particularly since they could normally operate at a pressure low enough that water leakage into the reactor would be highly improbable. A quantitative evaluation of the reliability of cooling pipes has not been made.

No firm conclusions can be drawn at this time from the above cost information. However, the use of a PCRV should not be excluded. The impact of PCRV use on the plant construction schedule needs to be evaluated, because it could be significant.

### 9.3.4 Review of Maintenance and In-Service Inspection Requirements, Construction Schedule, and Balance of Plant Design and Costs — H. I. Bowers

A review of the GE report, *A Preliminary Assessment of the Maintenance and In-Service Inspection Requirements for Modular Reactor Systems*, by C. R. Davis[24] indicates that it is reasonably complete and covers most areas in about the right depth. The author points out that the estimated

times are probably optimistic for the first plant. An important shortcoming of the report concerns the steam generator. A comparison GE report, *A Preliminary Assessment of the Availability and Capacity Factors for a Modular Reactor System with Reformer (MRS-R)* by C. R. Hermann and O. Gokuk[25] estimates about 50 years' meantime to failure (MTF) for steam generator leaks for a single module. On this basis, no allowance is made between refuelings for unscheduled outages due to steam generator leaks. Furthermore, the design of the reactor vessel requires removal of the upper half of the vessel for steam generator replacement. Although helium-to-water-steam heat exchangers should be highly reliable, 50 years' MTF appears to be extremely optimistic. It is therefore recommended that an additional assessment of MTF for steam generators be made and that an assessment of the practicability of steam generator replacement be made.

A review was made of the construction schedule for an eight-module MRS-reformer plant to be constructed in sets of four modules, presented by Bechtel (BGI) at the MRS Evaluation Coordination Meeting between BGI and GE on July 2, 1982. The schedule is based on two sources of supply for the reactor vessels and a 48-month manufacturing lead time for delivery of the first vessel. Reactor vessels must be ordered about 14 months before start of construction. If the construction schedule is to be shortened, either the vessels must be ordered earlier or the vessel manufacturing schedule must be improved. This schedule appears to be the minimum construction schedule for a plant designed and constructed in sets of four units. However, if the plant is designed, constructed, and operated in a 100% modular approach (single-unit sets), it might be possible to start commercial operation of the first module 48 months after start of construction, with subsequent modules following at intervals of 3 to 6 months, but the total construction schedule for eight units would be longer, that is, 69 to 90 months. In summary, the BGI schedule is as optimistic as should be developed with currently available information. The schedule should be refined as the design progresses.

The BGI reports, *Modular HTGR Balance of Plant Design and Cost Status Report*[26] and *Monolithic Versus Modular HTGR Cost Comparison Report*,[27]

published in September 1982, were reviewed. They are reasonably complete and have followed the designated study ground rules and economic assumptions closely. The economic comparisons are sufficiently favorable to the MRS to warrant continued study of this concept. Reduction in fuel cycle costs could make both reactor concepts more attractive. Future work should include economic comparisons with conventional sources of process steam, including coal-fired boilers. It is not possible to examine the capital investment cost estimates in detail because they are presented at only the major account level. The cost estimates were developed by a combination of materials and equipment takeoff, scaling, and factoring. The capital investment cost estimates may be too optimistic, being based on an *n*th plant, tight construction schedule, and favorable regulatory actions. However, modest increases in costs should not significantly alter the overall results of the analyses.

## 9.4. REFERENCES

1. W. R. Gambill and C. O. Peinado, *Economic Evaluations of HTGR Applications to Fossil-Fuel Conversion Processes*, GA-A16745, GA Technologies, Inc., San Diego, Calif., May 1982; also see Proceedings of British Nuclear Energy Society Conference on Gas-Cooled Reactors Today, Bristol, England, Sept. 20–24, 1982.

2. L. Thompson, "EPRI Research on Hydrogen Combustion and Control for Nuclear Reactor Safety," pp. 1675–84 in *Hydrogen Energy Progress – IV*, Proceedings of the 4th World Hydrogen Energy Conference, Pasadena, Calif., June 13–17, 1982, Pergamon Press, Elmsford, N.Y., 1982.

3. K. Gugan, *Unconfined Vapor Cloud Explosions*, Gulf Publishing Co., Houston, Tex., 1979.

4. J. A. Davenport, "A Survey of Vapor Cloud Explosions," *Chem. Eng. Prog.* 73(9), 54–63 (September 1977).

5. H. B. Stewart, *Transitional Energy Policy, 1980–2030, Alternative Nuclear Technologies*, Pergamon Press, Elmsford, N.Y., 1981.

6. H. B. Stewart, "Energy Growth Projections and the Role of the HTGR," presented at Gas-Cooled Reactor Associates Utility/User Conference on the HTGR, San Diego, Calif., Sept. 30–Oct. 1, 1980.

7. H. B. Stewart, "Economic Growth as Affected by Technologies," presented at Gas-Cooled Reactor Associates Utility/User Conference on the HTGR, San Diego, Calif., Sept. 10–11, 1981.

8. C. Marchetti, "Glimpses into the Pre-Programmed Society: On Energy, Invention, Innovation, and Other Things," IIASA paper, International Institute for Applied Systems Analysis, Laxenburg, Austria, 1980.

9. C. Marchetti, "Society as a Learning System: Discovery, Invention, and Innovation Cycles Revisited," IIASA paper, International Institute for Applied Systems Analysis, Laxenburg, Austria, October 1980.

10. W. B. Cottrell, "Progress in Reactor Operating Experience Studies: A Focus on Precursors to Severe Core Damage," presented at ORNL Engineering Technology Division Annual Information Meeting, Oak Ridge, Tenn., Mar. 25–26, 1982.

11. J. W. Minarick and C. A. Kukielka, *Precursors to Potential Severe Core Damage Accidents: 1969–1979, A Status Report*, NUREG-CR 2497, Nuclear Regulatory Commission, Washington, D.C., June 1982.

12. "Using Experience to Calculate Nuclear Risks," *Science* 217, 338–39 (July 23, 1982).

13. W. Häfele, *Energy in a Finite World*, 2 vols. and Executive Summary, International Institute for Applied Systems Analysis, Laxenburg, Austria, Ballinger Publishing Co., Cambridge, Mass., 1981.

14. J. G. Delene et al., *Nuclear Energy Cost Data Base*, Version 1, DOE/NE-0044, U.S. Department of Energy, October 1982.

15. *Energy Review* 6(3) (entire volume), Data Resources, Inc., Lexington, Mass. (autumn 1982).

16. *HTGR Modular Reactor System (MRS) Design Status Reports*, General Electric Company Advance Reactor Systems Department, Sunnyvale, Calif., October 1982.

17. E. Teuchert, *Once Through Cycles in the Pebble Bed HTR*, JUL-1470 Kernforschungsanlage, Jülich GMbH, Federal Republic of Germany, December 1977.

18. C. L. Smith, "SiC-Fission Product Reactions in HTGR Triso UCO and $UC_xO_y$ Fissile Fuel: I. Kinetics of Reactions in a Thermal Gradient," *J. Am. Ceram. Soc.* 62(11–12), 600–06, (1979).

19. C. L. Smith, "SiC-Fission Product Reactions in HTGR Triso UCO and $UC_xO_y$ Fissile Fuel: II. Reactions Under Isothermal Conditions," *J. Am. Ceram. Soc.* 62(11–12), 607–13 (1979).

20. B. I. Shamasundar et al., *HTGR Fuel Performance Basis*, GA-A16767, GA Technologies, Inc., San Diego, Calif., May 1982; also presented at the Third Japan-U.S. HTGR Safety Technology Seminar, Upton, N.Y., June 2–3, 1982.

21. C. B. Scott et al., *Postirradiation Examination of Capsules P13R and P13S*, GA-A13827, GA Technologies, Inc., San Diego, Calif., October 1976.

22. R. L. Pearson and T. B. Lindemer, "Summary of Simulated Fission Product-SiC Interactions," presented at Workshop on Fission Product-SiC Interactions held at GA Technologies, Inc., San Diego, Calif., Oct. 21–24, 1980.

23. D. J. Naus, "An Evaluation of Pressure Vessel Concepts for Application to High-Temperature Gas-Cooled Modular Reactor Systems," unpublished data, July 1982.

24. C. R. Davis, *A Preliminary Assessment of the Maintenance and In-Service Inspection Requirements for Modular Reactor Systems*, XL-848-00568/P2773, General Electric Company, Sunnyvale, Calif., July 1982.

25. C. R. Hermann and O. Gokuk, *A Preliminary Assessment of the Availability and Capacity Factors for a Modular Reactor System with Reformer (MRS-R)*, General Electric Company report, Sunnyvale, Calif., July 30, 1982.

26. *Modular HTGR Balance of Plant Design and Cost Status Report*, Bechtel Group, Inc., report, San Francisco, Calif., September 1982.

27. *Monolithic Versus Modular HTGR Cost Comparison Report*, Bechtel Group, Inc., report, San Francisco, Calif., September 1982.

# GAS-COOLED REACTOR PROGRAMS

JANUARY 1, 1983

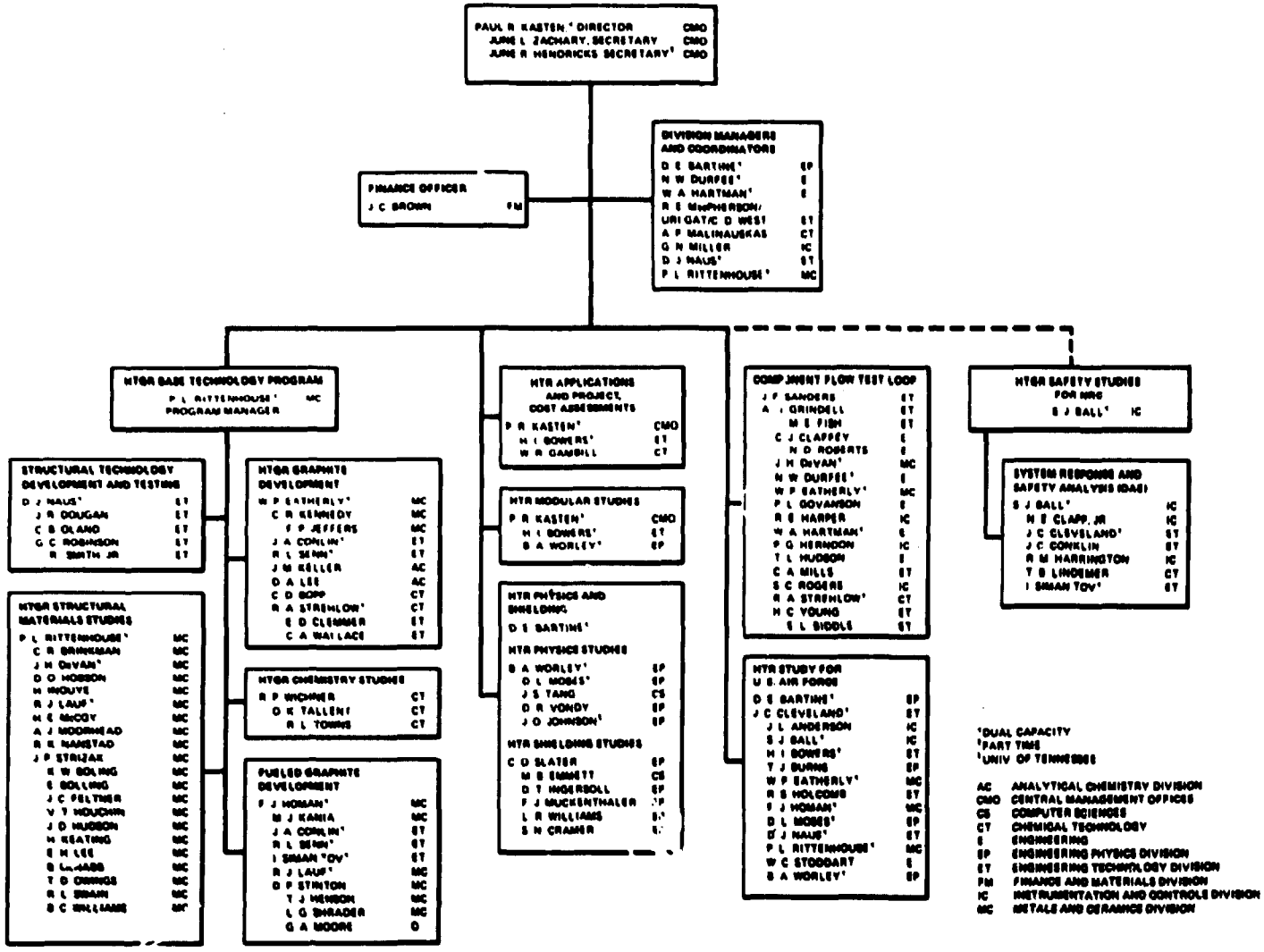


*DUAL CAPACITY
†PART TIME
‡UNIV OF TENNESSEE

| | |
|---|---|
| AC | ANALYTICAL CHEMISTRY DIVISION |
| CMO | CENTRAL MANAGEMENT OFFICES |
| CS | COMPUTER SCIENCES |
| CT | CHEMICAL TECHNOLOGY |
| E | ENGINEERING |
| EP | ENGINEERING PHYSICS DIVISION |
| ET | ENGINEERING TECHNOLOGY DIVISION |
| FM | FINANCE AND MATERIALS DIVISION |
| IC | INSTRUMENTATION AND CONTROLS DIVISION |
| MC | METALS AND CERAMICS DIVISION |

CREDITS:
Composition and makeup: Debbie LeComte
Editing: Irene Brogden

ORNL-5960
Distribution
Category UC-77

## INTERNAL DISTRIBUTION

1–2. Central Research Library
3. Document Reference Section
4–5. Laboratory Records Department
6. Laboratory Records, ORNL RC
7. ORNL Patent Section
8. D. E. Bartine
9. I. H. Brogden
10. J. C. Cleveland
11. J. A. Clinard
12. C. W. Collins
13. J. A. Conlin
14–16. F. R. Cox
17. J. R. Dougan
18. W. P. Eatherly
19. U. Gat
20. R. W. Glass
21. G. M. Goodwin
22–23. A. G. Grindell
24. F. J. Homan
25. J. R. Horton
26. D. W. Jared
27. M. J. Kania
28–37. P. R. Kasten
38. C. R. Kennedy
39. J. F. King
40. W. J. Lackey
41. R. J. Lauf
42. D. A. Lee
43. T. B. Lindemer
44. C. T. Liu
45. A. P. Malinauskas
46. R. W. McClung
47. H. E. McCoy
48. R. K. Nanstad
49. D. J. Naus
50. C. B. Oland
51. C. E. Pugh
52. P. L. Rittenhouse
53. G. C. Robinson
54–56. J. P. Sanders
57. R. L. Senn
58. G. M. Slaughter
59. J. O. Stiegler
60. D. P. Stinton
61. J. P. Strizak
62. D. R. Vondy
63. J. L. Wantland
64. B. A. Worley
65. H. C. Young

## EXTERNAL DISTRIBUTION

66–69. DOE, DIVISION OF HTR DEVELOPMENT, Washington, DC 20545

J. E. Fox
I. L. Helms
G. A. Newby
L. M. Welshans

70. DOE, OFFICE OF CONVERTER REACTOR DEPLOYMENT, Washington, DC 20545

Director

71. DOE, SAN-SAN DIEGO, 110 West A Street, Suite 460,
San Diego, CA 92101

Manager

72. DOE, OAK RIDGE OPERATIONS OFFICE, P.O. Box E, Oak Ridge, TN 37830

Office of Assistant Manager for Research and Development

73–206. DOE, TECHNICAL INFORMATION CENTER, P.O. Box 62, Oak Ridge, TN 37830

For distribution as shown in TID-4500 Distribution Category, UC-77 (Gas-Cooled Reactor Technology)

* U.S. GOVERNMENT PRINTING OFFICE 1983 646 055 51